

Alma Mater Studiorum – Università di Bologna

DOTTORATO DI RICERCA IN

Chimica

Ciclo XXXIII

Settore Concorsuale di afferenza: 03/C1

Settore Scientifico disciplinare: CHIM/06

**SPATIALLY DEFINED PEPTIDOMIMETICS FOR PAIN RELIEF
AND FOR TARGETED CANCER THERAPY AND DIAGNOSTICS**

Presentata da: Junwei Zhao

Coordinatore Dottorato

Domenica Tonelli

Relatore

Luca Gentilucci

Esame finale anno 2021

Contents

Abstract	VII
Chapter 1. Introduction: Spatially Defined Peptidomimetics in Drug Discovery, Especially in Pain Relief	1
1. Cancer Pain and Analgesics	1
2. Peptidomimetics	2
2.1 Peptidomimetics in Drug Design	3
2.2 Modified and Non-Natural / Unusual Amino Acids	4
2.3 Cyclic Peptidomimetics.....	5
2.4. Global Restrictions	5
References	6
Chapter 2. In-Peptide Synthesis of Imidazolidin-2-One Scaffolds, Equippable with Proteinogenic or Taggable/Linkable Side Chains, General Promoters of Unusual Secondary Structures	9
1. Introduction	9
2. Results and Discussion.....	10
2.1 Conformational Analysis.....	11
2.2 Imidazolidin-2-Ones Substituted at the Position 1.....	16
3. Conclusions	20
4. Experimental Section	20
4.1 General Experimental Methods.....	20
4.2 Synthesis of Peptides 1 in Solution.....	21
4.3 Synthesis of Imi-Peptides 2d, e in Solid-Phase.....	22
4.4 Conformational Analysis by NMR.....	23
4.5 Synthesis of Peptides 3	26
4.6 NMR Spectra.....	31
References	50
Chapter 3. Constraining Endomorphin-1 by β,α -Hybrid Dipeptide/Heterocycle Scaffolds: Identification of a Novel κ -Opioid Receptor Selective Partial Agonist.	53
1. Introduction	53
2. Results and Discussion.....	54
2.1 Peptide Synthesis.....	54

2.2 Human ORs Binding Affinity.	55
2.3 Stability of 1 and 4 in Mouse Serum.	56
2.4 Pharmacological Characterization of 1 and 4	56
2.5 Conformational Analysis in-Solution.	58
2.6 Molecular Docking (MDK).	58
3. Conclusions	60
4. Experimental Section	60
4.1 General Methods of Synthesis and Analysis	60
4.2 Synthetic Procedures	61
4.3 Analytical Characterization of 1-4	62
4.4 General Methods of Biological Procedures	66
4.5 Receptor Binding to Cloned Human OR.	66
4.6 Enzymatic Stability.	67
4.7 Determination of Inhibition of cAMP Accumulation for 1 and 4	68
4.8 Warm-Water Tail-Immersion Test.	68
4.9 Conformational Analysis.	69
4.10 Molecular Docking (MDK) for 1 and hKOR (PDB ID: 6B73).	69
References	75
Chapter 4. Synthesis of new selective high-affinity analogs of CJ-15,208 for screening kappa opioid receptor agonists/antagonists.	79
1. Introduction	79
2. Results and Discussion	80
2.1 Synthesis of Cyclic Peptide/Peptidomimetic Minilibrary	80
2.2 Biological Assays in Cells.	84
3. Experimental Section	85
3.1 General Experimental Methods.	85
3.2 General Procedure for the Synthesis of Cyclic Tetra-Peptides/Peptidomimetics	86
3.3 Variable Temperature NMR, gCOSY and 2D ROESY	99
3.4 ¹ H- ¹ H ROESY Data.	100
3.5 Human KOR Binding Affinity.	104
3.6 Assay of Inhibition of cAMP Accumulation for Cyclic Peptides/Peptidomimetics.	104
4. Conclusions	105

References	105
Chapter 5. Review: Integrin-Targeting Peptides for the Design of Functional Cell-Responsive Biomaterials	107
1. Introduction	107
2. Integrins Structure and Functions.....	107
3. Integrin-Related Diseases	108
4. Peptide and Peptidomimetic Integrin Ligands	109
Addressing Integrins with Agonist Ligands	111
5. Integrin-Targeted Peptide Conjugates.....	112
6. Integrin-Targeted NPs	113
6.1. Integrin-Targeted Organic NPs	113
6.2. Integrin-Targeted Inorganic NPs and QDs.....	115
7. Surfaces and Materials Functionalized with Peptidic Integrin Ligands	116
7.1. Self-Assembled Monolayers (SAMs)	117
7.2. Interfaces for Studying of Cell Adhesion, Spreading, and Differentiation	117
7.3. Application in Regenerative Medicine and Tissue Engineering	118
7.4. Fabrication Methods of Integrin Ligand Immobilized Nanostructured Surfaces.....	118
7.5. Detection of Tumor Cells.....	123
7.6. Ligands other than RGD.....	124
7.7. Multifunctional Integrin-Targeting Biocompatible Surfaces	124
8. Nanostructured 2D or 3D Smart Interfaces for Dynamic Cell Adhesion.....	125
8.1. Thermoresponsive Polymers	125
8.2. Enzyme-Triggered Polymers.....	125
8.3. Redox-Switchable Polymers	126
8.4. Potential Responsive Polymers	126
8.5. Photo Responsive Polymers	127
8.6. Electrochemically Controlled Polymers.....	128
8.7. Dynamically Competitive Polymers	128
8.8. Dynamically Controlled Smart Interfaces for 3D Cell Culture.....	128
9. Conclusions	129
References	130

Chapter 6. Integrin-Targeting Dye-Doped PEG-Shell/Silica-Core Nanoparticles Mimicking the Proapoptotic Smac/DIABLO Protein.....	139
1. Introduction.....	139
2. Results.....	140
2.1 Chemistry.....	140
2.2 Cytotoxicity of the Peptide-NPs.....	141
2.3 Caspase-9 Activity.....	142
2.4 Cellular Uptake of Peptide-NPs.....	143
3. Discussion.....	144
4. Conclusions.....	145
5. Experimental Procedures.....	145
5.1 General Methods.....	145
5.2 Solid-Phase Synthesis of H-Asp(OtBu)-D-Phe-Lys(Cbz)-Arg(Mtr)-Gly-OH (Mtr = 4-methoxy-2,3,6-trimethylbenzenesulphonyl).....	146
5.3 Synthesis of c[Arg(Mtr)-Gly-Asp(OtBu)-D-Phe-Lys(Cbz)](Cbz = carbobenzyloxy).....	146
5.4 Synthesis of c[Arg(Mtr)-Gly-Asp(OtBu)-D-Phe-Lys(alkyne)].....	146
5.5 Synthesis of c[Arg-Gly-Asp-D-Phe-Lys(alkyne)] (cRGD-alkyne).....	147
5.6 Synthesis of Boc-Ala-Val-Pro-Ile-Gly-OH.....	147
5.7 Synthesis of Boc-Ala-Val-Pro-Ile-Gly-pent-4-yn-1-amine.....	147
5.8 Dansyl-AVPI-alkyne.....	147
5.9 H-Ala-Val-Pro-Ile-Gly-pent-4-yn-1-amine (AVPI-alkyne).....	147
5.10 Dimesylate Derivative of Pluronic®F127.....	148
5.11 Diazide Derivative of PF127, PF127-(N ₃) ₂	148
5.12 PEG-Shell/Silica-Core NPs.....	148
5.13 Peptide Conjugation to NPs by CuAAC.....	148
5.14 Cell Lines and Culture Conditions.....	148
5.15 Cell Viability Assays.....	149
5.16 Apoptosis.....	149
5.17 Cell Internalization.....	149
5.18 Competition Experiments.....	149
5.19 Determination of NPs Peptide Functionalization.....	149
5.20 Quantification of Dansyl-AVPI-NP.....	150

References	152
Chapter 7. MiniAP4 as Vehicle to Facilitate the Delivery of PEG-Cholic Acid Micellar Nanoparticle Encapsulated Anti-Cancer Drugs Across the Blood Brain Barrier.	157
1. Introduction	157
2. Discussion and results	158
2.1 Synthesis procedure.....	158
2.2 in vivo Assay of the Conjugates of MiniAP4-Biotin and Streptavidin-Cy5.5	160
2.3 in vivo Assay of Dye Loaded N ₃ -NPs(DID) and MiniAP4-NPs(DID) in Healthy Mice.....	161
2.4 in vivo Assay of Dye Loaded N ₃ -Nps(DID) and Miniap4-Nps(DID) in Tumor Bearing Mice	163
3. Experimental Section	164
3.1 General Experimental Methods.....	164
3.2 Synthesis Procedure	165
3.3 Biological and In Vivo Assays	172
4. Conclusion.....	173
References	173
Acknowledgement.....	175

Abstract

The main research content of this thesis includes two parts. The first part is the synthesis of new analgesics related to kappa opioid receptor, and the second part is the tumor-targeted precise cancer therapy and diagnosis.

Cancer is a disease that has plagued scientists for decades, and how to treat cancer and its complications are inevitable topics in current scientific research. Cancer pain is a major factor that reduces the quality of life of patients. Therefore, the development of analgesic agents with minimal adverse side effects, especially with low addiction, has attracted more and more attention. Among them, opioid analgesics are widely used to alleviate cancer pain and improve the quality of life of patients with advanced cancer, such as in the palliative therapy. Although peptide drugs are efficient, selective and safe, they have several unignorable disadvantages such as poor biological stability, rapid excretion, difficulty in penetrate blood brain barrier. In order to solve these problems, peptidomimetics were developed by introducing unnatural/modified amino acids, decorated peptide backbone, conformational restrictions and secondary structure mimics in peptide sequence. Compared with peptides, peptidomimetics have improved biological stability, increased bioavailability, high affinity and selectivity for receptor binding, and decreased adverse side effects.

Firstly, we introduced a flat imidazolidin-2-one (Imi) structure into the peptide backbone. This heterocycle can be regarded as a pseudoproline; While (S)-Imi-containing peptide tends to form a γ -turn conformation, the (R)-configuration Imi promotes the formation of ε -turn. In addition, functional groups can be introduced at the N1 position of Imi to mimic the side chain of natural amino acids. The N1-substituted (R)-Imi peptide still maintains the ability to form an ε -turn. Further chemical reactions on substituted groups for chemospecific derivatization will not affect this conformation. Pseudoproline Imi structure can find many applications prospects in the development of peptidomimetic drugs (Figure 1a).

Secondly, we investigated the use of the aminomethyloxazolidin-2,4-dione (Amo) dipeptide mimetic. These can be regarded as β^2 -variants of the Friedinger lactams. In order to improve biological stability and bioavailability and hence the therapeutic utility of the the natural opioid peptide Tyr-Pro-Trp-PheNH₂ (EM1), stereoisomeric Amo-Trp hybrid scaffolds were introduced in place of Pro-Trp. The compound H-Tyr-(R)-Amo-(R)-Trp-PheNH₂ maintains the MOR preference of the parent peptide, but the affinity to MOR was strongly decreased. However, H-Tyr-(S)-Amo-(S)-Trp-PheNH₂ (Figure 1b) exhibited high selectivity and affinity for KOR. We found that it is a partial KOR agonist, and the related analgesic effect in vivo was determined in vivo by the tail-immersion test. Compared with MOR agonists, selective KOR partial agonists can reduce addiction and other adverse side effects.

Subsequently, in order to find new high-selectivity, high-affinity KOR agonists or antagonists, inspired by our previously synthesized tetrapeptide LOR17, c[Phe-Gly-(beta-Ala)-D-Trp], we replaced Gly² and beta-Ala³ with more flexible residues to prepare a minilibrary of 12-, 13-, or 14-membered cyclic hybrids of LOR17 and of the naturally occurring CJ-15,208, c [Phe-D-Pro-Phe-Trp]. Among these compounds, we found that c[β Ala-D-Trp-Phe- β Ala] has a strong affinity for κ opioid receptors ($K_i = 0.55 \pm 0.04$ nM, Figure 1c) and it is a KOR antagonist, while c[Gly-D-Trp-Phe-GABA] ($K_i = 102 \pm 3$ nM) is a partial agonist of KOR.

As the second part of this thesis, I explored the opportunity to design peptide-functionalized responsive biomaterials for the detection of cancer cell and the selective delivery of cytotoxic drugs. The conjugation of peptides with biomaterials enhanced the stability of the loaded drugs, improved targeted delivery, decreased side effects, and increased bioavailability. The precise and controllable drug delivery platform has profound application prospects in cancer treatment. Grafting specific peptides sequence on the surface of biomaterials can satisfy different drug delivery demands according to the characteristics of both peptides and biomaterials. For example, the introduction of tumor-targeting peptides can guide biomaterials into tumor lesions, and blood-brain barrier (BBB) shuttle peptides can lead biomaterials to penetrate the BBB, etc.

Firstly, we grafted the tumor cell targeting peptide c[RGDfK] and the cytotoxic peptide AVPI onto the surface of PEG-modified and Rhodamine B-doped silica nanoparticles to obtain tumour-targeted cytotoxic NPs (Figure 1d). c[RGDfK] is a potent and selective inhibitor of $\alpha v \beta 3$ integrin, which is selectively expressed in tumors. The AVPI peptide is the N-terminal tetrapeptide region of

Smac/DIABLO protein. The binding of SMAC to IAPs prevents the latter to lose the ability to bind to caspases, resulting in the pro-apoptotic effect. Silica NPs are photophysically inert, non-toxic materials, there are many approaches to tune their size, pore size, shape and surface/pore functionalization. In the *in vitro* assay, we found that AVPI/RGD-NPs show excellent toxicity towards cancer cells A549, U373 and HeLa at micromolar concentrations, and showed little toxicity to non-integrins expressing cells; the NPs did not show any cytotoxicity towards cells not expressing $\alpha 5$ integrin subunits.

Sequently, during my stay at the University of California Davis, I worked on the conjugation of MiniAP4 peptide with PEG_{5k}-Lys₇-CA₈ dendrimers to prepare nanocarrier that can cross the BBB, so as to find a drug delivery platform to treat brain tumors. MiniAp-4 is a cyclic nonapeptide that can penetrate the BBB. It was reported by Professor Giralt and Professor Teixid y in 2016 under the inspiration of Apamin, the neurotoxin of bee venom. As a drug delivery biomaterial, PEG_{5k}-Lys₇-CA₈ dendrimers have preference for tumor penetration. In the *in vivo* experiments, MiniAP4-NPs increased the concentration of cargos delivered into the brain. Interestingly, we also found that MiniAP4@NPs can penetrate tumors, and MiniAP4 peptide may also be a shuttle peptide that crosses the blood tumor barrier. Furthermore, we immobilized MiniAP4, tumor targeting peptide LXY30 and cytotoxic peptide AVPI onto the surface of the PEG_{5k}-Lys₇-CA₈ dendrimers to find a drug delivery platform for brain tumor therapy (Figure 1e).

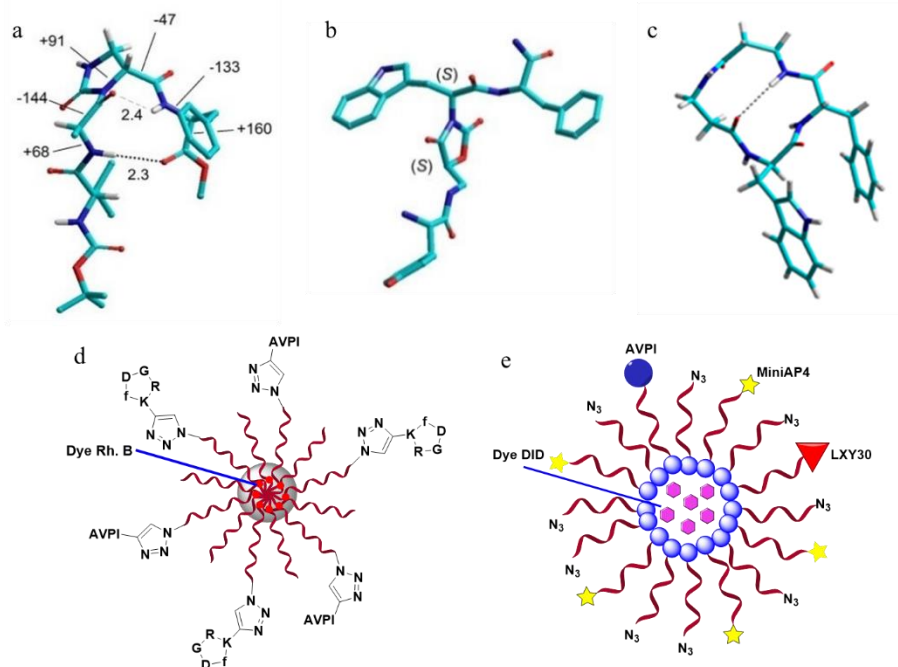


Figure 1. The main research topics of this thesis include the synthesis of new analgesics related to kappa opioid receptor ligands (a,b,c) and biomaterials for tumor-targeted precise cancer therapy and diagnosis (d,e). These results support the use of peptidomimetic for applications in drug discovery for pain relief and in drug delivery for precise cancer therapy.

Key words: peptidomimetics, kappa opioid receptor, ϵ -turn, analgesics, tumor-targeting, peptide conjugate.

Chapter 1. Introduction: Spatially Defined Peptidomimetics in Drug Discovery, Especially in Pain Relief

The research topics of this thesis include two parts, one is pain relief, such as the treatment of cancer pain, and the other is targeted cancer therapy. Peptides and peptidomimetics play an irreplaceable role in the research of drug discovery and tumor targeting therapy. Especially in the field of alleviating cancer pain, such as opioid analgesics. Compared with peptides, peptidomimetics have many advantages as therapeutic agents, such as enhanced bioavailability and biological stability, and improved receptor binding affinity and selectivity. One of the research goals described in this thesis is to discovery peptide/peptidomimetic analgesics with improved efficiency, decreased adverse side effects and addiction. Unlike nonsteroidal anti-inflammatory drugs, opioid receptor agonists play an important role in reducing severe pain. Most of the discoveries of analgesics related to opioid receptor agonists are based on the studies of their subtypes of μ opioid receptor and κ opioid receptor. Another research goal described in this thesis is to construct drug delivery platform for precisely deliver anti-cancer drugs to specific cancer sites without affecting normal tissues. In recent years, more and more attention has been attracted to the research of precise targeted therapy for cancer. To achieving this purpose, the peptides/peptidomimetics with specific biological activity were grafted onto the drug delivery platform. About targeted therapy and diagnosis will be discussed in Chapter 5.

1. Cancer Pain and Analgesics

For decades, a lot of cancer patients have suffered from cancer pain, which is sometimes more unbearable for them than the cancer itself. In palliative cares, when exploring cancer-related pain through phenomenographic study, patients expressed their hope to release pain with minimized adverse side effects. Meanwhile, open and sincere communication between medical staff and patients, formulating pain treatment plans, and the patient's trust in medical staff can help patients to release pain more effectively.^[1]

In 1997, in a study of prospective data on the prevalence and severity of cancer, the two indispensable conditions for service evaluation, a palliative care team found that 70% of the 659 patients with advanced cancer suffered from pain, but after referral to the services, the pain experienced by patients is significantly reduced.^[2]

In the 1980s, the term "hospice care" was changed to "palliative care", and the WHO Cancer Pain Relief Program and its 3-step analgesic ladder were established to ensure that all (advanced) cancer patients can use oral morphine and the use of non-opioid "adjuvant" drugs should also be considered.^[3,4]

In 1988, the palliative care department of a hospital evaluated the WHO Analgesic Guidelines for cancer pain. Among 20 patients, all of them achieved effective pain relief within one week and were maintained for the following 72 weeks. Among them, 18 patients received strong opioid pain medication with an average period of 25.2 weeks, and no serious adverse effects occurred.^[5] In 2012, European Association for Palliative Care (EAPC) updated its guidelines on the use of opioids to treat cancer pain.^[6] In 2013, the European Palliative Care Research Collaborative (EPCRC) studied the quality of life of 1051 incurable cancer patients and found that 63.75% of them suffered from pain. Among them, 50.80% of them suffered from nociceptive pain, and 10.75% of them suffered from neuropathic pain. Patients with neuropathic cancer pain had poorer quality of life in physical, cognitive, and social function, and were more likely to receive strong opioid therapy.^[7]

Cancer pain mostly occurs under the condition of progressive disease, which not only leads to other multiple physical/psychological symptoms and functional decline, but also has mental, survival, family, economic issues to reduce the quality of life of patients.^[8] Tumor-related chronic cancer pain syndromes, including neuropathic syndromes, visceral nociceptive syndromes, somatic nociceptive syndromes. Drug therapy based on opioids is the main method for long-term treatment of chronic pain in patients with active cancer. Opioid analgesics, especially μ -agonist opioids, such as buprenorphine, a partial μ -receptor agonist and κ -receptor antagonist; tramadol and tapentadol, the pure μ -agonist. Of course,

codeine and morphine, which were recommended for WHO analgesic ladder; In addition, for some mild pain patients, some non-opioid analgesics such as, paracetamol and non-steroidal anti-inflammatory drugs can be used.^[9]

In 2020, after secondary data analysis of European Palliative Care Cancer Symptom (EPCCS) data for adults with incurable cancer, it was found that the use of opioids was associated with reduced survival rates, but it may also be due to the reduced survival rate caused by cancer-related systemic inflammation.^[10]

2. Peptidomimetics

The final goal of this topic is to develop peptides/peptidomimetics with high selectivity for each receptor to specifically cause the desired biological effects.

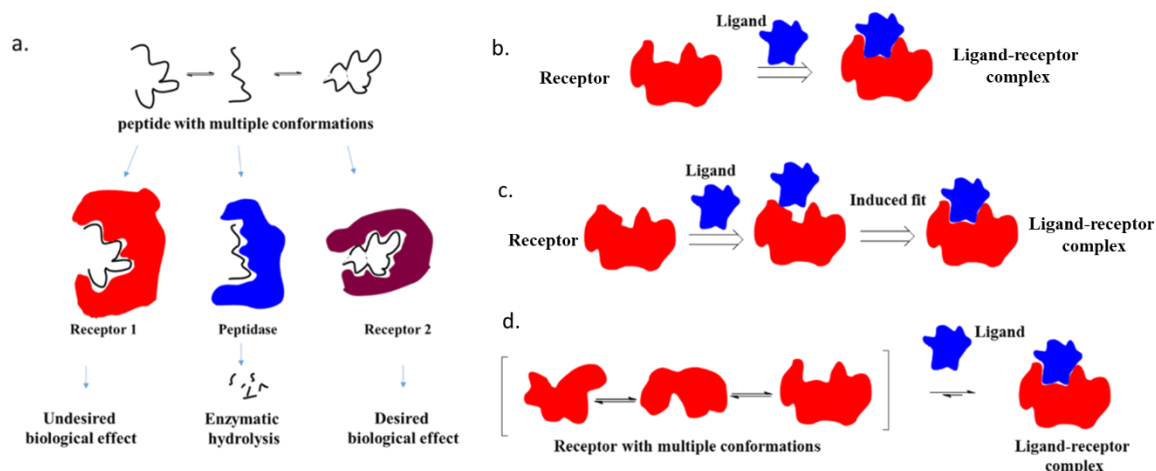


Figure 1. (a) The destiny of peptide with multiple conformations in the process of receptor recognition. Three models of ligand-receptor binding, (b) “lock” and “key” model; (c) induced fit model; (d) “stabilization of receptor conformational ensembles” model.

In solution, peptides have multiple conformations and they are in equilibrium with each other. Therefore, peptides can interact with a variety of receptors or enzymes, thereby reducing the desired activity and bioavailability of the peptides. If the conformational restriction was introduced in peptide sequence, its binding affinity to specific receptors will be increased due to the gain of ligand configurational entropy,^[11] and reduce the interaction with other receptors or enzymes, thereby promoting the desired biological effects (Figure 1a).^[12]

About ligand-receptor binding, Emil Fisher first proposed the “lock and key” rationale in 1894 to illustrate the binding of the ligand to the receptor. In this model, the “key” (ligand) will accurately fit the “lock” (rigid receptor, Figure 1b). In 1958, Koshland proposed an induced fit model (Figure 1c). He believed that the binding of the receptor and the ligand will result in a change in the three-dimensional relationship of the active site. This fit only occurs after the receptor changes, which is caused by the ligand binding. In 1999, the third model was proposed by Nussinov et al., that is, “stabilization of receptor conformational ensembles” model (Figure 1d). They believed that macromolecules exist in a variety of mutually balanced conformations in solution, and the process of ligand binding effectively shifts this balance from the distribution of multiple natural conformations to the receptor-binding conformation.^[13]

Peptides, as drugs, have limited application due to their shortcomings: a) low metabolic stability to proteolysis in the gastrointestinal tract and serum; b) poor absorption after oral administration, especially due to their relatively high molecular weight or lack of specific transport system; c) rapid excretion through the liver and kidney; d) adverse effects due to its conformational flexibility and the ability to interact with various receptors.^[12]

Peptidomimetics are designed based on natural active peptides as lead compounds. Compared with linear peptides, peptidomimetics usually have higher metabolic stability, good bioavailability, enhanced receptor affinity and selectivity, and minimal adverse side effects. The strategy of synthetic

peptidomimetic usually includes: ^[12] a) Modification of amino acids; b) dipeptide analogs instead of dipeptides, such as bridging two neighboring amino acids in peptide sequence, modification of peptide backbone, e.g. isosteric replacement of the amide bond and retro/retro-inverso isomers; ^[14,15] c) cyclization of peptides to restrain the flexibility of peptides strand; d) imitation of secondary structures, such as β -turn, γ -turn. Some successes have been achieved in mimic endogenous peptide ligands, such as Opioids, Tachykinins, Somatostatin (Somatotropin-Release Inhibiting Factor, SRIF); Gastrin-Releasing Peptide (GRP, Bombesin-27); Cholecystokinin and Gastrin; Gonadotropin-Releasing Hormone (GnRH, LH-RH); Angiotensin II (A II); Endothelins; and so on. ^[12] At the same time, peptidomimetics has great potential in drug discovery, such as in analgesics, ^[16] antiobesity agents, ^[17] immunomodulators, autoimmune diseases (such as multiple sclerosis, rheumatoid arthritis, systemic lupus and HIV infection), ^[18] cancer, ^[19] cardiovascular disease, ^[20] antibacterial, ^[21] etc.

2.1 Peptidomimetics in Drug Design

According to the degree of modification of the peptide backbone, in 2015, peptidomimetics were classified by Grossmann et al. into four categories: 1) only a few amino acids were modified in peptide sequence to stabilize the bioactive conformation, with few side chain and backbone changes; 2) various of unnatural amino acids and small molecular blocks have been introduced in the parent peptides, which means that the side chain and backbone of peptides have undergone multiple changes, and the foldamers were included in this category; 3) highly modified structure with small-molecular characteristics, and the peptide backbone was completely replaced; 4) small molecules that simulate the mode of action of biologically active peptides, and have no relationship with side chain functions. ^[22]

In 2018, Perez described two different pathways of designing peptidomimetics drugs: one is the medicinal chemistry method, that is, part of the peptides are successively replaced with non-peptide structures until a non-peptide compound was obtained; the other is the biophysical method, that is, through an overview of the biologically active forms of peptides, and on this basis, appropriate chemical parts are hung on various scaffolds to design peptidomimetics. ^[23]

For biophysical method, in 2020, Kappo et al. described the development of peptidomimetic anticancer drugs by using PPI (Protein-Protein Interaction) inhibition as a potential target of therapeutic drugs. Through the description of PPI and PPI interface, and the discussion of peptidomimetic classification, they finally focused on the application of peptidomimetic in targeting PPI in cancer pathways. ^[24]

For medicinal chemistry method, in 2020, Lenci and Trabocchi described many strategies for peptidomimetics design, mainly including local modification, global restrictions and the use of secondary structure mimics. Local modification is mainly to replace peptide bonds, side chains or dipeptide units by introducing conformationally restricted isosteric groups. This strategy is mostly used in the development of enzyme inhibitors and receptor ligands. Secondary structure mimics are designed to reproduce the structure of helices, turns and β -sheets, mainly used in the development of PPI regulators. Global restrictions are mainly used to develop small-molecule peptidomimetics and stabilize the secondary structure of peptides. Peptide stapling and hydrogen bond replacement are conducive to stabilizing the α -helix, while the introduction of chemical tethers tends to stabilize the β -turn and β -hairpins structure. ^[25]

In 2011, Kemmink et al. described that the study of oligomeric peptidomimetics such as peptoids, peptidosulfonamides, urea peptidomimetics, as well as β -peptides have sprouted. Small peptides have no secondary structure, and their secondary structure is usually controlled by introducing α,α -disubstituted amino acids, or (di)peptidomimetic structures, such as the Freidinger lactam, intra-amino acid constraints and inter-amino acid constraints, providing an excellent pathway for the diversity of cyclic peptides. There are many examples of intra- /inter- amino acid restrictions, such as disulfide bonds, sulfide and triazole bridges, single/double/triple bond substitution. Besides β -peptides and peptoids, urea peptidomimetics, peptidosulfonamides are more suitable to replace specific amino acid residues or part of peptide sequence. Peptide-peptidomimetic hybrids are also very important, as TS isosteres, or helix, or β -sheet breakers. The goal of development of oligomeric peptidomimetics is to improve biological activity and availability. For a specific peptidomimetic with a defined spatial structure, the most important thing is to increase its affinity. So there are many β -, γ -turn, even α -helix mimetics was described for this purpose. A lot of works on α,α -disubstituted amino acids show that it is more likely to promote the formation of 3_{10} -helical structures. In addition, it is assumed that short oligomers of β -amino

acids have defined helical structure, which has attracted research interests in related fields. Disulfide and sulfide bridges are used to control shape and folding in many peptidomimetic structures (“stapled” peptides). At the same time, the alkene bridge formed by ring-closing metathesis and its derived alkane bridge are also good choices for improving structural stability and biological properties. The introduction of triazole ring through click chemistry to achieve conformational restriction is more suitable for constructing less flexible peptidomimetic structures.^[26]

In 2008, Hraby et al. discussed the synthesis of conformationally restricted building blocks and peptide bond isosteres.^[27] In 2009, König et al. discussed the modification of amino acid and backbone in peptidomimetic design with examples, and global restrictions were realized through cyclization and synthetic backbone scaffolds.^[28]

In 2014, Fairlie et al. described a simple and convenient method to reconstruct the smallest structural elements of proteins in small cyclic peptides. Proteins exert their biological activity through folded peptides with three-dimensional structures exposed on their surfaces, and these short peptides cannot form thermodynamically stable protein-like structures in water. However, through cyclization and other molecular constraints, it can be induced and folded into a protein-like biologically active conformation, which can be used to develop therapeutic, diagnostic drugs and vaccines. They introduced cyclic peptides to mimic the three-dimensional structure of proteins, such as chains, turns or helical segments, and also introduced other constraints to improve the peptide structure and transform this structure into effective and subtle selective biological activities.^[29]

2.2 Modified and Non-Natural / Unusual Amino Acids

Among all peptidomimetic synthesis strategies, modifying amino acids is the simplest and most effective strategy, and of course it is also an important strategy for peptidomimetic synthesis. In order to improve the properties of peptides, for example, using non-natural/unusual amino acids to introduce H-bonding groups on side chains, unnatural amino acids were utilized to substitute natural amino acids, such as D-conformational, N-alkylated, C α tetra-substituted, side chain modified and β -, γ - amino acids, sugar amino acids, aza-amino acids, aminoxy acids, and β -branched amino acids, etc.^[30]

In addition, some other interesting modified amino acids have been reported in recent years, Shown as follows:

In 2008, synthetic strategies about α -trifluoromethyl and α -difluoromethyl substituted α -amino acids were reported by Kocsch and coworkers.^[31] In the same year, Guama et al. introduced bicyclic amino acids with diverse structures.^[32] Also in 2008, Kessler and coworkers described several approaches for synthesis of mono- and multiple N-methylation of peptides. By giving space constraints in the peptide backbone to clarify its remarkable spatial regulation ability and improve the pharmacokinetic properties of peptides. It simplifies the synthesis of N-methylation amino acids under mild conditions in solution, and optimizes the method of quick and inexpensive synthesis of N-methylation peptides on solid support.^[33] Regulating the conformation of the peptidomimetic can not only enhance receptor-binding affinity and selectivity, but also increase cell membrane permeability. The inherent flexibility of peptides and their dynamic conformational changes when binding to receptors make the design of three-dimensional peptidomimetic structures challenging. To solve this problem, in 2017, Shuto et al. introduced cyclopropane in peptidomimetic structure due to its unique three-dimensional electronic characteristics, it is very attractive in terms of structural limitations of peptoids, such as cis- / trans-restriction by cyclopropane, and peptoids oriented synthesis strategy with three-dimensional structural diversity.^[34] In 2016, Cavelier et al. summarized a series of synthetic methods of silicon-containing amino acids, also conformational studies, biological activity. Silicon-containing peptides have excellent oral bioavailability and increased stability of proteolytic enzymes. In addition, the lipophilicity of silicon atoms can facilitate their transmembrane ability, thereby increasing its bioavailability. Silicon-containing compounds have attracted more and more attention in the development of new drugs, and many new silicon-containing medicines have already been on the market.^[35] In 2011, Mollica et al. described the χ -space control of histidine analogs to design peptidomimetic drugs, introducing χ -space restricted amino acids into biologically active peptides so that the χ^1 and χ^2 torsion angles of the pharmacophore of amino acids are related to the structure of the lead compound. Consistently, this is very important for the activity and selectivity of the peptidomimetic.^[36]

2.3 Cyclic Peptidomimetics

Compared with linear peptides, cyclic peptides are more likely to form intramolecular hydrogen bonds, salt bridges, disulfide bonds, etc., thereby stabilizing their structure. Due to the rigid conformation of cyclic peptides, it exhibits better biological activity than linear peptides. In 2012, Joo et al. discussed the role of cyclic peptides in therapy, such as the bactericidal activity of tyrosine and gramicidin S, the immunosuppressive activity of cyclosporin A, the anti-angiogenic activity of RGD peptide, the cyclic peptide found in natural peptide hormones. The methods for developing cyclic peptide compounds also be described, such as phage display technology, synthesis in vivo, from mRNA display, chemical synthesis method, from split-and-pool synthesis. Cyclic peptides are used as biochemical tools as receptor agonists/antagonists, as enzyme inhibitors and RNA binding.^[37] Li et al. discussed strategies for peptide macrolactamization, methodology for synthesis of disulfide-bridged and ether-bridged cyclic peptides/peptidomimetics.^[38] Hunter et al. discussed a series of strategies for fine-tuning the conformations of cyclic peptides by applying greater rigidity, subtly changing certain side chain vectors, or by adjusting the global shape of the macrocycle.^[39] The method of fine-tuning the cyclic peptides are as follows.^[22,28,39]

2.3.1 Modification of Amino Acid

a) Modifications on the α -carbon, for example, after introducing a single D-amino acid into the peptide chain of L-amino acid, the D-amino acid tends to occupy the $i + 1$ position of β II'-turn;^[40] when the L-amino acid and D-amino acid alternately appeared in the cyclic peptide structure, they were more likely to form macromolecule aggregation to form nanotubes; about retro-inverso cyclic peptides, inverting all of the stereocenters of peptide and direction of the amino acid sequence will remain their biological activity and increase their biological stability, but not all retro-inverso cyclic peptides retained their biological activity;^[14] α,α -disubstituted amino acids resulted in conformational homogenization, which may lead the structure to be highly strained in the small ring, and tend to form a turn structure in the large ring structure.

b) N-methylation was most commonly used modification in peptidomimetics. By introducing constraints in space, N-methylation promoted the formation of *cis*- amides and prevented specific hydrogen bond formation to affect molecular conformation. Besides methyl substitution, the introduction of a larger N-alkyl group can promote the formation of a better rigid structure and thus a better biological activity.^[41]

2.3.2. Modification of Peptide Backbone

The strategy of isosteric replacement of the amide bond is most interesting topic in peptide backbone modification. Isosteres of the amide bond include thioamides, alkenes, reduced amides, esters, phosphinic acid, and heterocyclic amide.^[38]

a) Thioamides increased structural rigidity, bonding capacity of hydrogen and metabolic stability, and reduced *cis/trans* isomerization of peptides. Meanwhile, if hydrogen-bonded amides in peptidomimetics sequence were replaced with thioamides, their conformations would be changed; on the contrary, if the replacement of amides did not break the hydrogen bonds, the conformation would be maintained.

b) E-alkenes usually used to mimic *trans*- amide.^[42]

c) Secondary amines are strong electron donors under physiological pH conditions and have the role of rigidifying the molecular structure.

d) The replacement of esters made the molecule flexible, recombined as required, and easily dissolved in polar solvents, but the conformation of its lead compound would not be changed.

e) The $-\text{PO}_2-$ oxygen atom of phosphinic acid (PO_2-CH_2) was usually placed outside the ring structure.

f) The introduction of small heterocycles (such as oxazole, oxazoline, thiazole, thiazoline, triazole, oxadiazole) made the compound more rigid, which can be used to introduce unique conformation to the structure of peptidomimetics, the unique structure is important for biological activity.

2.4. Global Restrictions

a) Converting linear peptides to macrocycles is an excellent strategy for producing peptidomimetics with reduced conformation, and the cyclization strategies include head-to-tail cyclisation, side chain-to-side chain cyclisation, and backbone-to-side chain cyclisation. [28]

b) Mimetics of turn structures, such as γ -, β -, α -turn mimetics

Single-turn mimetics were stabilized by performing of macrocyclization, N-methylation, or introducing turn-inducing amino acids, structural mimetics and turn motif mimetics. [22] Macrocyclization is usually carried out through disulfide bonds or sulfide bridges, etc. Incorporating proline/proline-type structures, dipeptide lactams into the backbone of cyclic peptidomimetics tend to introduce β -turns into the structure. L-proline tends to form cis amides, and non-natural proline analogues tend to form cis α -pro amide configuration. [39] N-methylation can reduce the number of hydrogen bond donors and increase steric hindrance, thereby affecting the conformational freedom of adjacent amino acids. The introduction of small molecular structure mimics has improved oral bioavailability and pharmacokinetic properties. [22]

c) Mimetics of β -strands, β -sheets and helices

The introduction of β -hairpin inducers, β -strand-enforcing amino acids, structural β -strand mimetics, or macrocyclization was used to stabilize β -sheets or β -strands. On the other hand, side chain to side chain cross-links, such as thiol-based cross-links, lactam cross-links, triazole cross-links, α -methylated hydrocarbon cross-links were served as to mimetic helices. In addition, the introduction of N-terminal caps, foldamers (β -peptides, α/β -peptides, peptoids), structural helix mimetics, or scaffolds with steric hindrance, hydrogen-bond guidance and covalent restraint was also a popular strategy for introducing and stabilizing secondary structure. [22]

Need to be mentioned, disulfide bonds can increase the structural restriction, thereby stabilizing secondary structures such as β -turns and β -sheets; while biaryls and biaryl ethers in cyclic peptides usually giving a cis amide containing β -turn; and lactam bridges usually giving a bicyclic structures, which gives no sequence of cyclic peptide conformational homogeneity. [39]

References

-
1. B. Bostrom, M.Sandh, D. Lundberg, B. Fridlund. Cancer-related pain in palliative care: patients' perceptions of pain management. *J. Adv. Nurs.* **2004**, *45*, 410-419.
 2. I.J. Higginson, J. Hearn. A multicenter evaluation of cancer pain control by palliative care teams. *J. Pain Symptom Manage.* **1997**, *14*, 29-35.
 3. S.H. Ahmedzai. Pain, Cancer and palliative care. *Rev. Pain.* **2010**, *4*, 1.
 4. M. Meldrum. The ladder of the clock: cancer pain and public policy at the end of the twentieth century. *J. Pain Symptom Manage.* **2005**, *29*, 41-54.
 5. V.A. Walker, P.J. Hoskin, G.W. Hanks, I.D. White. Evaluation of WHO analgesic guidelines for cancer pain in a hospital-based palliative care unit. *J. Pain Symptom Manag.* **1988**, *3*, 145-149.
 6. A Caraceni, G Hanks, S Kaasa, MI Bennett, C Brunelli, et al. Use of opioid analgesics in the treatment of cancer pain: evidence-based recommendations from the EAPC. *Lancet Oncol.* **2012**, *13*, 58-68
 7. C. Rayment, M. J. Hjermstad, N. Aass, S. Kaasa, A. Caraceni, F. Strasser, E. Heitzer, R. Fainsinger, M. I. Bennett. Neuropathic cancer pain: prevalence, severity, analgesics and impact from the european palliative care research collaborative-computerised symptom assessment study. *Palliat. Med.* **2013**, *27*, 714-721.
 8. R.K. Portenoy, P. Lesage. Management of cancer pain. *Lancet* **1999**, *353*, 1695-1700.
 9. R.K. Portenoy. Treatment of cancer pain. *Lancet* **2011**, *377*, 2236-2247.
 10. J.W. Boland, V. Allgar, E.G. Boland, M.I. Bennett, S. Kaasa, M. Jensen, H. & M. Johnson. The relationship between pain, analgesics and survival in patients with advanced cancer; a secondary data analysis of the international European palliative care cancer symptom study. *Eur. J. Clin. Pharmacol.* **2020**, *76*, 393-402.

-
11. C.-E.A. Chang, W. Chen, and M.K. Gilson. Ligand configurational entropy and protein binding. *PNAS*, **2007**, *104*, 1534-1539.
 12. A. Giannis and T. Kolter. Peptidomimetics for receptor ligands-discovery, development, and medical perspectives. *Angew. Chem. Int. Ed.* **1993**, *32*, 1244-1267.
 13. M.G. Bursavich and D.H. Rich. Designing non-peptide peptidomimetics in the 21st century: inhibitors targeting conformational ensembles. *J. Med. Chem.* **2002**, *45*, 541-558.
 14. R.A. Altman, K.K. Sharma, L.G. Rajewski, P.C. Toren, M.J. Baltezor, M. Pal, and S.N. Karad. Tyr¹-ψ[(Z)CF=CH]-Gly² fluorinated peptidomimetic improves distribution and metabolism properties of Leu-Enkephalin. *ACS Chem. Neurosci.* **2018**, *9*, 1735-1742.
 15. J. Rai. Peptide and protein mimetics by retro and retroinverso analogs. *Chem. Biol. Drug Des.* **2019**, *93*, 724-736.
 16. A.K. Giri and V.J. Hruby. Investigational peptide and peptidomimetic μ and δ opioid receptor agonists in the relief of pain. *Expert Opin. Investig. Drugs.* **2014**, *23*, 227-241.
 17. M.S. Kumar. Peptides and peptidomimetics as potential antiobesity agents: overview of current status. *Front. Nutr.* **2019**, *6*, 11.
 18. A.S. Gokhale, S. Satyanarayanajois. Peptides and peptidomimetics as immunomodulators. *Immunotherapy.* **2014**, *6*, 755-774.
 19. L. Stone. Peptidomimetics have potential. *Nat. Rev. Urol.* **2017**, *14*, 328.
 20. C. Recio, F. Maione, A.J. Iqbal, N. Mascolo, V. De Feo. The potential therapeutic application of peptides and peptidomimetics in cardiovascular. *Front. Pharmacol.* **2017**, *7*, 526.
 21. H.I. Mosberg, L. Yeomans, A.A. Harland, A.M. Bender, K. Sobczyk-Kojiro, J.P. Anand, M.J. Clark, E.M. Jutkiewicz, and J.R. Traynor. Opioid peptidomimetics: leads for the design of bioavailable mixed efficacy μ opioid receptor (MOR) agonist/δ opioid receptor (DOR) antagonist ligands. *J. Med. Chem.* **2013**, *56*, 2139-2149.
 22. M. Pelay - Gimeno, A. Glas, O. Koch, T.M. Grossmann. Structure - based design of inhibitors of protein-protein interactions: mimicking peptide binding epitopes. *Angew. Chem. Int. Ed.* **2015**, *54*, 8896-8927.
 23. J.J. Perez. Designing peptidomimetics. *Curr. Top. Med. Chem.* **2018**, *18*, 566-590.
 24. L. Mabonga, A.P. Kappo. Peptidomimetics: a synthetic tool for inhibiting protein-protein interactions in cancer. *Int. J. Pept. Res. Ther.* **2020**, *26*, 225-241.
 25. E. Lenci and A. Trabocchi. Peptidomimetic toolbox for drug discovery. *Chem. Soc. Rev.* **2020**, *49*, 3262-3277.
 26. R.M.J. Liskamp, D.T.S. Rijkers, J.A W. Kruijtzter, J. Kemmink. Peptides and proteins as a continuing exciting source of inspiration for peptidomimetics. *ChemBioChem* **2011**, *12*, 1626-1653.
 27. J. Vagner, H. Qu and V. J. Hruby .Peptidomimetics, a synthetic tool of drug discovery. *Curr. Opin. Chem. Biol.* **2008**, *12*, 292-296.
 28. A. Grauer and B. König. Peptidomimetics - a versatile route to biologically active compounds. *Eur. J. Org. Chem.* **2009**, *2009*, 5099-5111.
 29. T.A. Hill, N.E. Shepherd, F. Diness, D.P. Fairlie. Constraining cyclic peptides to mimic protein structure motifs. *Angew. Chem. Int. Ed.* **2014**, *53*, 13020-13041.
 30. D. Goodwin, P. Simerska and I. Toth. Peptides as therapeutics with enhanced bioactivity. *Curr. Med. Chem.* **2012**, *19*, 4451-4461.
 31. R. Smits, C.D. Cadicamo, K. Burger and B. Kocsch. Synthetic strategies to α-trifluoromethyl and α-difluoromethyl substituted α-amino acids. *Chem. Soc. Rev.* **2008**, *37*, 1727-1739.
 32. A. Trabocchi, D. Scarpi, and A. Guarna .Structural diversity of bicyclic amino acids. *Amino Acids* **2008**, *34*, 1-24.

-
33. J. Chatterjee, C. Gilon, A. Hoffman, and H. Kessler. N-Methylation of peptides: a new perspective in medicinal chemistry. *Acc. Chem. Res.* **2008**, *41*, 1331-1342.
34. A. Mizuno, K. Matsui, S. Shuto. From peptides to peptidomimetics: a strategy based on the structural features of cyclopropane. *Chem. Eur. J.* **2017**, *23*, 14394-14409.
35. E. Rémond, C. Martin, J. Martinez, F. Cavelier. Silicon-containing amino acids: synthetic aspects, conformational studies, and applications to bioactive peptides. *Chem. Rev.* **2016**, *116*, 11654-11684.
36. A. Stefanucci, F. Pinnen, F. Feliciani, I. Cacciatore, G. Lucente and A. Mollica. Conformationally constrained histidines in the design of peptidomimetics: strategies for the χ -space control. *Int. J. Mol. Sci.* **2011**, *12*, 2853-2890.
37. S. H. Joo. Cyclic peptides as therapeutic agents and biochemical tools. *Biomol. Ther.* **2012**, *20*, 19-26.
38. P. Li, P.P. Roller and J. Xu. Current synthetic approaches to peptide and peptidomimetic cyclization. *Curr. Org. Chem.* **2002**, *6*, 411-440.
39. R. Jwad, D. Weissberger and L. Hunter. Strategies for fine-tuning the conformations of cyclic peptides. *Chem. Rev.* **2020**, *120*, 9743-9789.
40. M. Kodaka, T. Shimizu, and M. Hatano. Conformation of Cyclo(L-Ser(O-Bzl)-D-Leu-L-His)₂ and Cyclo(L-Ser-D-Leu-L-His)₂ in solution. *Polymer Journal* **1984**, *16*, 217-222.
41. O. Demmer, A.O. Frank, F. Hagn, M. Schottelius, et al. A conformationally frozen peptoid boosts CXCR4 affinity and anti-HIV activity. *Angew. Chem., Int. Ed.* **2012**, *51*, 8110-8113.
42. H. Tamamura, K. Hiramatsu, S. Ueda, Z. Wang, et al. Stereoselective synthesis of [L-Arg-L/D-3-(2-Naphthyl)-Alanine]-type (E)-alkene dipeptide isosteres and its application to the synthesis and biological evaluation of pseudopeptide analogues of the CXCR4 antagonist FC131. *J. Med. Chem.* **2005**, *48*, 380-391.

Chapter 2. In-Peptide Synthesis of Imidazolidin-2-One Scaffolds, Equippable with Proteinogenic or Taggable/Linkable Side Chains, General Promoters of Unusual Secondary Structures

Peptidomimetics containing (S)- or (R)-imidazolidin-2-one-4-carboxylate (Imi) have been obtained by the expedient in-peptide cyclization of (S)- or (R)- α,β -diaminopropionic acid (Dap) residues. These Imi scaffolds behave as proline analogues characterized by a flat structure and a transrestricted geometry of the preceding peptide bond and induce well-defined secondary structures in a biomimetic environment. While (S)-Imi peptides adopted a γ' -turn conformation, (R)-Imi induced the contemporary formation of a γ -turn and a rare 11-membered H-bonded structure in the 2 \rightarrow 4 opposite direction of the sequence, identified as a ϵ -turn. In order to exploit these Imi scaffolds as general promoters of unusual secondary structures, proteinaceous side chains have been introduced at the N1 position of the five-membered ring, potentially mimicking any residues. Finally, the Imi rings have been equipped with unnatural side chains or with functionalized substituents, which can be utilized as linkers to chemoselectively bind the Imi-peptides onto nanoparticles, biomaterials, or diagnostic probes.

1. Introduction

Heterocyclic-based peptidomimetics have been widely utilized to increase metabolic and conformational stability of the parent peptides. [1] Amid them, N-heterocycles are prevalent in biologically active peptides and are increasingly attractive scaffolds in the development of new pharmaceuticals. [2] Relevant examples include pseudo-prolines, [3] Freidinger–Veber lactams or analogues, [4] and cyclic urea scaffolds. [5]

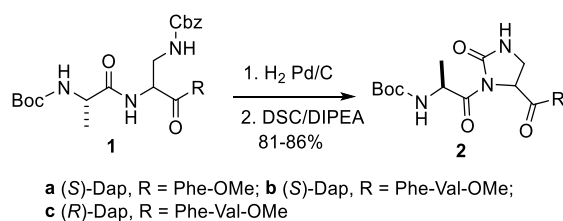
In particular, the latter have been utilized as structural elements in peptidomimetic inhibitors of HIV protease and HIV replication, [6] antibacterial MurB inhibitors, [7] dopamine D4 and CGRP receptor antagonists, [8] angiotensin converting enzyme (ACE) inhibitors, [9] serine protease inhibitors, [10] and integrin inhibitors. [11] In the literature, cyclic ureas are most commonly constructed via treatment of 1,2-diamine precursors with carbonyldiimidazole, [6] or by intramolecular diamination of alkenes, [12] via rearrangement of Asn, [9,13] via ring expansion of aziridine derivatives, [14] by cyclization of aza-propargylglycine-mides, [5b] by alkylation of the urea nitrogen of semicarbazone residues, [15] by Pd-catalyzed urea carboamination reactions, [16] and so on. Although a number of synthetic methods are available, many are not feasible in peptide chemistry. Thus, alternative strategies for the construction of cyclic ureas would provide more facile access to a class of peptidomimetics that are not readily available. In this context, herein, we report the expedient synthesis of peptidomimetics containing imidazolidin-2-one-4-carboxylate (Imi) scaffolds by cyclization of sequences containing α,β -diaminopropionic acid (Dap). The unexpected conformational features of the Imi-peptides are also discussed with the aid of NMR analysis and molecular dynamics simulations.

Furthermore, peptides containing N β -substituted Dap have been obtained from β -iodoalanine by displacement with N-nucleophiles. The cyclization of the substituted Dap residues gave access to Imi-peptides carrying proteinogenic or unnatural side chains at the position 1 or eventually providing useful handles at which to undertake site-selective modifications of the sequences. [17] As a proof of

concept, the allyl substituent at the position 1 of the Imi ring was selectively derivatized by the Heck reaction.

2. Results and Discussion

Imi-Peptides Synthesis. Model peptides **2** containing (S)- or (R)-Imi scaffolds have been obtained by the easy cyclization of the corresponding sequences **1** containing Dap (Scheme 1 and Table 1). The preparation of the peptides **1a–c** was conducted by coupling in solution Boc-protected amino acids to amino ester counterparts under MW irradiation ^[18] using a microwave oven specifically designed for organic synthesis, with N-(3-dimethylaminopropyl)-N'-ethylcarbodiimide (EDC·HCl) and 1-hydroxybenzotriazole (HOBt) as activating agents, in the presence of triethylamine (TEA). Several Dap-protected variants are commercially available; herein, Dap was introduced as Boc-Dap(Cbz)-OH. In any case, Dap can be rapidly prepared following the literature ^[19] and protected thereafter with the appropriate group.



Scheme 1. Cyclization of Dap-peptides **1** to Imi-peptides **2**.

Boc deprotection was performed with 25% trifluoroacetic acid (TFA) in dichloromethane (DCM). The intermediates, obtained in quantitative yield, were not purified, while the final sequences **1a–c** were isolated in 80–85% yield by flash chromatography over silica gel (eluent 1:2 cyclohexane/EtOAc). Their identity was confirmed by ESI MS analysis, and purity was assessed to be 80–90% by RP HPLC.

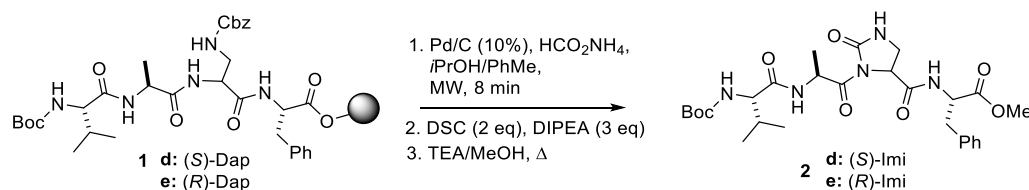
Table 1. Synthesis of Model Imi-Peptides **2** by Cyclization of the Corresponding Dap-Containing Peptides with DSC/DIPEA.

2	sequence	peptide synthesis	yield %	purity %^a
a	Boc-Ala-(S)-Imi-Phe-OMe	in-solution	86 ^b	92
b	Boc-Ala-(S)-Imi-Phe-Val-OMe	in-solution	88 ^b	93
c	Boc-Ala-(R)-Imi-Phe-Val-OMe	in-solution	91 ^b	93
d	Boc-Val-Ala-(S)-Imi-Phe-OMe	SPPS	84 ^c	95
e	Boc-Val-Ala-(R)-Imi-Phe-OMe	SPPS	86 ^c	96

^aDetermined by RP HPLC. ^bYield of the cyclization step, after isolation by RP HPLC. ^cCalculated on the average resin load, after isolation by RP HPLC.

After removal of the Nβ-Cbz group by catalytic hydrogenation, the Dap-peptides were treated without further purifications with N,N'-disuccinimidyl carbonate (DSC) ^[3b,c] and N,N-diisopropylethylamine (DIPEA) in 3:1 DCM/DMF, giving the Imi-peptides **2a–c** in good yield (86–91%) after isolation by semipreparative RP HPLC (Scheme 1, Table 1), >90% pure as determined by analytical RP HPLC. The identity of the compounds **2a–c** (and of the Imi-peptides described in the next sections) was confirmed

by exact mass, proton-decoupled ^{13}C NMR, and ^1H NMR (the unambiguous assignment of the resonances was done by 2D gCOSY).



Scheme 2. SPPS of Imi-peptides **2d** or **2e**.

Also, Imi-peptides were successfully obtained by solid-phase peptide synthesis (SPPS) (Scheme 2). The tetrapeptides Boc-Val-Ala-(S)/(R)-Dap(Cbz)-Phe-resin (**1d**, **1e**) were prepared onto a Phe-preloaded Wang resin using standard Fmoc-protected amino acids and the HOBt/dicyclohexylcarbodiimide (DCC) coupling agents under MW irradiation. Fmoc was removed by treatment with piperidine/DMF. After deprotection of the Cbz group by catalytic hydrogenation with ammonium formate (4 equiv) in isopropanol/toluene, ^[20] cyclization was done on resin with DSC and DIPEA (3 equiv each) under recently refined reaction conditions. ^[21] Subsequently, the cleavage from the resin with refluxing MeOH/TEA (Scheme 2) gave the peptides **2d** or **2e**, isolated in a very satisfactory yield and purity (84 and 86%, respectively, calculated on the basis of the average resin load, Table 1) as described above. These peptides were prepared as methyl esters and with Boc at the N-terminus, for structural comparison with the peptides **2b**, **c** (see next paragraph).

Epimerization of Dap during peptide synthesis and cyclization, in solution or in solid phase, was excluded on the basis of the analysis of the reaction mixtures of **2a–c** by HPLC MS and NMR.

2.1 Conformational Analysis.

X-ray crystallographic analysis of 3-acyl-imidazolidine-2-one-4-carboxylates showed that these heterocycles have a planar imidazolidine-2-one ring, and the amide bond at the 3-position is restricted to the trans geometry, coplanar with the five-membered ring. ^[22] Theoretical computations quantified that the differences in potential energy between the cis- and trans-conformers were so large that the unstable cis-conformer would have an extremely low concentration. ^[23] This is in contrast to proline, which shows a puckered conformation of the pyrrolidine ring and is involved in a trans/cis equilibrium about the preceding amide bond. ^[24] Hence, it is expected that the introduction of Imi scaffolds into a peptide sequence might impose alternative conformations and unusual secondary structures. Previous investigations on oligopeptides containing oxazolidin-2-one-4-carboxylates as pseudo-prolines showed the ability of the heterocycles to stabilize turns, foldamers, ^[3c,d,25] or even to form hydrogels. ^[26]

In this perspective, the conformational bias exerted by the Imi scaffold on the overall structure of model tetrapeptides was analyzed by NMR experiments at 400 MHz in 8:2 $[\text{D}_6]\text{DMSO}/\text{H}_2\text{O}$, a solvent mixture recommended by several authors as an excellent biomimetic medium, in which intermolecular interactions are generally negligible for peptide concentrations in the millimolar range. ^[27] In any case, self-association of the peptides was excluded based on the absence of concentration effects on the chemical shift of non-exchangeable protons. ^[25,28] As representative examples, we analyzed the tetrapeptides **2b** and **2c**, which include (S)- or (R)-configured Imi, respectively, at the position 2 of the sequence, and peptides **2d** and **2e** having (S)- or (R)-Imi at the position 3. All spectra showed a single set of sharp resonances, suggestive of conformational homogeneity or of a fast equilibrium between slightly

different conformers. gCOSY experiments were utilized for the unambiguous assignment of the resonances.

In analogy to what was observed for peptides containing oxazolidin-2-one-4-carboxylates, a nonconventional $\text{ImiC=O}\cdots\text{H-C}(\alpha-1)$ intramolecular H-bond was expected (Figure 1).^[3c,d,25] Indeed, the ^1H NMR analyses of all of the compounds showed a significantly downfield position of the α -proton of the residues preceding the Imi rings, consistent with the deshielding effect exerted by ImiC=O for a trans conformation of the amide bond between $\text{Ala}^1\text{-Imi}^2$ (Figure 1). For instance, in Boc-Ala-(S)-Imi-Phe-Val-OMe (**2b**), the resonance of $\text{AlaH}\alpha$ appeared at about 5.2 ppm, while $\text{PheH}\alpha$ and $\text{ValH}\alpha$ appeared at about 4.6 and 4.2 ppm.

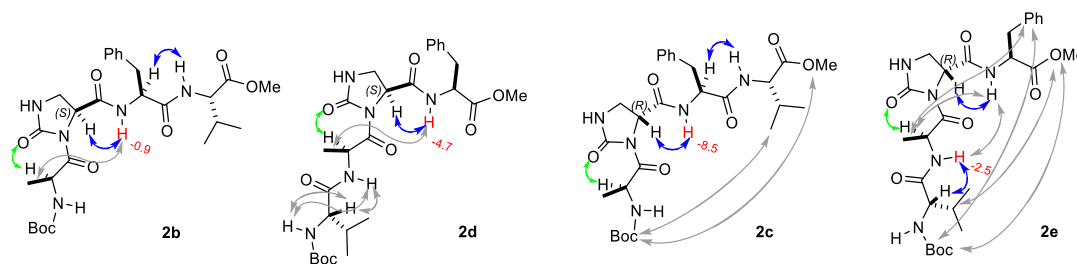


Figure 1. Sketches of **2b–e** showing selected, meaningful proton-proton NMR correlations indicated by arrows. The nonconventional $\text{ImiC=O}\cdots\text{H-C}(\alpha-1)$ intramolecular interaction is rendered in green, strong ROESY correlations are given in blue, medium-intensity correlations in grey. The $\Delta\delta/\Delta t$ values for selected amide protons are also shown as red figures.

Variable-temperature (VT) ^1H NMR experiments have been widely utilized as a tool for structure investigation in polypeptides. Usually, for proteins or “rigid” peptides, the bonded amide-NH signals are characterized by modest temperature gradients in absolute value, that is, $|\Delta\delta_{\text{NH}}/\Delta t| \leq 2.5$ ppb/K,^[29] while solvent-exposed NHs have larger negative values. Unfortunately, for acyclic peptides, this “rule” has many exceptions.^[30] Starting from these assumptions, we analyzed the $\Delta\delta_{\text{NH}}/\Delta t$ of 0.01 M **2b–e**, in a 8:2 mixture of $[\text{D}_6]\text{DMSO}/\text{H}_2\text{O}$ (Table 2 and Figure 1). For Boc-Ala-(S)-Imi-Phe-Val-OMe (**2b**), the comparatively much lower $\Delta\delta_{\text{NH}}/\Delta t$ absolute value of Phe^3NH (-0.9 ppb/K) with respect to Ala^1NH and Val^4NH (-3.7 , and -4.5 ppb/K, respectively) indicatively suggested that the former might be involved in a H-bond. On the other hand, peptides **2c**, **d** showed high $|\Delta\delta/\Delta t|$ values for all amide-NHs. Unexpectedly, Ala^2NH in Boc-Val-Ala-(R)-Imi-Phe-OMe (**2e**) appeared to be significantly less sensitive to increasing temperature than Val^1NH and Phe^4NH ($\Delta\delta/\Delta t = -2.4$ vs -6.5 and -5.2 ppb/K, respectively), which might be compatible with a preference for a conformation having AlaNH involved in a H-bond.

Table 2. $\Delta\delta_{\text{NH}}/\Delta t$ values (ppb/K) for the amide protons of 0.01 M peptide **2b–e** in 8:2 $[\text{D}_6]\text{DMSO}/\text{H}_2\text{O}$.

2	HN1	HN2	HN3	HN4	
b	-3.7	a	-0.9	-4.5	
c	-6.3	a	-3.4	-6.5	
d	-5.5	-4.9	a	-4.7	
e	-6.5	-2.4	a	-5.2	a = Imi

The model compounds were analyzed by 2D-ROESY in 8:2 [D₆]DMSO/H₂O, using 0.01 M peptide concentration, and the resulting cross-peaks were ranked by the intensity to infer plausible interproton distances. Compared to the homochiral Imi-peptides **2b** and **2d**, the heterochiral sequences **2c** and **2e** showed several inter-residue proton–proton correlations between nonconsecutive residues (Figure 1).

The estimated distances were analyzed by simulated annealing and restrained molecular dynamics simulations^[31] using the AMBER force field^[32] in explicit water as a solvent. In brief, random geometries of each peptide were obtained by high-temperature unrestrained molecular dynamics simulation in a box of standard TIP3P models of equilibrated water.^[33] For each random structure, the interproton distances deduced by ROESY were introduced as constraints. Neither H-bond interactions nor torsion angle restraints were introduced, while ω bonds were restricted at 180° because the absence of H α _i - H α _(i + 1) cross-peaks excluded the occurrence of cis peptide bonds.^[34] Then, the structures were subjected to high- temperature restrained molecular dynamics with a scaled force field, followed by a simulation period with full restraints. After slowly cooling the boxes, the geometries were minimized and the backbones of the Imi-peptides were clustered by the rmsd analysis.^[31] In all cases, this procedure gave one major cluster comprising the majority of the structures (Figure 2). The representative conformers with the lowest energy are reported in Figure 3.

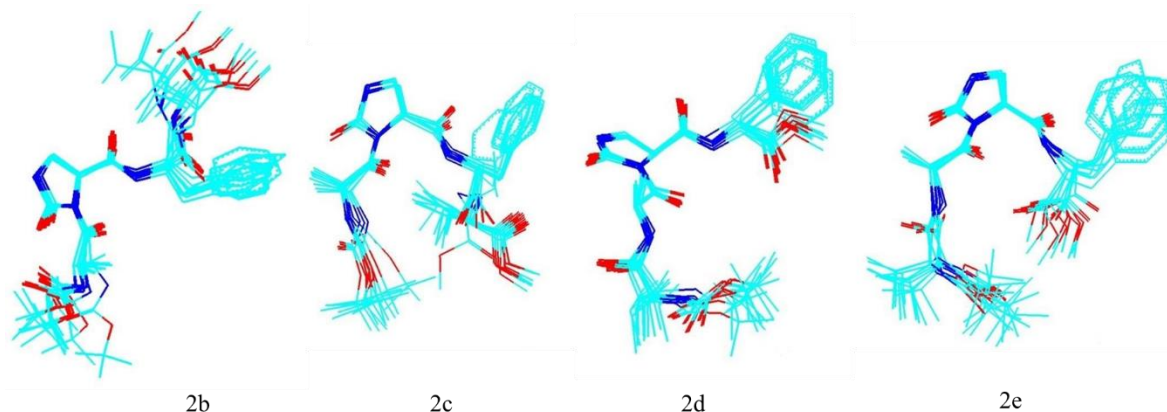


Figure 2. Superimposed low energy structures obtained from NMR-restrained molecular dynamics.

Among the four peptide models, the homochiral structures **2b** and **2d** showed comparatively more extended backbone conformations, as expected on the basis of the negligible number of inter-residue ROESY cross-peaks (Figure 1). Yet, both showed a clear inverse γ -turn centered on the Imi residue (Figure 3), and in particular for peptide **2b**, having its Imi residue at the position 2 of the sequence, the turn was stabilized by an explicit H-bond with a H to O distance of 2.0 Å (Figure 2 and 3), consistent with the evidence of VT NMR (Table 2 and Figure 1).

To simulate the dynamic behavior of the peptides, the ROESY-derived conformers were analyzed by unrestrained molecular dynamics in explicit water, for 10 ns at rt. During the simulations, the γ -turn of **2b** resulted to be remarkably stable, correlated to the highly rigid Ala-Imi central scaffold and the flat imidazolidine-2-one ring. For **2d**, having Imi at position 3, the formation of a definite H-bond was prevented by a certain conformational freedom of the short Phe-OMe portion, but the γ -turn appearance was in general maintained. These results were not unexpected; also peptides containing the homochiral oxazolidin-2-one scaffold showed the preferential formation of γ -turns in [D₆]DMSO or other competitive solvents.^[25]

As for the heterochiral **2c** and **2e**, because of the many inter- residue ROESY cross-peaks (Figure 1), the

calculated structures were tightly folded (**2c** and **2eA**, Figure 3). The sequence **2c**, containing Imi at the position 2, presented a γ -turn centered on Imi (Figure 3). Unexpectedly, the ROESY-derived structure A of **2e** (Figure 3) showed a regular γ -turn centered on Imi, plus an atypical turn involving the residues Ala-(R)-Imi-Phe, which seemed compatible with a ε -turn.^[35]

The conformer **2eA** was analyzed by unrestrained molecular dynamics, and the analysis of the trajectories revealed the formation of a 11-membered macrocycle closed by an intramolecular H-bond between the Ala²NH and Phe⁴C=O, which is in agreement with the VT NMR temperaturecoefficient of AlaNH (Table 2). The representative structure **2eB** shown in Figure 3 is characterized by a distance of 2.4 Å between Ala²C=O and Phe⁴NH and of 2.3 Å between Ala²NH and Phe⁴C=O (Figure 3 and 4).

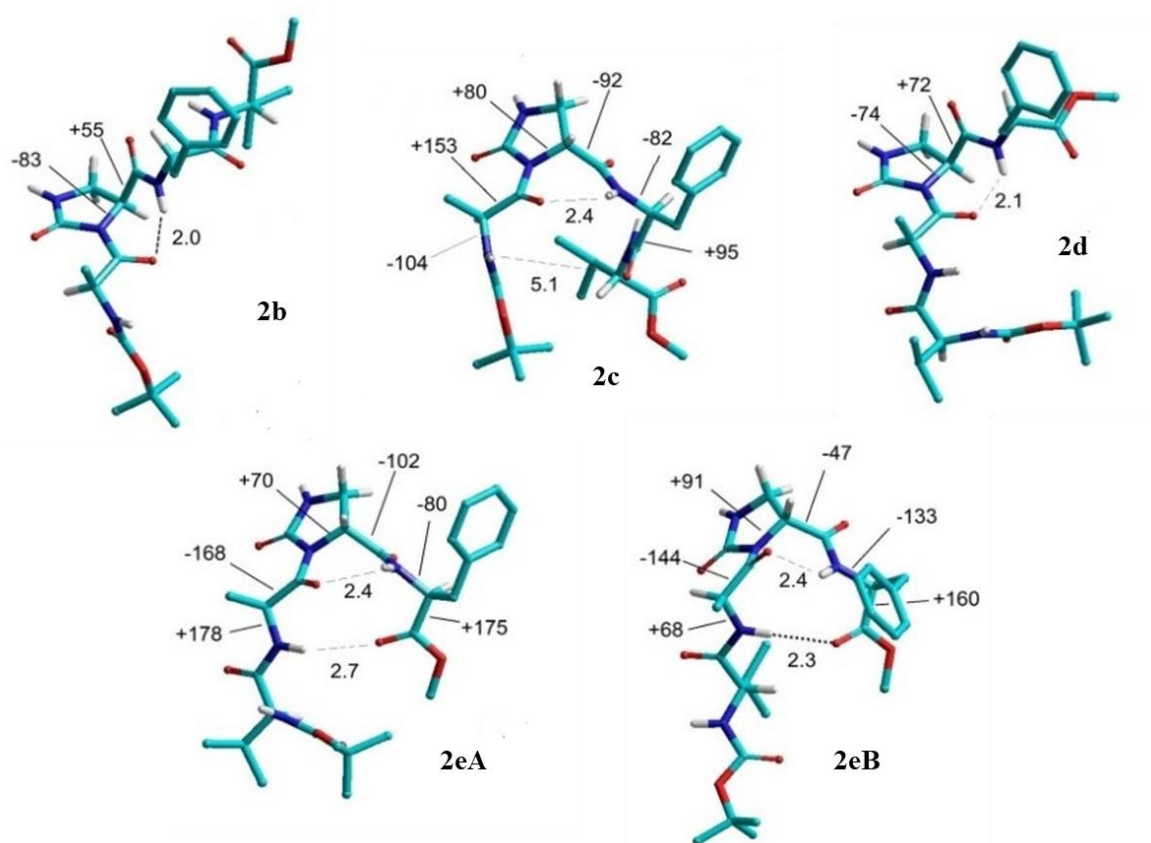


Figure 3. Representative conformers of **2b-e** calculated by ROESY-restrained in a 30x30x30 Å³ box of standard TIP3P models of equilibrated water. Heavy dotted lines represent H-bonds; light dotted gray lines indicate distances; and ϕ/ψ dihedral angles of selected residues are also reported in degrees.

The ε -turn is a rare kind of secondary structure which can be observed in oligo-cyclopeptides and more seldom in linear peptides and proteins composed of all α -amino acids.^[35] Unlike the more common 5 \rightarrow 1 13-membered α -, 4 \rightarrow 1 10-membered β -, and 3 \rightarrow 1 7-membered γ -turns, the ε -turn involves 3 residues to form a hydrogen-bonded structure encompassing 11 atoms in the opposite 2 \rightarrow 4 direction (Figure 4A). The ϕ/ψ dihedral angles found in **2eB** (Figure 3) assign the ε -turn to the all-trans class A in the convention of Toniolo and Balaram:³⁵ (ϕ/ψ in degrees) Ala, -144/+68; (R)-Imi, +91/-47; Phe, -133/+160.

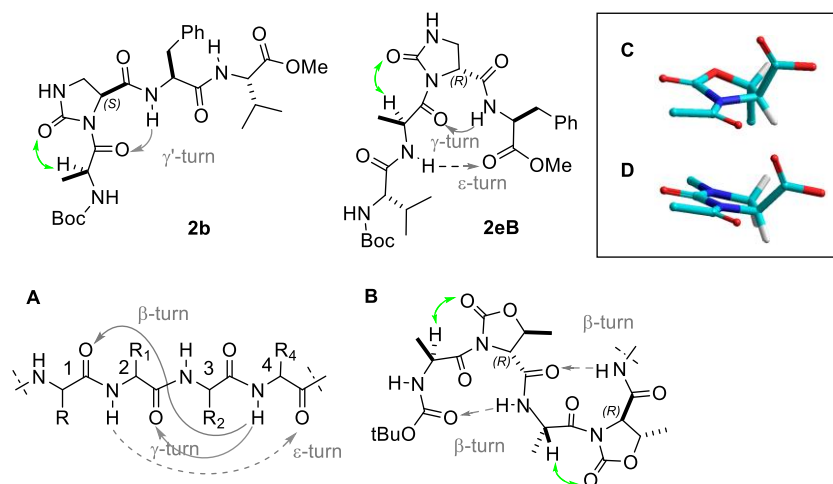
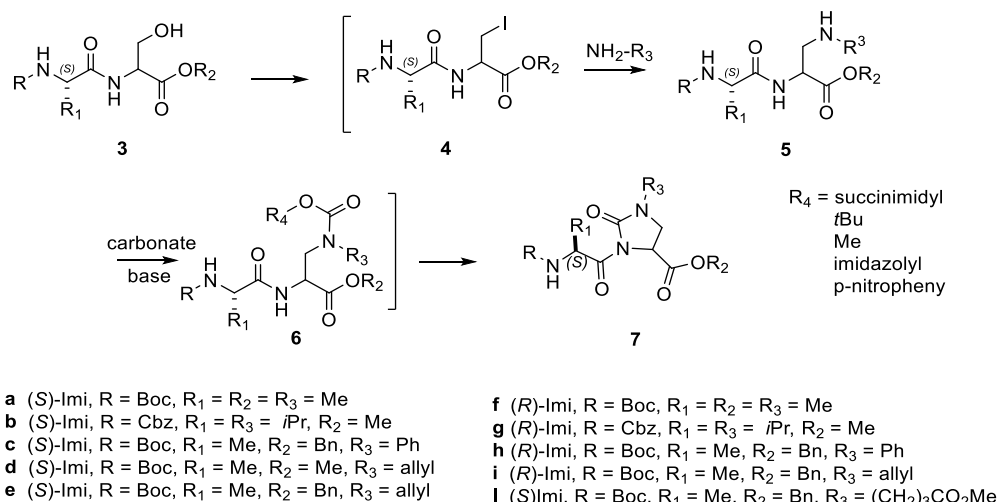


Figure 4. Sketch of the expected inverse γ -turn of the homochiral **2b**; the $\text{ImiC}=\text{O}\cdots\text{H}-\text{C}$ (α -1) interaction is rendered in green. Sketch of the class A ϵ/γ -mixed turns^[35] in **2eB**. (A) “Common way” intramolecular hydrogen bonds in a tetrapeptide (residues numbered 1 to 4) rendered as continuous gray arrows and atypical 11-membered ϵ -turn in the 2 \rightarrow 4 reversed direction as a dotted arrow. (B) Oligomers composed of Ala-oxazolidin-2-one units produce a helix of “normal” β -turns.^[3c,25] (C) Crystal structure of the oxazolidin-2-one^[25c] and (D) of the imidazolidin-2-one scaffolds.^[23]

The comparison between the structures of **2c** and **2e** in Figure 3 showed that the ϵ -turn was not completely formed in **2c**, albeit both compounds share the same Ala-(R)-Imi-Phe tripeptide sequence. Possibly, the failure of **2c** in forming an unequivocal H-bonded 2 \rightarrow 4 turn can be attributed to the presence of the bulky Boc group at Ala¹, as suggested by the analysis of the trajectories of the unrestrained molecular dynamics, which showed the clash between the tBu and Val⁴. Finally, it is worth mentioning that in spite of the structural similarity with (R)-Imi, the (R)-oxazolidin-2-one-4-carboxylate scaffolds produced only “normal” conformations, that is, γ -turns in $[\text{D}_6]\text{DMSO}$ and β -turns in CDCl_3 .^[25a,b] Also, oligomers formed of repetitive Ala-(R)-oxazolidin-2-one-4-carboxylate dipeptide units (≥ 5) folded in an ordered structure to give a variant of the 3_{10} -helix, namely, a series of consecutive regular 4 \rightarrow 1 β -turns (Figure 4B), in the crystal state and in MeOH.^[25c] At present, the exhaustive investigation of the structural features of the Imi scaffold is beyond the scope of this work. Nevertheless, some clues can be perceived by the inspection of the X-ray crystal structures of 3-acyl-oxazolidin-2-one-4-carboxylates^[25c] and 3-acyl-imidazolidin-2-one-4-carboxylates^[23] (Figure 4C,D). The comparison highlighted some relevant 3D differences which might be responsible for the different H-bonding patterns. While the geometry of the five-membered rings is quite twisted in the oxazolidin-2-one (Figure 4C),^[25c] it is extraordinarily flat in the Imi ring (Figure 4D).^[23] This necessarily translates into different orientations of C4-carboxylate vectors, reasonably fundamental to the development of the overall conformations, and in particular the carboxylate group in the oxazolidin-2-one adopts an axial, almost vertical orientation above the five-membered ring (Figure 4C).



Scheme 3. Synthesis of N1-substituted Imi-peptides **7**.

2.2 Imidazolidin-2-Ones Substituted at the Position 1.

The formation of the Imi ring was attained by sacrificing the N β -amino group of Dap. Hence, Imi can be regarded as a pseudo-Pro showing the sole trans conformation at the preceding peptide bond. Intriguingly, conformational analysis by NMR and molecular dynamics has shown that (S)-Imi peptides adopt an inverse γ -turn conformation, while (R)-Imi promotes the formation of the rare ϵ/γ -secondary structure. This unexpected observation prompted us to possibly expand the scope of the Imi rings, making possible their use as general promoters of such unusual secondary structures also in sequences having at the position *i* residues other than a (pseudo) Pro. For this reason, we tackled the opportunity to introduce any substituents at the position 1 of the Imi scaffolds.

The strategy we adopted is outlined in Scheme 3. Dipeptides containing (S)- or (R)-serine **3** were prepared in solution as described in the literature.^[36] The dipeptide esters **3** were isolated in good yield (in the 70–85% range, 80–90% pure according to analytical RP HPLC) by flash chromatography over silica gel. The dipeptides **3** were treated with a mixture of triphenylphosphine, iodine (1.2 equiv each), and imidazole (2.5 equiv),^[37] affording β -iodo-Ala-dipeptides **4**, not isolated because of intrinsic instability;^[37] TLC analyses of the reaction mixtures revealed the complete consumption of **3**.

The displacement of iodine with alkyl or arylamines, that is, methylamine, isopropylamine, aniline, allylamine, and γ -aminobutyric acid (GABA) methyl ester (2.0 equiv) in dimethylformamide (DMF) gave the N β -substituted Dap dipeptides **5**. Again, the TLC analyses of the crude reaction mixtures showed the disappearance of the reagents. Unfortunately, with the exception of Boc-Ala-Dap(N-allyl)-OMe **5d**, the isolation of these dipeptides **5** was not possible, either by chromatography over silica gel or by preparative RP HPLC, for the accumulation of the many side products.

Hence, we opted for the direct cyclization of the crude dipeptides **5** with DSC/DIPEA, as reported above for the synthesis of Imi-peptides **2**. This reaction gave the formation of the intermediate N β -carbamate **6**, and of desired **7** only in traces, as observed by RP HPLC and ESI MS analysis of the reaction mixture. Even the highly pure **5d** failed to give the corresponding **7d**, suggesting that the scarce purity of the other reagents **5** was not the only responsible for the disappointing result. Thereafter, the procedure was repeated upon varying the conditions, using as the model reagent the crude dipeptide Boc-Ala-Dap(N₁Me)-OMe (**5a**), obtained from the Boc-Ala- β -iodoAla-OMe **4a** and methylamine.

Besides DIPEA, also Na₂CO₃, 4-dimethylaminopyridine (DMAP), and 1,8-diazabicyclo[5.4.0]undec-7-ene (DBU) were tested. The increase of the amounts of DSC and/or of the base and the increase of temperature and of reaction time had very little impact (not shown), while the use of DMF as the only solvent gave a modest increase of the yield (Table 3, entry 1).

Apart from DSC, the use of other carbonates or dicarbonates such as triphosgene, Boc₂O, methyl chloroformate, CDI, entries 2 to 5, respectively, in combination with DIPEA or the other bases as above, was also poorly effective. Gratifyingly, p-nitrophenylchloroformate (pNPC)^[38] and DIPEA (1.5 equiv each) in DMF at rt after 12 h gave **7a** in 70% yield over 3 steps, accompanied by the Nβ-p-nitrophenoxycarbonyl-Dap(Me) intermediate **6** (25%) (entry 6). The yield was further increased by replacing DIPEA with DBU, and **7a** was isolated in excellent amount (90%) by flash chromatography over silica gel (entry 7).

Table 3. Formation of imi-dipeptides **7** using carbonate/base (1.5 equiv) in DMF, after 12 h at rt.

entry	compd	carbonate/base	7 (%)	purity (%) ^a	6 (%)
1	a	DSC/DIPEA	<10 ^b	—	70 ^b
2	a	(Cl ₃ CO)CO/base ^c	traces	d	d
3	a	Boc ₂ O/base ^c	traces	—	75
4	a	ClCO ₂ Me/base ^c	traces	—	80
5	a	CDI/base ^c	<5 ^b	—	traces
6	a	pNPC/DIPEA	70 ^b	—	25
7	a	pNPC/DBU	90 ^e	95	traces
8	b	pNPC/DBU	85 ^e	91	traces
9	c	pNPC/DBU	80 ^e	92	10 ^b
10	e	pNPC/DBU	93 ^e	94	traces
11	f	pNPC/DBU	87 ^e	93	traces
12	g	pNPC/DBU	82 ^e	91	traces
13	h	pNPC/DBU	77 ^e	96	11 ^b
14	i	pNPC/DBU	90 ^e	92	traces
15	l	pNPC/DBU	74 ^e	94	traces

^aAfter isolation, determined by RP HPLC ESI MS, elemental analysis, and exact mass. ^bDetermined by the RP HPLC analyses of the reaction mixtures. ^cBase: DIPEA, carbonate, DMAP, DBU. ^dComplex mixture of by-products. ^eDetermined after isolation by flash chromatography over 3 synthetic steps respect to peptides **3**.

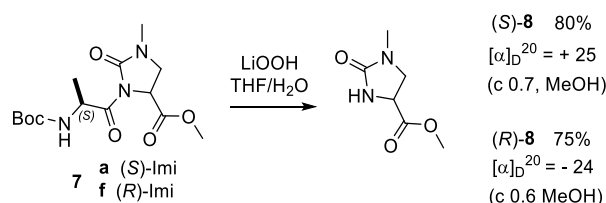
The same conditions were applied to the crude dipeptides **5b**, **c**, **e**, obtained as reported in Scheme 3 from the corresponding β-iodo-derivatives **4** and isopropylamine, aniline, allylamine, respectively. The N-terminal capping group, the ester, and the amino acid preceding Dap, were varied to check the generality of the process. The benzyl ester **5e** was preferred to the methyl ester **5d** for the convenience of further transformations, as discussed in the next sections. In all cases, the reactions gave results comparable to **5a** (entries 8 to 10). Subsequently, the procedure was repeated starting from the dipeptides containing D-serine. As for the (S)-configured series, the formation of the dipeptides containing (R)-β-iodoAla, followed by displacement with the same amines, gave the dipeptides containing

N-methyl, isopropyl, phenyl, and allyl (R)-Dap. Then, the treatment with pNPC/DBU gave (R)-Imi peptides **7f**, **7g**, **7h**, and **7i** in good to excellent yields (entries 11 to 14).

Finally, the dipeptide Boc-Ala-(S)-Imi[(CH₂)₃CO₂Me]OBn (**7l**) (Scheme 3) was prepared in sufficient yield by treatment of the β-iodoAla-dipeptide with GABA methyl ester, followed by cyclization under the usual conditions (entry 15).

Epimerization during the displacement of iodine from β-iodoAla by the amines, or during the following cyclization step, was excluded based on the comparison of the ¹H NMR of the (S,S)/(S,R) diastereomeric pairs with the peptides **2b–e** containing unsubstituted Imi. In particular, for all compounds containing (R)-Imi in CDCl₃, the proton ImiH4 appeared ≤4.75 ppm, while compounds containing (S)-Imi ImiH4 appeared ≥ 4.8 ppm.

In any case, to confirm that the stereochemistry was maintained, the diastereomeric **7a** and **7f** were treated with LiOOH in THF/water at rt for 4 h, followed by 0.1 M HCl,^[39] leading to the detachment of Boc-Ala-OH and the release of the enantiomeric methyl 1-methyl-2-oxoimidazolidine-4-carboxylates (S)-**8** and (R)-**8**. After purification by flash chromatography over silica gel (eluent cyclohexane/EtOAc 1:3), their specific optical rotation was determined (Scheme 4) and judged in agreement with the literature for (S)-**8**: [α]_D²⁰ +26.9 (*c* 1, MeOH).^[23]



Scheme 4. Cleavage of the Imi Rings **8** from **7a, f**

These Imi dipeptide scaffolds carrying three possible different pharmacophores can be of some interest in peptidomimetic chemistry. There is evidence for the optimality of three-residue motifs for biological activity.^[40] In a similar way as shown for trans-pyrrolidine-3,4-dicarboxamide templates by Boger et al. (Figure 5A),^[41] the triply functionalized Imi dipeptides **7** (Figure 5) might be regarded as potential β-turn mimetics when the turn amino acid *i* + 1 serves as a structural rather than a recognition role, for example, Pro or Gly (Figure 5A). Hence, Imi scaffolds reproducing the side chains of the residues *i*, *i* + 2, *i* + 3, could still maintain the bioactivity of the native peptides.

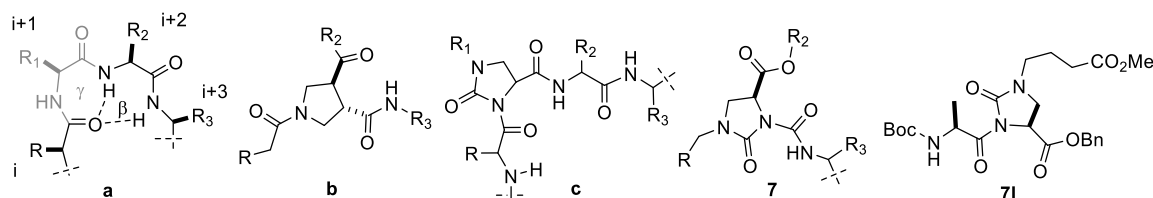
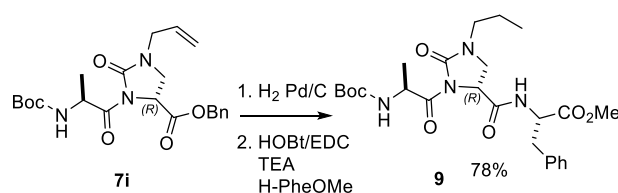


Figure 5. (A) Pyrrolidine- and Imi-based β-turn mimetics **7**.^[41] (B) Classic γ- or β-turns. (C) Imi as a turn-inducing element for peptidomimetics equipped with side chains at each residue. Triply substituted Imi peptide **7l** with orthogonally protected, further functionalizable groups.

As for the oligomers, the Imi scaffolds have been shown to act as proline mimics inducing all-trans conformations in the sequences, and to promote classic or unusual turn structures, depending on the stereochemistry. Interestingly, while most of the conformationally restricted turn-inducing elements (e.g.,

pseudoproline, Freidinger lactams, spirolactams, bicyclic thiazolidines, etc.) are generally deprived of some relevant pharmacophores,^[1,42] the Imi rings can be equipped with proteogenic side chains (Figure 5C), for example, of Ala, Val, Phe (Scheme 3).

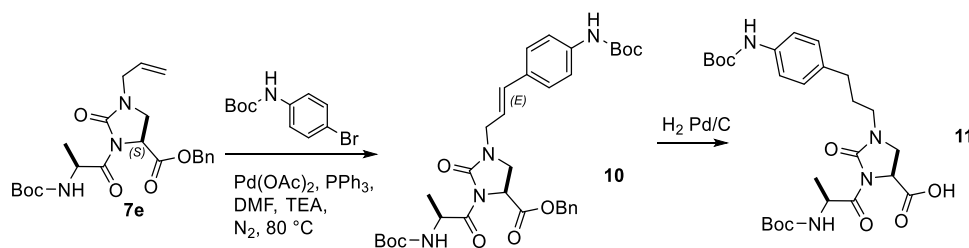
To further challenge the potential utility of the N₁-substituted Imi dipeptides, Boc-Ala-(R)-Imi(N₁allyl)-OBn (**7i**) was subjected to catalytic hydrogenation, and the resulting (R)-Imi(N₁propyl) dipeptide acid was coupled with H-Phe-OMe-HCl, giving the tripeptide **9** equipped with a non-proteogenic side chain (Scheme 5). As expected, the ¹H NMR analysis of **9** in 8:2 [D₆]DMSO/H₂O supported the fact that this Imi-N₁-propyl tripeptide adopted a conformation consistent to that of the heterochiral models **2c** or **2e**. Indeed, the ¹H NMR of **9** was practically superimposable to that of the Boc-Ala-(R)-Imi-Phe portion of **2c**, while the only difference with the corresponding portion in **2d** was the obviously different chemical shift of AlaNH. See for instance the highly reproducible pattern of the resonances of H4 and the two H5 protons.



Scheme 5. Synthesis of the N₁-substituted Imi-tripeptide **9** from the N₁-Allyl Imi-tripeptide **7i**.

On the other hand, the synthetic strategy described above was utilized also for introducing substituents carrying orthogonally protected functional groups. A first example was the dipeptide Boc-Ala-(S)-Imi[(CH₂)₃CO₂Me]OBn (**7l**) (Table 3, entry 15, and Figure 5), prepared with GABA methyl ester. In perspective, after hydrolysis under basic conditions, the N₁-butanoic acid side chain might be exploited to graft the peptide onto, for example, surfaces, polymeric materials, nanoparticles, and so forth.

Finally, the N₁-substituent of Imi can be equipped with a tag residue for site-selective modifications of the sequences. Among the most popular reactions utilized to transform such handles without perturbing the remaining amino acids, it is possible to cite the Cu-catalyzed azide-alkyne cycloaddition, the Sonogashira, Suzuki-Miyaura, Mizoroki-Heck, Diels-Alder reactions, the photo-1,3-dipolar cycloaddition, the Staudinger ligation, and the olefin metathesis with Grubbs or Hoveyda-Grubbs catalysts.^[17]



Scheme 6. Heck reaction of the N₁-Allyl Imi-tripeptide **7e**, giving **10** and then **11**

As a proof of concept, the allyl substituent at the position 1 of the Imi ring in **7e** was selectively derivatized with N-Boc-4-bromoaniline by the Heck reaction (Scheme 6). Conducted in DMF in the presence of Pd(OAc)₂/PPh₃/TEA, under an inert atmosphere, at 80 °C,^[43] the reaction gave the adduct **10** characterized by an exclusively trans connection between the two portions, as determined by the –

CH=CH- coupling constants in the ^1H NMR, $J = 15.6$ Hz (for trans alkenes $J = 12\text{--}18$ Hz, for cis alkenes $J = 6\text{--}12$ Hz). The reduction by catalytic hydrogenation gave a fully flexible linkage, and at the same time removed the benzyl ester protection, giving the dipeptide acid **11**, ready in prospective for the extension of the peptidic backbone.

3. Conclusions

The introduction of nitrogen heterocycles into peptide sequences represents an effective approach to increase enzymatic stability and to induce well-defined secondary structures. To this purpose, we developed an expedient synthesis of hybrid peptides containing Imi scaffolds. These exceptionally flat pseudo-prolines demonstrated the ability to favor unusual conformations in a competitive and biomimetic solvent. While (S)-Imi peptides adopted a γ -turn conformation, (R)-configured Imi promoted the additional formation of a ϵ -turn, an infrequent secondary structure characterized by a 11-membered 2 \rightarrow 4 H-bond going opposite respect to the classic γ - or β -turns. Besides, Imi can be equipped at the position N_1 with substituents that reproduce the side chains of native amino acids, including Ala, Val, or Phe, in either L- or D- configuration, as well as with non-proteinogenic substituents, such as n-propyl or allyl. In this respect, the N_1 -substituted(R)-Imi rings represent a new class of general promoters the rare ϵ -turn in a variety of peptide sequences. On the other hand, Imi can also carry functional groups, for instance, the allyl group, capable of selective reactions without perturbing the rest of the structure, for example by the Heck reaction. Potential future applications might include the glycosylation, prenylation, PEGylation, biotinylation, or attachment to solid surfaces, self-assembled monolayers, proteins, or the conjugation with fluorophores or antibodies. [17,44]

4. Experimental Section

4.1 General Experimental Methods.

All purchased reagents were used without further purifications. Purities were assessed by analytical RP HPLC and confirmed by exact mass and elemental analysis. MW lab station: MicroSYNTH equipped with a built-in ATC-FO advanced fiber optic automatic temperature control. RP HPLC: Agilent 1100 series apparatus, with a RP column Phenomenex mod. Gemini 3 μ C18 110 Å 100 \times 3.0 mm, stationary phase octadecyl carbon chain-bonded silica with trimethylsilyl endcapping, fully porous organo-silica solid support, particle size 3 μm , pore size 110 Å, length 100 mm, internal diameter 3 mm, DAD 210 and 254 nm, mobile phase from 9:1 to 2:8 water/ CH_3CN , in 20 min, at a flow rate of 0.5 mL min^{-1} , followed by 10 min at the same composition. Semipreparative RP-HPLC: Agilent 1100 series, RP column ZORBAX mod. Eclipse XDBC18 PrepHT cartridge 21.2 \times 150 mm 7 μm , stationary phase octadecyl carbon chain bonded silica, double endcapped, particle size 7 mm, pore size 80 Å, length 150 mm, internal diameter 21.2 mm, DAD 210 nm; mobile phase from $\text{H}_2\text{O}/\text{CH}_3\text{CN}$ (8:2) to CH_3CN (100%) in 10 min at a flow rate of 12 mL min^{-1} . HRMS: Waters Xevo QTof. Routine ESI MS: MS single quadrupole HP 1100MSD detector, drying gas flow of 12.5 L min^{-1} , nebulizer pressure 30 psig, drying gas temp 350 $^\circ\text{C}$, capillary voltage 4500(1) and 4000(2), scan 50–2600 amu. Elemental analysis: Thermo Flash 2000CHNS/O. NMR characterization was done on a Varian Gemini 400 or 200, using 0.01–0.04 M peptide in 5 mm tubes at rt, using the solvents CDCl_3 , or $[\text{D}_6]\text{DMSO}$, or 8:2 $[\text{D}_6]\text{DMSO}/\text{H}_2\text{O}$ (water suppression by the solvent presaturation procedure PRESAT); ^1H spectra were recorded at 400 MHz, and the unambiguous assignment of the resonances was done by 2D gCOSY; proton-decoupled ^{13}C NMR was recorded at 100 or 75 MHz; chemical shifts were reported

as δ values in ppm relative to solvent as internal standard.

4.2 Synthesis of Peptides **1** in Solution.

The general procedure is as follows: A mixture of the Boc-amino acid (0.3 mmol) and HOBt (0.049 g, 0.36 mmol) was stirred in 3:1 DCM/DMF (5 mL) at rt, and after 10 min, the amino ester counterpart (0.36 mmol), EDC·HCl (0.069 g, 0.36 mmol), and TEA (0.13 mL, 0.94 mmol) were added in sequence while stirring at rt. After 2 h, the solvents were removed at reduced pressure, and the residue was diluted with ethyl acetate (EtOAc; 20 mL). The slurry mixture was washed with 0.1 M HCl (5 mL) and a saturated solution of NaHCO₃ (5 mL). The organic layer was dried over Na₂SO₄ and the solvent was evaporated at reduced pressure. The intermediate crude peptides, obtained in quantitative yield, were analyzed by RP HPLC and ESI MS and were used without further purifications.

Boc deprotection was accomplished by stirring the crude peptides in 1:3 TFA/DCM (4 mL) for 30 min. Then, the mixture was concentrated at reduced pressure, and the treatment was repeated. The residue was suspended in Et₂O (20 mL), and the peptide–TFA salts which precipitated in almost quantitative yield were used for the next couplings without further purifications. The final sequences **1** were isolated by flash chromatography over silica gel (eluent 1:2 cyclohexane/EtOAc), 80–85% yield, 80–90% pure by RP HPLC (general methods). The identity was confirmed by ESI MS analysis (general methods).

Cyclization to Imi-Peptides **2a–c** in Solution. The general procedure is as follows: The peptides **1** (0.2 mmol) were dissolved in EtOH (15 mL), and a 2 L balloon filled with H₂ was applied in the presence of a catalytic amount of 10% Pd/C, while stirring at rt. The reactions were monitored by TLC and were generally judged complete in 6 h. Then, the mixture was filtered over Celite and the solvent was evaporated at reduced pressure.

The residue was dissolved in 3:1 DCM/DMF (5 mL), and DSC (0.061 g, 0.24 mmol) and DIPEA (0.044 mL, 0.24 mmol) were added at rt under inert atmosphere. The mixture was stirred for 3 h, then the solvent was distilled under reduced pressure, the residue was diluted with 0.1 M HCl (5 mL), and the mixture was extracted three times with DCM (10 mL). The combined organic layers were dried over Na₂SO₄ and concentrated at reduced pressure. The residue was separated by semipreparative RP HPLC on a C18 column, eluent from H₂O/CH₃CN (8:2) to CH₃CN (100%) in 10 min, at a flow rate of 12 mL min⁻¹ (general methods), and purity was determined by RP HPLC (general methods).

Boc-Ala-(S)-Imi-Phe-OMe (2a).

Cyclization of **1a** (0.11 g, 0.19 mmol) according to the general procedure gave **2a** (0.077 g, 86%, 92% pure). ¹H NMR (8:2 [D₆]DMSO/H₂O, 400 MHz): δ 1.17 (d, J = 7.1 Hz, 3H, AlaMe), 1.35 (s, 9H, tBu), 2.93–3.02 (m, 2H, PheH β), 3.08 (dd, J = 3.0, 9.6 Hz, 1H, ImiH5), 3.57 (s, 3H, OMe), 3.63 (dd, J = 9.6, 10.0 Hz, 1H, ImiH5), 4.44 (m, 1H, PheH α), 4.75 (dd, J = 3.0, 10.0 Hz, 1H, ImiH4), 5.18 (dd, J = 7.1, 14.4 Hz, 1H, AlaH α), 7.09 (d, J = 8.0 Hz, 1H, AlaNH), 7.18–7.35 (m, 5H, ArH), 7.73 (s, 1H, ImiNH1), 8.58 (d, J = 6.8 Hz, 1H, PheNH); ¹³C{¹H} NMR ([D₆]DMSO, 100 MHz): δ 18.2, 29.1, 37.5, 41.3, 49.0, 52.8, 54.7, 55.3, 78.8, 127.6, 129.3, 130.0, 137.7, 156.1, 170.6, 172.7, 174.4; HRMS (ESI/QTOF) m/z : [M+H]⁺ calcd for C₂₂H₃₁N₄O₇, 463.2193; found, 463.2164. Anal. Calcd for C₂₂H₃₀N₄O₇: C, 57.13; H, 6.54; N, 12.11. Found: C, 57.19; H, 6.49; N, 11.99.

Boc-Ala-(S)-Imi-Phe-Val-OMe (2b).

Cyclization of **1b** (0.14 g, 0.21 mmol) according to the general procedure gave **2b** (0.10 g, 88%, 93% pure). ¹H NMR (8:2 [D₆]DMSO/H₂O, 400 MHz): δ 0.82–0.93 (m, 6H, ValMe), 1.17 (d, J = 7.2 Hz, 3H, AlaMe), 1.34 (s, 9H, tBu), 2.01 (m, 1H, ValH β), 2.80 (dd, J = 8.8, 13.4 Hz, 1H, PheH β), 2.99 (dd, J = 4.0,

13.4 Hz, 1H, PheH β), 3.08 (dd, $J = 2.2, 9.8$ Hz, 1H, ImiH5), 3.58 (m, 1H, ImiH5), 3.62 (s, 3H, OMe), 4.14 (dd, $J = 7.2, 7.6$ Hz, 1H, ValH α), 4.56 (m, 1H, PheH α), 4.73 (dd, $J = 2.8, 7.2$ Hz, 1H, ImiH4), 5.16 (m, 1H, AlaH α), 7.00 (d, $J = 7.6$ Hz, 1H, AlaNH), 7.16–7.30 (m, 5H, PheArH), 7.71 (s, 1H, ImiNH1), 8.24 (d, $J = 7.6$ Hz, 1H, ValNH), 8.28 (d, $J = 8.0$ Hz, 1H, PheNH); $^{13}\text{C}\{^1\text{H}\}$ NMR (CDCl₃, 100 MHz): δ 17.8, 18.8, 28.3, 29.7, 31.1, 38.1, 49.0, 52.2, 54.9, 56.0, 57.5, 79.9, 127.1, 127.2, 128.8, 129.1, 129.3, 136.0, 154.6, 155.2, 168.5, 170.2, 171.6, 175.0; HRMS (ESI/QTOF) m/z : [M+H]⁺ calcd for C₂₇H₄₀N₅O₈, 562.2877; found, 562.2821. Anal. Calcd for C₂₇H₃₉N₅O₈: C, 57.74; H, 7.00; N, 12.47. Found: C, 57.81; H, 6.90; N, 12.54.

Boc-Ala-(R)-Imi-Phe-Val-OMe (2c).

Cyclization of 1c (0.12 g, 0.18 mmol) according to the general procedure gave **2c** (0.092 g, 91%, 93% pure). ^1H NMR (8:2 [D₆]DMSO/H₂O, 400 MHz): δ 0.88 (d, $J = 7.2$ Hz, 3H, ValMe), 0.91 (d, $J = 6.8$ Hz, 3H, ValMe), 1.15 (d, $J = 6.4$ Hz, 3H, AlaMe), 1.35 (s, 9H, tBu), 2.05 (m, 1H, ValH β), 2.42 (m, 1H, ImiH5), 2.71 (dd, $J = 10.0, 13.7$ Hz, 1H, PheH β), 3.06 (dd, $J = 3.8, 13.7$ Hz, 1H, PheH β), 3.34 (dd, $J = 4.8, 12.0$ Hz, 1H, ImiH5), 3.63 (s, 3H, OMe), 4.30 (m, 1H, ValH α), 4.56 (m, 1H, ImiH4), 4.71 (ddd, $J = 3.8, 8.8, 10.0$ Hz, 1H, PheH α), 5.31 (dq, $J = 6.4, 8.8$ Hz, 1H, AlaH α), 6.62 (d, $J = 8.8$ Hz, 1H, AlaNH), 7.17–7.27 (m, 5H, PheArH), 7.62 (s, 1H, ImiNH1), 8.20 (d, $J = 7.6$ Hz, 1H, ValNH), 8.37 (d, $J = 8.8$ Hz, 1H, PheNH); $^{13}\text{C}\{^1\text{H}\}$ NMR ([D₆]DMSO, 100 MHz): δ 18.5, 19.0, 19.2, 28.3, 29.9, 30.8, 38.0, 48.1, 51.8, 53.0, 55.2, 57.8, 78.1, 126.4, 128.0, 129.4, 137.6, 154.6, 155.0, 169.2, 171.3, 171.8, 172.9; HRMS (ESI/QTOF) m/z : [M+H]⁺ calcd for C₂₇H₄₀N₅O₈, 562.2877; found, 562.2849. Anal. Calcd for C₂₇H₃₉N₅O₈: C, 57.74; H, 7.00; N, 12.47. Found: C, 57.55; H, 7.13; N, 12.17.

4.3 Synthesis of Imi-Peptides 2d, e in Solid-Phase.

The general procedure is as follows: Wang resin pre-loaded with Fmoc-Phe (0.25 g, 0.4–0.8 mmol g⁻¹, particle size 100–200 mesh) was placed into a reactor equipped with a filter and suspended in DCM (5 mL). Fmoc was removed by treatment with 1:4 piperidine/DMF (5 mL) under MW irradiation at 40 W while bubbling N₂ in an open vessel, monitoring the internal temperature at 45 °C. After 2 min, the suspension was filtered, and the procedure was repeated. Then, the resin was washed three times in sequence with DCM, DMF, and MeOH (5 mL each).

The resin was swollen in DCM (8 mL), and a mixture of Fmoc-Dap(Cbz)-OH (0.137 g, 0.3 mmol) and HOBt (0.041 g, 0.3 mmol) in DMF (4 mL) was added, followed by DCC (0.078 g, 0.38 mmol). The mixture was heated at 45 °C for 10 min under MW irradiation as described above, while bubbling N₂. The resin was filtered and washed three times with the sequence DCM, DMF, MeOH (5 mL each). Coupling efficacy was determined by means of the Kaiser test. All the remaining residues were attached by the same protocols.

The resulting peptidyl-resin **1d** or **1e** was suspended in 1:3 iPrOH/toluene (10 mL), and HCO₂NH₄ (0.038 g, 0.6 mmol) and a catalytic amount of 10% Pd/C were added in sequence. The mixture was irradiated at 600 W for eight cycles of 1 min each. The resin-bound peptide was filtered and washed three times in sequence with DCM, DMF, and MeOH (5 mL each).

Then, the peptidyl-resin was suspended in 3:1 DCM/DMF (5 mL), and DSC (0.116 g, 0.45 mmol) and DIPEA (80 μL , 0.45 mmol) were added at rt under inert atmosphere. After 3 h, the mixture was filtered, and the resin-bound peptide was washed three times in sequence with DCM, DMF, and MeOH (5 mL each).

A suspension of the peptidyl-resin in 1:3 TEA/MeOH (20 mL) was heated at 60 °C for 20 min under

MW irradiation in an open vessel. After filtration, the resin was washed twice with DCM and Et₂O (10 mL each), the filtrates were collected, and the volatiles were evaporated at reduced pressure. The Imi-peptides were separated by semipreparative RP HPLC on a C18 column (general methods) giving **2d** or **2e** in good yield (calculated on an average resin load of 0.6 mmol g⁻¹), and high purity, as determined by analytical RP HPLC (general methods).

Boc-Val-Ala-(S)-Imi-Phe-OMe (2d).

The procedure gave peptide **2d** (0.069 g, 84%, 95% pure). ¹H NMR (8:2 [D₆]DMSO/H₂O, 400 MHz): δ 0.85 (d, *J* = 6.8 Hz, 3H, ValMe), 0.87 (d, *J* = 6.8 Hz, 3H, ValMe), 1.24 (d, *J* = 7.0 Hz, 3H, AlaMe), 1.38 (s, 9H, *t*Bu), 1.93 (m, 1H, ValHβ), 2.97 (dd, *J* = 7.6, 13.8 Hz, 1H, PheHβ), 3.02 (dd, *J* = 5.6, 13.8 Hz, 1H, PheHβ), 3.09 (dd, *J* = 3.4, 9.4 Hz, 1H, ImiH5), 3.57 (s, 3H, OMe), 3.62 (m, 1H, ImiH5), 3.79 (m, 1H, ValHα), 4.44 (ddd, *J* = 5.6, 6.8, 7.6 Hz, 1H, PheHα), 4.75 (dd, *J* = 3.4, 10.0 Hz, 1H, ImiH4), 5.45 (m, 1H, AlaHα), 6.59 (d, *J* = 9.2 Hz, 1H, ValNH), 7.19–7.24 (m, 3H, PheArH), 7.25–7.31 (m, 2H, PheArH), 7.77 (s, 1H, ImiNH1), 8.00 (d, *J* = 7.6 Hz, 1H, AlaNH), 8.59 (d, *J* = 6.8 Hz, 1H, PheNH); ¹³C{¹H} NMR ([D₆]DMSO, 75 MHz): δ 18.5, 19.1, 20.1, 29.1, 29.9, 30.4, 31.5, 37.4, 52.8, 54.7, 55.3, 60.1, 79.9, 127.6, 129.2, 130.0, 137.7, 156.0, 156.7170.5, 171.7, 172.6, 174.4; HRMS (ESI/QTOF) *m/z*: [M+H]⁺ calcd for C₂₇H₄₀N₅O₈, 562.2877; found, 562.2822. Anal. Calcd for C₂₇H₃₉N₅O₈: C, 57.74; H, 7.00; N, 12.47. Found: C, 57.85; H, 6.85; N, 12.58.

Boc-Val-Ala-(R)-Imi-Phe-OMe (2e).

The procedure gave peptide **2e** (0.071 g, 86%, 96% pure). ¹H NMR (8:2 [D₆]DMSO/H₂O, 400 MHz): δ 0.76 (d, *J* = 6.8 Hz, 3H, ValMe), 0.81 (d, *J* = 6.0 Hz, 3H, ValMe), 1.20 (d, *J* = 6.4 Hz, 3H, AlaMe), 1.35 (s, 9H, *t*Bu), 1.94 (m, 1H, ValHβ), 2.67 (dd, *J* = 2.2, 9.8 Hz, 1H, ImiH5), 2.88 (dd, *J* = 10.0, 13.3 Hz, 1H, PheHβ), 3.06 (dd, *J* = 5.4, 13.3 Hz, 1H, PheHβ), 3.45 (m, 1H, ImiH5), 3.61 (s, 3H, OMe), 3.80 (dd, *J* = 6.6, 8.0 Hz, 1H, ValHα), 4.48 (ddd, *J* = 5.4, 8.0, 10.0 Hz, 1H, PheHα), 4.60 (dd, *J* = 2.2, 9.8 Hz, 1H, ImiH4), 5.58 (m, 1H, AlaHα), 6.75 (d, *J* = 8.0 Hz, 1H, ValNH), 7.16–7.22 (m, 3H, PheArH), 7.23–7.30 (m, 2H, PheArH), 7.73 (s, 1H, ImiNH1), 7.86 (d, *J* = 8.0 Hz, 1H, AlaNH), 8.54 (d, *J* = 8.0 Hz, 1H, PheNH); ¹³C{¹H} NMR ([D₆]DMSO, 100 MHz): δ 18.9, 19.2, 19.6, 28.6, 30.7, 37.4, 41.0, 47.1, 52.3, 53.7, 55.4, 56.5, 60.0, 78.6, 124.8, 126.0, 127.0, 128.6, 129.6, 137.4, 155.2, 155.9, 169.6, 171.0, 172.0, 172.7; HRMS (ESI/QTOF) *m/z*: [M+H]⁺ calcd for C₂₇H₄₀N₅O₈, 562.2877; found, 562.2845. Anal. Calcd for C₂₇H₃₉N₅O₈: C, 57.74; H, 7.00; N, 12.47. Found: C, 57.90, H, 6.83, N, 12.60.

4.4 Conformational Analysis by NMR.

Peptide samples were dissolved in 8:2 [D₆]DMSO/H₂O in 5 mm tubes to the final concentration of 0.01 M. At this concentration, the intramolecular aggregation in mixtures of [D₆]DMSO and H₂O is usually unimportant. Besides, self-association of the peptides was excluded based on the reproducibility of the chemical shift of non-exchangeable protons in the concentration range 0.01–0.04 M (not shown). Water suppression was achieved by the PRESAT procedure implemented in Varian. Proton resonance assignment was accomplished through gCOSY. VT ¹H NMR experiments were recorded over the range of 298–348 K; temperature calibration was done with the ethylene glycol OHCH_n chemical shift separation method. 2D ROESY experiments were done at rt, phase-sensitive mode, spin-locking field (γb₂) = 2000 Hz, mixing time = 250 ms; spectra were processed in the hypercomplex approach; peaks were calibrated on solvent. Only ROESY-derived constraints were included in the restrained molecular dynamics (MD). Cross-peak intensities were ranked and associated to the distances (Å): very strong =

2.3, strong = 2.6, medium = 3.0, weak = 5.0. The intensities of the cross peaks arising from protons separated by known distances (e.g., geminal) were found to match with these associations, but were discarded. For the absence of $H\alpha(i, I + 1)$ ROESY cross peaks, all of the ω bonds were set at 180° (force constant: $16 \text{ kcal mol}^{-1} \text{ \AA}^{-2}$).

MD Simulations.

The restrained MD simulations were conducted at 300 K and 1 atm by using the AMBER force field in a $30 \times 30 \times 30 \text{ \AA}^3$ box of standard TIP3P models of equilibrated water, periodic boundary conditions dielectric scale factor = 1, and cutoff for the nonbonded interactions = 12 \AA ; all water molecules closer than 2.3 \AA to a solute atom were eliminated, and 50 random structures were generated by a 100 ps simulation at 1200 K; these were subsequently subjected to restrained MD, 50 ps with a 50% scaled force field at 1200 K, then by 50 ps with full distance restraints, force constant = $7 \text{ kcal mol}^{-1} \text{ \AA}^{-2}$, after which the system was cooled in 20 ps to 50 K. H-bond interactions were not included, nor were torsion angle restraints. The resulting structures were minimized by 3000 cycles of steepest descent and 3000 cycles of conjugated gradient, and convergence = $0.01 \text{ kcal \AA}^{-1} \text{ mol}^{-1}$. The backbones of the structures were clustered by the rmsd analysis.

Unrestrained MD simulations were performed starting with the conformation derived from ROESY in the box of standard TIP3P water for 10 ns at 298 K using periodic boundary conditions, at constant temperature and pressure (Berendsen scheme, ^[45] bath relaxation constant of 0.2). For 1–4 scale factors, van der Waals and electrostatic interactions are scaled in AMBER to half their nominal value. The integration time step was set to 0.1 fs. The system coordinates were collected every picosecond.

Table 4. Non-obvious REOSY cross peaks for 0.01 M Boc-Ala-(S)-Imi-Phe-Val-OMe (**2b**) in 8:2 $[D_6]$ DMSO/ H_2O at rt; vs = very strong, s = strong, m = medium, w = weak.

Cross peak	Intensity	Cross peak	Intensity	Cross peak	Intensity
PheNH - ValMe	m	ValNH - ValH α	m	ImiH4 - ImiH5(3.6)	s
PheNH - AlaMe	m	ValNH - PheH α	vs	ImiH4 - PheH α	w
PheNH - PheH β (2.8)	s	ValNH - ImiH4	w	PheH α - ValMe	w
PheNH - PheH β (3.0)	s	ImiNH1 - AlaMe	w	PheH α - ValH β	w
PheNH - ImiH5(3.1)	w	ImiNH1 - AlaH α	w	PheH α - PheH β (2.8)	s
PheNH - ImiH5(3.6)	w	PheArH - AlaMe	w	PheH α - PheH β (3.0)	m
PheNH - PheH α	m	PheArH - COOMe	m	PheH α - ValH α	w
PheNH - ImiH4	vs	PheArH - ValH α	m	ValH α - ValMe	s
PheNH - PheH α	w	PheArH - PheH α	s	ValH α - ValH β	m
PheNH - AlaNH	w	PheArH - AlaNH	w	ValH α - COOMe	vs
PheNH - PheArH	m	AlaNH - AlaMe	vs	COOMe - ValMe	s
PheNH - ValNH	m	AlaNH - tBu	s	COOMe - ValH β	m
ValNH - ValMe	s	AlaNH - AlaH α	m	ImiH5(3.6) - ValMe	w
ValNH - ValH β	s	AlaH α - tBu	s	ImiH5(3.1) - ValMe	m
ValNH - PheH β (2.8)	w	AlaH α - ImiH4	m	PheH β (3.0) - AlaMe	m
ValNH - PheH β (3.0)	w	ImiH4 - ValMe	s	PheH β (2.8) - AlaMe	m
ValNH - ImiH5(3.1)	w	ImiH4 - AlaMe	w	tBu - AlaMe	m

ValNH - COOMe	m	ImiH4 - ImiH5(3.1)	w		
---------------	---	--------------------	---	--	--

Table 5. Non-obvious REOSY cross peaks for 0.01 M Boc-Ala-(R)-Imi-Phe-Val-OMe (**2c**) in 8:2 [D₆]DMSO/H₂O at rt; vs = very strong, s = strong, m = medium, w = weak. Residue stereochemistry has been omitted.

Cross peak	Intensity	Cross peak	Intensity	Cross peak	Intensity
PheNH - ValMe	w	ValNH - PheH α	vs	PheH α - ValMe	m
PheNH - tBu	w	ValNH - PheArH	w	PheH α - ValH β	m
PheNH - AlaMe	w	ImiNH1 - AlaMe	w	PheH α - ImiH5(2.4)	w
PheNH - ValH β	w	PheArH - ValMe	w	PheH α - PheH β (2.7)	s
PheNH - ImiH5(2.4)	m	PheArH - AlaMe	w	PheH α - PheH β (3.0)	s
PheNH - PheH β (2.7)	s	PheArH - tBu	w	PheH α - COOMe	w
PheNH - PheH β (3.0)	w	PheArH - ValH β	m	PheH α - ValH α	w
PheNH - ImiH5(3.3)	w	PheArH - ImiH5(2.4)	s	PheH α - ImiH4	m
PheNH - ValH α	w	PheArH - ImiH5(3.3)	w	ImiH4 - AlaMe	m
PheNH - ImiH4	vs	PheArH - COOMe	m	ImiH4 - ImiH5(2.4)	m
PheNH - PheH α	m	PheArH - ValH α	m	ImiH4 - PheH β (3.0)	w
PheNH - AlaNH	w	PheArH - ImiH4	w	ImiH4 - ImiH5(3.3)	s
PheNH - PheArH	s	PheArH - PheH α	s	ValH α - tBu	m
PheNH - ValNH	w	AlaNH - ValMe	w	ValH α - ValH β	m
ValNH - ValMe	s	AlaNH - AlaMe	vs	ValH α - COOMe	m
ValNH - AlaMe	w	AlaNH - tBu	m	COOMe - ValMe	s
ValNH - tBu	w	AlaNH - ImiH4	w	COOMe - tBu	w
ValNH - ValH β	s	AlaNH - PheH α	w	COOMe - ValH β	s
ValNH - PheH β (2.7)	w	AlaNH - AlaH α	m	ValH β - tBu	w
ValNH - PheH β (3.0)	m	AlaH α - ValMe	m	tBu - ValMe	m
ValNH - COOMe	m	AlaH α - tBu	w	tBu - AlaMe	w
ValNH - ValH α	m	AlaH α - ImiH4	w		

Table 6. Non-obvious REOSY cross peaks for 0.01 M Boc-Val-Ala-(S)-Imi-Phe-OMe (**2d**) in 8:2 [D₆]DMSO/H₂O at rt; vs = very strong, s = strong, m = medium, w = weak.

Cross peak	Intensity	Cross peak	Intensity	Cross peak	Intensity
PheNH - AlaMe	w	AlaNH - ImiH4	w	ImiH4 - ImiH5(3.1)	m
PheNH - PheH β	m	AlaNH - AlaH α	m	ImiH4 - ImiH5(3.6)	s
PheNH - ImiH5(3.1)	w	AlaNH - ValNH	m	ImiH4 - PheH α	w
PheNH - COOMe	m	ImiNH1 - AlaMe	w	PheH α - ImiH5(3.1)	w
PheNH - ImiH5(3.6)	w	ImiNH1 - AlaH α	w	PheH α - COOMe	s
PheNH - PheH α	m	PheArH - AlaMe	m	PheH α - ImiH4	w
PheNH - ImiH4	vs	PheArH - COOMe	m	ValH α - ValMe	vs
PheNH - AlaH α	w	PheArH - PheH α	s	ValH α - tBu	m

PheNH - PheArH	s	ValNH - ValMe	vs	ValH α - ValH β	s
PheNH - AlaNH	m	ValNH - tBu	vs	COOMe - PheH β	m
AlaNH - ValMe	m	ValNH - ValH β	m	PheH β - AlaMe	w
AlaNH - AlaMe	vs	ValNH - ValH α	m	ValH β - tBu	w
AlaNH - tBu	w	AlaH α - ValMe	m	tBu - ValMe	m
AlaNH - ValH β	w	AlaH α - ValH β	w	AlaMe - ValMe	m
AlaNH - PheH β	w	AlaH α - ValH α	w		
AlaNH - ValH α	m	AlaH α - ImiH4	w		

Table 7. Non-obvious REOSY cross peaks for 0.01 M Boc-Val-Ala-(R)-Imi-Phe-OMe (**2e**) in 8:2 [D₆]DMSO/H₂O at rt; vs = very strong, s = strong, m = medium, w = weak. Residue stereochemistry has been omitted.

Cross peak	Intensit -y	Cross peak	Intensit -y	Cross peak	Intensit -y
PheNH - AlaMe	w	ImiNH1 - AlaH α	w	ImiH4 - PheH α	w
PheNH - ImiH5(2.7)	w	PheArH - AlaMe	w	PheH α - ImiH5(2.7)	m
PheNH - PheH β (2.9)	s	PheArH - tBu	m	PheH α - PheH β (2.9)	s
PheNH - PheH β (3.1)	s	PheArH - COOMe	m	PheH α - PheH β (3.1)	s
PheNH - ImiH5(3.5)	m	PheArH - ValH α	m	PheH α - COOMe	m
PheNH - COOMe	w	PheArH - PheH α	s	ValH α - ValMe	vs
PheNH - PheH α	m	PheArH - ImiH4	w	ValH α - AlaMe	w
PheNH - ImiH4	vs	PheArH - ValNH	w	ValH α - tBu	s
PheNH - AlaH α	w	ValNH - ValMe	vs	ValH α - ValH β	s
PheNH - PheArH	m	ValNH - AlaMe	m	ValH α - COOMe	m
PheNH - AlaNH	m	ValNH - tBu	s	COOMe - ValMe	w
AlaNH - ValMe	m	ValNH - ValH β	m	COOMe - tBu	m
AlaNH - AlaMe	vs	ValNH - COOMe	w	COOMe - PheH β (2.9)	s
AlaNH - tBu	w	ValNH - ValH α	m	COOMe - PheH β (3.1)	m
AlaNH - ValH β	m	AlaH α - ValMe	m	ImiH5(3.5) - AlaMe	w
AlaNH - PheH β (3.1)	w	AlaH α - ValH β	w	PheH β (2.9) - tBu	w
AlaNH - COOMe	w	AlaH α - ValH α	w	PheH β (3.1) - tBu	w
AlaNH - ValH α	s	AlaH α - ImiH4	m	ValH β - AlaMe	w
AlaNH - ImiH4	w	ImiH4 - AlaMe	m	ValH β - tBu	m
AlaNH - AlaH α	m	ImiH4 - ImiH5(2.7)	m	tBu - ValMe	s
AlaNH - ValNH	m	ImiH4 - PheH β (3.1)	w	AlaMe - ValMe	m
ImiNH1 - AlaMe	w	ImiH4 - ImiH5(3.5)	s		

4.5 Synthesis of Peptides 3.

The reaction was performed under conditions which allow using (S)- or (R)-serine esters without protection of the hydroxy group.³⁶ Briefly, a stirred solution of the N-protected amino acid (0.5 mmol) in 4:1 DCM/DMF (4 mL) was treated with HOBt (0.6 mmol) and 2-(1H-benzotriazol-1-yl)-1,1,3,3-

tetramethyluronium hexafluorophosphate (HBTU, 0.6 mmol) at rt and under inert atmosphere. After 5 min, serine ester (0.55 mmol) and DIPEA (1.2 mmol) were added, and the reaction was stirred for 10 min under MW irradiation, setting the internal reaction temperature at 80 °C. After concentration of the mixture at reduced pressure, the residue was diluted with EtOAc (20 mL). The organic layer was washed with 0.1 M HCl (5 mL), and a saturated solution of NaHCO₃ (5 mL) was dried over Na₂SO₄. After evaporation of the solvent at reduced pressure, the crude dipeptide esters **3** were isolated (70–85%, 80–90% pure according to analytical RP HPLC) by flash chromatography over silica gel (eluent 1:3 cyclohexane/EtOAc) and were identified by ESI MS.

Synthesis of *N*₁-Substituted Imi-Peptides **7.**

The general procedure is as follows: To a solution of triphenylphosphine (0.080 g, 0.31 mmol) in anhydrous DCM (4 mL), iodine (0.080 g, 0.32 mmol) was added at rt under inert atmosphere and magnetic stirring. After 15 min, imidazole (0.043 g, 0.6 mmol) was also added and the mixture was stirred for additional 15 min. The dipeptide **3** (0.25 mmol), dissolved in DCM (2 mL), was finally added and the reaction mixture refluxed for 2 h. The mixture was then cooled, diluted with DCM (6 mL), and washed with 10% Na₂S₂O₄ in water (4 mL). The organic layer was dried over Na₂SO₄, and the solvents were evaporated at reduced pressure to the final volume of 3 mL. The solution was allowed to stand at 5 °C overnight, and some white solid Ph₃PO which precipitated not quantitatively was removed by filtration and washed with DCM (5 mL). The filtrate was evaporated at reduced pressure to give the crude iodides **4**.

The crude iodides **4** (0.25 mmol) were dissolved in anhydrous DMF (5 mL), the amine (0.5 mmol) was added, and the mixture was heated at 50 °C for 3 h. Then, DMF was distilled at reduced pressure, the residue was suspended in 0.1 M HCl (12 mL), and the mixture was washed with Et₂O (5 mL). The pH of the water layer was corrected to 9–10 with sat. Na₂CO₃, and then it was extracted 3 times with EtOAc (5 mL). The collected organic layers were dried over Na₂SO₄, and solvent was removed at reduced pressure. The crude residues were utilized for the next step without further purifications, the only exception being **5d**, which was purified as described thereafter.

Boc-Ala-Dap(Allyl)-OMe (5d).

The residue was purified by flash chromatography over silica gel (eluent EtOAc/MeOH 98:2), giving the dipeptide (0.058 g, 70%, 94% pure by RP HPLC). ¹H NMR (CDCl₃, 400 MHz): 2 conformers δ 1.39 (d, *J* = 6.8 Hz, 3H, AlaMe), 1.44 + 1.45 (s, 9H, *t*Bu), 1.69 (br s, 1H, NH), 2.98 (dd, *J* = 4.4, 12.7 Hz, 1H, DapHβ), 3.08 (dd, *J* = 5.4, 12.7 Hz, 1H, DapHβ), 3.22–3.27 (m, 2H, NCH₂), 3.76 (s, 3H, OMe), 4.19 (m, 1H, AlaHα), 4.63 (m, 1H, DapHα), 4.99 (br d, 1H, AlaNH), 5.05–5.19 (m, 2H, CH₂), 5.82 (m, 1H, CH), 6.92 + 7.06 (br d, 1H, DapNH); ¹³C{¹H} NMR (CDCl₃, 100 MHz): 2 conformers δ 18.7, 28.6, 49.8, 52.3, 52.6, 52.8, 55.2, 77.6, 116.7 + 116.8, 136.5 + 136.6, 155.7, 172.0 + 172.1, 172.9 + 173.0; HRMS (ESI/QTOF) *m/z*: [M+H]⁺ calcd for C₁₅H₂₈N₃O₅, 330.2029; found, 330.2060. Anal. Calcd for C₁₅H₂₇N₃O₅: C, 54.70; H, 8.26; N, 12.76. Found: C, 54.84; H, 8.33; N, 12.87.

The oily residues containing the crude dipeptides **5** were dissolved in DMF (5 mL), pNPC (0.075 g, 0.38 mmol) and DBU (0.055 g, 0.38 mmol) were added, and the mixture was stirred at rt for 12 h. The solvent was distilled at reduced pressure, and 0.1 M HCl (4 mL) was added, and then the residue was extracted 3 times with EtOAc (5 mL). The collected organic layers were dried over Na₂SO₄, and the solvent was removed at reduced pressure. The Imi dipeptides **7** were isolated from the resulting mixtures by flash chromatography over silica gel (eluent EtOAc/MeOH 98:2), and purity was determined by RP HPLC (general methods).

Boc-Ala-(S)-Imi(N₁Me)-OMe (7a).

Starting from **3a** (0.070 g, 0.24 mmol), the general procedure gave **7a** (0.071 g, 90%, 95% pure). ¹H NMR (CDCl₃, 400 MHz): δ 1.38–1.48 (m, 12H, AlaMe + *t*Bu), 2.87 (s, 3H, NMe), 3.38 (dd, *J* = 3.4, 9.8 Hz, 1H, ImiH5), 3.71 (t, *J* = 10.0 Hz, 1H, ImiH5), 3.77 (s, 3H, OMe), 4.82 (dd, *J* = 3.4, 9.8 Hz, 1H, ImiH4), 5.08 (d, *J* = 7.6 Hz, 1H, AlaNH), 5.51 (m, 1H, AlaHα); ¹³C {¹H} NMR (CDCl₃, 100 MHz): δ 18.4, 28.3, 30.5, 46.6, 48.7, 51.9, 52.9, 79.6, 153.1, 155.3, 169.9, 174.1; HRMS (ESI/QTOF) *m/z*: [M+H]⁺ calcd for C₁₄H₂₄N₃O₆, 330.1665; found, 330.1688. Anal. Calcd for C₁₄H₂₃N₃O₆: C, 51.06; H, 7.04; N, 12.76. Found: C, 50.84; H, 7.28; N, 13.00.

Cbz-Val-(S)-Imi(N₁*i*Pr)-OMe (7b).

Starting from **3b** (0.088 g, 0.25 mmol), the general procedure gave **7b** (0.089 g, 85%, 91% pure). ¹H NMR (CDCl₃, 400 MHz): δ 0.86 (d, *J* = 7.2 Hz, 3H, ValMe), 0.95 (d, *J* = 7.2 Hz, 3H, ValMe), 1.02 (d, *J* = 6.4 Hz, 3H, *i*PrMe), 1.10 (d, *J* = 6.4 Hz, 3H, *i*PrMe), 2.25 (m, 1H, ValHβ), 2.35 (m, 1H, N₁CH), 3.33 (dd, *J* = 3.6, 9.8 Hz, 1H, ImiH5), 3.66 (t, *J* = 9.8 Hz, 1H, ImiH5), 3.78 (s, 3H, OMe), 4.82 (dd, *J* = 3.6, 9.8 Hz, 1H, ImiH4), 5.11 (br s, 2H, PhCH₂), 5.41 (d, *J* = 8.0 Hz, 1H, ValNH), 5.61 (m, 1H, ValHα), 7.33–7.41 (m, 5H, ArH); ¹³C {¹H} NMR (CDCl₃, 100 MHz): δ 16.6, 18.8, 21.1, 22.6, 28.7, 41.4, 48.3, 50.2, 52.5, 56.7, 61.2, 128.0, 129.0, 129.1, 137.7, 153.4, 155.9, 173.5, 175.3; HRMS (ESI/QTOF) *m/z*: [M+H]⁺ calcd for C₂₁H₃₀N₃O₆, 420.2135; found, 420.2172. Anal. Calcd for C₂₁H₂₉N₃O₆: C, 60.13; H, 6.97. N, 10.02. Found: C, 60.22; H, 7.26; N, 10.10.

Boc-Ala-(S)-Imi(N₁Ph)-OBn (7c).

Starting from **3c** (0.084 g, 0.23 mmol), the general procedure gave **7c** (0.072 g, 80%, 92% pure). ¹H NMR (CDCl₃, 400 MHz): δ 1.40 (d, *J* = 6.8 Hz, 3H, AlaMe), 1.44 (s, 9H, *t*Bu), 3.84 (dd, *J* = 3.2, 9.6 Hz, 1H, ImiH5), 4.19 (dd, *J* = 9.6, 10.0 Hz, 1H, ImiH5), 5.00 (dd, *J* = 3.2, 10.0 Hz, 1H, ImiH4), 5.10 (d, *J* = 7.2, 1H, AlaNH), 5.17 (d, *J* = 12.0 Hz, 1H, PhCH), 5.26 (d, *J* = 12.0 Hz, 1H, PhCH), 5.53 (m, 1H, AlaHα), 7.18 (m, 1H, ArH), 7.30–7.41 (m, 7H, ArH), 7.43–7.50 (m, 2H, ArH); ¹³C {¹H} NMR (CDCl₃, 100 MHz): δ 18.2, 28.3, 45.3, 49.1, 51.6, 67.9, 79.8, 119.3, 124.9, 128.5, 128.7, 128.8, 129.1, 134.6, 137.9, 150.9, 155.3, 168.9, 174.4; HRMS (ESI/QTOF) *m/z*: [M+H]⁺ calcd for C₁₉H₂₆N₃O₆, 392.1822; found, 392.1856. Anal. Calcd for C₁₉H₂₅N₃O₆: C, 58.30; H, 6.44; N, 10.74. Found: C, 58.47; H, 6.35; N, 10.83.

Boc-Ala-(S)-Imi(N₁Allyl)-OBn (7e).

Starting from **3c** [46] (0.091 g, 0.25 mmol), the general procedure gave **7e** (0.099 g, 93%, 94% pure). ¹H NMR (CDCl₃, 400 MHz): δ 1.36 (d, *J* = 7.2 Hz, 3H, AlaMe), 1.43 (s, 9H, *t*Bu), 3.32 (dd, *J* = 3.0, 9.8 Hz, 1H, ImiH5), 3.65 (dd, *J* = 9.8, 10.4 Hz, 1H, ImiH5), 3.78 (dd, *J* = 5.2, 14.8 Hz, 1H, CH₂–CH), 3.92 (dd, *J* = 6.2, 15.8 Hz, 1H, CH₂–CH), 4.87 (dd, *J* = 3.0, 10.4 Hz, 1H, ImiH4), 5.08 (d, *J* = 8.0 Hz, 1H, AlaNH), 5.17–5.27 (m, 4H, 7.30–7.40 (m, 5H, ArH); ¹³C {¹H} NMR, (CDCl₃, 100 MHz): δ 18.7, 28.6, 44.5, 46.5, 49.2, 52.5, 68.1, 80.1, 119.5, 126.5, 128.8, 129.0, 131.5, 135.1, 153.1, 155.7, 169.6, 174.5; HRMS (ESI/QTOF) *m/z*: [M+H]⁺ calcd for C₂₂H₃₀N₃O₆, 432.2135; found, 432.2166. Anal. Calcd for C₂₂H₂₉N₃O₆: C, 61.24; H, 6.77; N, 9.74. Found: C, 61.38; H, 6.84; N, 9.81.

Boc-(S)-Ala-(R)-Imi(N₁Me)-OMe (7f).

Starting from **3f** (0.073 g, 0.25 mmol), the general procedure gave **7f** (0.072 g, 87%, 93% pure). ¹H NMR (CDCl₃, 400 MHz): δ 1.36 (d, *J* = 7.2, 1H, AlaMe), 1.42 (s, 9H, *t*Bu), 2.88 (s, 3H, NMe), 3.38 (dd, *J* = 3.4, 9.7 Hz, 1H, ImiH5), 3.71 (dd, *J* = 9.7, 10.4 Hz, 1H, ImiH5), 3.76 (s, 3H, OMe), 4.70 (dd, *J* = 3.4, 10.4 Hz, 1H, ImiH4), 5.36 (br d, 1H, AlaNH), 5.51 (m, 1H, AlaHα); ¹³C {¹H} NMR (CDCl₃, 100 MHz): δ 19.3, 28.2, 30.5, 46.6, 51.8, 52.4, 52.8, 79.3, 153.1, 154.8, 169.7, 173.9; HRMS (ESI/ QTOF) *m/z*:

[M+H]⁺ calcd for C₁₄H₂₄N₃O₆, 330.1665; found, 330.1692. Anal. Calcd for C₁₄H₂₃N₃O₆: C, 51.06; H, 7.04; N, 12.76. Found: C, 50.76; H, 7.39; N, 13.04.

Cbz-Val-(R)-Imi(N_iPr)-OMe (7g).

Starting from **3g** (0.084 g, 0.24 mmol), the general procedure gave **7g** (0.082 g, 82%, 91% pure). ¹H NMR (CDCl₃, 400 MHz): δ 0.83 (d, *J* = 7.2 Hz, 3H, ValMe), 0.86 (d, *J* = 7.2 Hz, 3H, ValMe), 1.05 (d, *J* = 6.4 Hz, 3H, *i*PrMe), 1.10 (d, *J* = 6.4 Hz, 3H, *i*PrMe), 2.19 (m, 1H, ValHβ), 2.37 (m, 1H, N₁CH), 3.32 (dd, *J* = 3.6, 9.8 Hz, 1H, ImiH5), 3.66 (t, *J* = 9.8 Hz, 1H, ImiH5), 3.78 (s, 3H, OMe), 4.69 (dd, *J* = 3.6, 9.8 Hz, 1H, ImiH4), 5.08–5.15 (m, 2H, PhCH₂), 5.57–5.62 (m, 2H, ValHα + ValNH), 7.28–7.39 (m, 5H, ArH); ¹³C{¹H} NMR (CDCl₃, 100 MHz): δ 16.3, 17.4, 20.3, 28.8, 40.5, 52.2, 53.4, 55.0, 59.2, 67.0, 127.9, 128.7, 129.1, 129.5, 137.1, 152.5, 155.0, 172.3, 174.5; HRMS (ESI/QTOF) *m/z*: [M+H]⁺ calcd for C₂₁H₃₀N₃O₆, 420.2135; found, 420.2166. Anal. Calcd for C₂₁H₂₉N₃O₆: C, 60.13; H, 6.97; N, 10.02. Found: C, 60.30; H, 7.20; N, 10.19.

Boc-Ala-(R)-Imi(N₁Ph)-OBn (7h).

Starting from **3h** (0.091 g, 0.25 mmol), the general procedure gave **7h** (0.074 g, 77%, 96% pure). ¹H NMR (CDCl₃, 400 MHz): δ 1.44 (d, *J* = 6.4 Hz, 3H, AlaMe), 1.47 (s, 9H, *t*Bu), 3.77 (dd, *J* = 2.6, 10.2 Hz, 1H, ImiH5), 4.23 (dd, *J* = 9.8, 10.2 Hz, 1H, ImiH5), 4.88 (dd, *J* = 2.6, 9.8 Hz, 1H, ImiH4), 5.23 (s, 2H, PhCH₂), 5.44 (br d, 1H, AlaNH), 5.65 (m, 1H, AlaHα), 7.19 (m, 1H, ArH), 7.30–7.41 (m, 7H, ArH), 7.43–7.51 (m, 2H, ArH); ¹³C {¹H} NMR (CDCl₃, 100 MHz): δ 19.5, 28.4, 45.3, 49.5, 52.1, 67.9, 79.6, 119.2, 125.0, 126.1, 128.3, 128.7, 129.2, 134.8, 137.8, 150.8, 154.8, 168.7, 174.2; HRMS (ESI/QTOF) *m/z*: [M+H]⁺ calcd for C₁₉H₂₆N₃O₆, 392.1822; found, 392.1861. Anal. Calcd for C₁₉H₂₅N₃O₆: C, 58.30; H, 6.44; N, 10.74. Found: C, 58.44; H, 6.51; N, 10.90.

Boc-Ala-(R)-Imi(N₁Allyl)-OBn (7i).

Starting from **3h**⁴⁶ (0.088 g, 0.24 mmol), the general procedure gave **7i** (0.093 g, 90%, 92% pure). ¹H NMR (CDCl₃, 400 MHz): δ 1.40 (d, *J* = 6.8 Hz, 3H, AlaMe), 1.46 (s, 9H, *t*Bu), 3.29 (dd, *J* = 3.4, 9.8 Hz, 1H, ImiH5), 3.64 (dd, *J* = 9.8, 10.4 Hz, 1H, ImiH5), 3.77 (dd, *J* = 5.8, 15.6 Hz, 1H, CH₂–CH=), 3.96 (dd, *J* = 5.4, 15.6 Hz, 1H, CH₂–CH=), 4.74 (dd, *J* = 3.4, 10.4 Hz, 1H, ImiH4), 5.15–5.22 (m, 4H, PhCH₂ + =CH₂), 5.40 (br d, 1H, AlaNH), 5.56 (m, 1H, AlaHα), 5.66 (m, 1H, =CH₂), 7.30–7.39 (m, 5H, Ar); ¹³C{¹H} NMR (CDCl₃, 100 MHz): δ 19.9, 28.7, 44.4, 46.5, 49.5, 53.1, 68.0, 79.9, 119.4, 128.8, 128.9, 120.0, 131.5, 135.3, 152.9, 155.1, 169.4, 174.3; HRMS (ESI/QTOF) *m/z*: [M+H]⁺ calcd for C₂₂H₃₀N₃O₆, 432.2135; found, 432.2167. Anal. Calcd for C₂₂H₂₉N₃O₆: C, 61.24; H, 6.77; N, 9.74. Found: C, 61.33; H, 6.68; N, 9.66.

Boc-Ala-(S)-Imi[N₁(CH₂)₃CO₂Me]-OBn (7l).

Starting from **3c** ^[46] (0.081 g, 0.22 mmol), the general procedure gave **7l** (0.080 g, 74%, 94% pure). ¹H NMR (CDCl₃, 400 MHz): δ 1.35 (d, *J* = 6.4 Hz, 3H, AlaMe), 1.43 (s, 9H, *t*Bu), 1.78–1.86 (m, 2H, CH₂), 2.30–2.38 (m, 2H, CH₂), 3.24 (m, 1H, CH₂), 3.35–3.40 (m, 2H, CH₂ + ImiH5), 3.63–3.77 (m, 4H, COOMe + ImiH5), 4.87 (dd, *J* = 3.4, 10.2, 1H, ImiH4), 5.07 (d, *J* = 8.4 Hz, 1H, AlaNH), 5.15 (d, *J* = 12.2 Hz, 1H, PhCH), 5.25 (d, *J* = 12.2 Hz, 1H, PhCH), 5.46 (m, 1H, AlaHα), 7.25–7.38 (m, 5H, ArH); ¹³C{¹H} NMR (CDCl₃, 100 MHz): δ 14.6, 22.6, 28.7, 31.3, 43.4, 44.9, 48.0, 52.5, 68.2, 80.0, 128.8, 129.1, 143.1, 153.4, 155.9, 173.5, 175.3; HRMS (ESI/QTOF) *m/z*: [M+H]⁺ calcd for C₂₄H₃₄N₃O₈, 492.2346; found, 492.2329. Anal. Calcd for C₂₄H₃₃N₃O₈: C, 58.64; H, 6.77; N, 8.55. Found: C, 58.78; H, 6.82; N, 8.60.

(S)- or (R)-Methyl-1-methyl-2-oxoimidazolidine-4-carboxylates (S)-8 or (R)-8.

To a stirred suspension of LiOH (0.028 g, 1.2 mmol) in tetrahydrofuran (THF; 6 mL) and water (1.5 mL),

a solution of H₂O₂ (30 wt %, 0.28 mL, 2.3 mmol) was added at 0 °C. After 15 min, a solution of **7a** or **7f** (0.13 g, 0.4 mmol) in THF (3 mL) was added at 0 °C while stirring. The temperature was allowed to rise to rt, and after 4 h, the pH was adjusted to 5–6 with 0.1 M HCl, THF was evaporated at reduced pressure, and the mixture was extracted three times with EtOAc. The collected organic layers were dried over Na₂SO₄, and the residue was purified by flash chromatography over silica gel (eluent cyclohexane/EtOAc 1:3) giving (*S*)-**8** (0.050 g, 0.32 mmol, 80% yield, 94% pure) or (*R*)-**8** (0.047 g, 0.30 mmol, 75% yield, 94% pure), and their [α]_D specific optical rotations were determined to be +25 (*c* 0.7, MeOH) and –24 (*c* 0.6, MeOH), respectively; literature for (*S*)-**8**: [α]_D²⁰ +26.9 (*c* 1, MeOH).^[23]

Boc-Ala-(*R*)-Imi(*N*₁*n*Pr)-Phe-OMe (9).

The dipeptide **7i** (0.1 g, 0.23 mmol) was subjected to hydrogenation in the presence of a catalytic amount of 10% Pd/C in EtOH (10 mL) at rt. The reaction was monitored by TLC, and after 6 h, the solution was filtered over Celite. The solvent was removed at reduced pressure, and the presence of the dipeptide acid was confirmed by RP HPLC and ESI MS.

The residue was dissolved in 3:1 DCM/DMF (6 mL) and reacted with HOBt (0.038 g, 0.28 mmol), H-Phe-OMe·HCl (0.060 g, 0.28 mmol), EDC·HCl (0.054 g, 0.28 mmol), and TEA (0.083 mL, 0.60 mmol). The reaction was conducted as described for peptides **1**, and after the usual work up, the Imi-tripeptide **9** was isolated as described for the Imi-peptides **2** (0.090 g, 78%, 88% pure according to analytical RP HPLC, general methods). ¹H NMR (8:2 [*D*₆]DMSO/H₂O, 400 MHz): δ 0.74 (t, *J* = 7.3 Hz, 3H, Me), 1.16 (d, *J* = 6.4 Hz, 3H, AlaMe), 1.27–1.34 (m, 2H, CH₂), 1.36 (s, 9H, *t*Bu), 2.56 (dd, *J* = 3.0, 9.5 Hz, 1H, ImiH₅), 2.85 (dd, *J* = 10.8, 13.2 Hz, PheH β), 2.95 (m, 1H, NCH₂), 3.07–3.17 (m, 2H, PheH β + NCH₂), 3.46 (dd, *J* = 9.5, 10.0 Hz, 1H, ImiH₅), 3.65 (s, 3H, OMe), 4.50–4.60 (m, 2H, PheH α + ImiH₄), 5.34 (m, 1H, AlaH α), 6.76 (d, *J* = 8.8 Hz, 1H, AlaNH), 7.17–7.22 (m, 3H, PheArH), 7.22–7.30 (m, 2H, PheArH), 8.59 (d, *J* = 8.0 Hz, 1H, PheNH); ¹³C{¹H} NMR ([*D*₆]DMSO, 100 MHz): δ 11.7, 19.9, 20.5, 29.1, 38.1, 45.0, 45.7, 49.0, 53.0, 53.5, HRMS (ESI/QTOF) *m/z*: [M+H]⁺ calcd for C₂₅H₃₇N₄O₇, 505.2662; found, 505.2685. Anal. Calcd for C₂₅H₃₆N₄O₇: C, 59.51; H, 7.19; N, 11.10. Found: C, 59.71; H, 7.22; N, 11.05.

Boc-Ala-(*S*)-Imi((*E*)-3-(4-((*tert*-butoxycarbonyl)amino)phenyl)-allyl)-OBn (10).

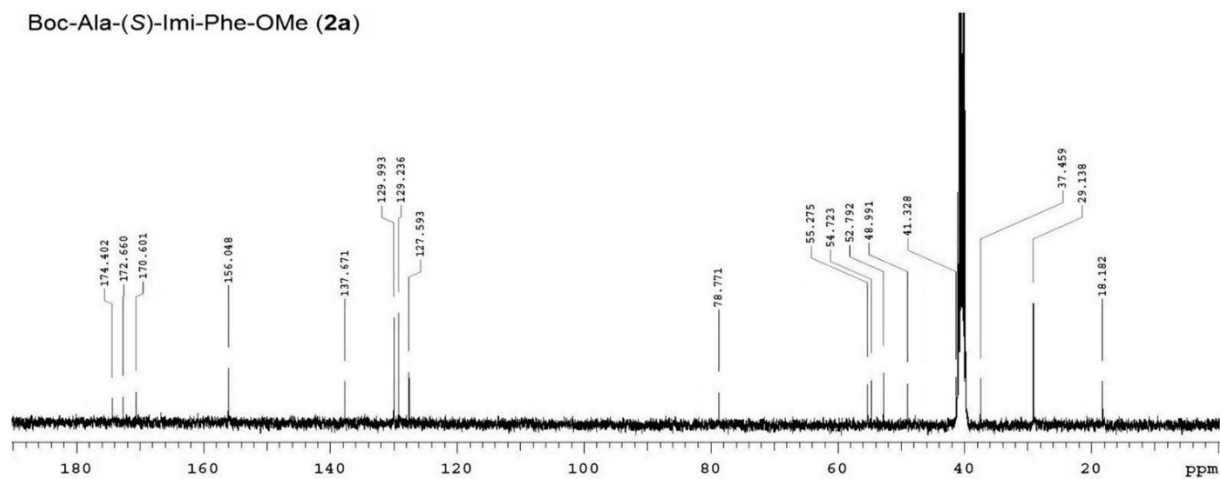
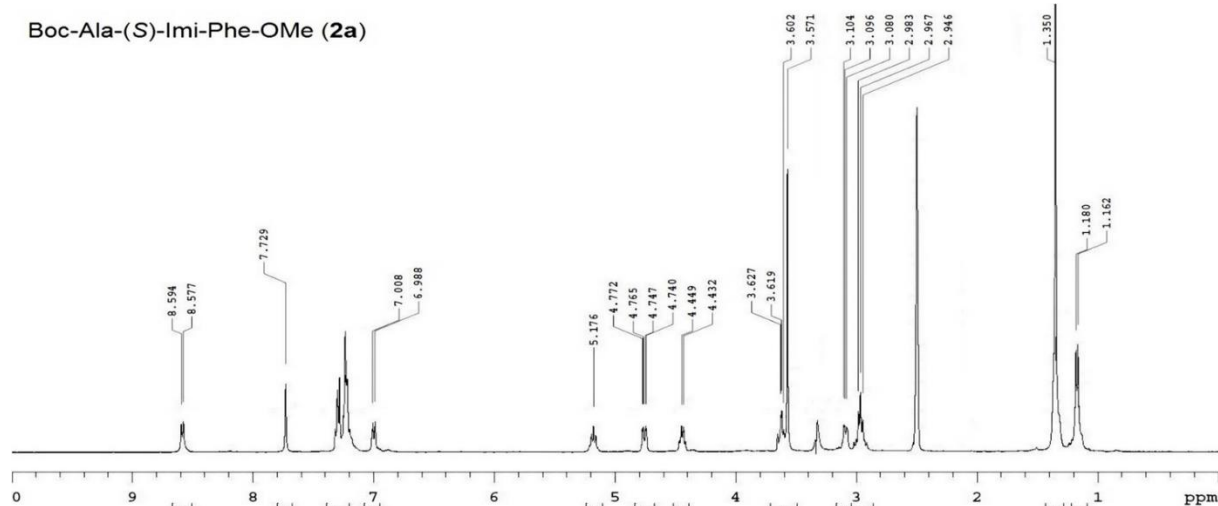
A mixture of dipeptide **7e** (0.056 g, 0.13 mmol), N-Boc-4-bromoaniline (0.054 g, 0.2 mmol), palladium acetate (0.3 mg, 0.0013 mmol), and triphenylphosphine (0.7 mg, 0.0026 mmol) were stirred in 1:2 TEA/DMF (3 mL) under inert atmosphere. The mixture was stirred for 18 h at 80 °C. Then, the mixture was evaporated at reduced pressure, MeOH (15 mL) was added to the residue, and the suspension was filtered through a Celite pad to remove the fine black Pd⁰. The solvent was evaporated at reduced pressure, and the residue was dissolved in EtOAc (20 mL) and washed with 1 M HCl (4 mL). The organic layer was dried over Na₂SO₄, and after evaporation at reduced pressure, the residue was purified by semipreparative RP HPLC over a C18 column (general methods), giving **10** (0.063 g, 0.10 mmol, 78%, 92% pure by analytical RP HPLC, general methods). ¹H NMR (CDCl₃, 400 MHz): δ 1.26 (s, 9H, *t*Bu), 1.38 (d, *J* = 6.8 Hz, 3H, AlaMe), 1.44 (s, 9H, *t*Bu), 3.35 (dd, *J* = 3.4, 9.9 Hz, 1H, ImiH₅), 3.70 (dd, *J* = 9.9, 10.3 Hz, 1H, ImiH₅), 3.97 (dd, *J* = 6.4, 15.4 Hz, 1H, CH–CH=), 4.07 (dd, *J* = 6.6, 15.4 Hz, 1H, CH–CH=), 4.88 (dd, *J* = 3.4, 10.3 Hz, 1H, ImiH₄), 5.07 (d, *J* = 7.6 Hz, 1H, AlaNH), 5.13 (d, *J* = 12.2 Hz, 1H, CHPh), 5.23 (d, *J* = 12.2 Hz, 1H, CHPh), 5.51 (m, 1H, AlaH α), 6.06 (m, 1H, CH=), 6.54 (d, *J* = 15.6 Hz, 1H, CH=), 7.28–7.36 (m, 7H, ArH), 7.39 (d, *J* = 8.8 Hz, 2H, ArH); ¹³C{¹H} NMR (CDCl₃, 100 MHz): δ 17.2, 28.7 \times 2, 43.6, 48.5, 50.8, 53.1, 66.3, 81.7, 120.4, 124.0, 126.9, 129.0, 130.1, 132.2, 135.0, 137.8, 151.8, 152.8, 155.0, 172.1, 175.5; HRMS (ESI/QTOF) *m/z*: [M+H]⁺ calcd for C₃₃H₄₃N₄O₈,

623.3081; found, 623.3101. Anal. Calcd for C₃₃H₄₂N₄O₈: C, 63.65; H, 6.80; N, 9.00. Found: C, 61.41; H, 6.68; N, 9.05.

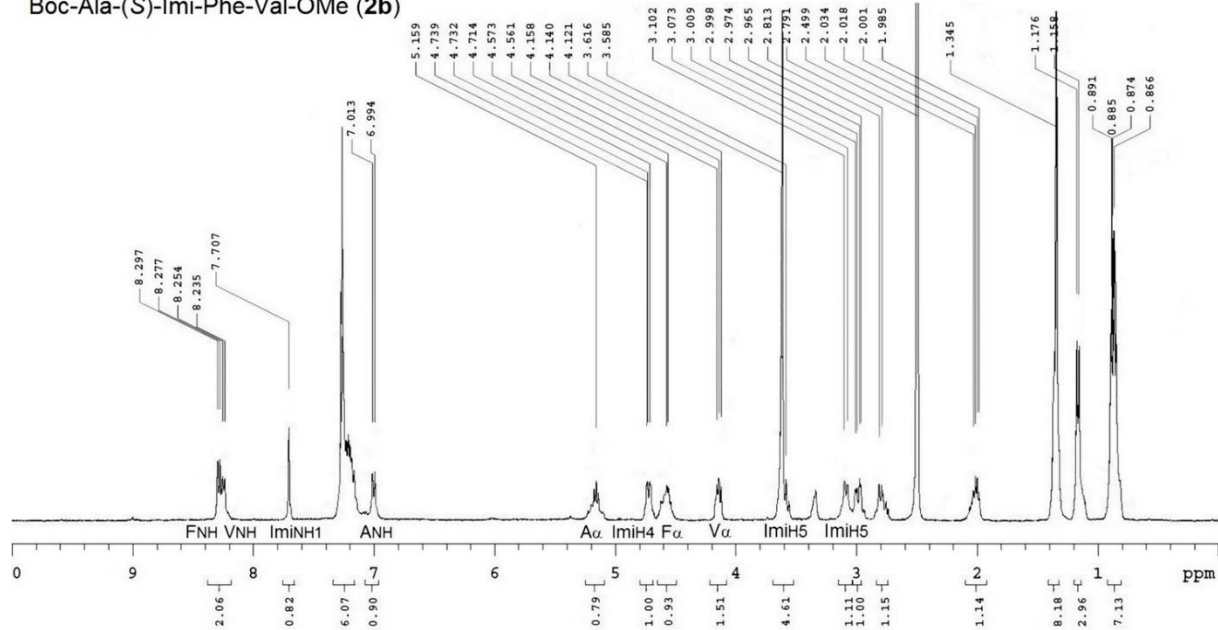
Boc-Ala-(S)-Imi(3-(4-((tert-butoxycarbonyl)amino)phenyl)-propyl)-OBn (11)

The dipeptide **10** (0.063 g, 0.10 mmol) was treated with H₂ in the presence of a catalytic amount of 10% Pd/C in EtOH at rt. The reaction was monitored by TLC, and after 8 h, the solution was filtered over Celite, and the solvent was removed at reduced pressure, giving dipeptide acid **11** (0.053 g, 99%, 85% pure by analytical RP HPLC, general methods). ¹H NMR (CDCl₃, 400 MHz): δ 1.12–1.23 (m, 12H, *t*Bu + AlaMe), 1.31, (s, 9H, *t*Bu), 1.57–1.64 (m, 2H, CH₂), 2.37–2.42 (m, 2H, CH₂), 2.93–3.17 (m, 2H, CH₂), 3.27 (m, 1H, ImiH₅), 3.41 (m, 1H, ImiH₅), 4.28 (m, 1H, ImiH₄), 5.27 (m, 1H, AlaH_α), 5.66 (br d, 1H, AlaNH), 6.96 (d, *J* = 8.0 Hz, 2H, ArH), 7.22 (d, *J* = 8.0 Hz, 2H, ArH), 10.50 (br s, 1H, COOH); ¹³C{¹H} NMR (CDCl₃, 100 MHz): δ 17.5, 25.7, 27.1, 28.9, 31.7, 40.9, 48.0, 50.0, 55.8, 80.4, 81.0, 119.9, 121.1, 126.3, 127.6, 134.1, 135.3, 152.0, 153.0, 155.1, 171.9, 174.3; HRMS (ESI/QTOF) *m/z*: [M+H]⁺ calcd for C₂₆H₃₉N₄O₈, 535.2768; found, 535.2804. Anal. Calcd for C₂₆H₃₈N₄O₈: C, 58.41; H, 7.16; N, 10.48. Found: C, 58.66; H, 7.30; N, 10.20.

4.6 NMR Spectra

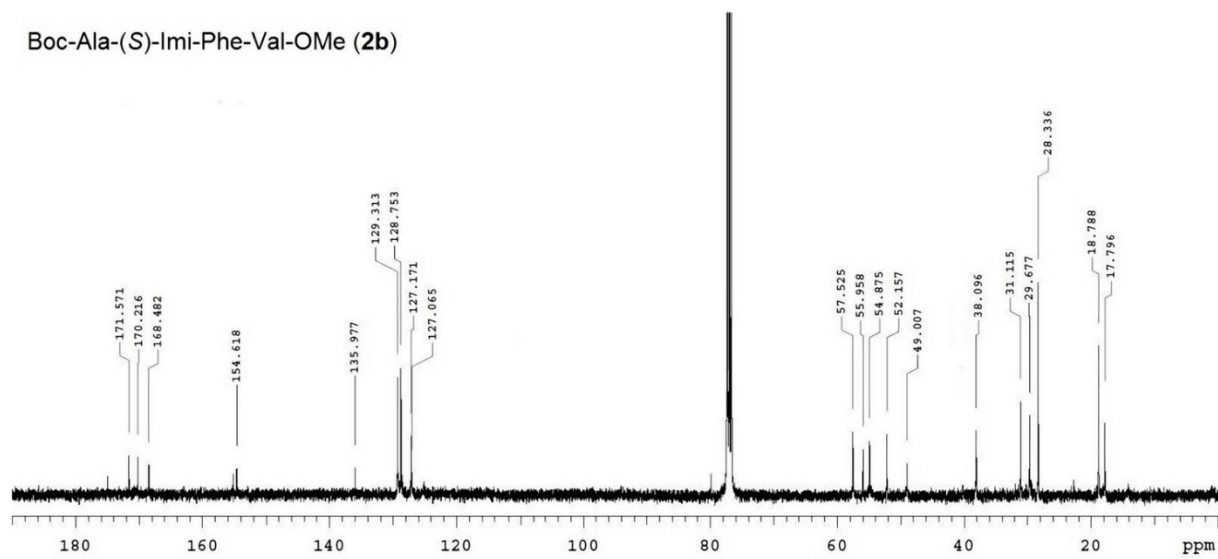


Boc-Ala-(S)-Imi-Phe-Val-OMe (2b)



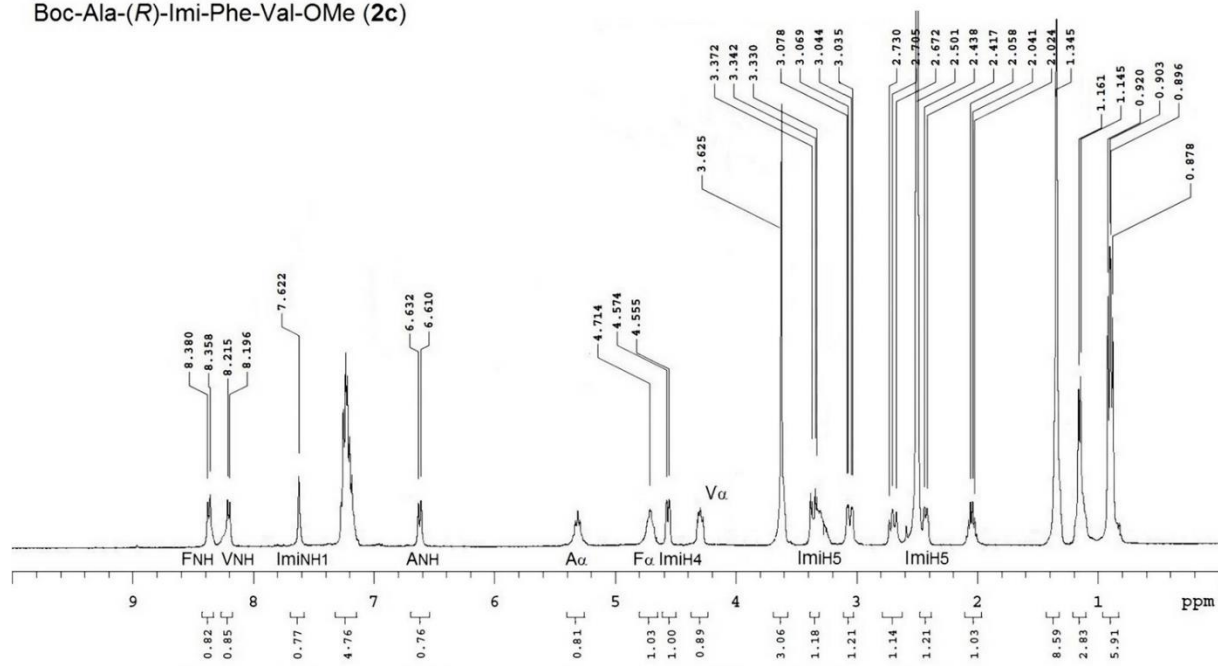
¹H NMR, 8:2 [D₆]DMSO/H₂O, 400 MHz.

Boc-Ala-(S)-Imi-Phe-Val-OMe (2b)



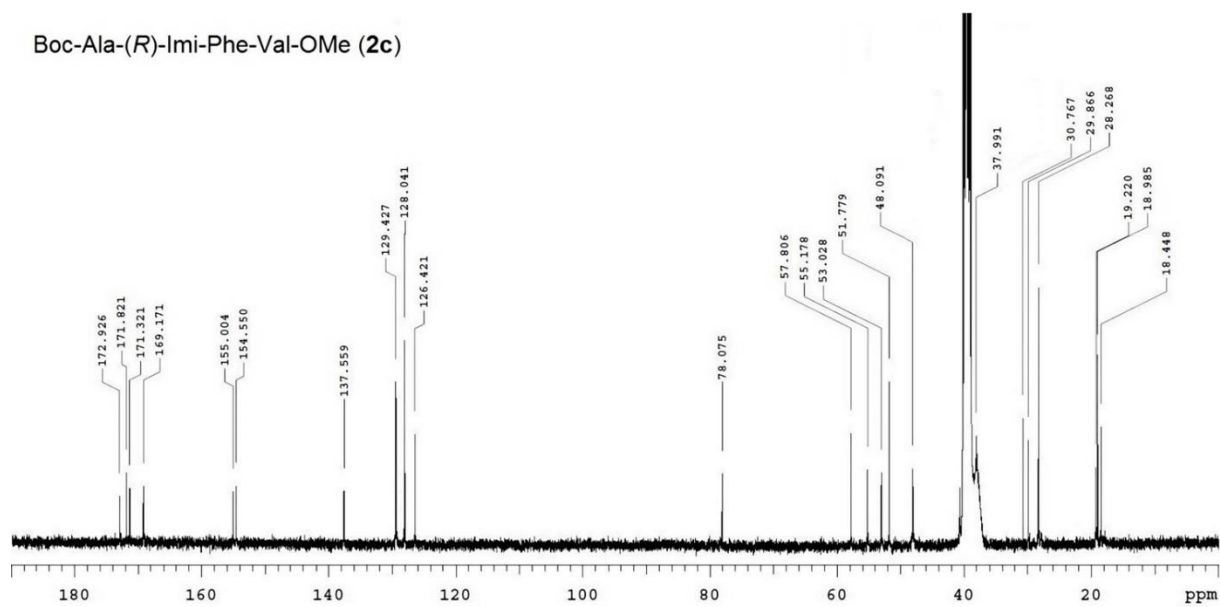
¹³C NMR, [D₆]DMSO, 100 MHz.

Boc-Ala-(R)-Imi-Phe-Val-OMe (**2c**)



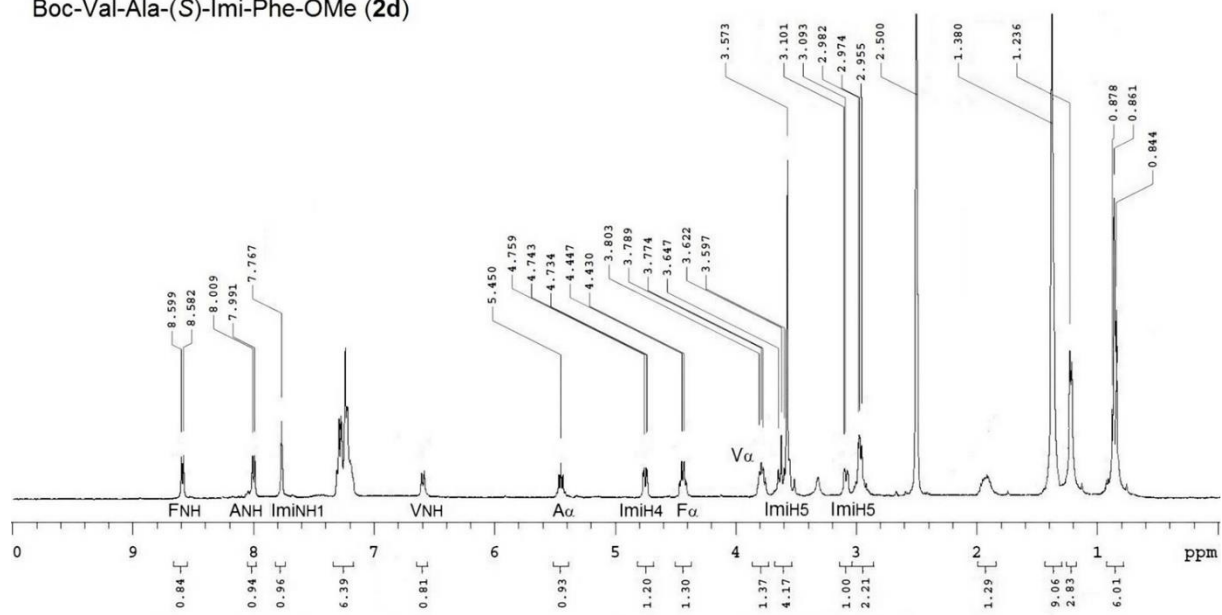
¹H NMR, 8:2 [D₆]DMSO/H₂O, 400 MHz.

Boc-Ala-(R)-Imi-Phe-Val-OMe (**2c**)



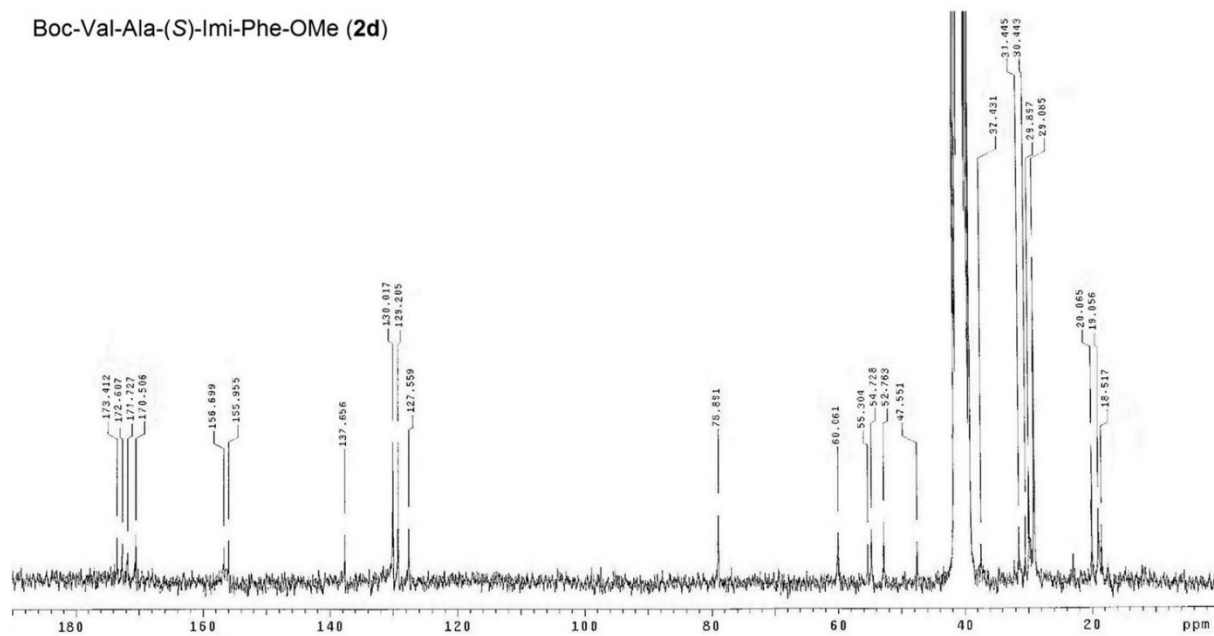
¹³C NMR, [D₆]DMSO, 100 MHz.

Boc-Val-Ala-(S)-Imi-Phe-OMe (2d)



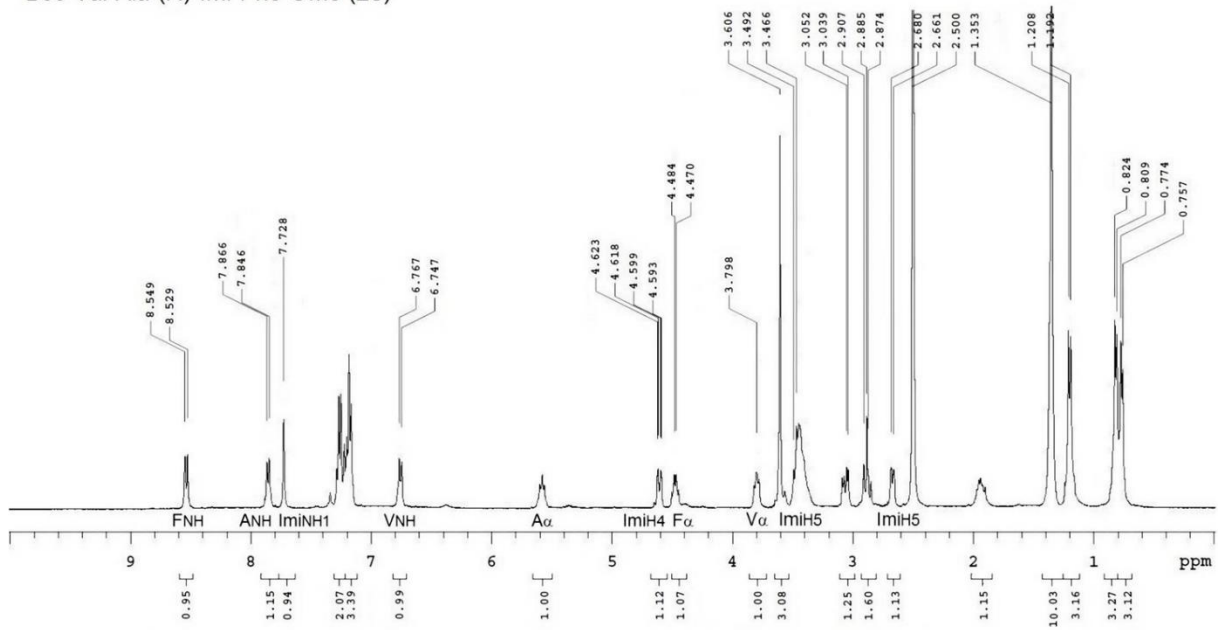
¹H NMR, 8:2 [D₆]DMSO/H₂O, 400 MHz.

Boc-Val-Ala-(S)-Imi-Phe-OMe (2d)



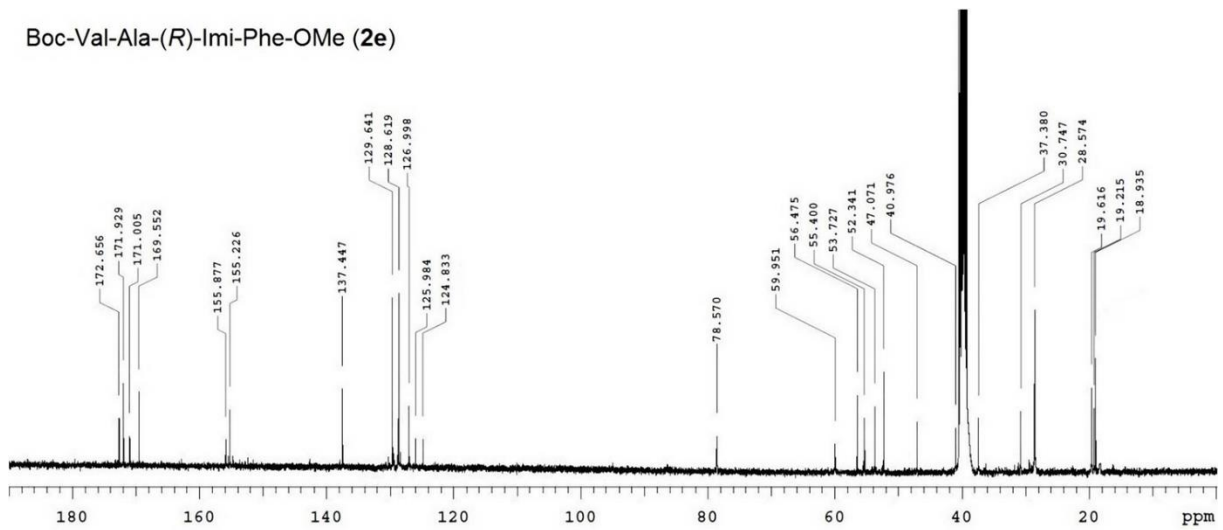
¹³C NMR, [D₆]DMSO, 100 MHz.

Boc-Val-Ala-(*R*)-Imi-Phe-OMe (**2e**)



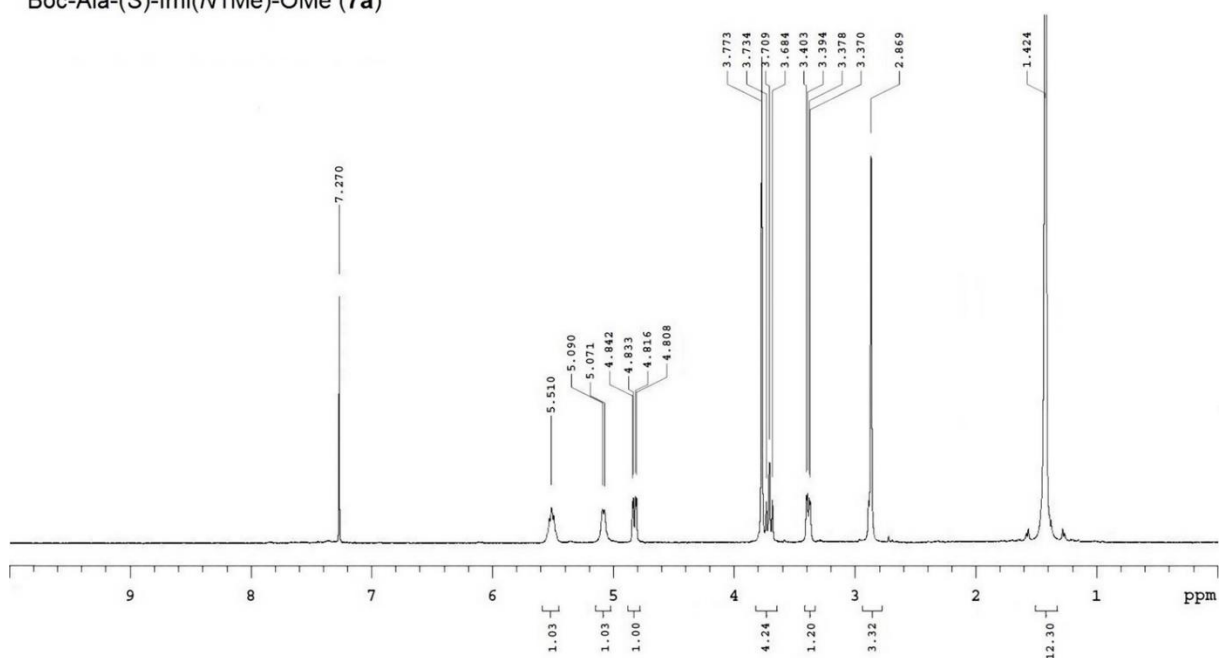
¹H NMR, 8:2 [D₆]DMSO/H₂O, 400 MHz.

Boc-Val-Ala-(*R*)-Imi-Phe-OMe (**2e**)



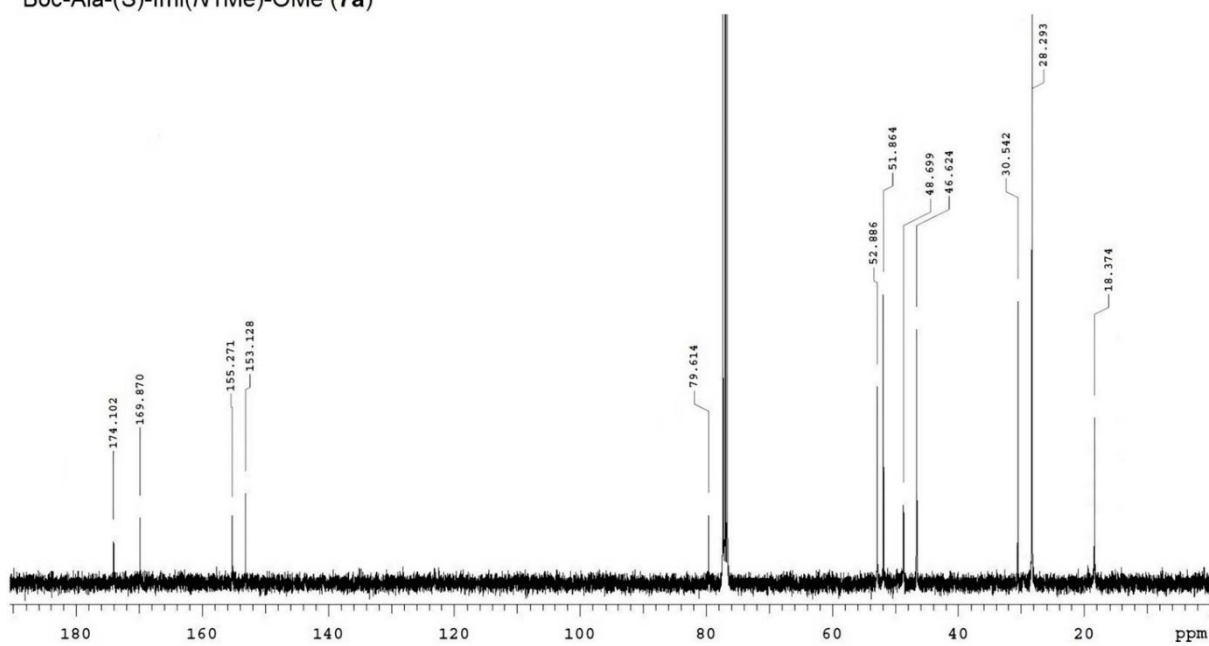
¹³C NMR, [D₆]DMSO, 100 MHz.

Boc-Ala-(S)-Imi(N1Me)-OMe (7a)

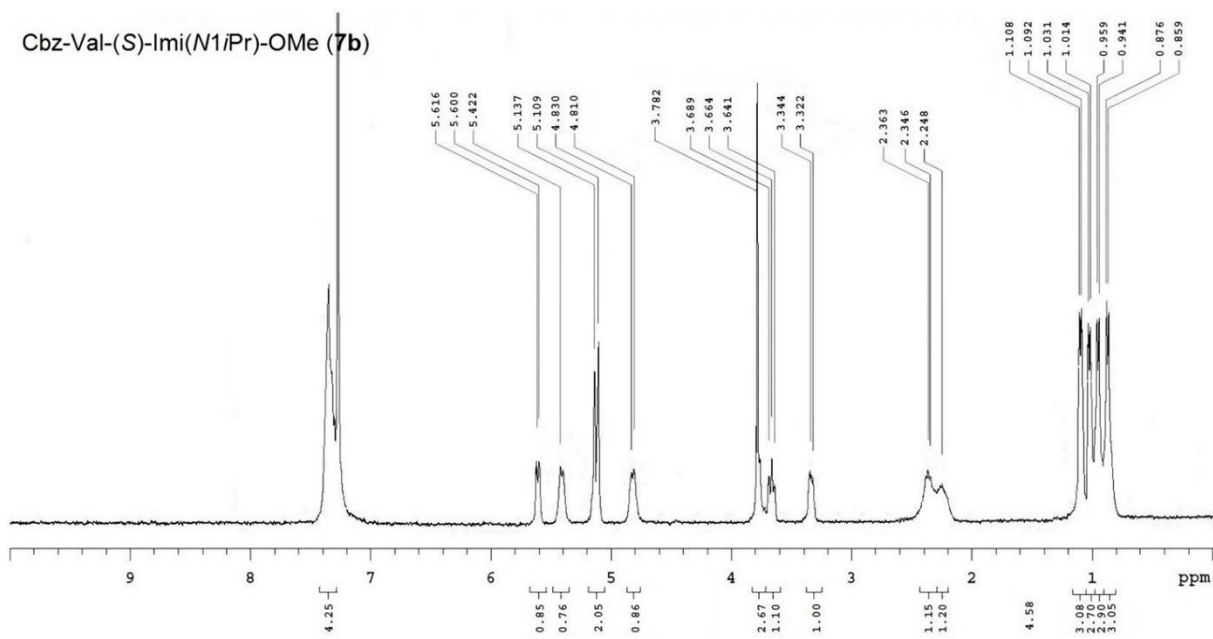


¹H NMR, 8:2 [D₆]DMSO/H₂O, 400 MHz.

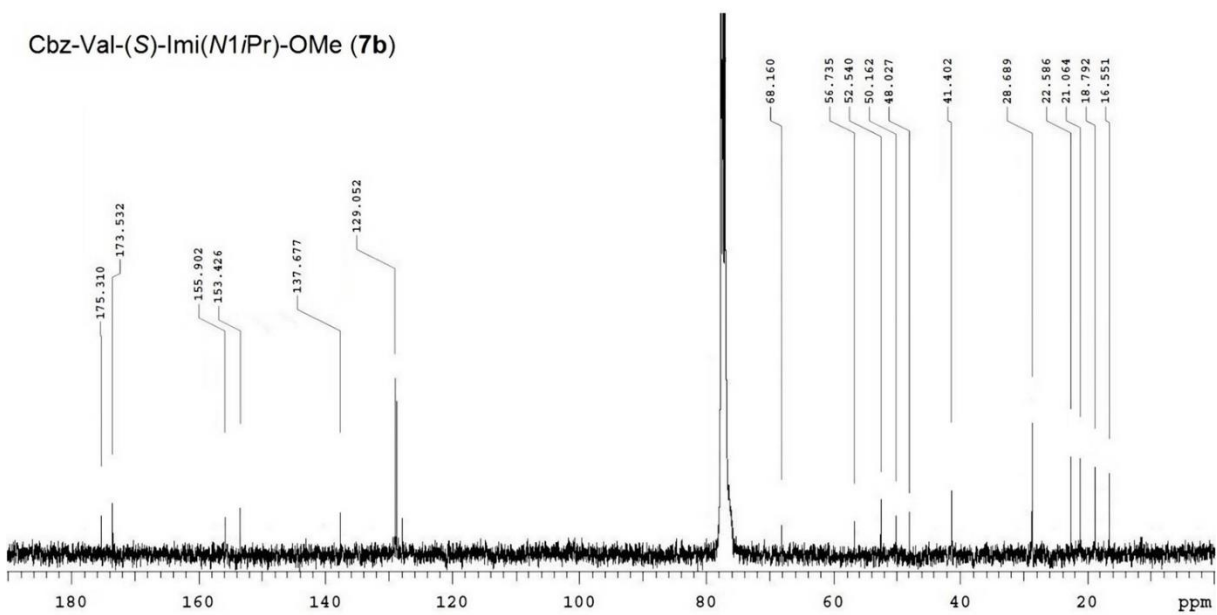
Boc-Ala-(S)-Imi(N1Me)-OMe (7a)



¹³C NMR, [D₆]DMSO, 100 MHz.

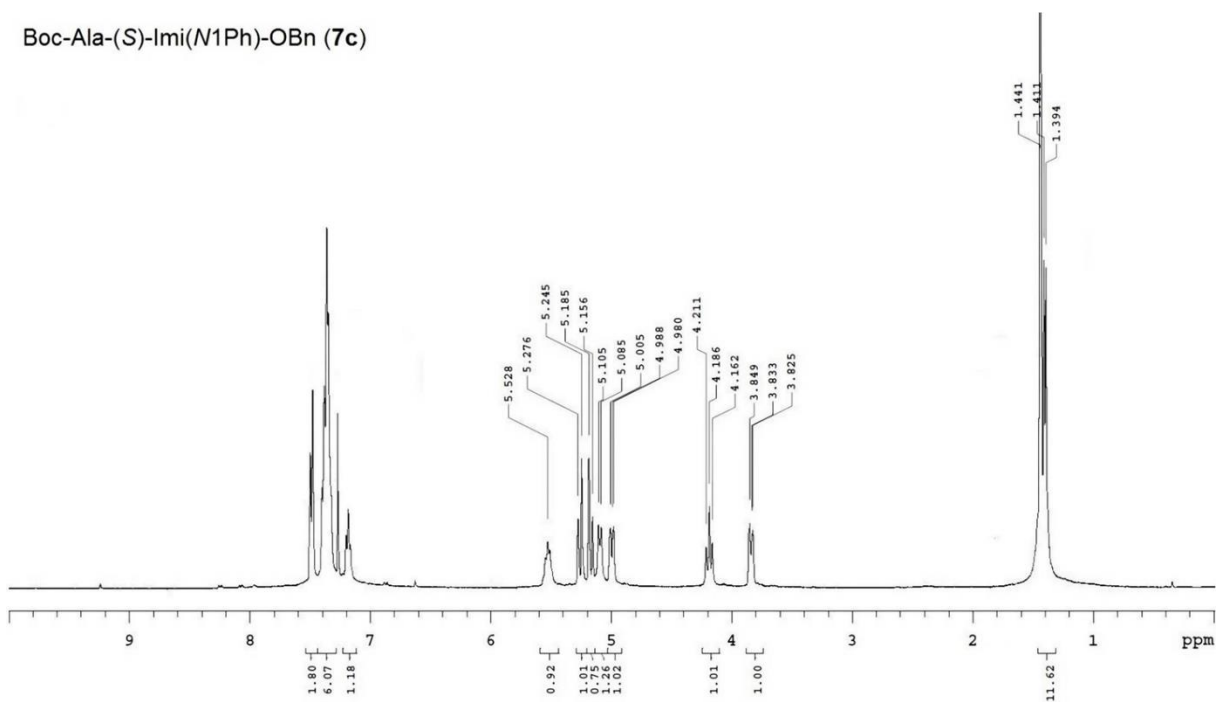


^1H NMR, 8:2 $[\text{D}_6]\text{DMSO}/\text{H}_2\text{O}$, 400 MHz.



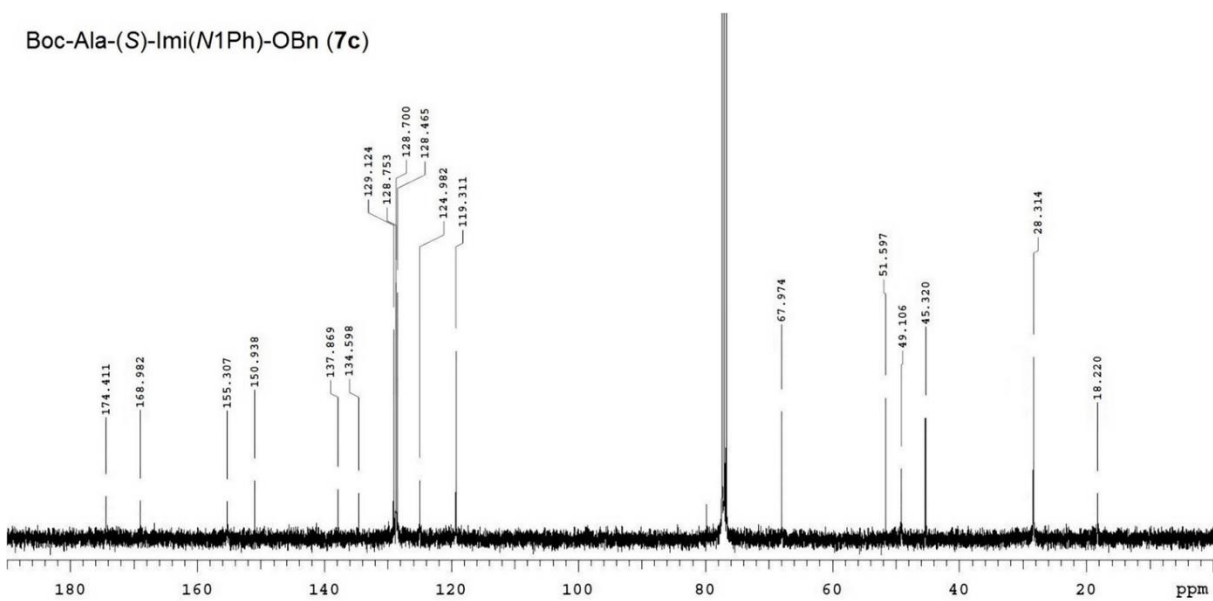
^{13}C NMR, $[\text{D}_6]\text{DMSO}$, 100 MHz.

Boc-Ala-(S)-Imi(N1Ph)-OBn (7c)



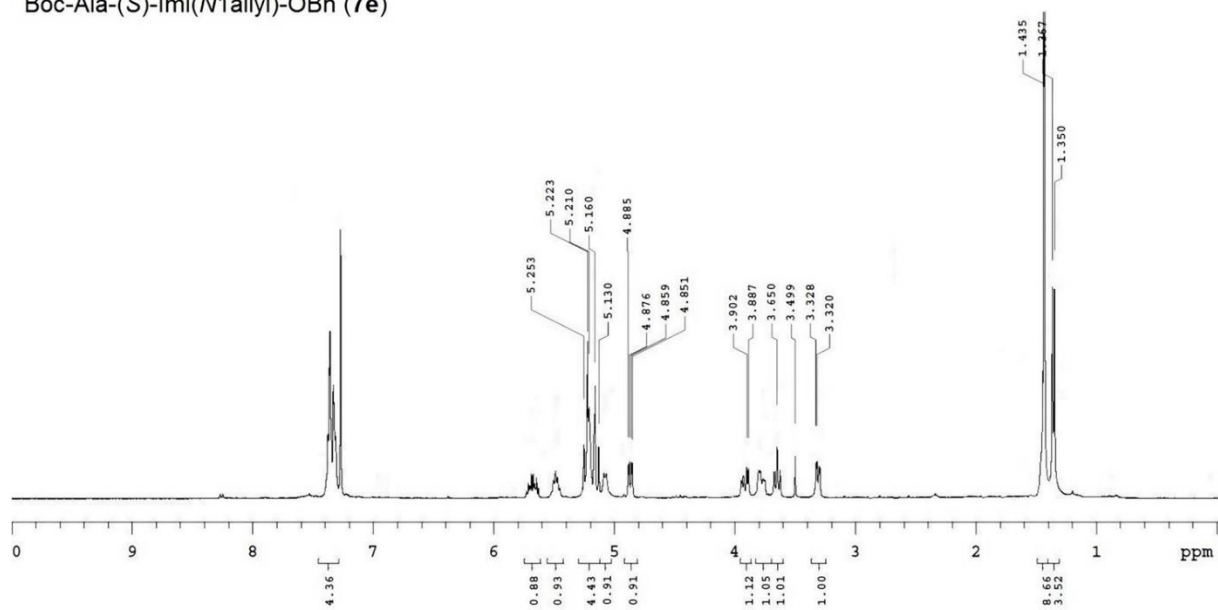
¹H NMR, 8:2 [D₆]DMSO/H₂O, 400 MHz.

Boc-Ala-(S)-Imi(N1Ph)-OBn (7c)



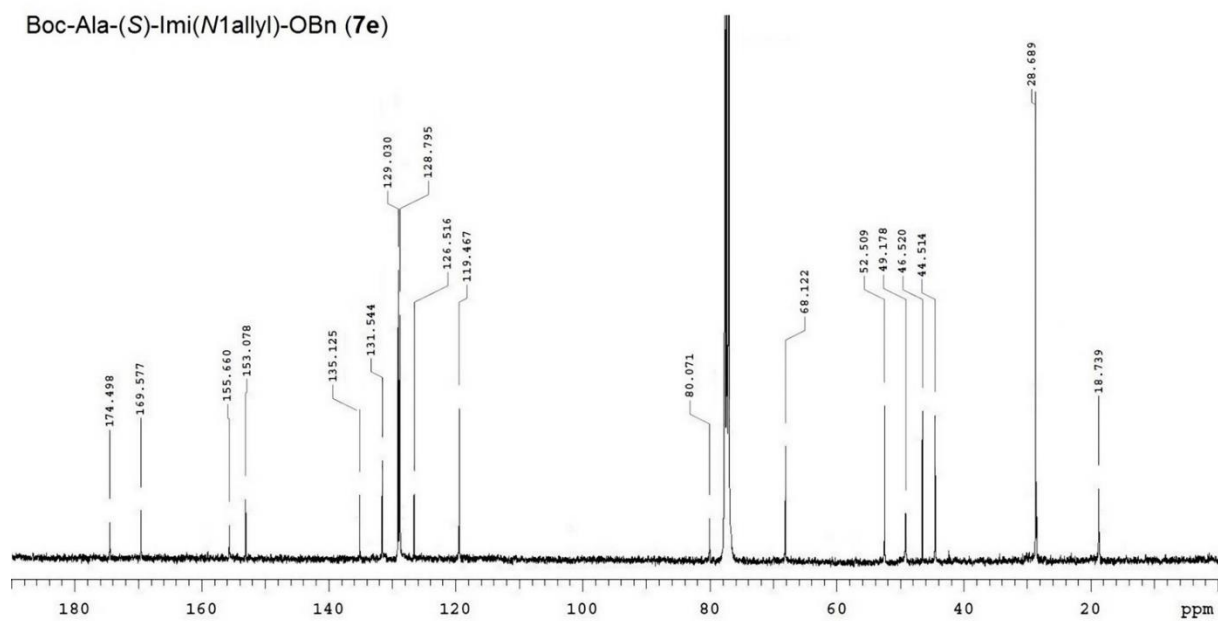
¹³C NMR, [D₆]DMSO, 100 MHz.

Boc-Ala-(S)-Imi(N1allyl)-OBn (7e)



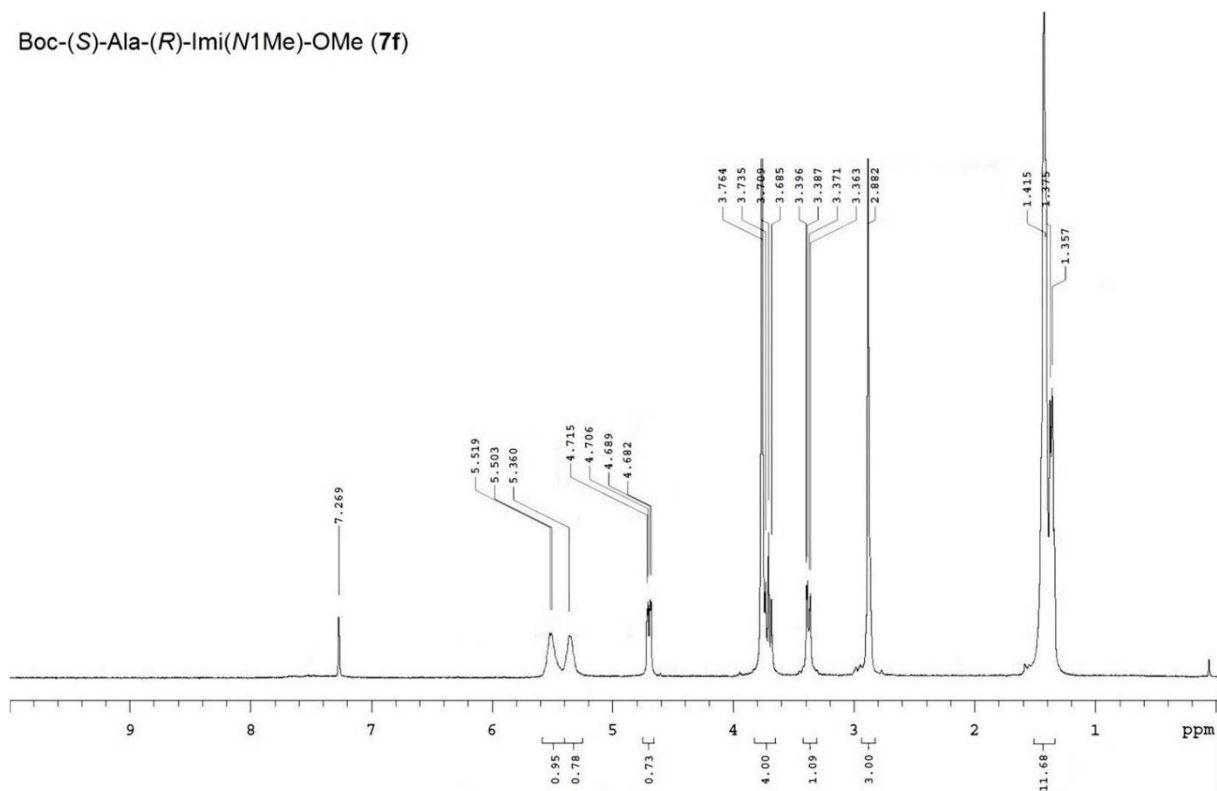
¹H NMR, 8:2 [D₆]DMSO/H₂O, 400 MHz.

Boc-Ala-(S)-Imi(N1allyl)-OBn (7e)



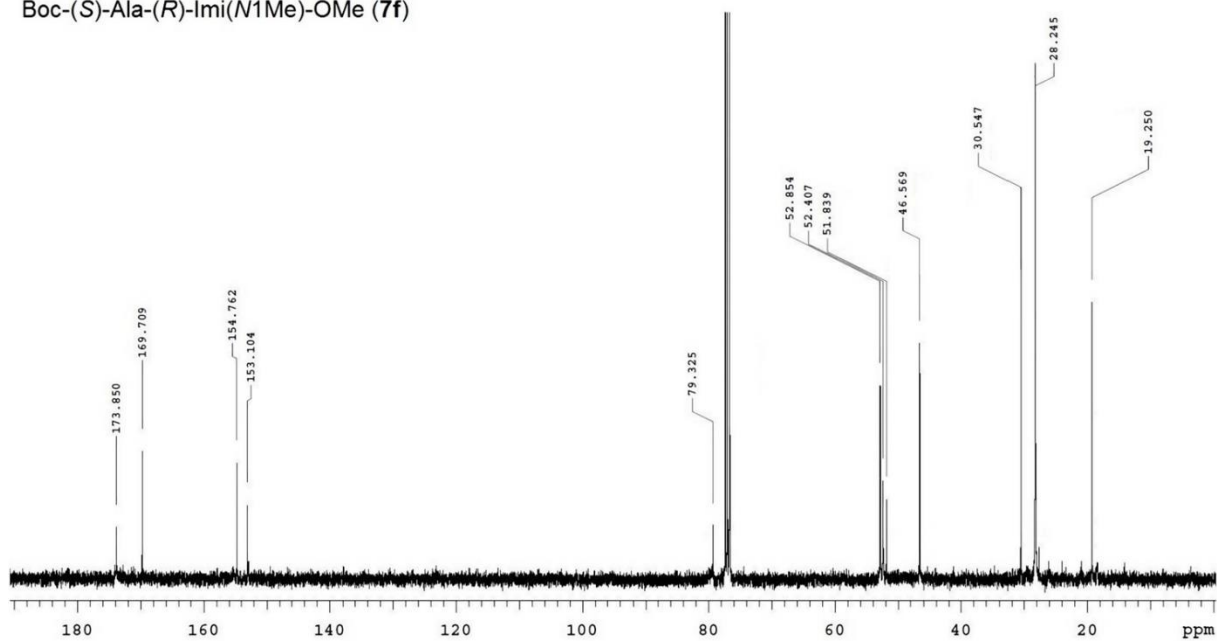
¹³C NMR, [D₆]DMSO, 100 MHz.

Boc-(S)-Ala-(R)-Imi(N1Me)-OMe (7f)

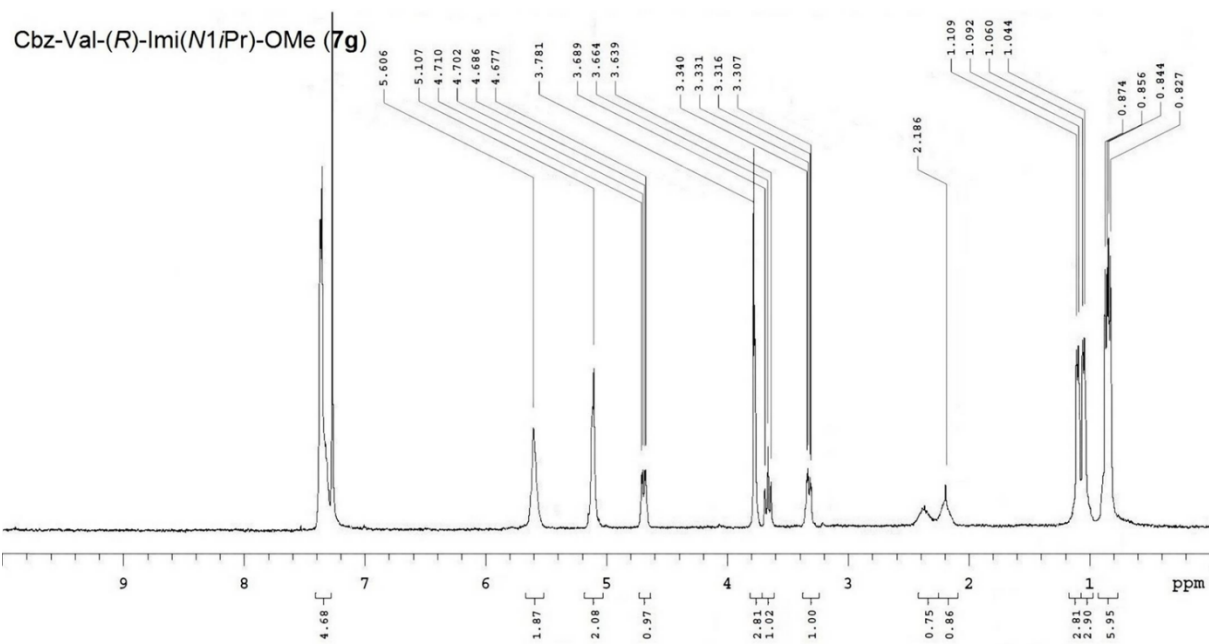


^1H NMR, 8:2 $[\text{D}_6]\text{DMSO}/^{13}\text{C}$, 400 MHz.

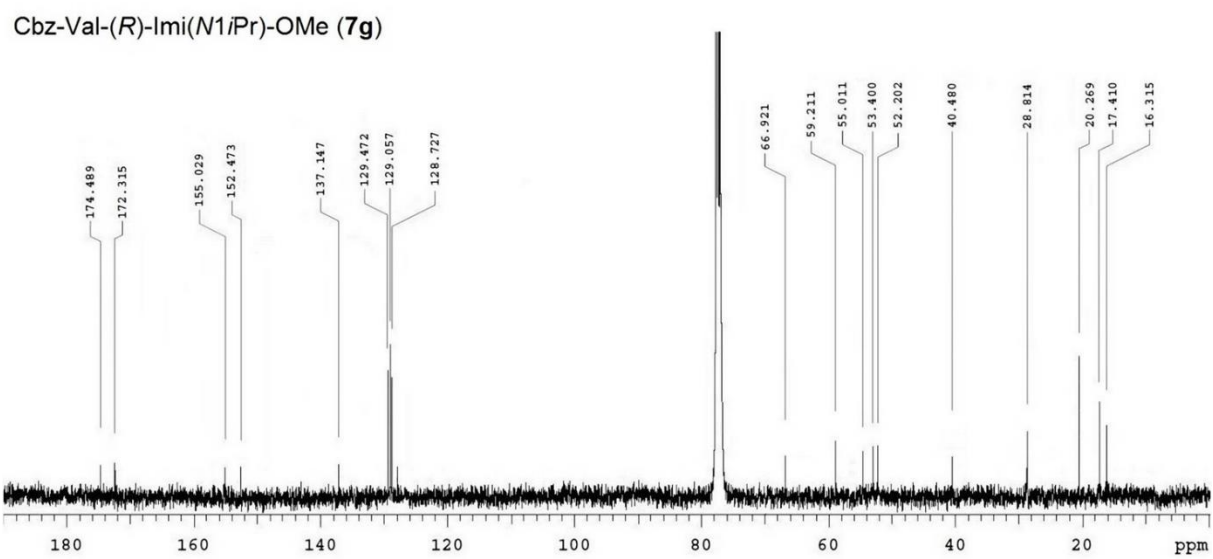
Boc-(S)-Ala-(R)-Imi(N1Me)-OMe (7f)



^{13}C NMR, $[\text{D}_6]\text{DMSO}$, 100 MHz.

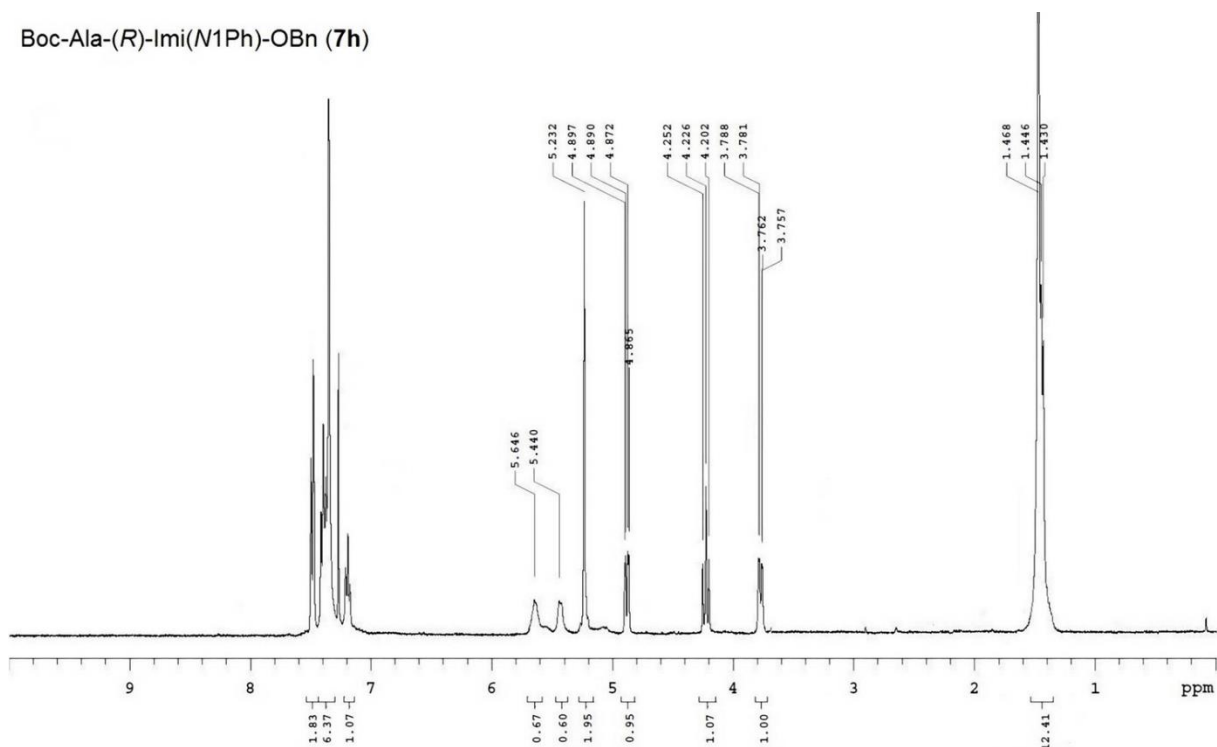


^1H NMR, 8:2 $[\text{D}_6]\text{DMSO}/\text{H}_2\text{O}$, 400 MHz.



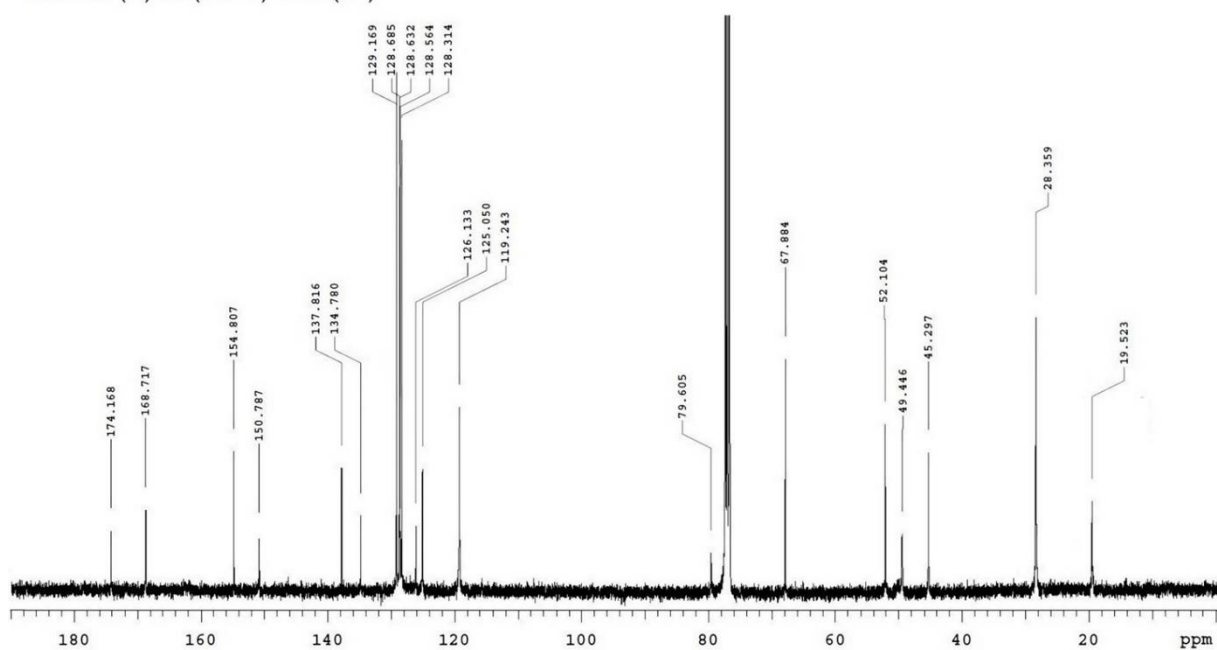
^{13}C NMR, $[\text{D}_6]\text{DMSO}$, 100 MHz.

Boc-Ala-(R)-Imi(N1Ph)-OBn (7h)



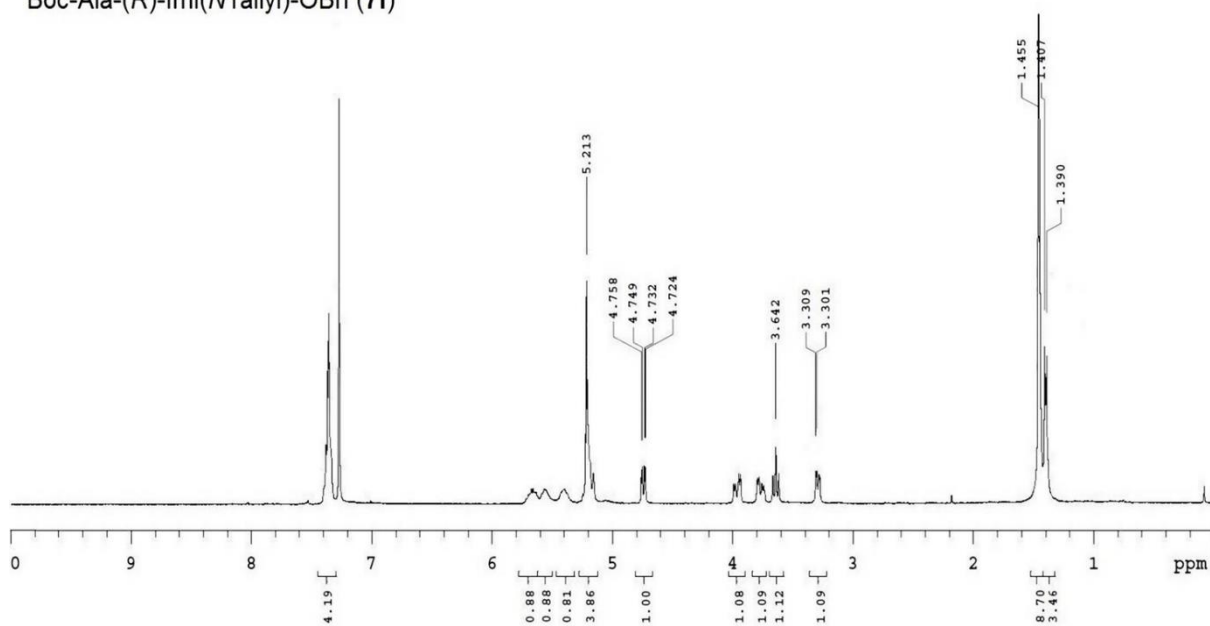
¹H NMR, 8:2 [D₆]DMSO/H₂O, 400 MHz.

Boc-Ala-(R)-Imi(N1Ph)-OBn (7h)



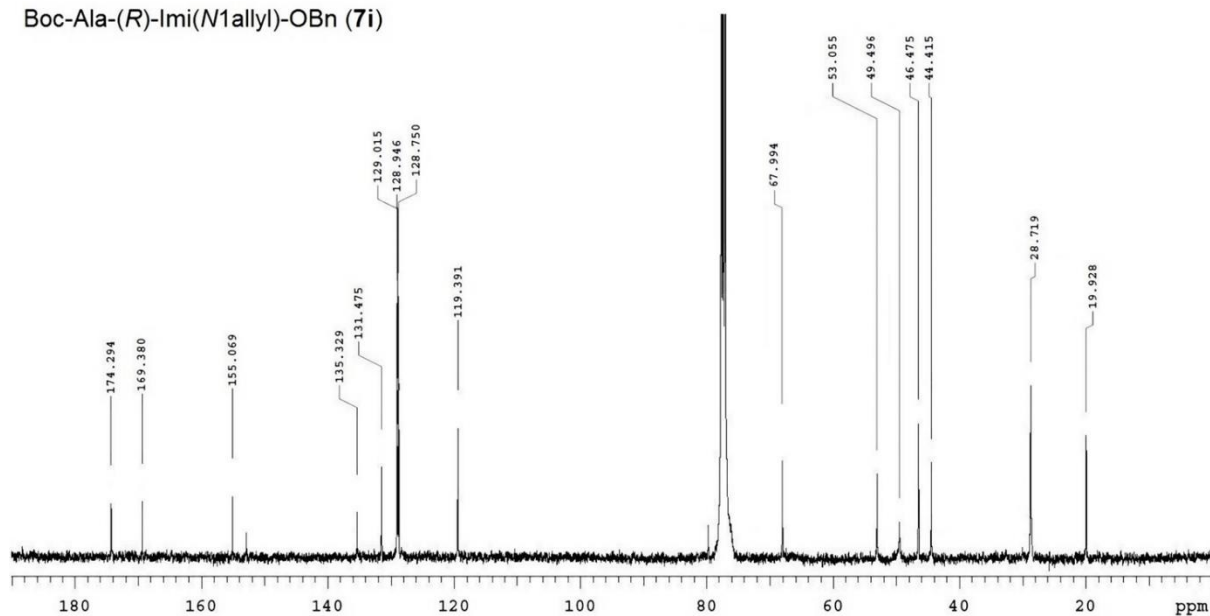
¹³C NMR, [D₆]DMSO, 100 MHz.

Boc-Ala-(*R*)-Imi(*N*1allyl)-OBn (**7i**)



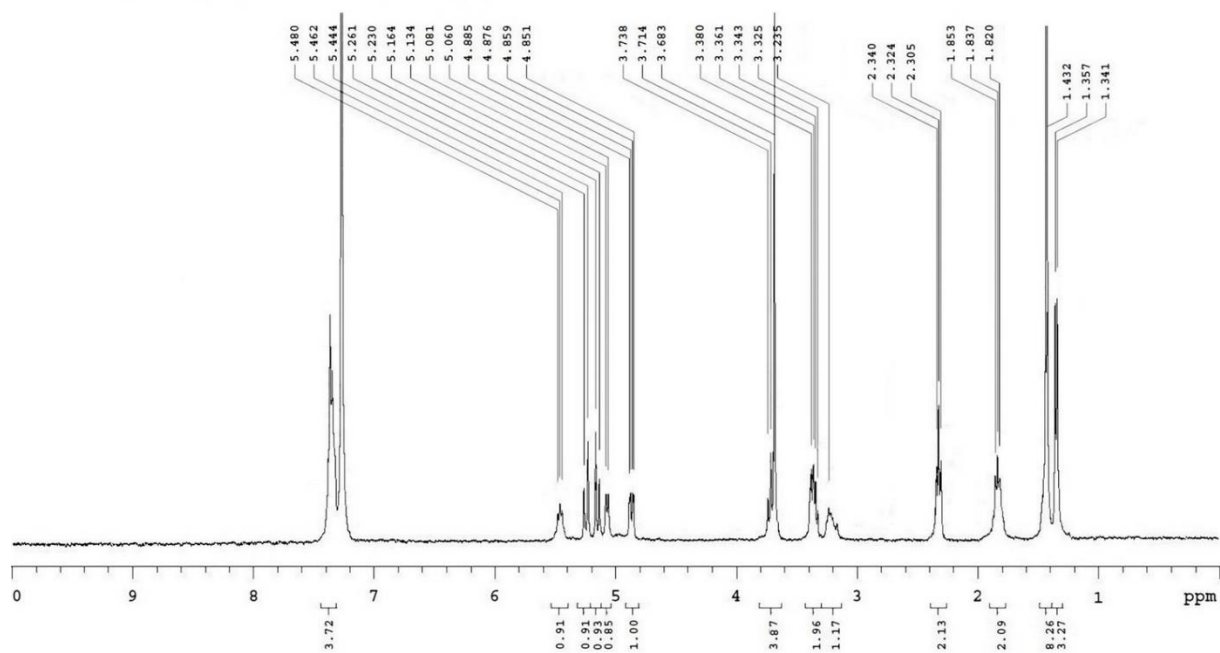
¹H NMR, 8:2 [D₆]DMSO/H₂O, 400 MHz.

Boc-Ala-(*R*)-Imi(*N*1allyl)-OBn (**7i**)



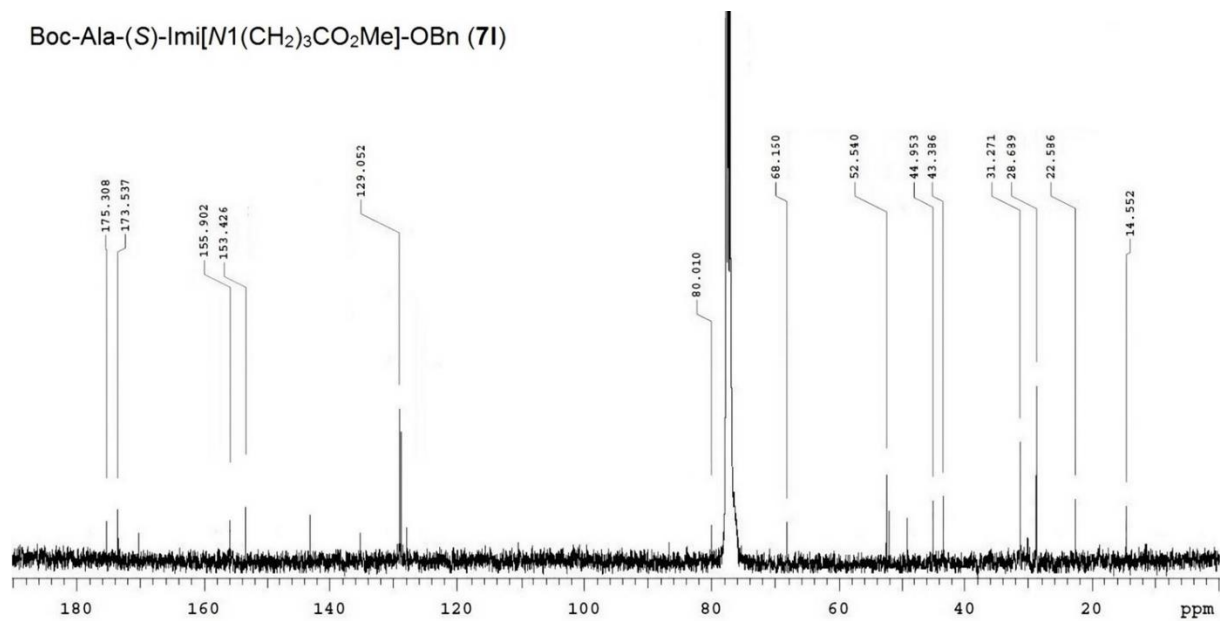
¹³C NMR, [D₆]DMSO, 100 MHz.

Boc-Ala-(S)-Imi[N1(CH₂)₃CO₂Me]-OBn (71)



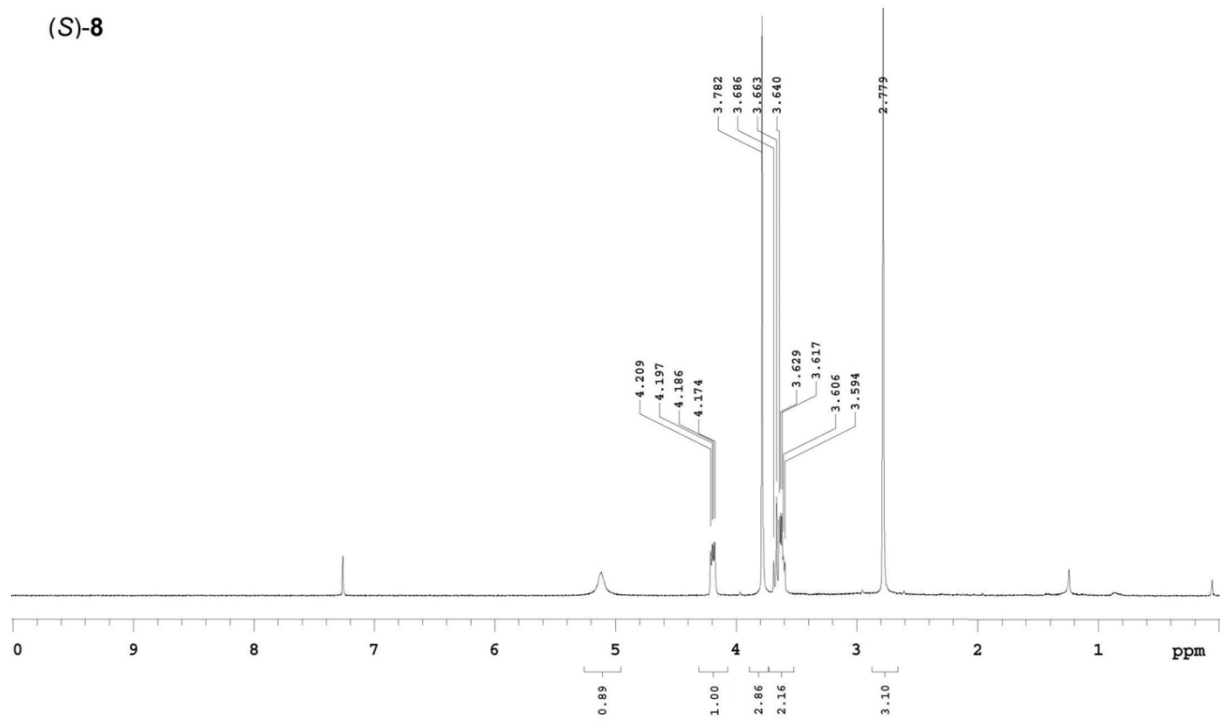
¹H NMR, 8:2 [D₆]DMSO/H₂O, 400 MHz.

Boc-Ala-(S)-Imi[N1(CH₂)₃CO₂Me]-OBn (71)



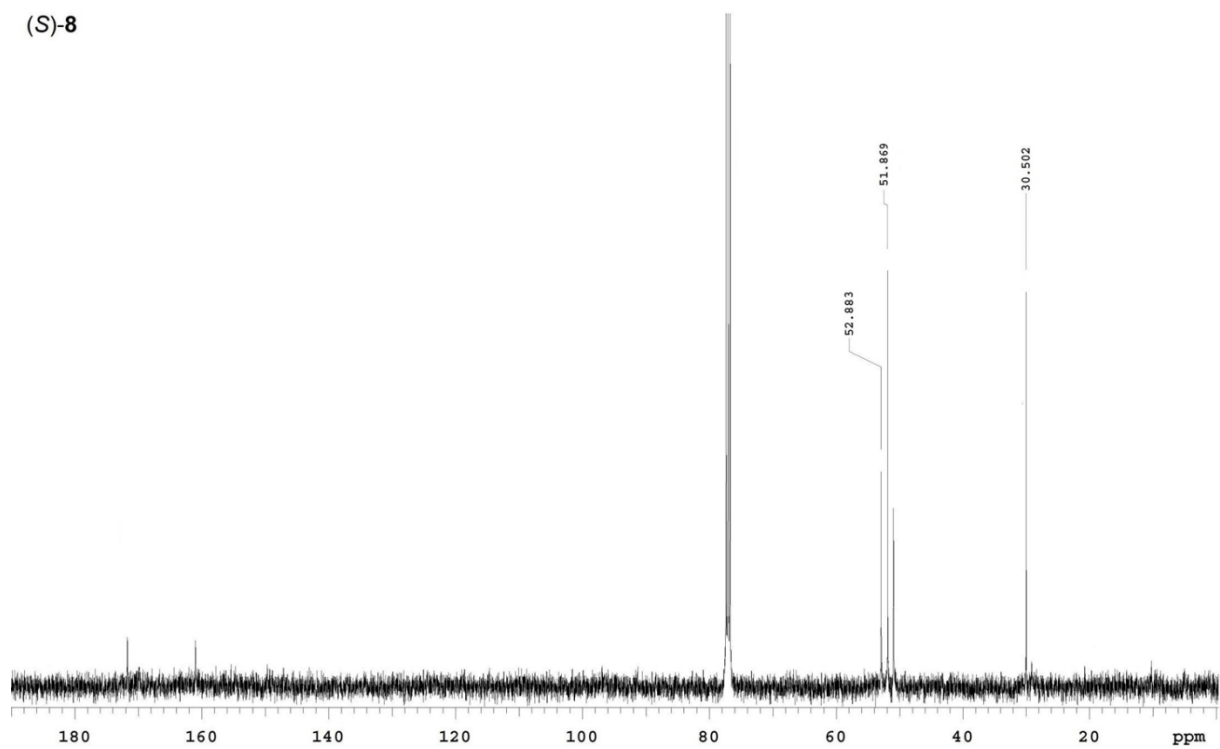
¹³C NMR, [D₆]DMSO, 100 MHz.

(S)-8



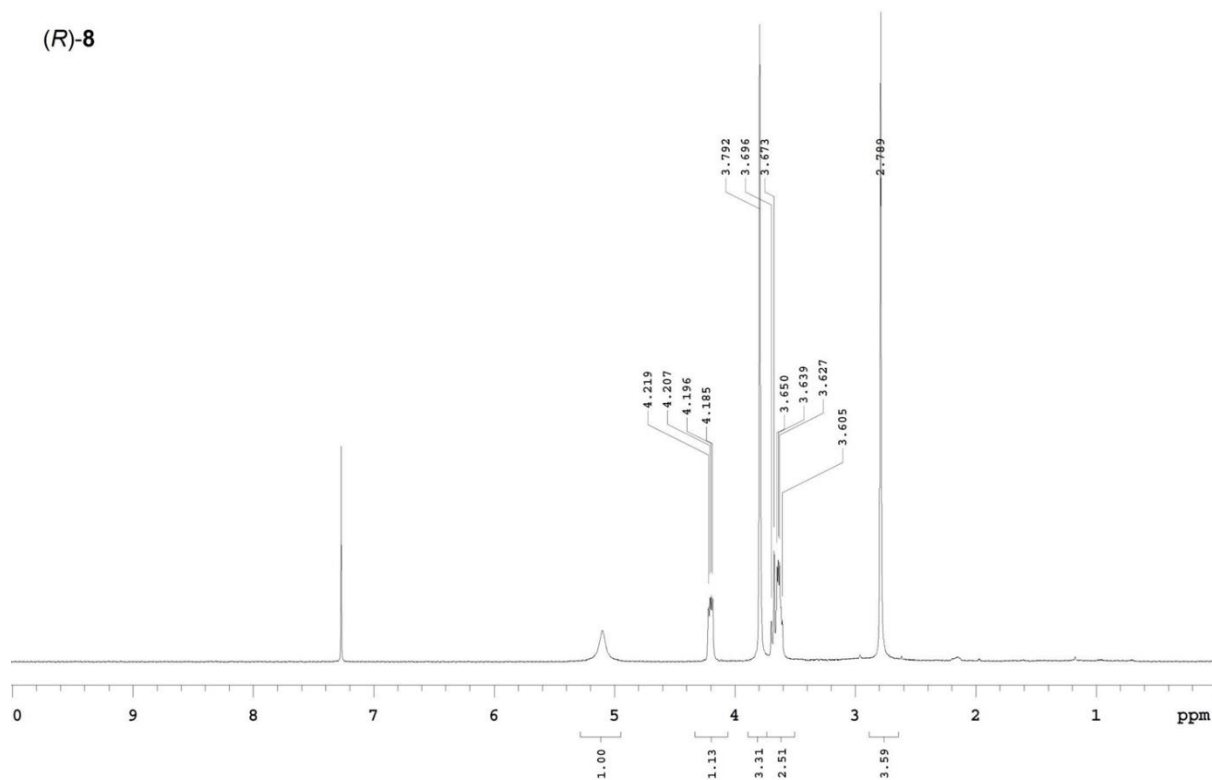
^1H NMR, 8:2 $[\text{D}_6]\text{DMSO}/\text{H}_2\text{O}$, 400 MHz.

(S)-8



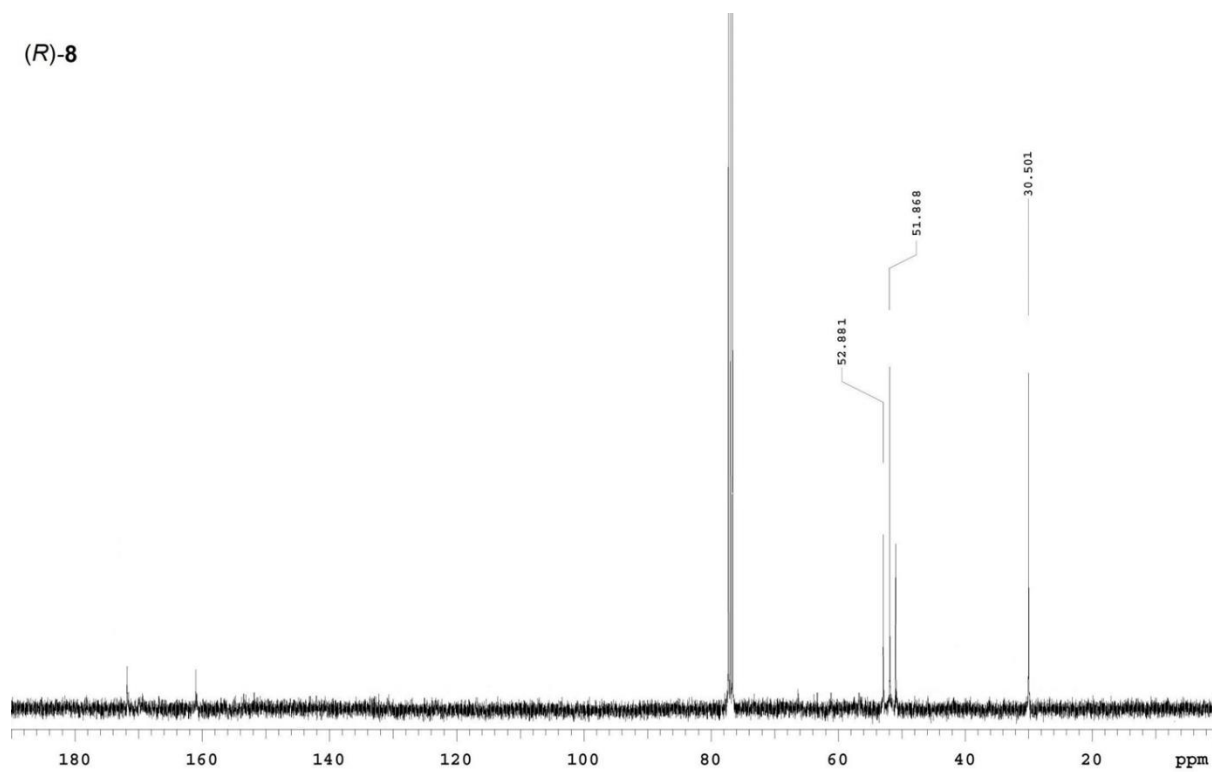
^{13}C NMR, $[\text{D}_6]\text{DMSO}$, 100 MHz.

(R)-8



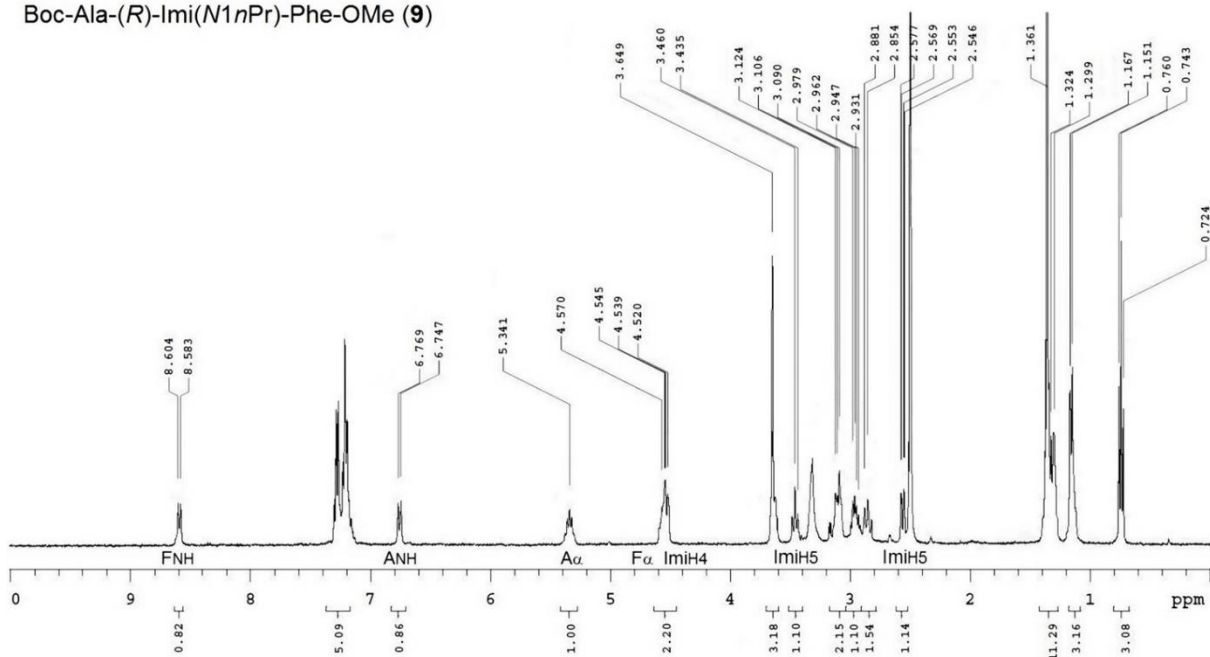
^1H NMR, 8:2 $[\text{D}_6]\text{DMSO}/\text{H}_2\text{O}$, 400 MHz.

(R)-8



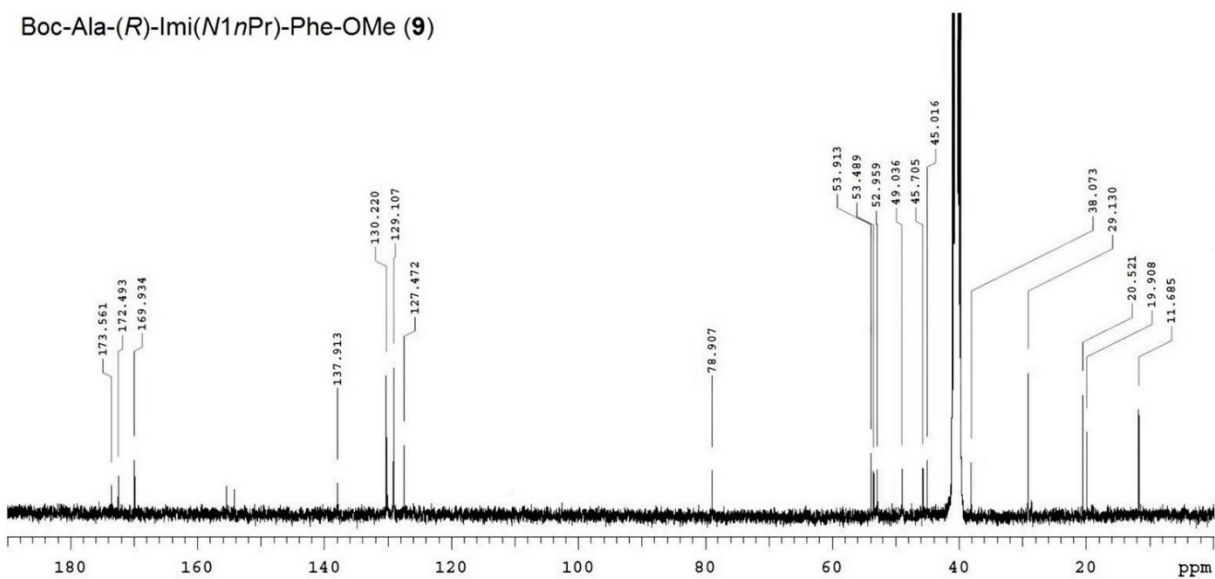
^{13}C NMR, $[\text{D}_6]\text{DMSO}$, 100 MHz.

Boc-Ala-(R)-Imi(N1nPr)-Phe-OMe (9)



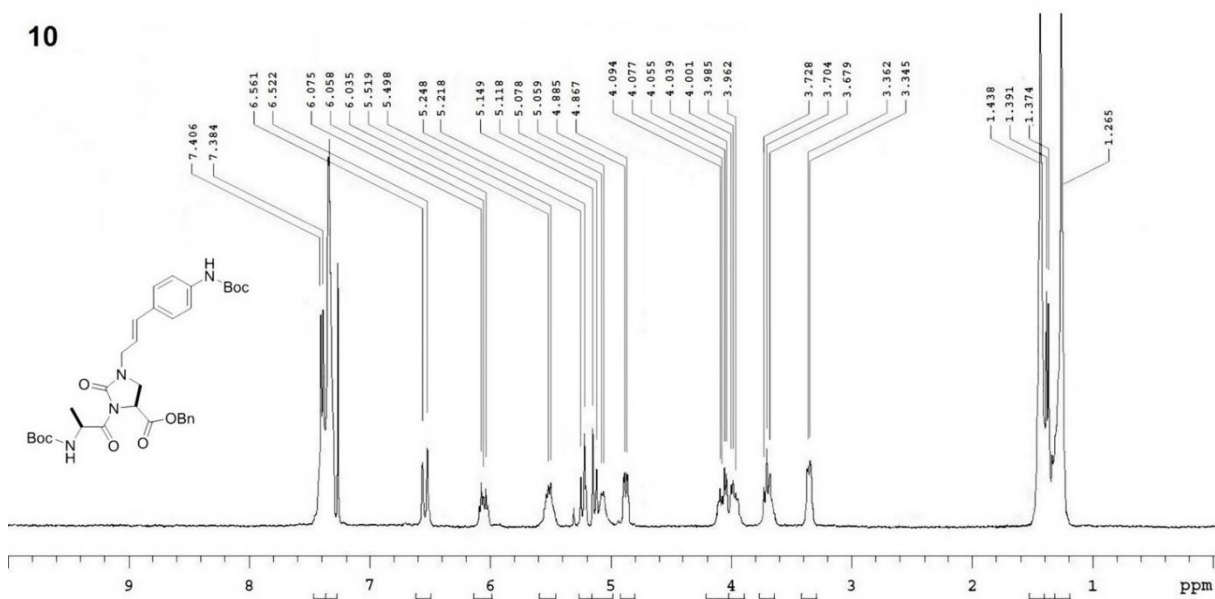
¹H NMR, 8:2 [D₆]DMSO/H₂O, 400 MHz.

Boc-Ala-(R)-Imi(N1nPr)-Phe-OMe (9)



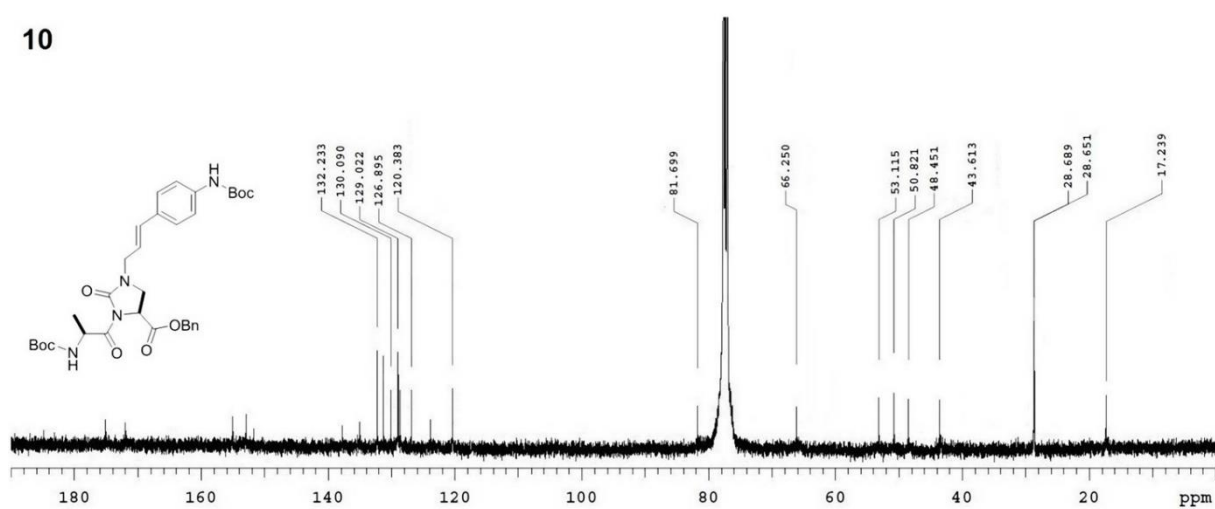
¹³C NMR, [D₆]DMSO, 100 MHz.

10

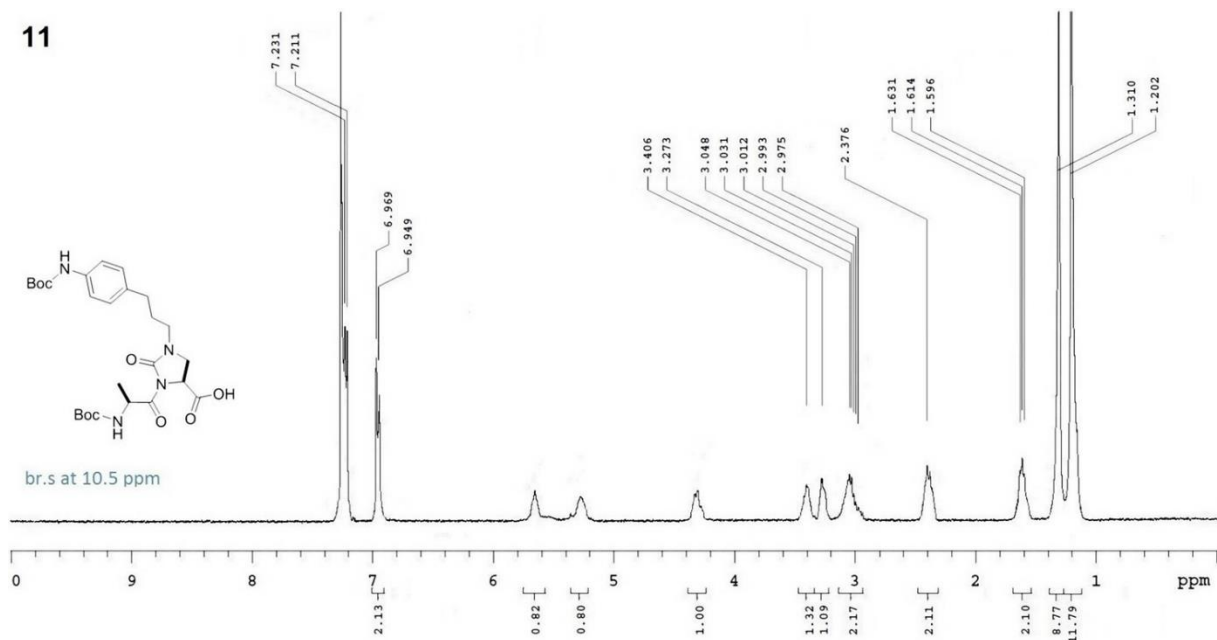


¹H NMR, 8:2 [D₆]DMSO/H₂O, 400 MHz.

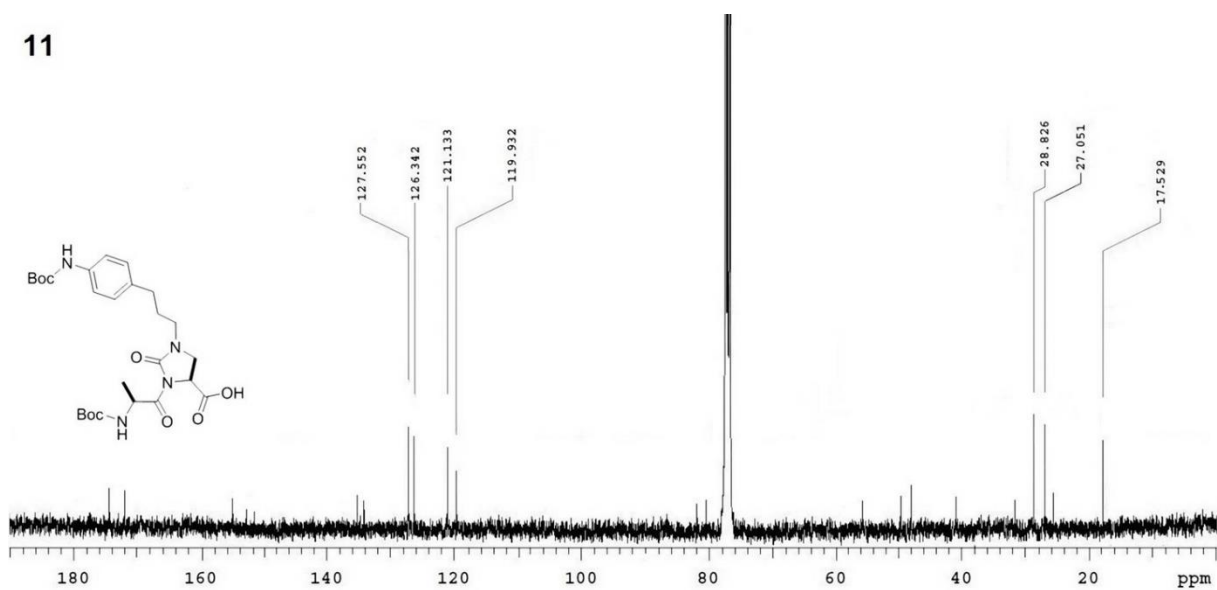
10



¹³C NMR, [D₆]DMSO, 100 MHz.



^1H NMR, 8:2 $[\text{D}_6]\text{DMSO}/\text{H}_2\text{O}$, 400 MHz.



^{13}C NMR, $[\text{D}_6]\text{DMSO}$, 100 MHz.

The work described in this chapter has already been published in *The Journal of Organic Chemistry* with slight modification and has been reproduced here with the permission of the copyright holder.

De Marco, Rossella*; **Zhao, Junwei**; Greco, Arianna; Ioannone, Simone; Gentilucci, Luca*. 2019. "In-peptide synthesis of imidazolidin-2-one scaffolds, equippable with proteinogenic or taggable/linkable side chains, general promoters of unusual secondary structures" *Journal of Organic chemistry* 84, no. 9: 4992-5004. <https://doi.org/10.1021/acs.joc.8b03055>.

References

- (a) Hraby, V.; Balse, P. *Curr. Med. Chem.* **2000**, *7*, 945-970. (b) Abell, A. D. *Lett. Pept. Sci.* **2001**, *8*, 267-272. (c) Gentilucci, L.; De Marco, R.; Cerisoli, L. *Curr. Pharm. Des.* **2010**, *16*, 3185-3203. (d) Liskamp, R. M. J.; Rijkers, D. T. S.; Kruijtzter, J. A. W.; Kemmink, J. *ChemBioChem*, **2011**, *12*, 1626-1653. (e) De Marco, R.; Mazzotti, G.; Greco, A.; Gentilucci, L. *Curr. Top. Med. Chem.* **2015**, *16*, 343-359.
- (a) Ritchie, T. J.; Macdonald, S. J. F.; Young, R. J.; Pickett, S. D. *Drug Discov. Today* **2011**, *16*, 164-171. (b) Lovering, F.; Bikker, J.; Humblet, C. *J. Med. Chem.* **2009**, *52*, 6752-6756. (c) Feher, M.; Schmidt, J. M. *J. Chem. Inf. Comput. Sci.* **2002**, *43*, 218-227. (d) Gentilucci, L.; Gallo, F.; Meloni, F.; Mastandrea, M.; Del Secco, B.; De Marco, R. *Eur. J. Org. Chem.* **2016**, *2016*, 3243-3251.
- (a) Keller, M.; Boissard, C.; Patiny, L.; Chung, N. N.; Lemieux, C.; Mutter, M.; Schiller, P. W. *J. Med. Chem.* **2001**, *44*, 3896-3903. (b) Gentilucci, L.; Tolomelli, A.; De Marco, R.; Tomasini, C.; Feddersen, S. *Eur. J. Org. Chem.* **2011**, *2011*, 4925-4930. (c) De Marco, R.; Tolomelli, A.; Campitiello, M.; Rubini, P.; Gentilucci, L. *Org. Biomol. Chem.* **2012**, *10*, 2307-2317. (d) De Marco, R.; Greco, A.; Rupiani, S.; Tolomelli, A.; Tomasini, C.; Pieraccini, S.; Gentilucci, L. *Org. Biomol. Chem.* **2013**, *11*, 4316-4326. (e) Galletti, P.; Soldati, R.; Pori, M.; Durso, M.; Tolomelli, A.; Gentilucci, L.; Dattoli, S. D.; Baiula, M.; Spampinato, S.; Giacomini, D. *Eur. J. Med. Chem.* **2014**, *83*, 284-293. (f) Tolomelli, A.; Baiula, M.; Viola, A.; Ferrazzano, L.; Gentilucci, L.; Dattoli, S. D.; Spampinato, S.; Juaristi, E.; Escudero, M. *ACS Med. Chem. Lett.* **2015**, *6*, 701-706. (g) Dattoli, S. D.; Baiula, M.; De Marco, R.; Bedini, A.; Anselmi, M.; Gentilucci, L.; Spampinato, S. *Br. J. Pharmacol.* **2018**, *175*, 3891-3910.
- (a) Freidinger, R.; Veber, D.; Perlow, D.; Brooks, J. R.; Saperstein, R. *Science* **1980**, *210*, 656-658. (b) Freidinger, R. M.; Perlow, D. S.; Veber, D. F. *J. Org. Chem.* **1982**, *47*, 104-109. (c) Freidinger, R. M. *J. Org. Chem.* **1985**, *50*, 3631-3633. (d) Wolfe, M. S.; Dutta, D.; Aubé, J. *J. Org. Chem.* **1997**, *62*, 654-663. (e) Lee, H.-J.; Song, J.-W.; Choi, Y.-S.; Park, H.-M.; Lee, K.-B. *J. Am. Chem. Soc.* **2002**, *124*, 11881-11893. (f) Jamieson, A. G.; Boutard, N.; Beaugard, K.; Bodas, M. S.; Ong, H.; Quiniou, C.; Chemtob, S.; Lubell, W. D. *J. Am. Chem. Soc.* **2009**, *131*, 7917-7927. (g) Boutard, N.; Jamieson, A. G.; Ong, H.; Lubell, W. D. *Chem. Biol. Drug Des.* **2010**, *75*, 40-50. (h) Greco, A.; Tani, S.; De Marco, R.; Gentilucci, L. *Chem. Eur. J.* **2014**, *20*, 13390-13404. (i) De Marco, R.; Mazzotti, G.; Dattoli, S. D.; Baiula, M.; Spampinato, S.; Greco, A.; Gentilucci, L. *Biopolymers* **2015**, *104*, 636-649.
- (a) Proulx, C.; Sabatino, D.; Hopewell, R.; Spiegel, J.; García Ramos, Y.; Lubell, W. D. *Future Med. Chem.* **2011**, *3*, 1139-1164. (b) Proulx, C.; Lubell, W. D. *Org. Lett.* **2012**, *14*, 4552-4555. (c) Proulx, C.; Lubell, W. D. *Biopolymers* **2014**, *102*, 7-15. (d) Skerlj, R.; Bridger, G.; Zhou, Y.; Bourque, E.; McEachern, E.; Metz, M.; Harwig, C.; Li, T.-S.; Yang, W.; Bogucki, D.; Zhu, Y.; Langille, J.; Veale, D.; Ba, T.; Bey, M.; Baird, I.; Kaller, A.; Krumpak, M.; Leitch, D.; Satori, M.; Vocadlo, K.; Guay, D.; Nan, S.; Yee, H.; Crawford, J.; Chen, G.; Wilson, T.; Carpenter, B.; Gauthier, D.; MacFarland, R.; Mosi, R.; Bodart, V.; Wong, R.; Fricker, S.; Schols, D. *J. Med. Chem.* **2013**, *56*, 8049-8065. (e) Lam, P.; Jadhav, P.; Eyermann, C.; Hodge, C.; Ru, Y.; Bacheler, L.; Meek, J.; Otto, M.; Rayner, M.; Wong, Y.; Weber, P. C.; Jackson, D. A.; Sharpe, T. R.; Erickson-Viitanen, S.; et al. *Science* **1994**, *263*, 380-384.
- Kazmierski, W. M.; Furfine, E.; Gray-Nunez, Y.; Spaltenstein, A.; Wright, L. *Bioorg. Med. Chem. Lett.* **2004**, *14*, 5685-5687.
- Bronson, J. J.; DenBleyker, K. L.; Falk, P. J.; Mate, R. A.; Ho, H.-T.; Pucci, M. J.; Snyder, L. B. *Bioorg. Med. Chem. Lett.* **2003**, *13*, 873-875.
- (a) Carling, R. W.; Moore, K. W.; Moyes, C. R.; Jones, E. A.; Bonner, K.; Emms, F.; Marwood, R.; Patel, S.; Patel, S.; Fletcher, A. E.; Beer, M.; Sohal, B.; Pike, A.; Leeson, P. D. *J. Med. Chem.* **1999**, *42*, 2706-2715. (b) Burgey, C. S.; Stump, C. A.; Nguyen, D. N.; Deng, J. Z.; Quigley, A. G.; Norton, B. R.; Bell, I. M.; Mosser, S. D.; Salvatore, C. A.; Rutledge, R. Z.; Kane, S. A.; Koblan, K. S.; Vacca, J. P.; Graham, S. L.; Williams, T. M. *Bioorg. Med. Chem. Lett.* **2006**, *16*, 5052-5056. (c) Shaw, A. W.; Paone, D. V.; Nguyen, D. N.; Stump, C. A.; Burgey, C. S.; Mosser, S. D.; Salvatore, C. A.;

- Rutledge, R. Z.; Kane, S. A.; Koblan, K. S.; Graham, S. L.; Vacca, J. P.; Williams, T. M. *Bioorg. Med. Chem. Lett.* **2007**, *17*, 4795-4798.
9. (a) Hayashi, K.; Nunami, K.; Kato, J.; Yoneda, N.; Kubo, M.; Ochiai, T.; Ishida, R. *J. Med. Chem.* **1989**, *32*, 289-297. (b) Takai, S.; Jin, D.; Yamamoto, D.; Li, Z.-L.; Otsuki, Y.; Miyazaki, M. *J. Pharmacol. Sci.* **2013**, *123*, 185-194.
10. Arasappan, A.; Njoroge, F. G.; Parekh, T. N.; Yang, X.; Pichardo, J.; Butkiewicz, N.; Prongay, A.; Yao, N.; Girijavallabhan, V. *Bioorg. Med. Chem. Lett.* **2004**, *14*, 5751-5755.
11. Yasuda, N.; Hsiao, Y.; Jensen, M. S.; Rivera, N. R.; Yang, C.; Wells, K. M.; Yau, J.; Palucki, M.; Tan, L.; Dormer, P. G.; Volante, R. P.; Hughes, D. L.; Reider, P. J. *J. Org. Chem.* **2004**, *69*, 1959-1966.
12. (a) Bar, G. L. J.; Lloyd-Jones, G. C.; Booker-Milburn, K. I. *J. Am. Chem. Soc.* **2005**, *127*, 7308-7309. (b) Streuff, J.; Hövelmann, C. H.; Nieger, M.; Muñoz, K. *J. Am. Chem. Soc.* **2005**, *127*, 14586-14587.
13. (a) Angelici, G.; Contaldi, S.; Lynn Green, S.; Tomasini, C. *Org. Biomol. Chem.* **2008**, *6*, 1849-1852. (b) Doyle, M. P.; Zhou, Q.-L.; Raab, C. E.; Roos, G. H. P.; Simonsen, S. H.; Lynch, V. *Inorg. Chem.* **1996**, *35*, 6064-6073. (c) Doyle, M. P.; Colyer, J. T. *Tetrahedron: Asymmetry*, **2003**, *14*, 3601-3604. (d) Doyle, M. P.; Morgan, J. P.; Fettingner, J. C.; Zavalij, P. Y.; Colyer, J. T.; Timmons, D. J.; Carducci, M. D. *J. Org. Chem.* **2005**, *70*, 5291-5301.
14. (a) Kim, M. S.; Kim, Y.-W.; Hahm, H. S.; Jang, J. W.; Lee, W. K.; Ha, H.-J. *Chem. Commun.* **2005**, 3062-3064. (b) Eum, H.-S.; Lee, Y.-N.; Kim, S.-M.; Baek, A.-Y.; Son, M.-K.; Lee, K.-W.; Ko, S.-W.; Kim, S.-H.; Yun, S.-Y.; Lee, W.-K.; Ha, H.-J. *Bull. Korean Chem. Soc.* **2010**, *31*, 611-614.
15. Doan, N.-D.; Hopewell, R.; Lubell, W. D. *Org. Lett.* **2014**, *16*, 2232-2235.
16. Fritz, J. A.; Nakhla, J. S.; Wolfe, J. P. *Org. Lett.* **2006**, *8*, 2531-2534.
17. Spicer, C. D.; Davis, B. G. *Nat. Commun.* **2014**, *5*, 4740-4753.
18. (a) Santagada, V.; Fiorino, F.; Perissutti, E.; Severino, B.; De Filippis, V.; Vivencio, B.; Caliendo, G. *Tetrahedron Lett.* **2001**, *42*, 5171-5173. (b) Bacsa, B.; Horváti, K.; Bösze, S.; Andrae, F.; Kappe, C. O. *J. Org. Chem.* **2008**, *73*, 7532-7542.
19. Zhang, L.-h.; Kauffman, G. S.; Pesti, J. A.; Yin, J. *J. Org. Chem.* **1997**, *62*, 6918-6920.
20. Daga, M. C.; Taddei, M.; Varchi, G. *Tetrahedron Lett.* **2001**, *42*, 5191-5194.
21. De Marco, R.; Bedini, A.; Spampinato, S.; Comellini, L.; Zhao, J.; Artali, R.; Gentilucci, L. *J. Med. Chem.* **2018**, *61*, 5751-5757.
22. (a) Cardillo, G.; Gentilucci, L.; Tolomelli, A. *Tetrahedron Lett.* **1999**, *40*, 8261-8264. (b) Cardillo, G.; Gentilucci, L.; Tolomelli, A. *Tetrahedron* **1999**, *55*, 15151-15158. (c) Davies, S. G.; Dixon, D. J. *Synlett* **1998**, *1998*, 963-964.
23. Kubota, H.; Kubo, A.; Takahashi, M.; Shimizu, R.; Da-te, T.; Okamura, K.; Nunami, K.-i. *J. Org. Chem.* **1995**, *60*, 6776-6784.
24. (a) Craveur, P.; Joseph, A. P.; Poulain, P.; de Brevern, A. G.; Rebehmed, J. *Amino Acids*, **2013**, *45*, 279-289. (b) Owens, N. W.; Braun, C.; O'Neil, J. D.; Marat, K.; Schweizer, F. *J. Am. Chem. Soc.* **2007**, *129*, 11670-11671.
25. (a) Bernardi, F.; Garavelli, M.; Scatizzi, M.; Tomasini, C.; Trigari, V.; Crisma, M.; Formaggio, F.; Peggion, C.; Toniolo, C. *Chem. Eur. J.* **2002**, *8*, 2516-2525. (b) Luppi, G.; Lanci, D.; Trigari, V.; Garavelli, M.; Garelli, A.; Tomasini, C. *J. Org. Chem.*, **2003**, *68*, 1982-1993. (c) Tomasini, C.; Luppi, G.; Monari, M. *J. Am. Chem. Soc.* **2006**, *128*, 2410-2420.
26. Zanna, N.; Focaroli, S.; Merlettini, A.; Gentilucci, L.; Teti, G.; Falconi, M.; Tomasini, C. *ACS Omega*, **2017**, *2*, 2374-2381.
27. (a) Temussi, P. A.; Picone, D.; Saviano, G.; Amodeo, P.; Motta, A.; Tancredi, T.; Salvadori, S.; Tomatis, R. *Biopolymers*, **1992**, *32*, 367-372. (b) Borics, A.; Toth, G. *J. Mol. Graph. Model.* **2010**, *28*, 495-505. (c) Sikorska, E.; Ślusarz, M. J.; Lammek, B. *Biopolymers*, **2006**, *82*, 603-614.
28. (a) Prabhakaran, P.; Kale, S. S.; Puranik, V. G.; Rajamohan, P. R.; Chetina, O.; Howard, J. A. K.; Hofmann, H.-J.; Sanjayan, G. *J. Am. Chem. Soc.*, **2008**, *130*, 17743-17754. (b) Giuliano, M. W.; Maynard, S. J.; Almeida, A. M.; Guo, L.; Guzei, I. A.; Spencer, L. C.; Gellman, S. H. *J. Am. Chem. Soc.* **2014**, *136*, 15046-15053.

29. (a) Smith, J. A.; Pease, L. G.; Kopple, K. D. *Crit. Rev. Biochem.*, **1980**, *8*, 315-399. (b) Chalmers, D. K.; Marshall, G. R. *J. Am. Chem. Soc.* **1995**, *117*, 5927-5937. (c) Venkatraman, J.; Shankaramma, S. C.; Balaram, P. *Chem. Rev.* **2001**, *101*, 3131-3152. (d) Rai, R.; Raghothama, S.; Balaram, P. *J. Am. Chem. Soc.* **2006**, *128*, 2675-2681.
30. Andersen, N. H.; Neidigh, J. W.; Harris, S. M.; Lee, G. M.; Liu, Z.; Tong, H. *J. Am. Chem. Soc.* **1997**, *119*, 8547-8561.
31. *HyperChem Pro Release 8.0.8*; Hypercube Inc., 1115 NW 4th St. Gainesville, FL 32608, USA, **2010**.
32. Cornell, W. D.; Cieplak, P.; Bayly, C. I.; Gould, I. R.; Merz, K. M.; Ferguson, D. M.; Spellmeyer, D. C.; Fox, T.; Caldwell, J. W.; Kollman, P. A. *J. Am. Chem. Soc.* **1995**, *117*, 5179-5197.
33. Jorgensen, W. L.; Chandrasekhar, J.; Madura, J. D.; Impey, R. W.; Klein, M. L. *J. Chem. Phys.* **1983**, *79*, 926-935.
34. Wüthrich, K. *NMR of Proteins and Nucleic Acids*; Wiley, New York, **1991**; p 320.
35. Toniolo, C.; Crisma, M.; Formaggio, F.; Alemán C.; Ramakrishnan, C.; Kalmankar, N.; Balaram, P. *Biopolymers*, **2017**, *108*, No. e22911.
36. De Marco, R.; Cavina, L.; Greco, A.; Gentilucci, L. *Amino Acids* **2014**, *46*, 2823-2839.
37. Caputo, R.; Longobardo, L. *Biopolymers*, **2007**, *32*, 401-404.
38. Blanco-Canosa, J. B.; Dawson, P. E. *Angew. Chem., Int. Ed.* **2008**, *120*, 6957-6961.
39. (a) Cardillo, G.; Gentilucci, L.; De Matteis, V. *J. Org. Chem.* **2002**, *67*, 5957-5962. (b) Gage, J. R.; Evans, D. A. *Org. Synth.* **1990**, *68*, 83-91.
40. Ung, P.; Winkler, D. A. *J. Med. Chem.* **2011**, *54*, 1111-1125.
41. Whitby, L. R.; Ando, Y.; Setola, V.; Vogt, P. K.; Roth, B. L.; Boger, D. L. *J. Am. Chem. Soc.*, **2011**, *133*, 10184-10194.
42. (a) Souers, A. J.; Ellman, J. A. *Tetrahedron*, **2001**, *57*, 7431-7448. (b) MacDonald, M.; Aube, J. *Curr. Org. Chem.*, **2001**, *5*, 417-438. (c) Hirschmann, R. F.; Nicolaou, K. C.; Angeles, A. R.; Chen, J. S.; Smith, A. B., *Acc. Chem. Res.* **2009**, *42*, 1511-1520.
43. Malek, N. J.; Moormann, A. E. *J. Org. Chem.*, **1982**, *47*, 5395-5397.
44. (a) Wilson, P. *Macromol. Chem. Phys.*, **2017**, *218*, 1600595-1600609. (b) Zong, J.; Cobb, S. L.; Cameron, N. R. *Biomater. Sci.*, **2017**, *5*, 872-886. (c) Arosio, D.; Manzoni, L.; Corno, C.; Perego, P. *Recent Pat. Anti-Cancer Drug Discovery* **2017**, *12*, 148-168. (d) Wang, L.; Zhang, Y.; Wu, A.; Wei, G. *Anal. Chim. Acta*, **2017**, *985*, 24-40. (e) Narayanaswamy, R.; Wang, T.; Torchilin, V. P. *Curr. Top. Med. Chem.* **2016**, *16*, 253-270. (f) Szweda, R.; Szweda, D.; Kosowski, D.; Dworak, A.; Trzebicka, B. *Curr. Org. Chem.* **2017**, *21*, 1579-1599. (g) Greco, A.; Maggini, L.; De Cola, L.; De Marco, R.; Gentilucci, L. *Bioconjugate Chem.* **2015**, *26*, 1873-1878. (h) De Marco, R.; Greco, A.; Calonghi, N.; Dattoli, S. D.; Baiula, M.; Spampinato, S.; Picchetti, P.; De Cola, L.; Anselmi, M.; Cipriani, F.; Gentilucci, L. *Peptide Science* **2018**, *110*, No. e23081.
45. Berendsen, H. J. C.; Postma, J. P. M.; van Gunsteren, W. F.; DiNola, A.; Haak, J. R. *J. Chem. Phys.* **1984**, *81*, 3684-3690.
46. 3c = 3e = 3l; 3h = 3i

Chapter 3. Constraining Endomorphin-1 by β,α -Hybrid Dipeptide/Heterocycle Scaffolds: Identification of a Novel κ -Opioid Receptor Selective Partial Agonist.

Herein we present the expedient synthesis of endomorphin-1 analogues containing stereoisomeric β^2 -homo-Freidinger lactam-like scaffolds ([Amo²]EM), and we discuss opioid receptor (OR) affinity, enzymatic stability, functional activity, *in vivo* antinociceptive effects, and conformational and molecular docking analysis. Hence, H-Tyr-Amo-Trp-PheNH₂ resulted to be a new chemotype of highly stable, selective, partial KOR agonist inducing analgesia, therefore displaying great potential interest as a painkiller possibly with reduced harmful side effects.

1. Introduction

The tetrapeptides endomorphine-1, H-Tyr-Pro-Trp-PheNH₂ (EM1), and endomorphine-2, H-Tyr-Pro-Phe-PheNH₂ (EM2), discovered in the mammalian brain by James Zadina in 1997, ^[1] are endogenous, highly selective μ -opioid receptor (MOR) agonists ^[1, 2] which exhibit outstanding antinociception upon icv and its administration, being effective even toward intractable acute and chronic neuropathic pain. ^[1,3] Despite their tremendous therapeutic potential as painkillers devoid of the undesired side-effects of the opiate alkaloids, ^[3,4] their clinical use remained unrealistic, due to poor metabolic stability, inability to cross the BBB, and efficient efflux. ^[3] Consequently, to improve their PK properties, the structure of the EMs has been subjected to a variety of modifications. ^[5,6,7,8]

Among the most effective manipulations, the introduction of β -variants in place of Pro² yielded bioactive EM analogues with improved metabolic stability. Selected examples include the use of pyrrolidine-3-carboxylic acid, ^[9,10,11,12] β -homo-Pro, ^[13,14] nipecotic acid, ^[15] and cis-2-aminocyclopenta or hexa or hexenecarboxylic acid. ^[16,17,18]

On the other hand, another widely utilized approach consisted in the introduction of local ^[19,20] or global conformational constraints, ^[21,22] to control the 3D structure while maintaining the fundamental interactions with the receptors. For instance, a Freidinger lactam-like structure mimicking a constrained Trp-Phe dipeptide was introduced in EM1 (Figure 1), but the resulting peptidomimetic failed to reproduce the desired bioactive conformation. ^[23] More interestingly, the spiro-Aba-Gly lactam scaffold (Aba: 4-amino-1,2,4,5-tetrahydro-2-benzazepine-3-one) was shown to induce a β -turn in a MOR-selective, partial agonist mimetic of EM2 (Figure 1). ^[24]

In this scenario, we figured EM1 analogues including a β^2 -residue at position 2, and a Freidinger lactam-like element across the positions 2 and 3, combined into a composite hybrid β,α -dipeptide/heterocycle scaffold (Figure 1). This was made possible by a procedure recently optimized by us, *i.e.* the expedient cyclization of oligopeptide sequences containing isoserine (iSer), by treatment with disuccinimidyl dicarbonate (DSC) and a catalytic amount of base.

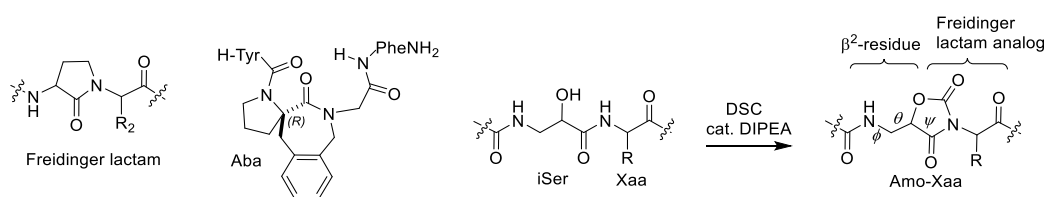


Figure 1. Top: classic Freidinger lactam, and spiro-Aba-Gly lactam; bottom: cyclization of iSer-Xaa to the hybrid β^2/α dipeptide/heterocycle scaffold Amo, with characteristic β^2 -residue torsional angles.

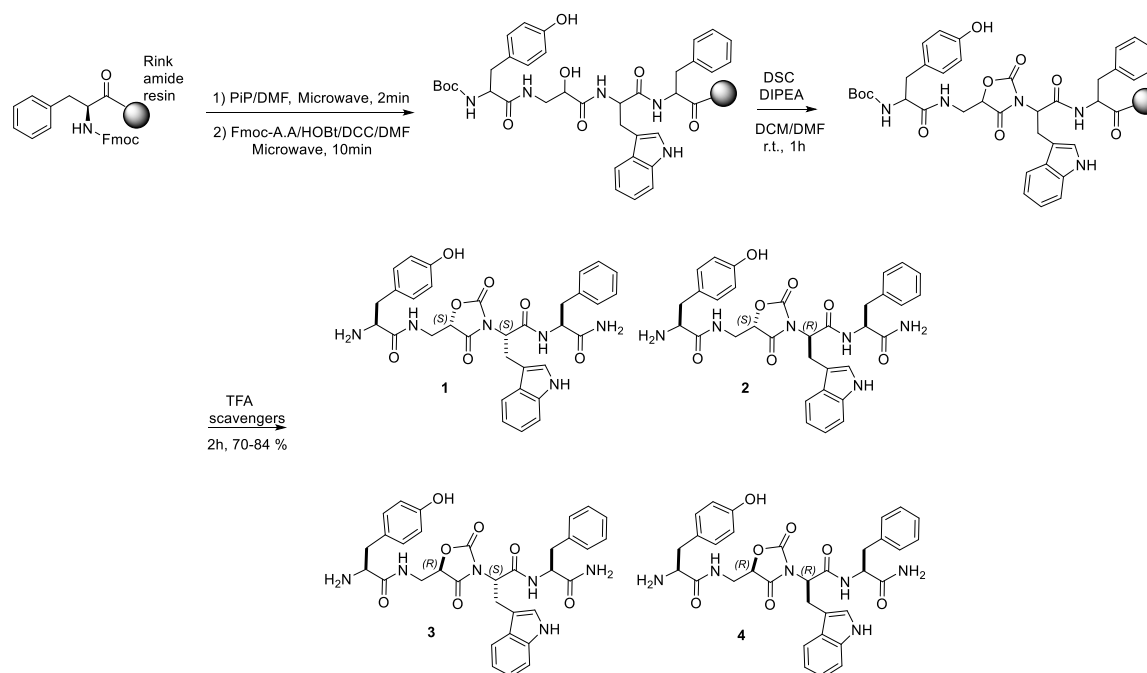
The reaction gave the unprecedented heterocycle 5-(aminomethyl)oxazolidine-2,4-dione (Amo), comprising iSer and the amine group of the following residue Xaa (Scheme 1).^[25] This scaffold was successfully exploited to stiffen cyclopeptide conformations,^[26] and for the preparation of the oxazolidinone antibiotic linezolid in enantiopure form,^[27] or enzymatically stable analogues of the $\alpha 4\beta 1$ integrin antagonist BIO1211.^[28]

In this paper we present the synthesis of a minilibrary of EM1 analogues containing the central Amo-Trp scaffold in place of Pro²-Trp³ ([Amo²]EM), constituted by the four stereoisomers of general sequence H-Tyr-(*S/R*)-Amo-(*S/R*)-Trp-PheNH₂ (Scheme 1), and we discuss their affinity for MOR, δ -, and κ -opioid receptors (DOR, and KOR). Subsequently, we analyze the functional activity, the enzymatic stability, and the potential antinociceptive effects of the peptide having the highest receptor affinity. Finally, we investigate the structural determinants for bioactivity by conformational analysis and molecular docking (MDK).

2. Results and Discussion

2.1 Peptide Synthesis.

The [Amo²]EMs **1-4** were prepared by solid phase peptide synthesis (SPPS) on a Rink amide resin preloaded with Fmoc-Phe (Scheme 1). Fmoc removal was done with 20% piperidine in DMF at 45°C under microwave irradiation (MW) in 2 min. Fmoc-(*S/R*)-TrpOH, Fmoc-(*S/R*)-iSerOH, Boc-TyrOH (Boc = tert-butyloxycarbonyl), were coupled in sequence using the activating agents DCC and HOBT at 45°C under MW for 10 min.



Scheme 1. SPPS of the diastereoisomeric [Amo²]EMs **1-4**.

The resin-bound peptides were treated with 3 equiv. of DSC and 1 equiv. of DIPEA for 1 h. Cleavage from the resin was carried out with TFA and scavengers, at rt for 2 h. The crude peptides were precipitated and collected by centrifuge, and purified by semi-preparative reversed phase (RP) HPLC. The identity of the [Amo²]EM analogues was confirmed by electrospray ionization mass spectrometry (ESI) MS, ¹H NMR, ¹³C NMR, and gCOSY spectroscopy; purity was determined by analytical RP HPLC (Table 1), exact mass, and elemental analysis.

2.2 Human ORs Binding Affinity.

To evaluate any affinity of the [Amo²]EMs **1-4** for the ORs, displacement binding assays were performed in HEK-293 cells stably expressing the cloned human (h)MOR, hDOR, or hKOR, using the respective specific radioligands [³H]DAMGO, [³H]-diprenorphine, or [³H]U69,593. The reference compounds DAMGO, DPDPE, and U50,488 showed *K_i* values in the nM range and high selectivity to the respective receptors (Table 1), as expected. As reported in Table 1, the peptides **2** and **3** did not show any significant receptor affinity. In contrast, H-Tyr-Amo-Trp-PheNH₂ (**1**) displayed a nM affinity for KOR (*K_i* = 9.8 nM) and high selectivity over MOR and DOR (Table 1). Finally, H-Tyr-(*R*)-Amo-(*R*)-Trp-PheNH₂ (**4**) was a selective MOR ligand, albeit with a modest affinity (*K_i* = 240 nM) as compared to native EM1 (*K_i* = 0.36 nM).^[1,3]

Table 1. In Vitro OR Affinities of the [Amo²]EMs and Reference Compounds for hORs.

Compd	Purity (%) ^[a]	<i>K_i</i> (nM) ^[b]		
		MOR	DOR	KOR
DAMGO	-	1.5 ± 0.1	-	-
DPDPE	-	-	3.30 ± 0.05	-
U50,488	-	-	-	2.90 ± 0.04
1	97	>10 ⁵	>10 ⁵	9.8 ± 4.1
2	95	>10 ⁵	>10 ⁵	>10 ⁵
3	96	>10 ⁵	>10 ⁵	>10 ⁵
4	98	240 ± 50	>10 ⁵	>10 ⁵

^[a] Determined by RP-HPLC (General Methods). ^[b] Mean of 4-6 determinations \pm SE.

These strikingly different OR preferences suggested that the stereoisomeric Amo-Trp dipeptides induce distinct, alternative 3D geometries to the EM1 analogues. This prompted to investigate the in-solution conformations of **1-4** by NMR spectroscopy and computations (see next sections).

2.3 Stability of **1** and **4** in Mouse Serum.

The stability of the only bioactive **1** and **4** and of the parent EM1 was determined in mouse serum by RP HPLC and ESI MS analysis, as previously reported.^[29] After 1 h, EM1 was almost completely degraded, being present only in traces, as expected on the basis of the literature,^[10,13,30] while **1** and **4** were hydrolyzed only to a moderate extent, <5% after 1h, and <10% after 4h, consistent to the peptidomimetic nature of the compounds.^[5]

2.4 Pharmacological Characterization of **1** and **4**.

The functional activity of **1** at KOR and of **4** at MOR was investigated by the cAMP test in whole HEK-293 cells stably expressing hKOR (HEK/hKOR) and hMOR (HEK/hMOR), respectively. As expected U50,488 and DAMGO, employed as KOR or MOR reference compounds, significantly inhibited forskolin-induced cAMP accumulation, with IC_{50} values of 1.2 nM and 1.5 nM, and E_{max} of 90% and 95% (E_{max} = maximal obtainable effect/vehicle), respectively (Table 2). Interestingly, **1** inhibited forskolin-induced cAMP accumulation in HEK/hKOR, with IC_{50} = 0.22 nM and E_{max} = 40%, suggestive of a partial agonist behavior, as compared to U50,488 (IC_{50} = 1.2 nM and E_{max} = 90%; Table 2 and Figure 2). Interestingly, when 1 μ M **1** was coadministered together with U50,488, 40% inhibition of forskolin-induced cAMP accumulation was observed and U50,488 concentration-response curve was shifted rightward; thus, confirming a partial agonist activity for **1** (Figure 2).

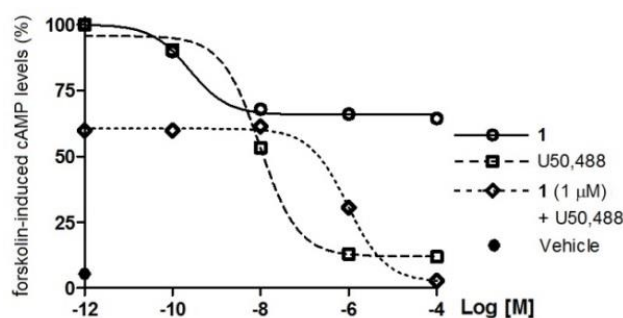


Figure 2. Inhibition of forskolin-induced cAMP accumulation determined by **1** (1 pM - 100 μ M) and U50,488 (1 pM - 100 μ M), alone or co-administered with 1 μ M **1**, in HEK/hKOR cells.

On the other hand, **4** inhibited forskolin-induced cAMP accumulation in HEK/hMOR with IC_{50} = 0.016 nM and E_{max} = 50% (Table 2), a surprising result when compared to the very modest MOR affinity, in the 10^{-7} M range (Table 1). The partial agonist activity of the [Amo²]EMs **1** and **4**, respect to the full agonism of U50,488 and DAMGO, is not completely unexpected. Indeed, the parent peptide EM1 is known to be itself a partial agonist of MOR (IC_{50} = 1.0 nM, E_{max} = 53%) in the cAMP assay,^[1,3] and in general its efficacy in many tests is lower than that of synthetic analogues, albeit its antinociceptive efficacy is higher.^[1,3]

The tail-immersion test was performed as previously described;^[29] the tail of the animal was immersed in hot water and the latency to withdrawal measured in both vehicle- and compound-treated animals. The

increase in the latency to response was expressed as MPE% (cutoff 10 s). The curves MPE vs time for ip administered **1** at the dose of 20 mg/kg are shown in Figure 3A.

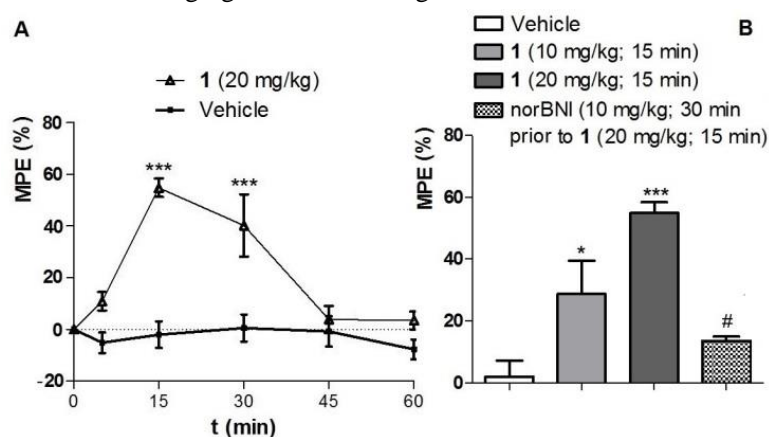


Figure 3. Antinociception produced by **1** in the mouse tail immersion test. **A** Time-dependent effects elicited by ip administered **1** (20 mg/kg); *** $p < 0.001$ vs vehicle; $n = 6$. **B** Dose-response and KOR-mediated effects induced by ip administered **1** with or without the KOR selective antagonist norBNI; * $p < 0.05$ vs vehicle mg/kg; *** $p < 0.001$ vs vehicle; # $p < 0.05$ vs 1 20 mg/kg; $n = 6$.

Peptide **1** determined a relevant analgesic effect, which peaked at 15 min (Figure 3A, 60% MPE) and was still significant at 30 min (42% MPE). Interestingly, 10 mg/kg of **1** induced a significant analgesia (15 min), albeit lower as compared to the 20 mg/kg dose (Figure 3B). Antinociceptive effects elicited by **1** (20 mg/kg, 15 min) were counteracted by the preemptive administration of the KOR selective antagonist nor-BNI (10 mg/kg, 30 min prior to **1**), thus confirming also *in vivo* a KOR-mediated activity (Figure 3B). The unprecedented pharmacological profile of **1** is of some interest, since this compound represents the first close analogue of EM1 showing nM KOR affinity, partial agonist behavior, high enzymatic stability, and *in-vivo* activity. While the endogenous ligands of KOR, *i.e.* the full agonist dynorphin A (dynA) and truncated sequences, show moderate preference for KOR over DOR and MOR, [31,32] **1** is completely KOR-selective. Among the opiates, KOR agonists and partial agonists have become the object of much interest as painkillers, due to the intrinsic drawbacks of MOR and DOR agonists. [4] Indeed, the former are regarded as the most potent analgesics, but they are accompanied by relevant side-effects, including constipation, respiratory depression, addiction; the latter have a reduced addictive potential, but possess lower antinociceptive effect. [4] KOR is different from the other ORs in terms of tissue expression, functional properties, and side effect profile upon activation. Hence, KOR agonists may produce analgesia without the unwanted effects associated to MOR or DOR, [33] but may induce hallucinations and dysphoria. [4,31] However, KOR partial agonists may allow an analgesic response to be produced at dosages lower than those required to produce the adverse effects. [34] Besides, some KOR agonists display anti-inflammatory and neuroprotective effects, and they suppress the rewarding effects of opiates and cocaine. Partial agonists may hold potential for the treatment of depression, mood disorders, [35] psychiatric co-morbidity, specific drug addictions. [32] Such compounds may restore homeostatic control of dopaminergic function underlying mood and reward. KOR partial agonism may also diminish severity of relapse/re-escalation. Mixed agonists/partial agonists/antagonists at different OR subtypes are employed to treat alcohol dependence and cocaine craving. [4,34,36] As for KOR antagonists, these are already used to treat opioid dependence and withdrawal. [4,37,38]

Interestingly, the [Amo²]EM **1** is able to selectively bind to and activate KOR with high affinity, in contrast to the parent EM1, which is a very poor KOR ligand ($K_i = 5430$ nM),^[1,3] albeit they share the same pharmacophores and the same all-*S* stereochemistry pattern. This consideration roused a question, whether the specific doubly (*S*)-configured Amo²-Trp³ central scaffold in **1** might represent a KOR-specific recognition element, or rather it could stabilize a specific bioactive conformation. To address this issue, we analyzed conformations of **1-4** in solution, and we applied MDK computations to gain structural insight into the binding mode to KOR.

2.5 Conformational Analysis in-Solution.

NMR analysis of **1-4** was performed in 8:2 [D₆]dimethylsulfoxide (DMSO)/H₂O, a solvent mixture often utilized as excellent representative of biologic environment for the analysis of opioid peptides.^[39,40] The occurrence of hydrogen (H)-bonded structures was excluded on the basis of variable temp NMR experiments. Indeed, the $\Delta\delta/\Delta t$ parameters of **1-4** suggested that all amide protons were solvent-exposed ($|\Delta\delta/\Delta t|$ in the 4.5-6.5 ppb K⁻¹ range, not shown). The compounds were analyzed by 2D ROESY, and cross-peaks intensities were utilized to infer constraints for restrained MD simulations. MD were conducted in a box of explicit water at high temp with scaled restraints, followed by a simulation with full restraints. After gradually cooling, the structures were minimized with AMBER force field and clustered by the rmsd analysis of the backbone atoms. For all compounds, this procedure gave one major cluster comprising the large majority of the structures. The representative structures with the lowest energy and the least number of restraint violations were selected and analyzed (Figure 4).

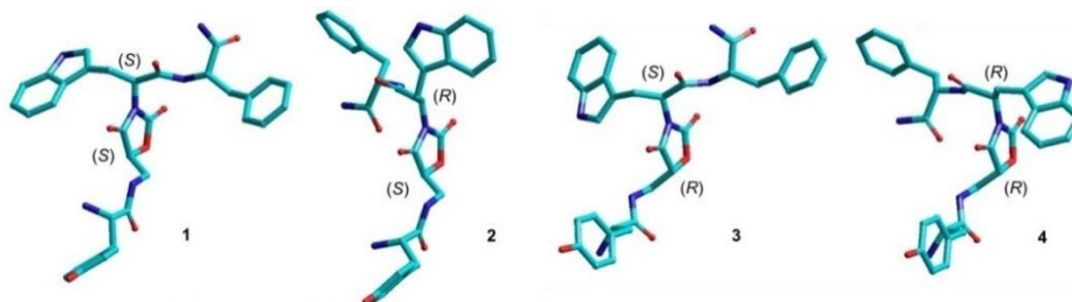


Figure 4. Representative conformers of [Amo²]EMs **1-4**, determined by ROESY and restrained MD.

These structures display partially bent backbones; the central dihedral angle Amo θ (Figure 4) is +*g* in **1** and **2**, -*g* in **3** and **4**. For **1** and **4**, Tyr and PheNH₂ lie on the same side of the central homochiral (*S,S*) and (*R,R*) Amo-Trp scaffolds. In contrast, for **2** and **3**, which include heterochiral (*S,R*) or (*R,S*) scaffolds, the ROESY derived structures reveal more extended backbone conformations, with Tyr on the opposite side respect PheNH₂.

Starting from these geometries, the dynamic behavior of the peptides was observed by unrestrained MD simulations in explicit water, at rt. During the simulations, the rotation of the backbones around the Amo-Trp bond was not observed, possibly due to the presence of the two carbonyl groups at the positions 2 and 4 of the heterocycle.

2.6 Molecular Docking (MDK).

The in-solution structures of **1-4** (Figure 4) were docked with Autodock within a receptor model built from an X-ray structure of the active conformation of KOR in complex with MP1104.^[41] All MDK poses were visually inspected for close intermolecular interactions of the binding residues. The pose of peptide **1** with

the best score is shown in Figure 5. This complex shows a tight fit of the ligand in the binding cleft, forming ionic, polar, and extensive hydrophobic interactions with the receptor. The plausible “message” portion Tyr¹ of **1** adopts a disposition alternative to that of tetrahydroisoquinoline ring of JD_{Tic},^[42] and to the docked pose of the Tyr of the KOR peptide ligand dynA(1-8),^[43,44] and finally to the tyramine portion of MP1104,^[41] while showing little in common with the binding pose of the conorphins.^[45] On the other hand, the rest of the structure of **1** adopts a peculiar, unique orientation within the receptor (Figure 5), occupying an “address-recognition” region which is not conserved across the other ORs.^[42,43,46]

This geometry is rather different from that observed in solution (Figure 4), in that Am_o ring adopts a *trans* conformation about the θ angle, and the Trp-PheNH₂ portion is rotated opposite respect to in-solution **1**. Modeling of KOR revealed that the binding pocket for “address” portion of the ligands is narrowed respect to the other ORs, mostly due to differences in the extracellular loop (EL) 2 and the extracellular parts of the transmembrane helix (TM) 6, and TM7.^[42,43] As a consequence, the ligand may be forced to assume a higher energy conformation for optimal fit.^[46]

In details, the Tyr of **1** is positioned into the pocket circumscribed by TM3-7 (Figure 5), with the protonated amine forming an hydrogen bond and a ionic interaction (1.5 and 1.2 Å) with the carbonyl and the carboxylate of Asp¹³⁸ (3:32 in the Ballesteros and Weinstein numbering system), a residue conserved in all aminergic GPCRs, thereby playing a critical role in binding and activation. The backbone oxygen forms an H-bond (3.0 Å) with the phenolic OH group of Tyr¹³⁹ (3:33), a residue postulated to be related to receptor function, while the phenolic OH interacts with the backbone oxygen of Ile³¹⁶ (7:39) and the nitrogen of Gly³¹⁹ (7:42) forming two H-bonds (1.5 and 2.3 Å, respectively). The phenol group is also stabilized by a favorable π - π stacking interaction with the aromatic side chains of Tyr³²⁰ (7:43). It is worth noting that Tyr phenol group holds Trp²⁸⁷ (6:48), a residue thought to be a key part of the activation mechanism of the receptor, in the rotamer observed in the active-state crystal structure.

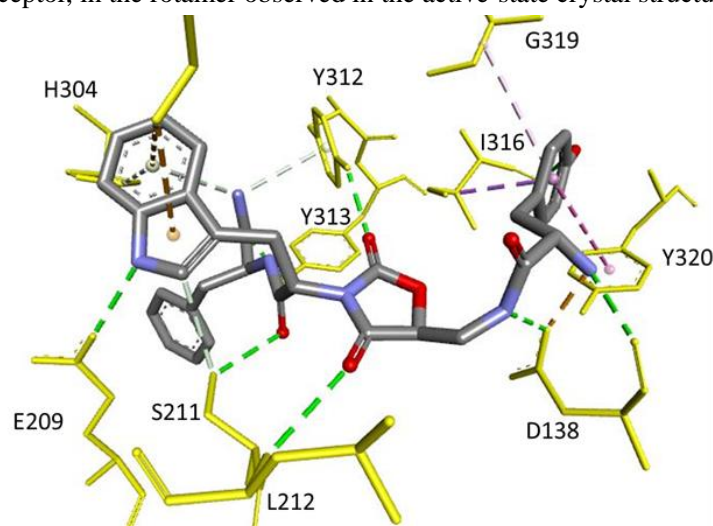


Figure 5. Stabilizing interaction within the complex KOR (PDB ID: 6B73)-**1** represented as dashed lines: H-bonds in green, salt bridges in orange, and π - π interactions in violet. KOR residues are rendered in line, while **1** is rendered in stick.

The Am_o residue is inserted between TM3, TM6, and TM7, and contributes to the stability of the complex with several H-bonds: two H-bonds between Am_oNH and the carboxylate and carbonyl groups of Asp¹³⁸ (3:32) (1.7 and 2.9 Å); the C=O in **4** interact with NH of Leu²¹² (EL2, 2.4 Å); C=O in **2** forms an H-bond to the phenolic OH of Tyr³¹² (7:35, 1.5Å), a residue deeply involved in receptor activation. The latter

interaction might contribute to the KOR selectivity of **1**, being such an interaction with a residue in the binding pocket that differ in other closely related ORs (residue 7:35 is Trp in MOR, Leu in DOR).^[43]

Trp³ of **1** resides between TM4-7 and EL2, forming H-bonds between indoleNH and the carboxylate side chain of Glu²⁰⁹ (EL2, 1.7 Å), and between the backbone carbonyl oxygen and OH of Ser²¹¹ (EL2, 2.7 Å). The indole is also stabilized by a π - π stacking interaction with the charged side chain of Lys²²⁷ (5:39). Finally, the C-terminal PheNH₂ of **1** is located between EL2, TM6, and TM7, with carbonyl group forming an H-bond to the phenolic OH of Tyr³¹³ (7:36, 1.6 Å), and is placed in position also by an intramolecular H-bond between PheNH and Amoc=O at position 2 (2.9 Å).

As for the other Amo-peptides **2-4**, the same MDK protocol as described above failed to furnish high-scoring, representative bioactive geometries in KOR, supporting the fundamental role of the specific stereochemistry of the Amo-Trp scaffold of **1** in orienting the pharmacophores for optimal receptor-specific interactions.

3. Conclusions

Aiming at improving stability and bioavailability, the sequence of EM1 was modified by the introduction of the stereoisomeric Amo-Trp hybrid scaffolds, which combine a β^2 -homo residue and a Friedinger lactam-like structure. Compound H-Tyr-(*R*)-Amo-(*R*)-Trp-PheNH₂ (**4**) maintained the MOR preference of the parent peptide, albeit with strongly reduced affinity. More intriguingly, H-Tyr-Amo-Trp-PheNH₂ (**1**) demonstrated high KOR affinity and selectivity, acting as a partial agonist *in vitro* and determining a relevant analgesia *in vivo* in the tail-immersion test. The clinical utility of opioid analgesics with partial efficacy has been well-documented.^[34] Besides, such compounds are currently thought to be a potential strategy in the treatment of psychiatric comorbidity, mood disorders,^[35] and specific addictive diseases. Selective KOR partial agonists may be beneficial in promoting more prolonged abstinence, as well as decreasing the severity of relapse episodes.^[32] Unfortunately, owing to lack of KOR>MOR selectivity in known ligands, these therapeutic opportunities have been not clinically exploited, so far.^[32,33] Molecular modeling and docking analysis shed light on the bioactive structure of this unprecedented chemotype^[43] of KOR ligand. The computations support the role of Amo in orienting the pharmacophores for optimal receptor fitting. Besides to the C-terminal Trp³-Phe⁴NH₂ portion, Amo² itself appear to belong to the “address” of the ligand, being responsible of interactions with residues which are not conserved across the other ORs.

4. Experimental Section

4.1 General Methods of Synthesis and Analysis

All reagents, were obtained from commercial sources and used without further purification. The MW-assisted synthesis was performed at 40 W using a MicroSYNTH microwave lab station equipped with a built-in ATC-FO advanced fiber optic automatic temperature control. Purities were determined to be $\geq 95\%$ by analytical RP HPLC and elemental analysis. RP HPLC was performed on an Agilent 1100 series apparatus, using a RP column Phenomenex mod. Gemini 3 μ C18 110 Å 100 3 3.0 mm (P/No 00D-4439-Y0); column description: stationary phase octadecyl carbon chain-bonded silica (C18) with TMS endcapping, fully porous organo-silica solid support, particle size 3 mm, pore size 110 Å, length 100 mm, internal diameter 3 mm; DAD 210 and 254 nm; mobile phase from 9:1 solvent A/solvent B to 2:8 solvent A/solvent B, A = 0.1% TFA in H₂O, B = 0.1% TFA in CH₃CN, in 20 min, at a flow rate of 0.5 mL min⁻¹, followed by 10 min at the same composition. Semi-preparative RP-HPLC was performed on an

Agilent 1100 series apparatus, using a RP column ZORBAX mod. Eclipse XDB-C18 PrepHT cartridge 21.2 x 3 x 150 mm 7 μ (P/No 977150-102); column description: stationary phase octadecyl carbon chain-bonded silica (C18), double end-capped, particle size 7 μ m, pore size 80 Å, length 150 mm, internal diameter 21.2 mm; DAD 210 and 254 nm; mobile phase from 8:2 solvent A/solvent B to 100% solvent B, A = 0.1% TFA in H₂O, B = 0.1% TFA in CH₃CN, in 10 min, at a flow rate of 12 mL min⁻¹. Exact mass was determined on a Waters Xevo QTOF apparatus. Routine ESI analysis was performed using a MS single quadrupole HP 1100MSD detector, with a drying gas flow of 12.5 L min⁻¹, nebulizer pressure 30 psig, drying gas temp. 350°C, capillary voltage 4500 (1) and 4000 (2), scan 50-2600 amu. Elemental analyses were performed using a Thermo Flash 2000 CHNS/O analyzer. ¹H NMR spectra were recorded using a Varian Gemini apparatus at 400 MHz in 5 mm tubes, using 0.01 M peptide in 8:2 [D₆]DMSO/H₂O at rt. Water suppression was performed by the solvent presaturation procedure implemented in Varian (PRESAT). ¹³C NMR spectra were recorded at 100 MHz in 8:2 [D₆]DMSO/H₂O at rt. Chemical shifts are reported as δ values relative to residual DMSO δ H (¹H NMR: 2.50 ppm; ¹³C NMR: 39.5 ppm) as internal standard. The unambiguous assignment of ¹H NMR resonances was performed by 2D gCOSY. VT-¹H NMR experiments were performed over the range of 298-348 K; temperature calibration was done with the ethylene glycol OHCHn chemical-shift separation method.

Solid-phase synthesis of the linear precursors. The linear peptides were assembled by MW-assisted SPPS on a commercially available Rink amide resin preloaded with Fmoc-Phe, using N-protected amino acids, and DCC/HOBt as coupling agents. All steps were performed according to the following general procedures. Boc-Tyr-OH, and Fmoc-isoSerOH were utilized with unprotected side chains; under the reaction conditions described, no trace of depsipeptide formation was detected by the analysis of the crude reaction mixtures.

4.2 Synthetic Procedures

Fmoc deprotection

The Fmoc-Phe-preloaded resin (0.5 g, Phe loading 0.2-0.6 mmol/g) was treated with 20% piperidine in DMF (5 mL) for 2 min under MW irradiation at 40W, monitoring the internal temperature at 45°C with a built-in ATC-FO advanced fiber optic automatic temperature control. The suspension was filtered and the resin was washed with CH₂Cl₂ (5 mL) and treated with a second portion of 20% piperidine in DMF under MW irradiation as described above. The suspension was then filtered, and the resin was washed three times in sequence with CH₂Cl₂ (5 mL), MeOH (5 mL), and DMF (5mL).

Peptide bond formation

The resin was swollen in CH₂Cl₂ (5 mL), and Fmoc-amino acid (0.6 mmol), the coupling reagents DCC (0.6 mmol), HOBt (0.6 mmol), were added under a nitrogen atmosphere to the resin, and the mixture was reacted while bubbling N₂ for 10 min, under MW irradiation at 45°C as described above. The resin was washed in sequence 3 times with CH₂Cl₂ (5 mL), MeOH (5 mL), and DMF (5mL), and coupling efficacy was determined by means of the Kaiser tests.

Cyclization of iSer-peptides to Amo-peptides

The resin-bound iSer-containing peptide (0.5 g, 0.2-0.6 mmol g⁻¹) were suspended in CH₂Cl₂/DMF (4:1), and DSC (3 equiv.), and DIPEA (3 equiv.) were added at room temp. The reaction was carried out under mechanical shaking for 1 h at r.t., then the suspension was filtered, and the resin was washed three times in sequence with DMF (5 mL), MeOH (5 mL), CH₂Cl₂ (5 mL).

Peptide cleavage

The peptidyl resins were treated with a mixture of TFA and TIPS/water/PhOH as scavengers (7:1:1:1 v/v, 15 mL), for 2 hours at rt. The mixture was filtered, and the resin was washed 3 times with 5% TFA in Et₂O (10 mL). The filtrate and the washes were collected and solvent and volatiles were removed at r.t. under N₂ flow. The resulting residue was suspended in ice-cold Et₂O, and the crude solid which precipitated was triturated and collected by centrifuge. The resulting crude residues were purified by semi-preparative RP HPLC (see General Methods). Purities were determined to be >95% by analytical RP HPLC and elemental analysis (for the conditions, see General Methods). The identity of the compounds was confirmed by ¹H NMR, 2D gCOSY (gradient correlation spectroscopy), ¹³C NMR, and ESI MS analyses.

4.3 Analytical Characterization of **1-4**.

H-Tyr-Amo-Trp-PheNH₂ (1). ¹H NMR (8:2 [D₆]DMSO/H₂O) δ 2.76-2.86 (m, 2H, TyrHβ + PheHβ), 2.88-2.98 (m, 2H, TyrHβ + AmoHβ), 3.00 (dd, *J* = 6.0, 13.6 Hz, 1H, PheHβ), 3.34-3.44 (m, 2H, TrpHβ), 3.55 (m, 1H, AmoHβ), 3.84 (m, 1H, TyrHα), 4.44 (m, 1H, PheHα), 4.76 (dd, *J* = 4.8, 10.8 Hz, 1H, AmoHα), 4.79 (dd, *J* = 5.8, 10.2 Hz, 1H, TrpHα), 6.70 (d, *J* = 8.0 Hz, 2H, TyrArH), 6.92-7.03 (m, 3H, TyrArH × 2 + TrpArH5), 7.04-7.13 (m, 3H, TrpArH2 + TrpArH6 + CONH₂), 7.13-7.28 (m, 5H, PheArH), 7.30 (d, *J* = 7.6 Hz, 1H, TrpArH7), 7.46-7.55 (m, 2H, TrpArH4 + CONH₂), 8.06 (br.s, 3H, TyrNH), 8.49 (br.d, 1H, PheNH), 8.72 (br.t, 1H, AmoNH), 9.36 (s, 1H, TyrOH), 10.87 (s, 1H, TrpArH1); ¹³C NMR (8:2 [D₆]DMSO/H₂O) δ: 29.6, 37.0, 38.0, 54.6, 55.6, 56.3, 78.8, 110.1, 110.5, 112.4, 116.3, 118.9, 119.4, 122.0, 124.8, 125.5, 127.1, 127.9, 128.3, 129.0, 130.0, 131.4, 137.0, 138.9, 154.9, 157.6, 167.6, 169.6, 171.3, 173.7; ESI MS (m/z) 627.2595 [M+H]⁺, calcd for C₃₃H₃₅N₆O₇ 627.2567; Elem. Anal. for C₃₃H₃₄N₆O₇: calcd C 63.25, H 5.47, N 13.41; found C 63.18, H 5.45, N 13.38.

H-Tyr-Amo-(R)-Trp-PheNH₂ (2). ¹H NMR (8:2 [D₆]DMSO/H₂O) δ 2.77 (dd, *J* = 7.8, 14.2 Hz, 1H, TyrHβ), 2.86 (dd, *J* = 10.4, 13.2 Hz, 1H, PheHβ), 2.95 (dd, *J* = 5.2, 14.0 Hz, 1H, TyrHβ), 3.00 (dd, *J* = 6.0, 12.0 Hz, 1H, 1H, AmoHβ), 3.10 (dd, *J* = 4.8, 14.0 Hz, 1H, PheHβ), 3.34-3.35 (m, 2H, (R)-TrpHβ), 3.56 (m, 1H, AmoHβ), 3.81 (m, 1H, TyrHα), 4.49 (m, 1H, PheHα), 4.85 (dd, *J* = 3.6, 7.2 Hz, 1H, AmoHα), 4.88 (dd, *J* = 7.8, 9.0 Hz, 1H, (R)-TrpHα), 6.70 (d, *J* = 8.4 Hz, 2H, TyrArH), 6.96-7.04 (m, 3H, TyrArH × 2 + (R)-TrpArH2), 7.07 (m, 2H, (R)-TrpArH5 + (R)-TrpArH6), 7.16-7.28 (m, 6H, PheArH + CONH₂), 7.32 (d, *J* = 7.6 Hz, 1H, TrpArH7), 7.49 (s, 1H, CONH₂), 7.64 (d, *J* = 7.6 Hz, 1H, (R)-TrpArH4), 8.03 (br.s, 3H, TyrNH), 8.52 (br.d, 1H, PheNH), 8.72 (br.t, 1H, AmoNH), 9.40 (br.s, 1H, TyrOH), 10.84 (s, 1H, (R)-TrpArH1); ¹³C NMR (8:2 [D₆]DMSO/H₂O) δ: 29.9, 37.0, 38.3, 54.8, 55.3, 56.7, 78.5, 110.0, 110.5, 112.4, 116.3, 119.3, 122.1, 124.7, 125.6, 127.3, 129.0, 130.1, 131.4, 137.0, 138.7, 155.1, 157.5, 165.6, 167.8, 169.7, 173.7; ESI MS (m/z) 627.2543 [M+H]⁺, calcd for C₃₃H₃₅N₆O₇ 627.2567; Elem. Anal. for C₃₃H₃₄N₆O₇: calcd C 63.25, H, 5.47, N 13.41; found C 63.19, H, 5.49, N 13.37

H-Tyr-(R)-Amo-Trp-PheNH₂ (3). ¹H NMR (8:2 [D₆]DMSO/H₂O) δ 2.66-2.77 (m, 2H, TyrHβ + PheHβ), 2.80-2.92 (m, 3H, TyrHβ + AmoHβ + PheHβ), 3.22-3.38 (m, 2H, TrpHβ), 3.50 (m, 1H, AmoHβ), 3.82 (m, 1H, TyrHα), 4.45 (m, 1H, PheHα), 4.73-4.85 (m, 2H, AmoHα + TrpHα), 6.66 (d, *J* = 8.0 Hz, 2H, TyrArH), 6.94-7.00 (m, 3H, TyrArH + TrpArH5), 7.03-7.12 (m, 2H, TrpArH2 + TrpArH6), 7.13-7.25 (m, 6H, PheArH + CONH₂), 7.32 (d, *J* = 8.0 Hz, 1H, TrpArH7), 7.46-7.55 (m, 2H, TrpArH4 + CONH₂), 8.04 (br.s, 3H, TyrNH), 8.50 (br. 1H, PheNH), 8.52 (br.t, 1H, AmoNH), 10.58 (s, 1H, TyrOH), 10.80 (s, 1H, TrpArH1); ¹³C NMR (8:2 [D₆]DMSO/H₂O) δ: 30.0, 37.0, 38.0, 54.7, 55.7, 56.4, 78.3, 110.1, 110.6, 112.5, 116.4, 118.9, 119.5, 120.1, 122.0, 124.9, 125.6, 127.1, 128.3, 128.8, 129.0, 130.1, 131.4, 137.1, 138.9, 155.1, 157.6, 167.6, 169.8, 171.1, 173.8; ESI MS (m/z) 627.2589 [M+H]⁺, calcd for C₃₃H₃₅N₆O₇ 627.2567; Elem. Anal. for C₃₃H₃₄N₆O₇: calcd C 63.25, H 5.47, N 13.41; found C 63.31, H 5.46, N 13.47

H-Tyr-(R)-Amo-(R)-Trp-PheNH₂ (4). ¹H NMR (8:2 [D₆]DMSO/H₂O) δ 2.56 (dd, *J* = 10.8, 13.2 Hz, 1H, TyrHβ), 2.66-2.80 (m, 2H, AmoHβ + TyrHβ), 2.84 (dd, *J* = 7.6, 13.2 Hz, 1H, PheHβ), 3.10 (dd, *J* = 7.2, 13.2 Hz, 1H, PheHβ), 3.22-3.39 (m, 3H, (R)-TrpHβ + AmoHβ), 3.73 (m, 1H, TyrHα), 4.53 (m, 1H, PheHα), 4.73 (dd, *J* = 5.8, 10.8 Hz, 1H, (R)-TrpHα), 4.90 (dd, *J* = 3.0, 7.8 Hz, 1H, AmoHα), 6.63 (d, *J* = 8.0 Hz, 2H, TyrArH), 6.85-7.03 (m, 4H, TyrArH × 2 + (R)-TrpArH2 + (R)-TrpArH5), 7.06 (dd, *J* = 6.4, 7.6 Hz, 1H, (R)-TrpArH6), 7.16-7.27 (m, 6H, PheArH + CONH₂), 7.32 (d, *J* = 7.6 Hz, 1H, (R)-TrpArH7), 7.40 (s, 1H, CONH₂), 7.55 (d, *J* = 7.6 Hz, 1H, (R)-TrpArH4), 8.03 (br.s, 3H, TyrNH), 8.23 (br.t, 1H, AmoNH), 8.39 (d, *J* = 8.4 Hz, 1H, PheNH), 9.17 (br.s, 1H, TyrOH), 10.84 (s, 1H, (R)-TrpArH1); ¹³C NMR (8:2 [D₆]DMSO/H₂O) δ: 29.9, 38.4, 39.7, 56.2, 56.7, 58.2, 77.8, 111.4, 113.8, 117.6, 121.2, 123.5, 126.1, 128.7, 130.5, 131.7, 132.8, 138.4, 140.2, 158.9, 159.6, 169.1, 171.1, 173.0, 175.1; ESI MS (*m/z*) 627.2598 [M+H]⁺, calcd for C₃₃H₃₅N₆O₇ 627.2567; Elem. Anal. for C₃₃H₃₄N₆O₇: calcd C 63.25, H 5.47, N 13.41; found C 63.32, H 5.49, N 13.38.

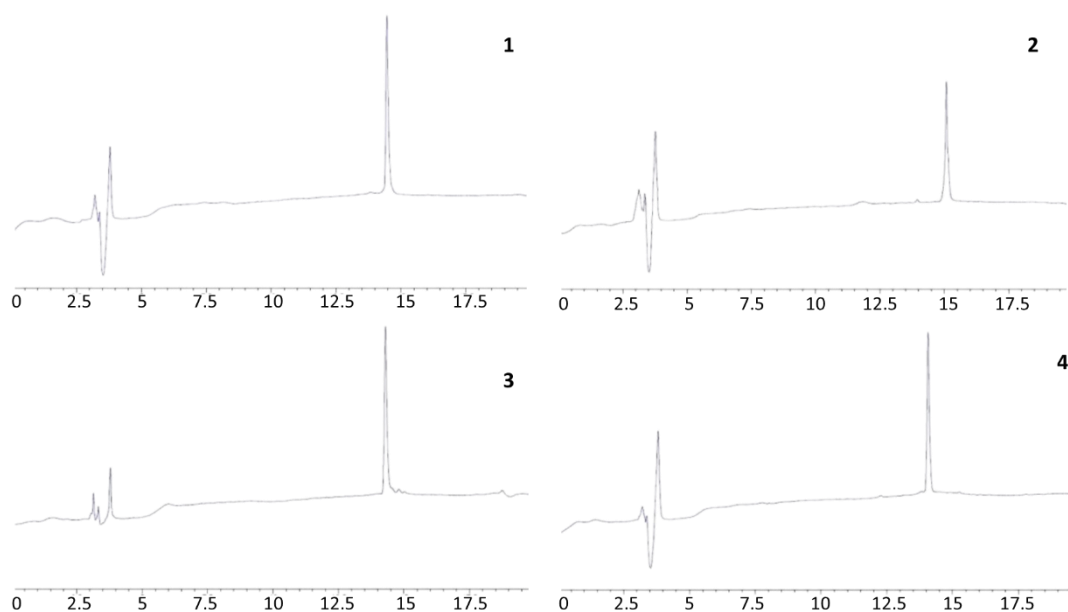
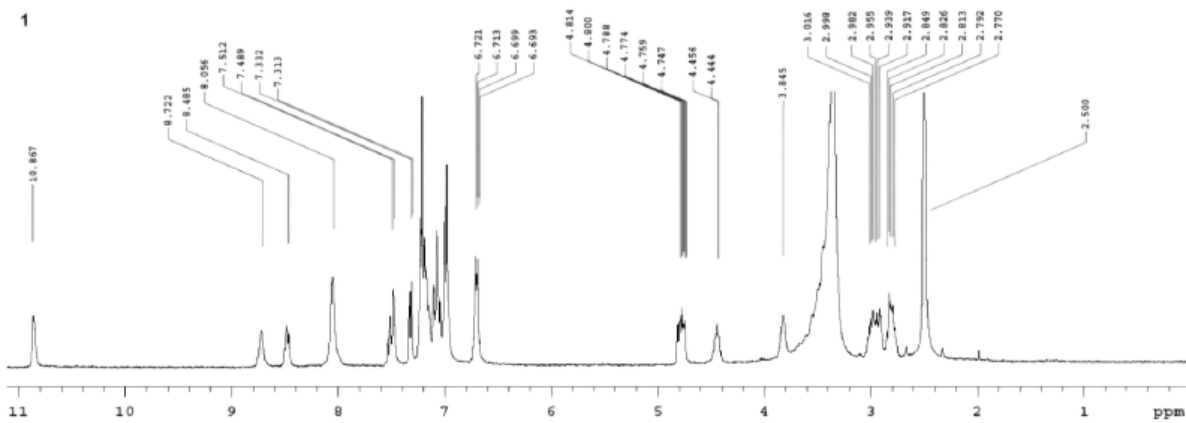
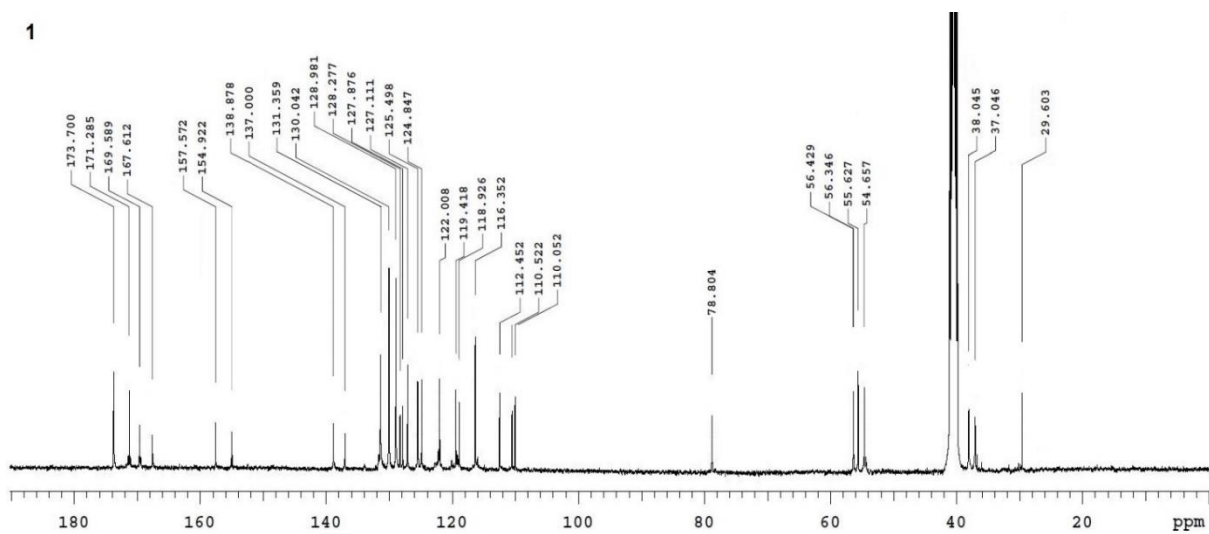


Figure 6. RP HPLC traces of the target compounds **1-4**, obtained using a RP column Phenomenex mod. Gemini 3 μ C18 110 Å 100 3 3.0 μ m, particle size 3 μ m, pore size 110 Å, length 100 mm, internal diameter 3 mm; DAD 210; mobile phase from 9:1 H₂O/CH₃CN/0.1% TFA, to 2:8 H₂O/CH₃CN/0.1% TFA, in 20 min at a flow rate of 0.5 mL min⁻¹.

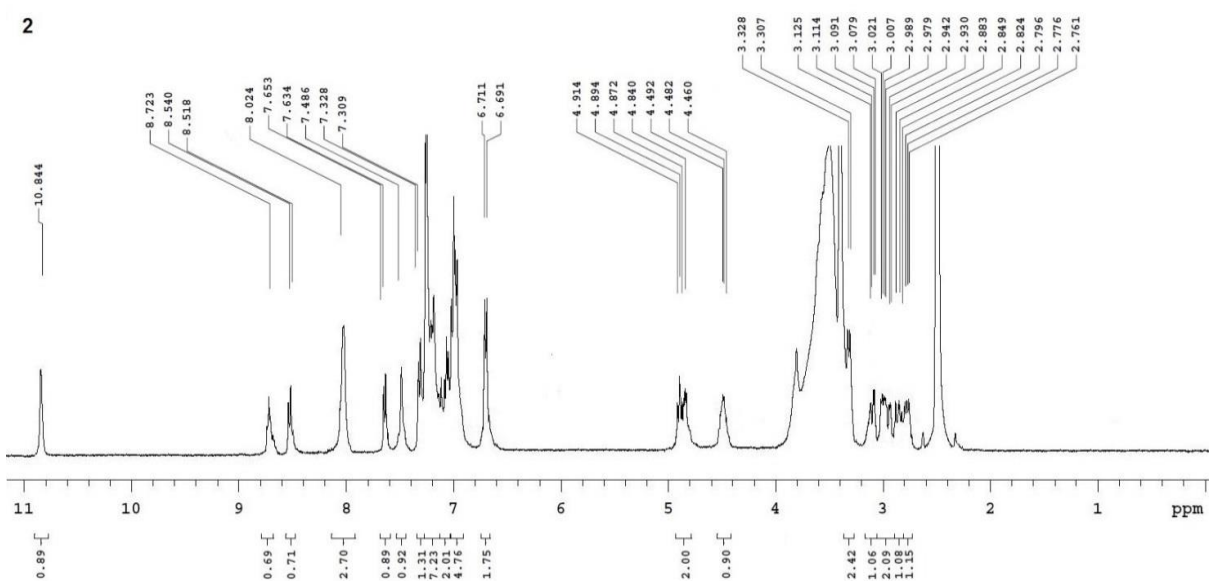
NMR spectra



^1H NMR of H-Tyr-Amo-Trp-PheNH₂ (1).

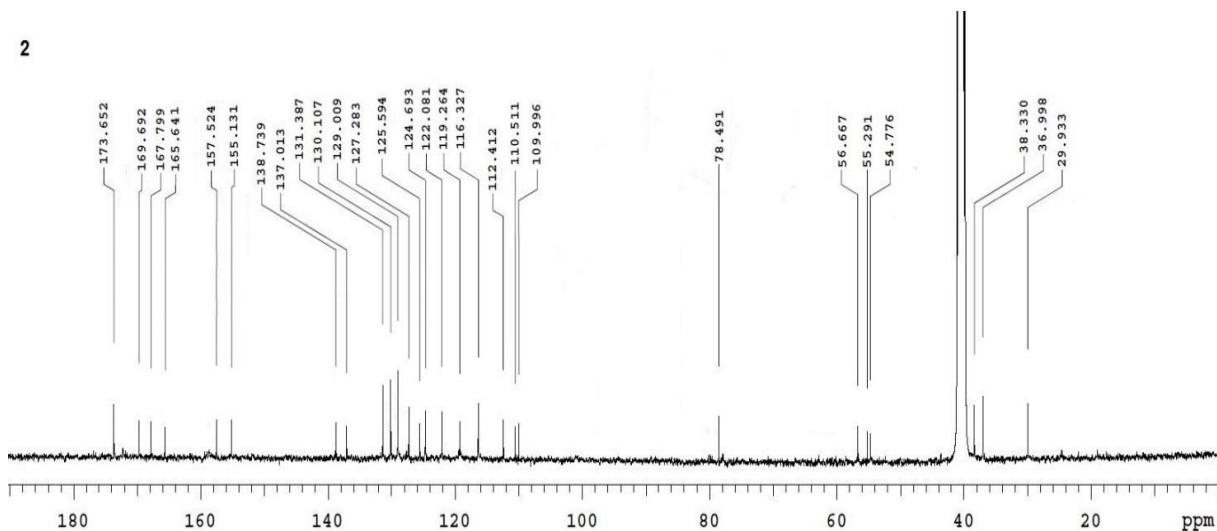


^{13}C NMR of H-Tyr-Amo-Trp-PheNH₂ (1).



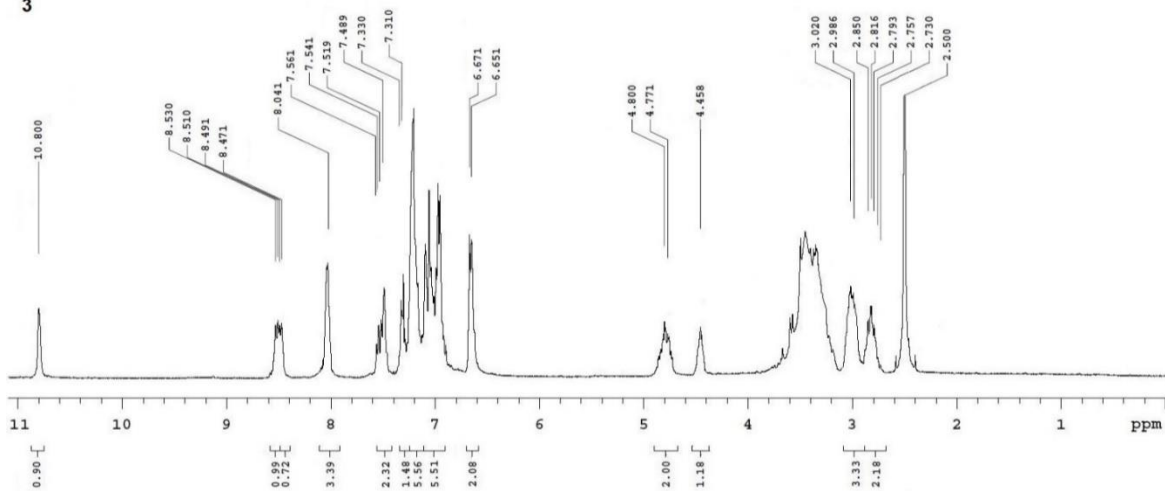
^1H NMR of H-Tyr-Amo-(R)-Trp-PheNH₂ (2).

2



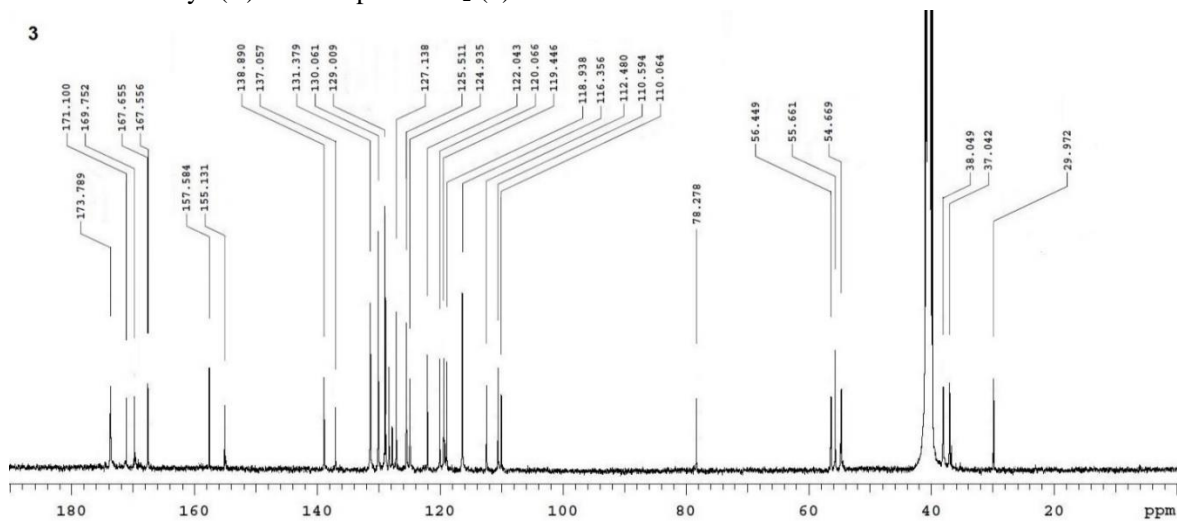
¹³C NMR of H-Tyr-Amo-(R)-Trp-PheNH₂ (2).

3

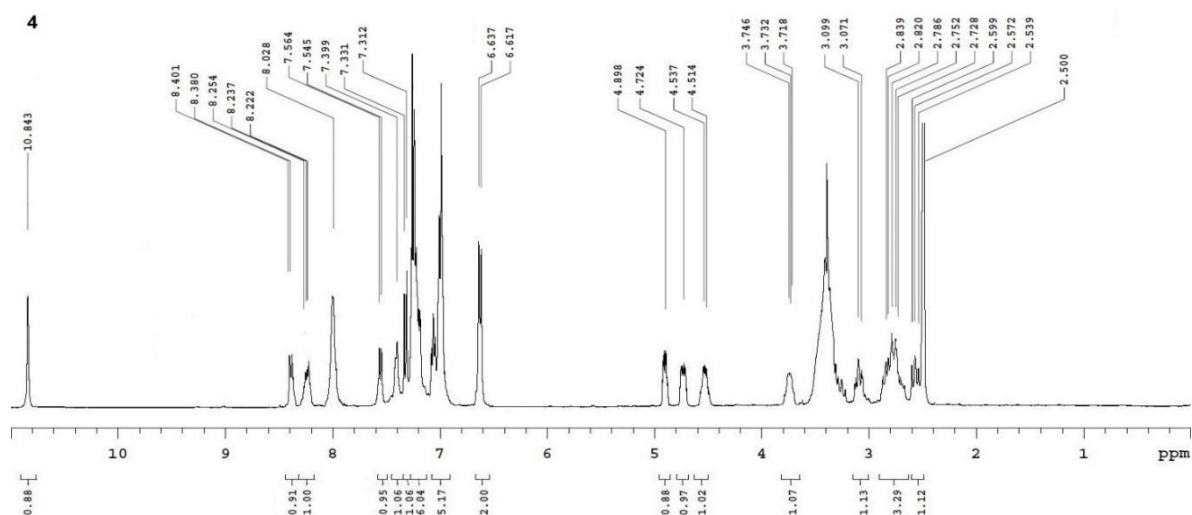


¹H NMR of H-Tyr-(R)-Amo-Trp-PheNH₂ (3).

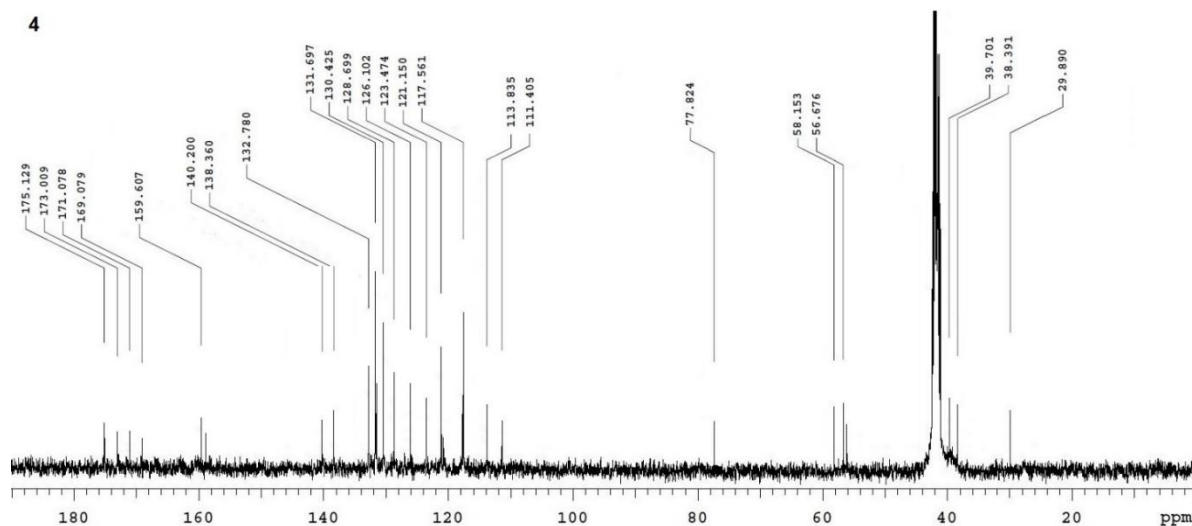
3



¹³C NMR of H-Tyr-(R)-Amo-Trp-PheNH₂ (3).



^1H NMR of H-Tyr-(R)-Amo-(R)-Trp-PheNH₂ (4).



^{13}C NMR of H-Tyr-(R)-Amo-(R)-Trp-PheNH₂ (4).

Figure 7. ^1H NMR and ^{13}C NMR of **1-4** in 8:2 [D₆]DMSO/H₂O; the TyrOH peaks are suppressed due to water presaturation.

4.4 General Methods of Biological Procedures

Biological reagents, disposables, cells, etc. were obtained from commercial sources. Cell culture media, phosphate-buffered saline (PBS) and fetal bovine serum (FBS): Lonza; black 96-well clear-bottom plates: Corning Costar; HEK-293 cells: ATCC, USA; plasmids from UMR cDNA Research Center, USA; pcDNA3.1(+) vector: Invitrogen; cAMP EIA kit: Cayman Chemical Co. Ann Arbor, MI, U.S.; minimum essential medium (MEM): Sigma, Steinheim, Germany; EXGEN 500: Fermentas, Hanover, MD, USA; nonessential amino acids: Invitrogen; geneticin: Invitrogen; mouse serum: Sigma-Aldrich.

4.5 Receptor Binding to Cloned Human OR.

The displacement binding assays were performed in HEK-293 cells stably expressing human MOR, DOR, or KOR, obtained as previously reported.^[47] In brief, HEK-293 cells stably expressing human ORs were generated with EXGEN500 by transfection with cDNAs cloned into the pcDNA3.1(+) vector. Stable transfectants were selected by exposure to G418 (500 mg mL⁻¹) for four weeks and then seeded in normal

MEM to perform binding assays. Cells expressing ORs were grown as a monolayer culture in tissue culture flasks that were incubated at 37°C in a humidified atmosphere (5% CO₂) in MEM containing 2 mM L-glutamine, 1 × nonessential amino acids and supplemented with 10% fetal calf serum, and maintained in the presence of 500 mg mL⁻¹ geneticin. Cells were washed with ice-cold PBS, pH 7.4; scraped into an ice-cold buffer containing 10 mM HEPES/NaOH, pH 7.4 and 1 mM EDTA; and lysed with a Dounce tissue grinder. The cell lysate was centrifuged at 1000 g for 2 min at 4°C. The supernatant was collected and centrifuged at 32000 g for 20 min at 4°C. The pellet was re-suspended in homogenization buffer at a protein concentration (determined by BCA assay) of 1.0 to 1.5 mg mL⁻¹ and stored in aliquots at -80°C. Cell surface human ORs were measured by saturation binding assays, using [³H]DAMGO as MOR-specific radioligand, while [³H]diprenorphine was utilized to label DOR, and [³H]U69,593 to label KOR. The concentrations of [³H]DAMGO ranged from 0.1 to 5.0 nM, [³H]diprenorphine was used in the range 40 pM to 3 nM, and [³H]U69,593 ranged from 20 pM to 5 nM. Nonspecific MOR binding was determined in the presence of naloxone (30 μM), nonspecific DOR binding with DPDPE (10 μM), and nonspecific KOR binding with U50,488 (10 μM). No any specific radioligand binding was detectable in HEK-293 cells transfected with an empty pcDNA3.1 plasmid (data not shown). For displacement binding assays, HEK-293 cells expressing human receptors were incubated at rt for 2 h in buffer containing 100 mM Tris-HCl and 0.3% BSA, with the specific radioligand at the appropriate concentration, i.e. [³H]DAMGO 2.5 nM, [³H]diprenorphine 1 nM, [³H]U69,593 2 nM, in the presence or absence of compounds at various concentrations (10⁻¹²-10⁻⁴ M). Compounds were prepared as stock solutions (10⁻² M) in EtOH and protected from light; compound dilutions were made in assay buffer. Nonspecific MOR binding was determined in the presence of naloxone (30 μM), nonspecific DOR binding with DPDPE (10 μM), and nonspecific KOR binding with U50,488 (10 μM). Triplicate determinations were made for each experiment. Reactions were terminated by filtration through Whatman GF/C filters presoaked with 0.3% polyethylenimine, which were washed three times with 5 mL of ice-cold buffer containing 50 mM Tris-HCl, pH 7.4. The radioactivity trapped was determined by liquid scintillation spectrometry. Data from at least three independent experiments were fitted by nonlinear regression analysis using GraphPad Prism. *K_i* values were calculated from the IC₅₀ using the Cheng-Prusoff equation. IC₅₀ values represent mean values from no less than four experiments. IC₅₀ values, relative potency estimates, and their associated standard errors were determined by fitting the data to the Hill equation by a computerized nonlinear least squares method. The reference compounds DAMGO (H-Tyr-D-Ala-Gly-NMePhe-Glyol), [¹⁴⁸] DPDPE (H-Tyr-c[D-Pen-Gly-Phe-D-Pen]-OH), [¹⁴⁹] and non-peptide U50,488, [¹⁵⁰] showed *K_i* values in the nM range and high selectivity to the respective receptors, as expected.

4.6 Enzymatic Stability.

The enzymatic stability of **1** and **4** was estimated by incubation in mouse serum for 4 h. During this period, samples of the incubation mixture were withdrawn and analyzed to check peptide hydrolysis. These assays were carried out in triplicate and repeated three times. To set the experiments, 10 μL aliquots of 10 mM peptide stock solution in Tris buffer pH 7.4 were added to 190 μL of mouse serum at 37°C. Aliquots of 20 mL were withdrawn from the incubation mixtures and enzyme activity was terminated by precipitating proteins with 90 mL of glacial acetonitrile. Samples were then diluted with 90 mL of 0.5% AcOH to prevent further enzymatic activity and centrifuged at 13000×g for 15 min. The supernatants were collected and the stability of peptide was determined by RP HPLC analysis.

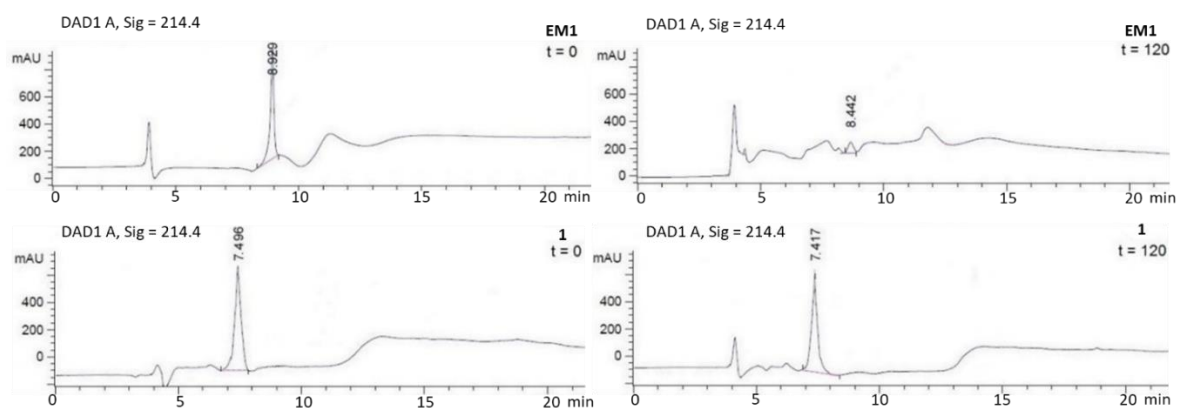


Figure 8. Incubation of EM1 and **1** in mouse serum, representative RP HPLC at t (min) = 0 and 120 min, stationary phase RP C18 column, particle size 3 μm , pore size 110 \AA , length 100 mm, internal diameter 3 mm; DAD 214; mobile phase from 9:1 $\text{H}_2\text{O}/\text{CH}_3\text{CN}/0.1\%$ TFA, to $\text{CH}_3\text{CN}/0.1\%$ TFA, in 10 min at a flow rate of 0.2 mL min^{-1} . Peak areas for EM1: t = 0, 5587.7; t = 120, 613.5; for **1**: t = 0, 8006.5, t = 120, 7365.9.

4.7 Determination of Inhibition of cAMP Accumulation for **1** and **4**.

The agonist activity of **1** and **4** was determined by measuring the inhibition of forskolin-stimulated cAMP accumulation in whole HEK-293 cells stably expressing KOR or MOR, respectively. Cells were grown at 37°C and 5% CO_2 in MEM, 2 mM Gln, and $1\times$ nonessential amino acids supplemented with 10% FBS. Samples in a 75 cm^2 flask at 95-100% confluence were split into 24 wells and incubated overnight. When the confluence became 85-95%, the medium was removed and the cells were washed three times with PBS; thereafter, cells were incubated in serum-free medium containing 0.5 mM 3-isobutyl-1-methylxanthine and exposed for 15 min to 10 μM forskolin without and with each compound (0.001 nM to 100 μM) at 37°C . Alternatively, HEK-293/hKOR cells were exposed to the reference KOR agonist U50,488 (0.001 nM to 100 μM) with or without 1 μM **1**. Cells were then lysed in 0.1 N HCl, scraped off, and centrifuged (2000 g, 5 min). Supernatants were assayed for cAMP concentration by using a cAMP EIA kit according to the manufacturer's instructions. The reference compounds inhibited forskolin-induced cAMP accumulation, with IC_{50} values in the nM range, in agreement to the literature.^[51]

Compounds **1-4** have been examined for known classes of assay interference compounds, as recommended in the Guidelines for Authors 2018.^[52]

Table 2. Inhibitory effects of **1** on forskolin-induced cAMP formation in HEK-293/hKOR, and of **4** in HEK-293/hMOR.

Compd	Cells/OR	IC_{50} (nM) ^[a]	E_{max} (% vehicle) ^[a]
U50,488	HEK-293/hKOR	1.2 ± 0.2	90 ± 5
1	HEK-293/hKOR	0.22 ± 0.2	40 ± 10
DAMGO	HEK-293/hMOR	1.5 ± 0.2	95 ± 5
4	HEK-293/hMOR	0.016 ± 0.004	50 ± 10

[a] Mean \pm SE of 5-6 independent experiments performed in triplicate.

4.8 Warm-Water Tail-Immersion Test.

Adult male CD-1 mice (Charles River, Calco, Como, Italy) weighing 25-30 g were used. They were housed in a light- and temperature-controlled room (light on 08.00–20.00 h, temperature 24°C) and had free access to food and water. This research was conducted in compliance with the guidelines of the Directive 2010/63/EU revising Directive 86/609/EEC on the protection of animals used for scientific

purpose. The procedures employed in this study were approved by the Animal Care and Use Committee of the University of Bologna (Prot. n. 29-IX/9, 25th July 2012) and conformed to the International Association for the Study of Pain (IASP) guidelines on ethical standards for investigations of experimental pain in animals.

The tail immersion test was performed as previously described.^[53] Mouse's tail was immersed in hot water (52 ± 0.5 °C) and the latency to withdrawal was measured as an indicator of pain perception. Prior to being treated, each mouse was tested and the latency to tail flick was recorded (control latency, CL). Animals not flicking their tails within 5 s were not used. Responding animals were then ip injected with either vehicle or **1** (10 or 20 mg/kg), with or without the KOR selective antagonist norBNI (10 mg/kg; 30 min prior than **1**). For ip injections, the compounds were dissolved in a 1:1 v/v solution of propylene glycol and saline (vehicle) and injected in a volume of 0.1 ml/10 g body weight. Latency to withdrawal was measured at 5, 15, 30, 45, and 60 min after drug administration and defined as the test latency (TL), with a cutoff point of 10 s. The antinociceptive response was expressed as the percentage of MPE = $100 \times (TL - CL)/(10 - CL)$.

4.9 Conformational Analysis.

2D ROESY experiments were performed in [D₆]DMSO/H₂O (8:2), in the phase-sensitive mode at r.t., spin-locking field (γb_2) was 2000 Hz, and mixing time was set to 250 ms; spectra were processed in the hypercomplex approach; peaks were calibrated on DMSO. Cross-peak intensities were classified as very strong, strong, medium, and weak and were associated with distances of 2.3, 2.7, 3.3, and 5.0 Å, respectively, utilized as constraints in the MD simulations.^[54] For the absence of $H\alpha(i)-H\alpha(i+1)$ cross-peaks, the ω bonds were set at 180° (f constant: 16 kcal mol⁻¹ Å⁻²). The restrained MD was conducted using the AMBER force field in a 30 Å³ box of TIP3P models of equilibrated water. Random structures were subjected to a 50 ps restrained MD with a 50% scaled force field at 1200 K, followed by 50 ps with full restraints, after which the system was cooled in 20 ps to 50 K. The resulting structures were minimized, and backbones were clustered by the rmsd analysis. Unrestrained MD simulations were conducted for 10 ns at 298 K using periodic boundary conditions.

4.10 Molecular Docking (MDK) for **1** and hKOR (PDB ID: 6B73).

The restrained MD simulations were conducted at 300 K and 1 atm by using the AMBER force field^[55] in a 30 Å × 30 Å × 30 Å box of standard TIP3P models of equilibrated water.^[56] Periodic boundary conditions were applied, a constant dielectric scale factor of 1 was used, and the cutoff distance for the nonbonded interactions was 12 Å. All water molecules with atoms that come closer than 2.3 Å to a solute atom were eliminated. A 100 ps simulation at 1200 K was used for generating 50 random structures that were subsequently subjected to a 50 ps restrained MD with a 50% scaled force field at the same temperature, followed by 50 ps with full restraints (distance force constant of 7 kcalmol⁻¹Å⁻²), after which the system was cooled in 20 ps to 50 K. Hydrogen-bond interactions were not included, nor were torsion angle restraints. The resulting structures were minimized with 3000 cycles of steepest descent and 3000 cycles of conjugated gradient (convergence of 0.01 kcal Å⁻¹mol⁻¹). The backbones of the structures were clustered by the rmsd analysis.^[54]

Table 3. Non-obvious REOSY cross peaks for H-Tyr-Amo-Trp-PheNH₂ (**1**) in 8:2 [D₆]DMSO/H₂O; vs = very strong, s = strong, m = medium, w = weak.

Cross peak	Intensity	Cross peak	Intensity	Cross peak	Intensity
AmoNH-TyrNH	s	PheArH-TyrArH2,4	w	PheNH-PheHβ _(2,8)	m

AmoNH-TyrArH3,5	w	PheArH-AmoH β _(3,4)	m	TyrNH-AmoH α	m
AmoNH-PheH α	w	TrpArH2-TrpH α	s	TyrNH-AmoH β _(3,3)	w
AmoNH-AmoH β _(3,4)	s	TyrArH3,5-TyrH α	s	CONH _{2(7,5)} -TrpArH2	w
AmoNH-TrpH β	w	AmoH α -TyrH α	w	CONH _{2(7,5)} -PheH α	m
AmoNH-TyrH β _(2,8)	w	AmoH α -AmoH β _(3,3)	s	CONH _{2(7,5)} -PheH β _(3,0)	w
PheNH-CONH _{2(7,3)}	m	AmoH α -TyrH β _(2,8)	w	TrpArH4-AmoH α	m
PheNH-TrpArH2	w	TrpH α -PheH β _(2,8)	w	CONH _{2(7,3)} -PheArH	m
PheNH-PheH α	m	PheH α -AmoH β _(3,4)	w	CONH _{2(7,3)} -TrpH α	w
PheNH-AmoH β _(3,3)	w	PheH α -TrpH β	m	CONH _{2(7,3)} -TrpH β	m
PheNH-PheH β _(3,0)	m	TyrH α -AmoH β _(3,3)	w	CONH _{2(7,3)} -PheH β _(2,8)	w
TyrNH-TyrArH3,5	s	AmoNH-TrpH4	w	PheArH-PheH α	m
TyrNH-AmoH β _(3,4)	w	AmoNH-AmoH α	m	PheArH-AmoH β _(3,3)	m
CONH _{2(7,5)} -PheArH	m	AmoNH-TyrH α	vs	TrpArH2-AmoH α	w
CONH _{2(7,5)} -TrpH α	w	AmoNH-AmoH β _(3,3)	s	AmoH α -TrpH α	m
CONH _{2(7,5)} -TrpH β	w	AmoNH-TyrH β _(3,0)	w	AmoH α -AmoH β _(3,4)	s
CONH _{2(7,5)} -PheH β _(2,8)	w	PheNH- CONH _{2(7,5)}	m	AmoH α -TyrH β _(3,0)	w
TrpArH4-TrpH α	m	PheNH-PheArH	m	TrpH α -PheH α	w
CONH _{2(7,3)} -TrpArH2	w	PheNH-TrpH α	vs	PheH α -TyrH α	w
CONH _{2(7,3)} -PheH α	vs	PheNH-AmoH β _(3,4)	w	PheH α -AmoH β _(3,3)	w
CONH _{2(7,3)} -PheH β _(3,0)	w	PheNH-TrpH β	w	TyrH α -AmoH β _(3,4)	w

Table 4. Non-obvious REOSY cross peaks for H-Tyr-Amo-(*R*)-Trp-PheNH₂ (**2**) in 8:2 [D₆]DMSO/H₂O; vs = very strong, s = strong, m = medium, w = weak.

Cross peak	Inten -sity	Cross peak	Inten -sity	Cross peak	Inten -sity
AmoNH-TyrNH	s	(<i>R</i>)-TrpArH2-PheH α	w	TyrNH-AmoH α	w
AmoNH-TyrArH3,5	w	TyrArH2,4-TyrH α	m	(<i>R</i>)-TrpArH4-PheArH	w
AmoNH-AmoH α	m	(<i>R</i>)-TrpH α -PheH α	w	(<i>R</i>)-TrpArH4-(<i>R</i>)-TrpH α	m
AmoNH-AmoH β _(3,6)	m	(<i>R</i>)-TrpH α -PheH β _(2,8)	w	(<i>R</i>)-TrpArH4-TyrH α	w
AmoNH-AmoH β _(3,0)	s	AmoH α -AmoH β _(3,0)	s	CONH _{2(7,5)} -PheH α	m

AmoNH-TyrH β _(2,8)	m	PheH α -PheH β _(2,8)	s	CONH _{2(7,5)} -PheH β _(2,8)	m
PheNH-PheArH	m	TyrH α -AmoH β _(3,0)	w	PheArH-(<i>R</i>)-TrpArH5	w
PheNH-(<i>R</i>)-TrpH α	s	TyrH α -TyrH β _(2,8)	s	TyrArH3,5-TyrH α	s
PheNH-PheH α	m	AmoH β _(3,6) -TyrH β _(2,8)	w	(<i>R</i>)-TrpArH5-TyrH α	w
PheNH-PheH β _(3,1)	m	AmoH β _(3,0) -TyrH β _(2,8)	w	(<i>R</i>)-TrpArH2-(<i>R</i>)-TrpH α	m
TyrNH-(<i>R</i>)-TrpArH4	w	AmoNH-(<i>R</i>)-TrpArH4	w	(<i>R</i>)-TrpArH2-TyrH α	w
TyrNH-(<i>R</i>)-TrpArH2	w	AmoNH-(<i>R</i>)-TrpArH2	w	(<i>R</i>)-TrpH α -AmoH α	w
TyrNH-AmoH β _(3,6)	w	AmoNH-TyrH α	vs	(<i>R</i>)-TrpH α -AmoH β _(3,0)	w
(<i>R</i>)-TrpArH4-TyrArH2,4	w	AmoNH-(<i>R</i>)-TrpH β	m	AmoH α -AmoH β _(3,6)	s
(<i>R</i>)-TrpArH4-PheH α	w	AmoNH-TyrH β _(3,0)	m	PheH α -PheH β _(3,1)	m
CONH _{2(7,5)} -PheArH	m	PheNH-CONH _{2(7,5)}	w	TyrH α -AmoH β _(3,6)	w
CONH _{2(7,5)} -PheH β _(3,1)	m	PheNH-(<i>R</i>)-TrpArH2	w	TyrH α -TyrH β _(3,0)	s
PheArH-(<i>R</i>)-TrpArH6	w	PheNH-AmoH α	m	AmoH β _(3,6) -TyrH β _(3,0)	w
PheArH-PheH α	s	PheNH-(<i>R</i>)-TrpH β	w	AmoH β _(3,0) -TyrH β _(3,0)	w
(<i>R</i>)-TrpArH5-TyrArH2,4	w	PheNH-PheH β _(2,8)	m		
(<i>R</i>)-TrpArH2-TyrArH2,4	w	TyrNH-TyrArH3,5	s		

Table 5. Non-obvious REOSY cross peaks for H-Tyr-(*R*)-Amo-Trp-PheNH₂ (**3**) in 8:2 [D₆]DMSO/H₂O; vs = very strong, s = strong, m = medium, w = weak.

Cross peak	Inten -sity	Cross peak	Inten -sity	Cross peak	Inten -sity
(<i>R</i>)-AmoNH-TyrNH	m	TrpArH2-(<i>R</i>)-AmoH β _(3,2)	m	TrpArH4-TrpH β _(3,2)	s
(<i>R</i>)-AmoNH-TyrArH3,5	w	TyrArH3,5-TyrH α	s	CONH _{2(7,5)} -TyrArH2,4	w
(<i>R</i>)-AmoNH-TyrH α	s	(<i>R</i>)-AmoH α -TyrH α	w	CONH _{2(7,5)} -PheH β _(2,9)	m
(<i>R</i>)-AmoNH-(<i>R</i>)-AmoH β _(2,8)	m	(<i>R</i>)-AmoH α -(<i>R</i>)-AmoH β _(2,8)	m	PheArH-TyrArH2,4	w
PheNH-PheArH	m	(<i>R</i>)-AmoH α -TyrH β _(2,7)	m	PheArH-PheH α	m
PheNH-(<i>R</i>)-AmoH α	w	TrpH α -TrpH β _(3,5)	m	CONH _{2(7,2)} -PheH α	s
PheNH-PheH α	m	PheH α -PheH β _(2,9)	s	CONH _{2(7,2)} -PheH β _(2,9)	m
PheNH-PheH β _(2,9)	m	TyrH α -(<i>R</i>)-AmoH β _(3,5)	w	TrpArH2-TyrArH3,5	w
TyrNH-TyrArH3,5	s	TyrH α -TyrH β _(2,7)	s	TrpArH2-TyrH α	w

TrpArH4-CONH _{2(7.2)}	w	(<i>R</i>)-AmoHβ _(3.5) -TyrHβ _(2.7)	w	TrpArH2-TrpHβ _(3.2)	m
TrpArH4-TrpHβ _(3.5)	s	(<i>R</i>)-AmoNH-TrpH2	m	TyrArH3,5-(<i>R</i>)-AmoHα	w
CONH _{2(7.5)} -PheArH	m	(<i>R</i>)-AmoNH-(<i>R</i>)-AmoHα	m	TyrArH2,4-TrpHβ _(3.5)	w
CONH _{2(7.5)} -PheHα	m	(<i>R</i>)-AmoNH-(<i>R</i>)-AmoHβ _(3.5)	s	(<i>R</i>)-AmoHα-(<i>R</i>)-AmoHβ _(3.5)	s
CONH _{2(7.5)} -PheHβ _(2.7)	w	PheNH-CONH _{2(7.5)}	w	(<i>R</i>)-AmoHα-TyrHβ _(2.8)	m
PheArH-(<i>R</i>)-AmoHα	w	PheNH-CONH _{2(7.2)}	m	TrpHα-PheHα	w
CONH _{2(7.2)} -TrpHα	w	PheNH-TrpHα	s	TrpHα-TrpHβ _(3.2)	s
CONH _{2(7.2)} -TrpHβ _(3.2)	m	PheNH-TrpHβ _(3.2)	w	PheHα-PheHβ _(2.7)	s
CONH _{2(7.2)} -PheHβ _(2.7)	m	PheNH-PheHβ _(2.7)	m	TyrHα-TyrHβ _(2.8)	s
TrpArH2-TrpHα	m	TyrNH-(<i>R</i>)-AmoHβ _(3.5)	w	(<i>R</i>)-AmoHβ _(3.5) -TyrHβ _(2.8)	w
TrpArH2-TrpHβ _(3.5)	s	TrpArH4-TrpHα	s		

Table 6. Non-obvious REOSY cross peaks for H-Tyr-(*R*)-Amo-(*R*)-Trp-PheNH₂ (**4**) in 8:2 [D₆]DMSO/H₂O; vs = very strong, s = strong, m = medium, w = weak.

Cross peak	Inten -sity	Cross peak	Inten -sity	Cross peak	Inten -sity
(<i>R</i>)-AmoNH-TyrNH	m	(<i>R</i>)-TrpArH5-TyrHβ _(2.8)	w	TyrNH-(<i>R</i>)-AmoHβ _(3.7)	w
(<i>R</i>)-AmoNH-TyrArH3,5	w	(<i>R</i>)-AmoHα-(<i>R</i>)-AmoHβ _(3.7)	s	(<i>R</i>)-TrpArH4-(<i>R</i>)-AmoHα	m
(<i>R</i>)-AmoNH-TyrHα	s	(<i>R</i>)-AmoHα-TyrHβ _(3.0)	w	(<i>R</i>)-TrpArH4-TyrHβ _(2.8)	w
(<i>R</i>)-AmoNH-(<i>R</i>)-AmoHβ _(3.4)	s	(<i>R</i>)-TrpHα-PheHα	w	CONH _{2(7.4)} -PheHα	m
(<i>R</i>)-AmoNH-TyrHβ _(2.8)	w	PheHα-(<i>R</i>)-TrpHβ	w	CONH _{2(7.4)} -PheHβ _(3.0)	m
PheNH-CONH _{2(7.2)}	w	PheHα-PheHβ _(2.8)	s	CONH _{2(7.2)} -PheArH	s
PheNH-(<i>R</i>)-TrpHα	s	TyrHα-(<i>R</i>)-AmoHβ _(3.4)	w	CONH _{2(7.2)} -PheHβ _(3.0)	m
PheNH-(<i>R</i>)-AmoHβ _(3.4)	m	TyrHα-TyrHβ _(2.8)	m	PheArH-(<i>R</i>)-TrpHα	w
PheNH-PheHβ _(2.8)	m	(<i>R</i>)-AmoHβ _(3.7) -TyrHβ _(2.8)	w	TyrArH3,5-(<i>R</i>)-AmoHα	w
TyrNH-(<i>R</i>)-AmoHα	w	(<i>R</i>)-AmoHβ _(3.4) -TyrHβ _(2.8)	w	(<i>R</i>)-TrpArH2-(<i>R</i>)-TrpHα	s
(<i>R</i>)-TrpArH4-TyrArH2,4	w	(<i>R</i>)-AmoNH-(<i>R</i>)-TrpArH4	w	(<i>R</i>)-AmoHα-TyrHα	w
(<i>R</i>)-TrpArH4-(<i>R</i>)-TrpHα	m	(<i>R</i>)-AmoNH-(<i>R</i>)-AmoHα	m	(<i>R</i>)-AmoHα-(<i>R</i>)-AmoHβ _(3.4)	m
CONH _{2(7.4)} -PheArH	m	(<i>R</i>)-AmoNH-(<i>R</i>)-AmoHβ _(3.7)	m	(<i>R</i>)-AmoHα-TyrHβ _(2.8)	w
CONH _{2(7.4)} -(<i>R</i>)-AmoHβ _(3.4)	w	(<i>R</i>)-AmoNH-TyrHβ _(3.0)	w	(<i>R</i>)-TrpHα-PheHβ _(2.8)	w

CONH ₂ (7.4)-PheH β (2.8)	w	PheNH-CONH ₂ (7.4)	w	PheH α -PheH β (3.0)	s
CONH ₂ (7.2)-PheH α	s	PheNH-PheArH	m	TyrH α -(R)-AmoH β (3.7)	m
CONH ₂ (7.2)-PheH β (2.8)	m	PheNH-PheH α	m	TyrH α -TyrH β (3.0)	m
PheArH-PheH α	m	PheNH-PheH β (3.0)	m	(R)-AmoH β (3.7)-TyrH β (3.0)	w
TyrArH3,5-TyrH α	m	TyrNH-TyrArH3,5	m	(R)-AmoH β (3.4)-TyrH β (3.0)	w

Unrestrained MD simulations^[54] were performed starting with the conformation derived from ROESY in a 30 Å × 30 Å × 30 Å box of standard TIP3P water for 10 ns at 298 K using periodic boundary conditions, at constant temperature and pressure (Berendsen scheme,^[57] bath relaxation constant of 0.2). For 1-4 scale factors, van der Waals and electrostatic interactions are scaled in AMBER to half their nominal value. The integration time step was set to 0.1 fs. The system coordinates were collected every picosecond.

Molecular Docking of KOR-1 complex. The in-solution conformation of **1** was refined using a systematic conformer search followed by geometry optimization of the lowest energy structure with MOPAC7 (PM3 Method, RMS gradient 0.0100). The crystal structure for hKOR (PDB ID: 6B73) was retrieved from the Protein Data Bank^[58] and prepared for docking calculation by eliminating hetero atoms and water molecules. MDK experiments were performed with Autodock 4.0. We used the Lamarckian Genetic Algorithm which combines global search (Genetic Algorithm alone) to local search (Solis and Wets algorithm). Ligands and receptors were further processed using the Autodock Tool Kit (ADT). Gasteiger-Marsili charges were loaded on the ligands in ADT and solvation parameters were added to the final structure using the Addsol utility of Autodock. Each docking consisted of an initial population of 100 randomly placed individuals, a maximum number of 200 energy evaluations, a mutation rate of 0.02, a crossover rate of 0.80, and an elitism value of 1. For the local search, the so-called pseudo-Solis and Wets algorithm was applied using a maximum of 250 iterations per local search. 250 independent docking runs were carried out for the ligand **1**. The grid maps representing the system in the actual docking process were calculated with Autogrid. The dimensions of the grids were 126 × 126 × 126, with a spacing of 0.153 Å between the grid points and the center close to the cavity left by the ligand after its removal. The simpler inter-molecular energy function based on the Weiner force field in Autodock was used to score the MDK results. In all MDK runs, residues within a radius of 5.0 Å from the center of the hKOR binding site were allowed to be flexible. Results differing by less than 1.0 Å in positional root-mean-square deviation (rmsd) were clustered together and were represented by the result with the most favorable free energy of binding.

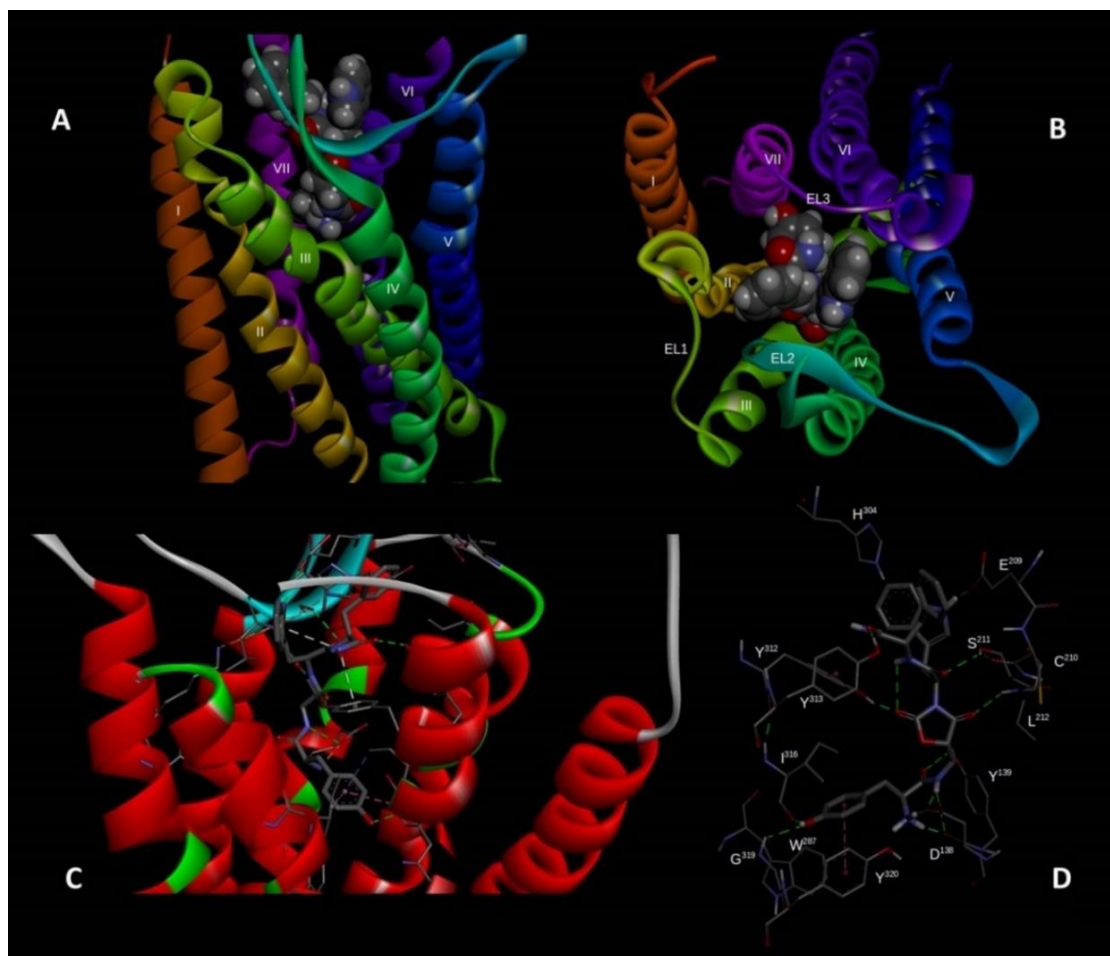


Figure 9. Views of the complex KOR (PDB ID: 4DJH)-1. A Side and B top views, showing the receptor rendered as solid ribbon, while the peptide is rendered in CPK, with the spheres sized to the van der Waals radii. C Side view showing the receptor rendered as solid ribbon, and the peptide in sticks; residues relevant to the interactions are also shown. D Side/rear view of the interactions of **1** with KOR represented as dashed lines: H-bonds in green, salt bridges in orange, and π - π interactions in violet. KOR residues are rendered in line, and indicated by their one-letter code, while **1** is rendered in stick.

Energy minimizations and molecular modeling calculations were performed by using the CUDA® version of the GROMACS package and the AMBER-03 force field, a variant of the AMBER-99 potential in which charges and main-chain torsion potentials have been derived based on QM+continuum solvent calculations and each amino acid is allowed unique main-chain charges. To perform molecular dynamics (MD) simulations, the best Autodock result was considered as the initial conformation. A distance of 1 nm was set between a cubic box of TIP3P water molecules and the solute and the final system was simulated for 1.0 ns to equilibrate at 300 K temp. and 1 bar pressure, respectively. Final simulation run was carried out for 10.0 ns with a time step of 2 fs under V-rescale temp. and Parrinello-Rahman pressure coupling algorithms. The particle-mesh Ewald (PME) algorithm was utilized to calculate long-range electrostatics, while Linear Constraint Solver (LINCS) method was used to constrain all covalent bond lengths. A 1.2 nm cutoff was set for van der Waals interactions.

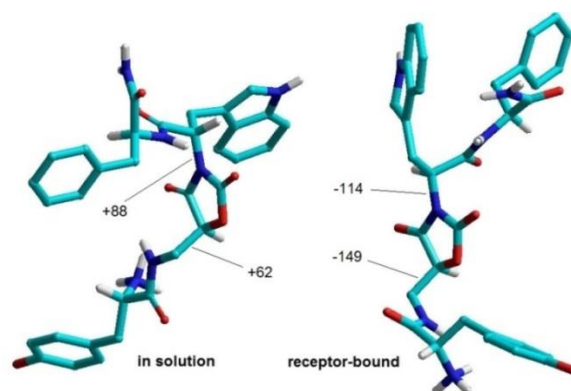


Figure 10. Comparison between the in -solution conformation of [Amo²]EMs **1** determined by ROESY and restrained MD, and the receptor-bound conformation determined by Molecular Docking; for clarity, only α and NH hydrogens are shown, along with relevant dihedral angles (in degrees).

The work described in this chapter has already been published in *Journal of Medicinal Chemistry* with slight modification and has been reproduced here with the permission of the copyright holder.

De Marco, Rossella; Bedini, Andrea; Spampinato, Santi*; Comellini, Lorenzo; **Zhao, Junwei**; Artali, Roberto; Gentilucci, Luca *. 2018. “Constraining endomorphin-1 by β , α -hybrid dipeptide/ heterocycle scaffolds: identification of a novel κ -opioid receptor selective partial agonist” *Journal of Medicinal Chemistry* 61, no. 13: 5751-5757. <https://doi.org/10.1021/acs.jmedchem.8b00296>.

References

1. Zadina, J. E.; Hackler, L.; Ge, L. J.; Kastin, A. J. A potent and selective endogenous agonist for the mu-opiate receptor. *Nature* **1997**, 386, 499-502.
2. Harrison, C.; McNulty, S.; Smart, D.; Rowbotham, D. J.; Grandy, D. K.; Devi, L. A.; Lambert, D. G. The effects of endomorphin-1 and endomorphin-2 in CHO cells expressing recombinant mu-opioid receptors and SH-SY5Y cells. *Br. J. Pharmacol.* **1999**, 128, 472-478.
3. Fichna, J.; Janecka, A.; Costentin, J.; Do Rego, J. C. The endomorphin system and its evolving neurophysiological role. *Pharmacol. Rev.* **2007**, 59, 88-123.
4. Aldrich, J. V.; McLaughlin, J. P. Opioid Peptides: Potential for drug development. *Drug Discov. Today Technol.* **2012**, 9, e23-e31.
5. Keresztes, A.; Borics, A.; Tóth, G. Recent advances in endomorphin engineering. *Chem. Med. Chem.* **2010**, 5, 1176-1196.
6. De Marco, R.; Janecka, A. Strategies to improve bioavailability and in vivo efficacy of the endogenous opioid peptides endomorphin-1 and endomorphin-2. *Curr. Top. Med. Chem.* **2015**, 16, 141-155
7. Varamini, P.; Tóth, I. Lipid- and sugar-modified endomorphins: novel targets for the treatment of neuropathic pain. *Front. Pharmacol.* **2013**, 4, 1-7.
8. Liu, W. X.; Wang, R. Endomorphins: potential roles and therapeutic indications in the development of opioid peptide analgesic drugs. *Med. Res. Rev.* **2012**, 32, 536-580.

-
9. Cardillo, G.; Gentilucci, L.; Melchiorre, P.; Spampinato, S. Synthesis and binding activity of endomorphin-1 analogues containing beta-amino acids. *Bioorg. Med. Chem. Lett.* **2000**, *10*, 2755-2758.
10. Cardillo, G.; Gentilucci, L.; Tolomelli, A.; Calienni, M.; Qasem, A. R.; Spampinato, S. Stability against enzymatic hydrolysis of endomorphin-1 analogues containing beta-proline. *Org. Biomol. Chem.* **2003**, *1*, 1498-1502.
11. Liu, X.; Wang, Y.; Xing, Y.; Yu, J.; Ji, H.; Kai, M.; Wang, Z.; Wang, D.; Zhang, Y.; Zhao, D.; Wang, R. Design, synthesis, and pharmacological characterization of novel endomorphin-1 analogues as extremely potent μ -opioid agonists. *J. Med. Chem.* **2013**, *56*, 3102-3114.
12. Perlikowska, R.; Pieklielna, J.; Mazur, M.; Koralewski R.; Olczak, J.; do Rego, J. C.; Fichna, J.; Modranka, J.; Janecki, T.; Janecka, A. Antinociceptive and antidepressant-like action of endomorphin-2 analogs with proline surrogates in position 2. *Bioorg. Med. Chem.* **2014**, *22*, 4803-4809.
13. Cardillo, G.; Gentilucci, L.; Qasem, A. R.; Sgarzi, F.; Spampinato, S. Endomorphin-1 analogues containing beta-proline are mu-opioid receptor agonists and display enhanced enzymatic hydrolysis resistance. *J. Med. Chem.* **2002**, *45*, 2571-2578.
14. Spampinato, S.; Qasem, A. R.; Calienni, M.; Murari, G.; Gentilucci, L.; Tolomelli, A.; Cardillo, G. Antinociception by a peripherally administered novel endomorphin-1 analogue containing beta-proline. *Eur. J. Pharmacol.* **2003**, *469*, 89-95.
15. Perlikowska, R.; Gach, K.; Fichna, J.; Tóth, G.; Walkowiak, B.; do-Rego, J. C.; Janecka, A. Biological activity of endomorphin and [Dmt1]endomorphin analogs with six-membered proline surrogates in position 2. *Bioorg. Med. Chem.* **2009**, *17*, 3789-3794.
16. Keresztes, A.; Szucs, M.; Borics, A.; Kövér, K. E.; Forró, E.; Fülöp, F.; Tömböly, C.; Péter, A.; Páhi, A.; Fábíán, G.; Murányi, M.; Tóth, G. New endomorphin analogues containing alicyclic beta-amino acids: influence on bioactive conformation and pharmacological profile. *J. Med. Chem.* **2008**, *51*, 4270-4279.
17. Borics, A.; Mallareddy, J. R.; Timári, I.; Kövér, K. E.; Keresztes, A.; Tóth, G. The effect of Pro(2) modifications on the structural and pharmacological properties of endomorphin-2. *J. Med. Chem.* **2012**, *55*, 8418-8428.
18. Mallareddy, J. R.; Borics, A.; Keresztes, A.; Kövér, K. E.; Tourwé, D.; Tóth, G. Design, synthesis, pharmacological evaluation, and structure-activity study of novel endomorphin analogues with multiple structural modifications. *J. Med. Chem.* **2011**, *54*, 1462-1472.
19. Harrison, B. A.; Gierasch, T. M.; Neilan, C.; Pasternak, G. W.; Verdine, G. L. High-affinity mu opioid receptor ligands discovered by the screening of an exhaustively stereodiversified library of 1,5-enediols. *J. Am. Chem. Soc.* **2002**, *124*, 13352-13353.
20. Keller, M.; Boissard, C.; Patiny, L.; Chung, N. N.; Lemieux, C.; Mutter, M.; Schiller, P. W. Pseudoproline-containing analogues of morphiceptin and endomorphin-2: evidence for a cis Tyr-Pro amide bond in the bioactive conformation. *J. Med. Chem.* **2001**, *44*, 3896-3903.
21. Cardillo, G.; Gentilucci, L.; Tolomelli, A.; Spinosa, R.; Calienni, M.; Qasem, A. R.; Spampinato S. Synthesis and evaluation of the affinity toward mu-opioid receptors of atypical, lipophilic ligands based on the sequence c[-Tyr-Pro-Trp-Phe-Gly-]. *J. Med. Chem.* **2004**, *47*, 5198-5203.
22. Perlikowska, R.; Pieklielna, J.; Gentilucci, L.; De Marco, R.; Cerlesi, M. C.; Calo, G.; Artali, R.; Tömböly, C.; Kluczyk, A.; Janecka, A. Synthesis of mixed MOR/KOR efficacy cyclic opioid peptide analogs with antinociceptive activity after systemic administration. *Eur. J. Med. Chem.* **2016**, *109*, 276-286.
23. Pulka, K.; Feytens, D.; Van den Eynde, I.; De Wachter, R.; Kosson, P.; Misicka, A.; Lipkowski, A.; Chung, N. N.; Schiller, P. W.; Tourwé, D. Synthesis of 4-amino-3-oxo-tetrahydroazepino[3,4-b] indoles: new conformationally constrained Trp analogs. *Tetrahedron* **2007**, *63*, 1459-1466.
24. Tömböly, C.; Ballet, S.; Feytens, D.; Kövér, K. E.; Borics, A.; Lovas, S.; Al-Khrasani, M.; Fürst, Z.; Tóth, G.; Benyhe,

-
- S.; Tourwé, D. Endomorphin-2 with a beta-turn backbone constraint retains the potent mu-opioid receptor agonist properties. *J. Med. Chem.* **2008**, *51*, 173-177.
25. Greco, A.; Tani, S.; De Marco, R.; Gentilucci, L. Synthesis and analysis of the conformational preferences of 5-aminomethyloxazolidine-2,4-dione scaffolds: First examples of $\beta(2)$ - and $\beta(2,2)$ -homo-freidinger lactam analogues. *Chem. Eur. J.* **2014**, *20*, 13390-13404.
26. Gentilucci, L.; Gallo, F.; Meloni, F.; Mastandrea, M.; Del Secco, B.; De Marco, R. Controlling cyclopeptide backbone conformation with β/α -hybrid peptide-heterocycle scaffolds. *Eur. J. Org. Chem.* **2016**, 3243-3251
27. Greco, A.; De Marco, R.; Tani, S.; Giacomini, D.; Galletti, P.; Tolomelli, A.; Juaristi, E.; Gentilucci, L. Controlling cyclopeptide backbone conformation with β/α -hybrid peptide-heterocycle scaffolds. *Eur. J. Org. Chem.* **2014**, *34*, 7614-7620.
28. De Marco, R.; Mazzotti, G.; Dattoli, S.D.; Baiula, M.; Spampinato, S.; Greco, A.; Gentilucci, L. 5-Aminomethyloxazolidine-2,4-dione hybrid α/β -dipeptide scaffolds as inductors of constrained conformations: applications to the synthesis of integrin antagonists. *Biopolymers* **2015**, *104*, 636-649.
29. Bedini, A.; Baiula, M.; Gentilucci, L.; Tolomelli, A.; De Marco, R.; Spampinato, S. Peripheral antinociceptive effects of the cyclic endomorphin-1 analog c[YpwFG] in a mouse visceral pain model. *Peptides* **2010**, *31*, 2135-2140.
30. Liu, H.; Zhang, B.; Liu, X.; Wang, C.; Ni, J.; Wang, R. Endomorphin 1 analogs with enhanced metabolic stability and systemic analgesic activity: design, synthesis, and pharmacological characterization. *Bioorg. Med. Chem.* **2007**, *15*, 1694-1702.
31. Kivell, B.; Prisinzano, T.E. Kappa opioids and the modulation of pain. *Psychopharmacology* **2010**, *210*, 109-119
32. Butelman, E.R.; Yuferov, V.; Kreek, M.J. κ -opioid receptor/dynorphin system: genetic and pharmacotherapeutic implications for addiction. *Trends Neurosci.* **2012**, *35*, 587-596.
33. Paton, K.F.; Kumar, N.; Crowley, R.S.; Harper, J.L.; Prisinzano, T.E.; Kivell, B.M. The analgesic and anti-inflammatory effects of Salvinorin A analogue β -tetrahydropyran Salvinorin B in mice. *Eur. J. Pain* **2017**, *21*, 1039-1050.
34. Bidlack, J.M.; McLaughlin, J.P.; Wentland, M.P. Partial opioids. Medications for the treatment of pain and drug abuse. *Ann. N. Y. Acad. Sci.* **2000**, *909*, 1-11
35. Carlezon, W.A. Jr.; Béguin, C.; Knoll, A.T.; Cohen, B. M. Kappa-opioid ligands in the study and treatment of mood disorders. *Pharmacol. Ther.* **2009**, *123*, 334-343.
36. Mann, K.; Torup, L.; Sørensen, P.; Gual, A.; Swift, R.; Walker, B.; van den Brink, W. Nalmefene for the management of alcohol dependence: review on its pharmacology, mechanism of action and meta-analysis on its clinical efficacy. *Eur. Neuropsychopharmacol.* **2016**, *26*, 1941-1949.
37. Aldrich, J.V.; Patkar, K.A.; McLaughlin, J.P. Zyklophin, a systemically active selective kappa opioid receptor peptide antagonist with short duration of action. *Proc. Natl. Acad. Sci. USA* **2009**, *106*, 18396-18401.
38. Urbano, M.; Guerrero, M.; Rosen, H.; Roberts, E. Antagonists of the kappa opioid receptor. *Bioorg. Med. Chem. Lett.* **2014**, *24*, 2021-2032.
39. Temussi, P.A.; Picone, D.; Saviano, G.; Amodeo, P.; Motta, A.; Tancredi, T.; Salvadori, S.; Tomatis, R. Conformational analysis of an opioid peptide in solvent media that mimic cytoplasm viscosity. *Biopolymers* **1992**, *32*, 367-372.
40. Borics, A.; Tóth, G. Structural comparison of mu-opioid receptor selective peptides confirmed four parameters of bioactivity. *J. Mol. Graphics Modell.* **2010**, *28*, 495-505.
41. Che, T.; Majumdar, S.; Zaidi, S.A.; Ondachi, P.; McCorvy, J.D.; Wang, S.; Mosier, P.D.; Uprety, R.; Vardy, E.; Krumm, B.E.; Han, G.W.; Lee, M.Y.; Pardon, E.; Steyaert, J.; Huang, X.P.; Strachan, R.T.; Tribo, A.R.; Pasternak, G.W.;

-
- Carroll, F.I.; Stevens, R.C.; Cherezov, V.; Katritch, V.; Wacker, D.; Roth, B.L. Structure of the nanobody-stabilized active state of the kappa opioid receptor. *Cell* **2018**, *172*, 55-67.
42. Wu, H.; Wacker, D.; Mileni, M.; Katritch, V.; Han, G.W.; Vardy, E.; Liu, W.; Thompson, A.A.; Huang, X.-P.; Carroll, F.I.; Mascarella, S.W.; Westkaemper, R.B.; Mosier, P.D.; Roth, B.L.; Cherezov, V.; Stevens, R.C. Structure of the human κ -opioid receptor in complex with JD1c. *Nature* **2012**, *485*, 327-332.
43. Vardy, E.; Mosier, P.D.; Frankowski, K.J.; Wu, H.; Katritch, V.; Westkaemper, R.B.; Aubé, J.; Stevens, R.C.; Roth, B.L. Chemotype-selective modes of action of κ -opioid receptor agonists. *J. Biol. Chem.* **2013**, *288*, 34470-34483.
44. O'Connor, C.; White, K.L.; Doncescu, N.; Didenko, T.; Roth, B.L.; Czaplinski, G.; Stevens, R. C.; Wüthrich, K.; Milon, A. NMR structure and dynamics of the agonist dynorphin peptide bound to the human kappa opioid receptor. *Proc. Natl. Acad. Sci. USA*, **2015**, *112*, 11852-11857.
45. Brust, A.; Croker, D.E.; Colless, B.; Ragnarsson, L.; Andersson, Å.; Jain, K.; Garcia-Caraballo, S.; Castro, J.; Brierley, S.M.; Alewood, P.F.; Lewis, R.J. Conopeptide-derived κ opioid agonists (Conorphins): potent, selective, and metabolically stable dynorphin A mimetics with antinociceptive properties. *J. Med. Chem.* **2016**, *59*, 2381-2395.
46. Przydział, M.J.; Pogozheva, I.D.; Bosse, K.E.; Andrews, S.M.; Tharp, T.A.; Traynor, J.R.; Mosberg, H.I. Roles of residues 3 and 4 in cyclic tetrapeptide ligand recognition by the kappa-opioid receptor. *J. Pept. Res.* **2005**, *65*, 333-342.
47. De Marco, R.; Bedini, A.; Spampinato, S.; Gentilucci, L. Synthesis of tripeptides containing D-Trp substituted at the indole ring, assessment of opioid receptor binding and in vivo central antinociception. *J. Med. Chem.* **2014**, *57*, 6861-6866.
48. Harrison, C.; McNulty, S.; Smart, D.; Rowbotham, D.J.; Grandy, D.K.; Devi, L.A.; Lambert, D.G. The effects of endomorphin-1 and endomorphin-2 in CHO cells expressing recombinant μ -opioid receptors and SH-SY5Y cells. *Br. J. Pharmacol.* **1999**, *128*, 472-478.
49. Schmidt, H.; Vormfelde, S.; Klinder, K.; Gundert-Remy, U.; Gleiter, C.H.; Skopp, G.; Aderjan, R.; Fuhr, U. Affinities of dihydrocodeine and its metabolites to opioid receptors. *Pharmacol. Toxicol.* **2002**, *91*, 57-63.
50. Clark, J.A.; Pasternak, G.W. U50,488: a kappa-selective agent with poor affinity for μ 1 opiate binding sites. *Neuropharm.* **1988**, *27*, 331-332.
51. Gong, J.; Strong, J.A.; Zhang, S.; Yue, X.; DeHaven, R.N.; Daubert, J.D.; Cassel, J.A.; Yu, G.; Mansson, E.; Yu, L. Endomorphins fully activate a cloned human mu opioid receptor. *FEBS Lett.* **1998**, *439*, 152-126.
52. Aldrich, C.; Bertozzi, C.; Georg, G.I.; Kiessling, L.; Lindsley, C.; Liotta, D.; Merz, K.M. Jr.; Schepartz, A.; Wang, S. The ecstasy and agony of assay interference compounds. *J. Med. Chem.* **2017**, *60*, 2165-2168.
53. Bedini, A.; Baiula, M.; Gentilucci, L.; Tolomelli, A.; De Marco, R.; Spampinato, S. Peripheral antinociceptive effects of the cyclic endomorphin-1 analog c[YpwFG] in a mouse visceral pain model. *Peptides* **2010**, *31*, 2135-2140.
54. HyperChem, Release 8.0.3, Hypercube Inc., 1115 NW 4th St. Gainesville, FL 32608, USA, 2007.
55. Cornell, W.D.; Cieplak, P.; Bayly, C.I.; Gould, I.R.; Merz, K.M.; Ferguson, D.M.; Spellmeyer, D.C.; Fox, T.; Caldwell, J.W.; Kollman, P.A. A second generation force field for the simulation of proteins, nucleic acids, and organic molecules. *J. Am. Chem. Soc.* **1995**, *117*, 5179-5197.
56. Jorgensen, W.L.; Chandrasekhar, J.; Madura, J.; Impey, R.W.; Klein, M.L. Comparison of simple potential functions for simulating liquid water. *J. Chem. Phys.* **1983**, *79*, 926-935.
57. Berendsen, H.J.C.; Postma, J.P.M.; van Gunsteren, W.F.; Di Nola, A.; Haak, J.R. Molecular dynamics with coupling to an external bath. *J. Chem. Phys.* **1984**, *81*, 3684-3690.
- 58 <https://www.rcsb.org/pdb/home/home.do>

Chapter 4. Synthesis of new selective high-affinity analogs of CJ-15,208 for screening kappa opioid receptor agonists/antagonists

Opioid receptor agonists were widely used as analgesics, especially for severe pain caused by cancer. Most opioid analgesics are ligands for mu opioid receptors (MOR), but these analgesics have some non-negligible side effects on patients, such as addiction, respiratory depression, hyperalgesia, and other adverse effects. Herein, in order to decrease the adverse side effects, we synthesized a minilibrary of cyclic peptides/peptidomimetics based on the modification of the structure of cyclic tetrapeptide CJ-15,208, aiming at finding selective agonists or antagonists for kappa opioid receptors (KOR). Among these compounds, compound RDM1127 has a high affinity for KOR ($K_i = 0.55 \pm 0.04$ nM). After further investigation of the inhibition of forskolin-induced cAMP accumulation in HEK-293/hKOR cells and U87-MG cells, it was found that RDM1127 is an antagonist of KOR. On the other hand, compound RDM1135 is a partial agonist of KOR ($K_i = 102 \pm 3$ nM). Conformational analyses of the cyclopeptides by NMR and molecular dynamics confirmed that these structures can be regarded as 3D distinct scaffolds for specifically targeting each of the opioid receptor.

1. Introduction

As a member of the G protein-coupled receptor family, opioid receptors (ORs) can be classified into four major subtypes, delta opioid receptor (DOR), kappa opioid receptor (KOR), mu opioid receptor (MOR), and nociceptin/orphanin FQ receptor (NOR).^[1] Besides those subtypes, there is another subtype, the zeta opioid receptor (ZOR), also known as the opioid growth factor receptor (OGFr), is different from other ORs in protein sequence similarity and functions^[2]. ORs agonists, partial agonists, and antagonists not only play an important role in the study of analgesia^[3], but also have a great potential in the research of anti-inflammatory^[4], mood disorders^[5], cardiovascular disease^[6], brain function and diseases^[7], cancers^[8], etc. According to synthetic methods, opioid analgesics can also be divided into alkaloids, semi-synthetic compounds and synthetic compounds.^[9]

MOR agonists are the most potent and widely used analgesics. Although their adverse side effects, such as addiction, tolerance, physical dependence, respiratory depression, hyperalgesia, euphoria and constipation, limit their clinical applications, MOR agonists are still an indispensable and effective strategy for developing opioid analgesics.^[10] In recent years, with the in-depth research on KOR agonists, due to low addiction and relatively minimal adverse effects compared to MOR agonists, they have great potential in developing opioid analgesics.^[11] Agonist activation of KOR can induce analgesia and can also prevent hyperalgesia caused by chronic use of therapeutic agents targeting MOR.^[12,13] However, there is no report about the use of KOR agonists for the treatment of human pain so far.^[14]

ORs antagonists were usually used to reverse opioid receptor agonist effects. Most widely used ORs antagonists are naloxone, naltrexone, nalmefene, and methylnaltrexone. As an ORs antagonist, naloxone has high affinity for MOR ($K_D = 3.9$ nM), KOR ($K_D = 16$ nM), and DOR ($K_D = 95$ nM);^[15] naltrexone is a nonselective opioid receptor antagonist,^[16] and nalmefene is a MOR antagonist and a partial KOR agonist;^[17] methylnaltrexone is a peripherally restricted MOR antagonist.^[18] ORs antagonists were commonly used for reversal and treatment of opioid overdose, opioid and alcohol use disorders, opioid-induced respiratory depression, opioid-related constipation, hyperalgesia and euphoria. On the

other hand, KOR antagonists can be used to treat stress-related disorders, such as stress, anxiety and depression.^[19]

The cyclic tetrapeptide CJ-15,208 (c[Phe¹-D-Pro²-Phe³-Trp⁴]) was isolated by Saito and coworkers from the fermentation broth of the fungus *Ctenomyces serratus* ATCC15502 in 2002.^[20] CJ-15,208 was a mixed KOR/MOR ligand: IC₅₀ KOR 47 nM, MOR 260 nM, DOR 2,600 nM. In the electrically-stimulated twitch response assay of rabbit *vas deferens* it recovered the suppression by a KOR agonist asimadoline with an ED₅₀ of 1.3 μM, indicating that it is a KOR antagonist.^[20] In 2009, Dolle et al.^[21] found that replacing Trp⁴ with (D)-Trp in the CJ-15,208 sequence increased the affinity for the KOR (K_i = 30 nM) and the MOR (K_i = 3.8 nM), c[Phe¹-D-Pro²-D-Phe³-Trp⁴] was a dual κ/μ opioid receptor antagonist. And the further substitution of Phe¹ with Ala did not change much receptor binding behavior, c[Ala¹-D-Pro²-D-Phe³-Trp⁴] was still a κ/μ antagonists with high affinity for KOR (K_i = 5.2 nM), and MOR (K_i = 22.9 nM). In 2014, Aldrich et al.^[22] investigated Ala analogues of [D-Trp]CJ-15,208, and observed the same results. On the contrary, if Phe³ was substituted with Ala, the affinity for ORs will be over 1000 nM, which means Phe¹ is less sensitive to aromatic substitution than Phe³. This observation was further confirmed and described by Aldrich et al. in 2011.^[23] In 2016, novel derivatives of cyclic tetrapeptide CJ-15,208 were synthesized and characterized in our group. And we also developed a strategy to regulate the selectivity and functional properties of the ligand for the three major opioid receptors.^[24] Among those derivatives, we found that if Phe¹ was changed to β-Alanine or γ-Aminobutyric acid (GABA), they will become of μ (K_i = 4.09 nM) or δ (K_i = 3.08 nM) selective opioid receptors agonists, respectively.

Recently, we have synthesized LOR17 (c[Phe-Gly-(β-Ala)-D-Trp]),^[25] which was a selective KOR agonist with nanomolar affinity for KOR (K_i = 1.19 nM). As we expected, in *in vivo* study of LOR17, there is no any alteration of motor coordination, spontaneous and exploratory activities, or anhedonia-related behavior was found. And based on the inspiration of compound LOR17 and CJ-15,208 derivatives described above, we introduced more flexible or rigid motifs in the structure of LOR17 to find more ORs agonists or antagonists.

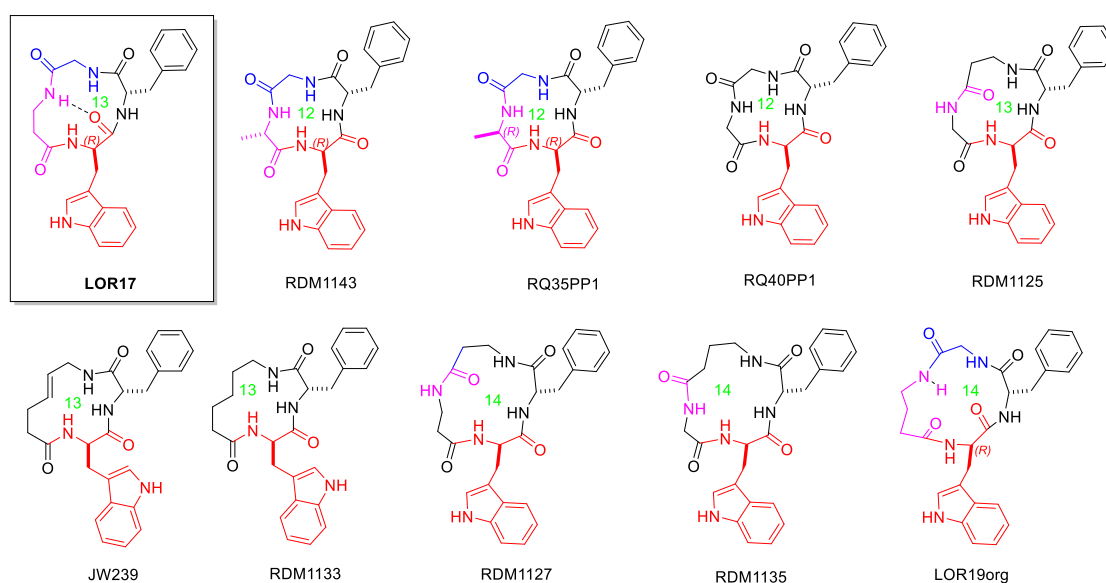
2. Results and Discussion

2.1 Synthesis of Cyclic Peptide/Peptidomimetic Minilibrary

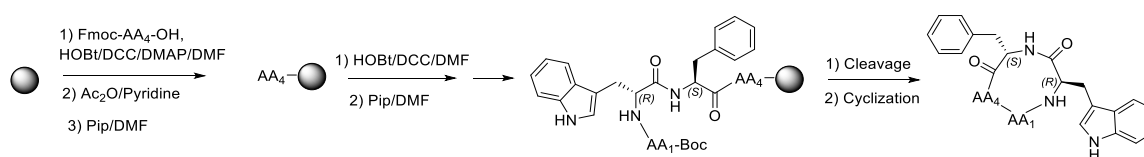
In this work, a minilibrary of cyclic peptides/peptidomimetics of CJ-15,208 analogues was prepared, as shown in Scheme 1, they include RDM1125 c[Gly-D-Trp-Phe-βAla], RDM1127 c[β-Ala¹-D-Trp-Phe-βAla⁴], JW239 c[ε-AHEA-D-Trp-Phe] (AHEA = 6-aminohept-4-enoic acid), RDM1133 c[ε-AHEA-D-Trp-Phe], RDM1135 c[Gly-D-Trp-Phe-GABA], RQ35PP1 c[D-Ala-D-Trp-Phe-Gly], RQ40PP1 c[Gly¹-D-Trp-Phe-Gly⁴], RDM11439 c[Phe-Gly-Ala-D-Trp] and LOR19org c[Phe-Gly-GABA-D-Trp]. The general synthesis procedure were described in experimental section. Peptides/peptidomimetics RDM1143, LOR19org, RDM1125, RDM1127, JW239, RDM1133 and RDM1135 were prepared on solid phase (Scheme 2). Amino acids preloaded rink amide resin was coupled with natural or unnatural amino acids in sequence according to typical Fmoc SPPS procedure. Besides other Fmoc protected amino acids Fmoc-AA-OH (Fmoc = 9H-fluoren-9-ylmethoxycarbonyl, AA = amino acid), the last amino acid to be coupled was Boc protected amino acid Boc-AA-OH, since Boc group will be removed in the cleavage cocktail and the obtained linear peptides can be directly cyclized after solvents removal and ether washing.

On the other hand, the preparations of RQ35PP1 and RQ40PP1 were accomplished in solution (Scheme 3). During the preparation, firstly, the first amino acid at C-terminus in sequence was protected with methyl on carboxyl group to give amino acid methyl ester, and followed by sequentially coupling with the Boc protected amino acids, in thimbleful of DMF (dimethylformamide) and in the presence of the mixture of HOBt (1-hydroxybenzotriazole), EDCI (1-ethyl-3-(3-dimethylaminopropyl)carbodiimide hydrochloride) and TEA (triethylamine). Before cyclization, the LiOH solution was utilized to remove methyl ester, followed by Boc deprotection in 25% TFA (trifluoroacetate) in DCM.

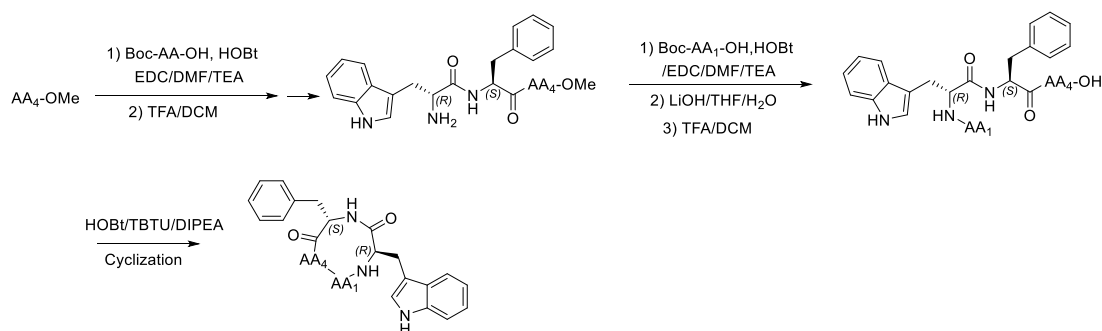
For cyclization, the DMF solution of linear peptides were added dropwise within 16 hours through a syringe pump into the mixture of HOBt/ TBTU / DIPEA (N,N-diisopropylethylamine) in DMF. The obtained cyclic peptides precipitated during work-up procedure, and it was purified by washing with cold EA (ethyl acetate), MeCN (acetonitrile) and H₂O in sequence. After washing, the most of peptides were over 95% pure. However, the purity of some peptides was still less than 95% and was further purified by preparative HPLC. Different from other obtained cyclic peptides, cyclic tetrapeptides and cyclic octopeptides were found during the cyclization of RDM1123. The appearance of octopeptides was due to the dimerization of the tetrapeptides. They were separated and purified by preparative HPLC. Final compounds were analyzed by HPLC-MS, ¹H NMR, ¹³C NMR, Variable temperature NMR, and ¹H-¹H COSY spectroscopy.



Scheme 1. Molecular structures of novel CJ-15,208 analogs

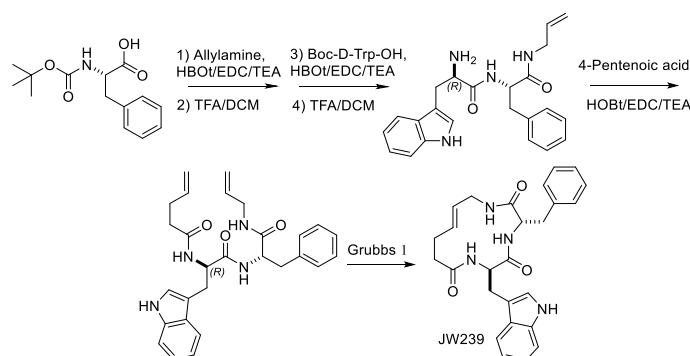


Scheme 2. SPPS of the linear tetra-peptides, and cyclization of linear tetra-peptides in solution.



Scheme 3. Synthesis of the cyclic tetra-peptides in solution.

Based on the study of our previously synthesized peptide LOR 17, we found that the aromatic groups of Phe and D-Trp act as two pharmacophores, and the third pharmacophore should be the amide bond formed by the amino group of the first amino acid and carboxyl group of the fourth amino acid. In order to mimic the third pharmacophore, a carbon-carbon double bond was introduced to mimic the amide bond, thus the peptidomimetic JW239 was prepared via ring-closing metathesis (RCM). The preparation of JW239 followed SPPS procedure, together with Phe³ and D-Trp², allylamine and 4-pentenoic were coupled sequentially as the last and first blocks of peptidomimetic. The RCM reaction was performed by using Grubbs 1 as catalyst in anhydrous DCM (Scheme 4). The obtained cyclic peptidomimetic JW239 was purified by flash chromatography, and was analyzed by HPLC-MS, ¹H NMR, ¹³C NMR, Variable temperature NMR, and ¹H-¹H COSY spectroscopy.



Scheme 4. Synthesis procedure of JW239

According to the $\Delta\delta/\Delta T$ values from variable temperature (VT) NMR (Table 1), it was found that there are hydrogen (H) bonds in the structure of some cyclic peptides/peptidomimetics. Namely, Gly in fourth position of RDM1123EA2, Phe in third position of RDM1125, Gly in fourth position of RQ40PP1 may have hydrogen bond ($|\Delta\delta/\Delta T| \leq 2.1$ ppb/K in [D₆]DMSO, DMSO = dimethylsulfoxide).

Table 1. Variable temperature NMR for analysis of hydrogen bond between NH groups and Carbonyl groups.

Compound ($\Delta\delta/\Delta T$)	Sequence	HN1	HN2	HN3	HN4
LOR17	c[Phe-Gly- β Ala-D-Trp]	-6.2	-3.6	-2.1	-3.2
RDM1123EA2	c[Gly ¹ -D-Trp-Phe-Gly ⁴] ₂	-2.2	-3.0	-6.3	-1.5
RDM1125	c[Gly-D-Trp-Phe- β Ala]	-3.7	-4.4	-2.1	-3.2

RDM1127	c[β Ala ¹ -D-Trp-Phe- β Ala ⁴]	-3.9	-5.9	-8.0	a
JW239	c[ϵ -AHEA-D-Trp-Phe]	-3.4	-7.0	-9.7	/
RDM1135(major)	c[Gly-D-Trp-Phe-GABA]	-3.8	-3.7	-3.0	-3.7
RDM1135(minor)	c[Gly-D-Trp-Phe-GABA]	-3.1	-5.6	-7.8	a
RQ35PP1	c[D-Ala-D-Trp-Phe-Gly]	-4.8	-4.0	-7.9	-3.2
RQ40PP1	c[Gly ¹ -D-Trp-Phe-Gly ⁴]	-2.9	-3.2	-6.3	-2.1
RDM1143	c[Phe-Gly-Ala-D-Trp]	-5.0	-4.1	-4.5	-3.5
LOR19org	c[Phe-Gly-GABA-D-Trp]	-8.7	-3.7	-2.7	-3.8

a The fourth NH group of peptides can not be distinguish from other signals.

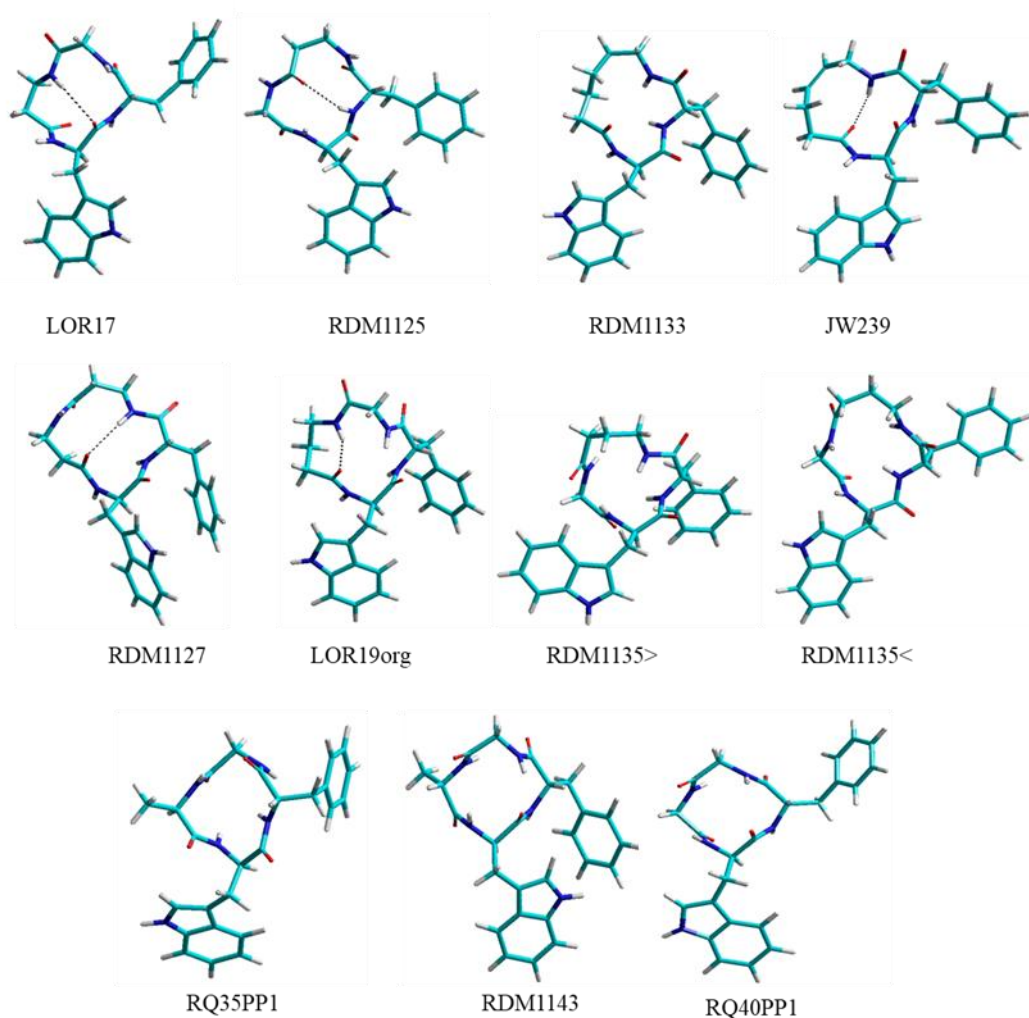


Figure 1. Representative conformers of peptides/peptidomimetics of CJ-15,208 analogs determined by ROESY-restrained calculation. Dotted lines indicate intramolecular hydrogen bonds.

All compounds were analyzed by 2D-ROESY in 8:2 [D₆]DMSO/H₂O, where the concentration of peptides/peptidomimetics was 0.01M. Then the intensities of the cross peaks obtained in 2D-ROESY spectrum were sorted to infer the possible distance between protons. Simulated annealing and restricted molecular dynamics simulations were used to analyze the estimated distance, using the AMBER force field in explicit water as the solvent. The representative conformers with the lowest energy were shown

in Figure 1.

From dynamics simulations, among these compounds, possible intramolecular hydrogen bonds could be observed in LOR17, RDM1125, JW239, RDM1127, and LOR19org. Similar to our previously synthesized peptide LOR17, peptides JW239 and RDM1125 had a restricted structure inside the ring and an extended structure outside the ring. No intramolecular hydrogen bonds were found in 12-membered cyclic peptides. Among them, RQ35PP1 and RQ40PP1 had more extended structures, while the structure of RDM1143 had more folded and rigid conformation. Due to the introduction of a flexible structure into the peptide ring, it was found that RDM1133, as a 13-membered cyclic peptide, has an extended backbone structure both inside and outside the ring. Comparing with other compounds, RDM1127 had a more folded and rigid conformational structure. From the analysis of the NMR spectrum, two isomers were found in peptide RDM1135. And from dynamics simulations, the conformational structure of the main isomer was more likely to be folded and rigid, but the backbone structure of the minor isomer was more expanded. In both of these two isomers, no possibility of forming hydrogen bonds was found.

2.2 Biological Assays in Cells

2.2.1 Binding Affinity of New Analogs to KOR.

HEK-293 cells stably expressing cloned human (h) KOR were utilized to study the affinity of the prepared cyclic peptides/peptidomimetics to the opioid κ receptor. In this procedure, radioligand [^3H]U69,593 was used to label KOR, then former was subsequently substituted by cyclic peptides/peptidomimetics by competition. The non-peptide compound U50,488 was used as a reference, it has nM level affinity for KOR ($K_i = 2.9 \pm 0.04$ nM, as shown in Table 2), and is highly selective for KOR. As showed in Table 2, compound RDM1127 shows sub-nM affinity to KOR ($K_i = 0.55 \pm 0.04$ nM), on the other hand, RDM1135 shows a moderate affinity to KOR ($K_i = 102 \pm 3$ nM).

Table 2. Competitive binding assay in HEK-293/hKOR Cells

Compound	Sequence	K_i KOR (nM)
U50,488	Not peptide	2.90 ± 0.04
LOR17	c[β Ala-D-Trp-Phe-Gly]	1.19 ± 0.28
RDM1125	c[Gly-D-Trp-Phe- β Ala]	$>10^5$
RDM1127	c[β Ala-D-Trp-Phe- β Ala]	0.55 ± 0.04
RDM1133	c[ϵ -AHEA-D-Trp-Phe]	$>10^5$
RDM1135	c[Gly-D-Trp-Phe-GABA]	102 ± 3
RDM1143	c[Ala-D-Trp-Phe-Gly]	$>10^5$
JW239	c[ϵ -AHAA-D-Trp-Phe]	$>10^5$
LOR19org	c[GABA-D-Trp-Phe-Gly]	$>10^5$
RQ35PP1	c[D-Ala-D-Trp-Phe-Gly]	$>10^5$
RQ40PP1	c[Gly-D-Trp-Phe-Gly]	$>10^5$

2.2.2 Determination of Inhibition of cAMP Accumulation.

The assay of inhibition of forskolin-induced cAMP accumulation was performed in whole HEK-293/hKOR cells stably expressing KOR, and U87-MG human astrocytoma cells endogenously express hKOR. As show in Table 3, U50,488 and LOR17 were used as KOR reference compounds ^[26],

remarkably inhibited forskolin-induced cAMP accumulation, with IC_{50} values of 1.2 nM and 2.8 nM, and E_{max} (E_{max} = maximal obtainable effect/vehicle) of 90 and 85 in HEK-293/hKOR cells, respectively; with IC_{50} values of 1.4 nM and 3.1 nM, and E_{max} of 88 and 87 in U87-MG cells, respectively. RDM1135WP inhibited forskolin-induced cAMP accumulation with IC_{50} = 16.6 nM and E_{max} = 32% in HEK-293/hKOR cells, and with IC_{50} = 59.6 nM and E_{max} = 42% in U87-MG cells, suggestive of a partial agonist behavior, as compared to U50,488 (IC_{50} = 1.2 nM and E_{max} = 90% in HEK-293/hKOR cells, and IC_{50} = 1.4 nM and E_{max} = 88% in U87-MG cells; Table 3). However, RDM1127 did not show any inhibition effect either in HEK-293/hKOR cells or in U87-MG cells, which means it is not a KOR agonist. Interestingly, when 10 μ M RDM1127 was coadministered together with U50,488, IC_{50} = 1.7 nM and 44% inhibition of forskolin-induced cAMP accumulation was observed. Comparing with U50,488 alone, IC_{50} = 2.1 nM and 88% inhibition of forskolin-induced cAMP accumulation was observed, that means RDM1127 is a KOR antagonist (Table 4).

Table 3. Inhibition of forskolin-induced cAMP accumulation in HEK-293/hKOR and U87-MG cells

Compound	IC_{50} HEK-293/ hKOR (nM)	E_{max} HEK-293/ hKOR (%)	IC_{50} U87-MG (nM)	E_{max} U87-MG (%)
U50,488	1.2 \pm 0.3	90 \pm 2	1.4 \pm 0.1	88 \pm 3
LOR17	2.8 \pm 0.6	85 \pm 5	3.1 \pm 0.8	87 \pm 4
RDM1127	Not an agonist	/	Not an agonist	/
RDM1135	16.6 \pm 6.1	32 \pm 5	59.6 \pm 3.8	42 \pm 7

Table 4. Inhibition of forskolin-induced cAMP by U50,488 accumulation with and without RDM1127

Compound	IC_{50} (nM)	E_{max} (%)
U50,488	1.7 \pm 0.3	88 \pm 3
U50,488 in presence of RDM1127 10 μ M	2.1 \pm 0.7	44 \pm 7***

N.B.: HEK-293/hKOR cells were transfected to express recombinant hKOR; U87-MG human astrocytoma cells endogenously express hKOR.

3. Experimental Section

3.1 General Experimental Methods.

All purchased reagents were used without further purifications. Purities were assessed by analytical RP HPLC and confirmed by mass spectra. Analytical RP-HPLC is Agilent 1100 series apparatus, with a RP column Phenomenex Gemini®, 3 μ m, C18, 110 Å, 100 \times 3.0 mm, compounds were detected at DAD 210 and 254 nm, mobile phase: from 9:1 to 2:8 H₂O/CH₃CN in 20 min, with a flow rate of 0.5 mL min⁻¹, followed by 2:8 H₂O/CH₃CN in 10 min. Semi-preparative RP-HPLC is Agilent 1100 series, RP column ZORBAX Eclipse, XDB-C18, PrepHT cartridge, 7 μ m, 80 Å, 21.2 \times 150 mm, compounds were detected at DAD 210 and 254 nm, mobile phase: from 8:2 to 4:6 H₂O/CH₃CN in 15min, to 0:10 H₂O/CH₃CN in 5 min with a flow rate of 10 mL min⁻¹. NMR spectra were obtained from Varian Gemini 400 or 200 at peptides concentration of 0.01–0.04 M in 5 mm tubes at rt. The solvent used for NMR analysis was CDCl₃, or

[D₆]DMSO, or 8:2 [D₆]DMSO/H₂O (water was suppressed by using PRESAT). ¹H NMR were analyzed under 400M Hz, ¹³C NMR were analyzed under 100M Hz or 75M Hz.

3.2 General Procedure for the Synthesis of Cyclic Tetra-Peptides/Peptidomimetics

3.2.1 Solid Phase Peptides Synthesis (SPPS)

Loading amino acid on Wang resin,

Fmoc-Gly-resin was used as received without further purification, and Fmoc-β-Ala-resin and Fmoc-GABA-resin was prepared as follows. Wang resin 0.5 g (1.1 mmol/g) was placed in SPPS reactor and activated in 5 mL DCM for 5 min, then DCM was removed under vacuum and 5 mL of DMF was introduced in the reactor, Fmoc-β-Ala-OH (or Fmoc-GABA-OH, 2 eq.), HOBt (2 eq.), DCC (2 eq.) and DMAP (catalytical amount) were introduced in sequence, and the mixture was shaken for 3 hours. Then, solvent was removed under vacuum and the resin was washed 3 times with 5 mL of DMF, DCM, MeOH (methanol) each in sequence. Unreacted OH groups on Wang resin was capped with Ac₂O (2mL) and pyridine (2mL) in 45 min, then it was washed with DMF, DCM, MeOH 3 times each.

Fmoc removal,

Fmoc group was removed by shaking the resin for 30 min with 6 mL of 20% Pip in DMF. Then, the resin was washed sequentially with DMF, DCM, MeOH. Treated the resin with 20% Pip in DMF again for 30 min and washed it with DMF, DCM, MeOH 3 times each.

Coupling,

After removing the Fmoc group from Fmoc-AA-resin, Fmoc-AA-OH (2 eq.) and HOBt (2 eq.) was dissolved in 5 mL of DMF and stirred for 10 min, then DCC (2 eq.) was added. The mixture was transferred into the resin-containing reactor and shaken for 3 hours. The solvents were removed under vacuum and the resin was washed with DMF, DCM, MeOH 3 times each.

Cleavage,

The peptide-coated resin was placed in 5 mL cocktail of TFA: TIPS: PhOH: H₂O: thioanisole (8: 0.5: 0.5: 0.5: 0.5, v/v) and shaken for 2 hours. The cocktail was collected and placed under compressed air to remove the solvents. The residue was washed with cold ether twice to give white powder. The obtained peptide was used in next step directly without further purification.

Cyclization,

In a 100 mL round bottom flask, HOBt (3 eq.), TBTU (3 eq.) and DIPEA (6 eq.) were dissolved in 30 mL of DMF and kept stirring at rt. In another flask, the linear peptide was dissolved in 10 mL DMF. Afterwards, the peptide solution was added dropwise into the stirred solution containing coupling reagents within 16 hours. The solvents were removed under compressed air, then obtained residue was dissolved in 30 mL EA and washed with HCl solution (1 M, 5 mL), saturated Na₂CO₃ (5 mL) and brine (5 mL). During the washing, precipitation was formed. The suspension was placed in an erlenmeyer flask overnight, and the precipitate was collected by filtration. The precipitate was washed with cold EA, MeCN and H₂O in sequence to remove impurities. The purity of precipitate was analyzed by analytical HPLC-MS.

3.2.2 Synthesis of the Cyclic Tetra-Peptides in Solution.

Coupling,

Boc protected amino acid (1.2 eq.) was dissolved in 1 mL of DMF, then HOBt (1.2 eq.) was added and the mixture was stirred for 10 min. Afterwards, EDC hydrochloride (1.2 eq.), amino acid methyl ester (or peptide methyl ester, 1.0 eq.) and TEA (3.0 eq.) were introduced, and the mixture was stirred for 3 hours.

The reaction was monitored by TLC (elute: 100% ethyl acetate). Work-up, solvents were removed under compressed air, 30 mL of ethyl acetate was introduced. Then it was washed with HCl solution (1 M, 5 mL) and saturated Na₂CO₃ (5 mL) respectively. Organic layer was collected and dried over anhydrous Na₂SO₄. Solvents were removed to get an oil-like residue. The residue was used in next step without further purification.

Boc-deprotection,

Boc-peptides were dissolved in TFA/DCM (1:4, v/v) and the mixture was stirred for 2 hours. Then the solvents were removed under compressed air and the residue was washed with cold ether twice. The residue was used in next step directly without further purification.

Remove methyl ester,

Methyl ester protected peptides were introduced in the solution of LiOH in dioxane/H₂O (1 M, 1:1, v/v), the mixture was stirred overnight. The accomplishment of the reaction was monitored with TLC (cyclohexane: EtOAc = 1:3). HCl solution (1M) was used to adjust pH value to 3, then the mixture was extracted with EtOAc 3 times. Organic layers were collected and dried over anhydrous Na₂SO₄. Solvents were removed under vacuum to obtain oil-like residue.

c[Ala-D-Trp-Phe-Gly] (RDM1143).

¹H NMR (400 MHz, 8:2 [D₆]DMSO/H₂O) δ 10.75 (s, ¹H, D-TrpArH1), 8.05 - 7.92 (m, 2H, PheNH + GlyNH), 7.86 (d, *J* = 8.8 Hz, 1H, D-TrpNH), 7.57 (d, *J* = 9.2 Hz, 1H, AlaNH), 7.51 (d, *J* = 7.6 Hz, 1H, D-TrpArH4), 7.32 (d, *J* = 8.4 Hz, 1H, D-TrpArH7), 7.24 - 7.13 (m, 5H, PheArH), 7.09-7.00 (m, 2H, D-TrpArH6 + D-TrpArH2), 6.96 (dd, *J* = 7.0, 7.6 Hz, 1H, D-TrpArH5), 4.65 (ddd, *J* = 14.8, 8.8, 8.7, Hz, 1H, D-TrpHα), 4.50 (m, 1H, PheHα), 4.38 (q, *J* = 7.1, 6.4 Hz, 1H, AlaHα), 4.10 (dd, *J* = 8.4, 12.8 Hz, 1H, GlyHα), 3.13 (dd, *J* = 14.8, 8.7 Hz, 1H, D-TrpHβ), 3.03-3.09 (m, 1H, GlyHα), 2.99 (dd, *J* = 14.1, 7.9 Hz, 1H, PheHβ), 2.93-2.80 (m, 2H, D-TrpHβ + PheHβ), 1.11 (d, *J* = 6.8 Hz, 3H, AlaMe). ¹³C NMR (8:2 [D₆]DMSO/H₂O) δ: 172.94, 172.60, 172.40, 170.96, 137.78, 136.11, 129.05, 128.30, 127.27, 126.40, 122.94, 121.05, 120.03, 118.37, 111.39, 110.20, 55.02, 54.03, 52.96, 48.72, 47.83, 43.73, 34.66, 25.04, 15.22. ESI MS (m/z) 462.20 [M+H]⁺, calcd for C₂₅H₂₈N₅O₄ 462.2141.

c[GABA-D-Trp-Phe-Gly] (LOR19org)

¹H-NMR (400 MHz, 8:2 [D₆]DMSO/H₂O) δ 10.79 (s, 1H, D-TrpArH₁), 9.00 (d, *J* = 7.6 Hz, 1H PheNH), 8.51 (d, *J* = 6.8 Hz, 1H, D-TrpNH), 7.67 (dd, *J* = 5.2, 6.4 Hz, 1H, GlyNH), 7.56 (d, *J* = 8.0 Hz, 1H, D-TrpArH₄), 7.34 (d, *J* = 8.4 Hz, 1H, D-TrpArH₇), 7.29 - 7.23 (m, 2H, PheArH_{3,5}), 7.23-7.16 (m, 3H, PheArH_{2,4,6}), 7.14 (d, *J* = 2.3 Hz, 1H, D-TrpArH₂), 7.08 (dd, *J* = 7.2, 7.6 Hz, 1H, D-TrpArH₆), 7.00 (t, *J* = 7.2 Hz, 1H, D-TrpArH₅), 6.84 (t, *J* = 5.2 Hz, 1H, GABANH), 4.42 (dt, *J* = 6.8, 7.2 Hz, 1H, D-TrpHα), 4.24 (ddd, *J* = 4.8, 7.6, 10.0 Hz, 1H, PheHα), 3.75 (dd, *J* = 6.4, 16.6 Hz, 1H, GlyHα), 3.63 (dd, *J* = 5.2, 16.6 Hz, 1H, GlyHα), 3.46 (m, 1H, GABAHγ), 3.04 (dd, *J* = 4.8, 14.4 Hz, 1H, PheHβ), 2.91 (d, *J* = 7.2 Hz, 2H, D-TrpHβ), 2.85 (d, *J* = 9.6 Hz, 1H, GABAHγ), 2.81 (d, *J* = 9.9 Hz, 1H, PheHβ) 2.25 (m, 1H, GABAHα), 2.08 (m, 1H, GABAHα), 1.79 (m, 1H, GABAHβ), 1.59 (m, 1H, GABAHβ). ¹³C NMR (101 MHz, 8:2 [D₆]DMSO/H₂O) δ 174.6, 174.2, 170.6, 168.5, 138.0, 136.2, 128.9, 128.3, 127.0, 126.4, 123.8, 121.0, 118.4, 118.3, 111.5, 109.7, 55.8, 54.6, 42.5, 35.6, 34.2, 30.8, 26.2, 24.0. ESI MS (m/z) 476.4, [M+H]⁺, calcd for C₂₆H₃₀N₅O₄ 476.2298;

c[D-Ala-D-Trp-Phe-Gly] (RQ35PPI)

¹H-NMR (8:2 [D₆]DMSO/H₂O): δ 10.74 (d, *J* = 13.9 Hz, 1H, D-TrpArH₁), 8.57 (d, *J* = 9.1 Hz, 1H, PheNH), 8.03 (d, *J* = 9.2 Hz, 1H, D-AlaNH), 7.78 (d, *J* = 8.3 Hz, 1H, GlyNH), 7.58 (d, *J* = 8.8 Hz, 1H, D-TrpNH), 7.48 (d, *J* = 7.8 Hz, 1H, D-TrpArH₄), 7.32 (d, *J* = 8.0 Hz, 1H, D-TrpArH₇), 7.10-7.2 (m, 5H, PheArH₂₋₆), 7.06 (t, *J* = 7.4 Hz, 1H, D-TrpArH₆), 6.97 (dd, *J* = 5, 13 Hz, 1H, D-TrpArH₅), 6.89 (s, 1H, D-TrpArH₂), 4.52 (ddd, *J* = 5.2, 6.8, 8.4 Hz, 1H, TrpH α), 4.50 (ddd, *J* = 4.8, 5.4, 9.6 Hz, 1H, PheH α), 4.25 (m, 1H, D-AlaH α), 4.13 (dd, *J* = 7.3, 15.0, Hz, 1H, GlyH α), 3.62 (dd, *J* = 9.2, 18.0 Hz, 1H, GlyH α), 3.11 (dd, *J* = 5.2, 15.6 Hz, 1H, D-TrpH β), 2.97 (dd, *J* = 5.4, 14.2 Hz, 1H, PheH β), 2.83 (dd, *J* = 4.8, 13.6 Hz, 1H, PheH β), 2.74 (dd, *J* = 6.8, 14.0 Hz, 1H, TrpH β), 1.23 (d, *J* = 6.8 Hz, 3H, D-AlaCH₃). ¹³C-NMR (8:2 [D₆]DMSO/H₂O) δ: 173.7, 172.2, 172.1, 171.6, 171.6, 171.0, 169.6, 168.3, 138.1, 136.0, 129.7, 129.0, 128.1, 127.7, 127.2, 127.1, 126.1, 125.9, 124.5, 122.4, 121.0, 120.9, 118.3, 118.1, 111.3, 110.1, 55.6, 53.7, 51.2, 44.0, 34.4, 29.0, 26.0, 16.9, 16.3. ESI MS (m/z) 462.4, [M+H]⁺, 479.4[M+H₂O], calcd for C₂₅H₂₈N₅O₄ 462.2141;

***c*[Gly¹-D-Trp-Phe-Gly⁴] (RQ40PPI)**

¹H NMR (401 MHz, 8:2 [D₆]DMSO/H₂O) δ 10.76 (d, *J* = 8.6 Hz, 1H, D-TrpArH₁), 8.26 (d, *J* = 9.5 Hz, 1H, PheNH), 7.76 (d, *J* = 12.6 Hz, 1H, GlyNH), 7.72 (d, *J* = 9.2 Hz, 1H, D-TrpNH), 7.65 (d, *J* = 6.0 Hz, 1H, GlyNH), 7.49 (d, *J* = 7.9 Hz, 1H, D-TrpArH₄), 7.32 (d, *J* = 8.1 Hz, 1H, D-TrpArH₇), 7.09-7.28(m, 5H, PheArH), 7.10-7.02 (m, 1H, D-TrpArH₆), 7.01 - 6.90 (m, 2H, D-TrpArH₅+D-TrpArH₂), 4.61 (q, *J* = 8.5 Hz, 1H, TrpH α), 4.52 (q, *J* = 8.2 Hz, 1H, PheH α), 3.95 (dd, *J* = 13.6, 8.4 Hz, 1H, Gly⁴H α), 3.80 (dd, *J* = 13.5, 6.3 Hz, 1H, Gly¹H α), 3.41 (dd, *J* = 13.4, 6.0 Hz, 1H, Gly¹H α), 3.24 (dd, *J* = 12, 4 Hz, 1H, Gly⁴H α), 3.11 (dd, *J* = 14.9, 9.0 Hz, 1H, TrpH β), 3.00 (dt, *J* = 14.0, 8.7 Hz, 1H, PheH β), 2.76(dd, *J* = 16, 8 Hz, 1H, TrpH β), 2.74 (dd, *J* = 16, 8 Hz, 1H, PheH β). ¹³C NMR (101 MHz, 8:2 [D₆]DMSO/H₂O) δ 172.3, 172.0, 170.9, 170.8, 137.9, 136.1, 129.1, 128.2, 127.2, 126.3, 122.7, 121.0, 118.3, 115.2, 111.4, 110.1, 54.0, 53.3, 44.1, 43.8, 34.6, 25.5. ESI MS (m/z) 448.2 [M+H]⁺, calcd for C₂₄H₂₆N₅O₄ 448.1985;

***c*[Gly-D-Trp-Phe- β Ala] (RDM1125)**

¹H NMR (401 MHz, 8:2 [D₆]DMSO/H₂O) δ 10.77 (s, 1H, D-TrpArH₁), 8.45 (dd, *J* = 5.8, 6.6 Hz, 1H, GlyNH), 7.87 (d, *J* = 8.8 Hz, 1H, D-TrpNH), 7.82 (d, *J* = 8.8 Hz, 1H, PheNH), 7.47 (d, *J* = 7.6 Hz, 1H, D-TrpArH₄), 7.33 (d, *J* = 8.0 Hz, 1H, D-TrpArH₇), 7.28 - 7.17 (m, 3H, PheAr H_{2,4,6}), 7.17 - 7.10 (m, 2H, PheAr H_{3,5}), 7.06 (dd, *J* = 7.2, 7.4 Hz, 1H, D-TrpArH₆), 7.03 - 6.93 (m, 2H, D-TrpArH₅ + β AlaNH), 6.82 (d, *J* = 2.3 Hz, 1H, D-TrpArH₂), 4.38 (ddd, *J* = 2, 7.4, 8.8 Hz, 1H, TrpH α), 4.32 (ddd, *J* = 5.7, 8.8, 14.4 Hz, 1H, PheH α), 3.68 (dd, *J* = 14.6, 6.1 Hz, 1H, GlyH α), 3.54 (dd, *J* = 14.6, 6.0 Hz, 1H, GlyH α), 3.47 (dd, *J* = 13.1, 6.0 Hz, 1H, β AlaH β), 3.18 (dd, *J* = 9.9, 4.6 Hz, 1H, β AlaH β), 3.13 (dd, *J* = 14.4, 5.7 Hz, 1H, PheH β), 2.88 (d, *J* = 7.4 Hz, 2H, TrpH β), 2.80 - 2.69 (m, 1H, PheH β), 2.44 - 2.25 (m, 2H, β AlaH α). ¹³C NMR (101 MHz, 8:2 [D₆]DMSO/H₂O) δ 171.7, 170.7, 170.5, 169.8, 138.2, 136.2, 129.2, 128.2, 127.0, 126.2, 123.3, 121.0, 118.4, 118.0, 111.5, 109.5, 55.8, 54.2, 43.7, 36.4, 35.7, 34.5, 27.3. ESI MS (m/z) 462.2 [M+H]⁺, calcd for C₂₅H₂₈N₅O₄ 462.2141;

***c*[β Ala-D-Trp-Phe- β Ala] (RDM1127)**

¹H NMR (401 MHz, 8:2 [D₆]DMSO/H₂O) δ 10.71 (s, 1H, D-TrpArH₁), 8.45 (d, *J* = 8.6 Hz, 1H, PheNH), 8.34 (d, *J* = 7.7 Hz, 1H, D-TrpNH), 7.56 - 7.41 (m, 2H, D-TrpArH₄ + β Ala¹NH), 7.34 (d, *J* = 8.1 Hz, 1H, D-TrpArH₇), 7.24 (d, *J* = 5.7 Hz, 1H, β Ala⁴NH), 7.22 - 7.15 (m, 3H, PheArH_{2,4,6}), 7.15 - 7.09 (m, 2H, PheArH_{3,5}), 7.06 (dd, *J* = 7.1, 7.9 Hz, 1H, D-TrpArH₆), 6.98 (dd, *J* = 7.0, 7.8 Hz, 1H, D-TrpArH₅), 6.95 - 6.89 (d, *J* = 2.3 Hz, 1H, D-TrpArH₂), 4.49 (ddd, *J* = 7.3, 7.7, 14.7 Hz, 1H, TrpH α), 4.32 (ddd, *J* = 7.4, 8.6,

14.1 Hz, 1H, PheH α), 3.54 - 3.42 (m, 1H, β Ala¹H β), 3.42 - 3.33 (m, 1H, β Ala⁴H β), 3.31 - 3.23 (m, 1H, β Ala⁴H β), 3.23 - 3.14 (m, 1H, β Ala¹H β), 3.07 (dd, J = 14.1, 4.2 Hz, 1H, PheH β), 2.90 (dd, J = 14.7, 6.9 Hz, 1H, TrpH β), 2.80 (dd, J = 14.7, 7.6 Hz, 1H, TrpH β), 2.72 (dd, J = 14.1, 10.5 Hz, 1H, PheH β), 2.37 (m, 1H, β Ala¹H α), 2.23 - 1.99 (m, 3H, β Ala¹H α + β Ala⁴H α ×2). ¹³C NMR (101 MHz, 8:2 [D₆]DMSO/H₂O) δ 171.6, 171.2, 170.6, 170.4, 138.5, 136.1, 128.8, 128.1, 127.2, 126.2, 123.2, 120.9, 118.3, 118.2, 111.4, 110.0, 54.7, 53.4, 36.4, 36.2, 35.8, 35.4, 34.9, 26.3. ESI MS (m/z) 476.2 [M+H]⁺, calcd for C₂₆H₃₀N₅O₄ 476.2298;

c[EACA-D-Trp-Phe] (RDM1133, EACA = ϵ -Aminocaproic acid)

¹H NMR (401 MHz, 8:2 [D₆]DMSO/H₂O) δ 10.71 (s, 1H, D-TrpArH₁), 8.79 (d, J = 8.6 Hz, 1H, PheNH), 8.63 (d, J = 8.4 Hz, 1H, D-TrpNH), 7.48 (d, J = 7.9 Hz, 1H, D-TrpArH₄), 7.34 (d, J = 8.1 Hz, 1H, D-TrpArH₇), 7.26 - 7.19 (m, 2H, PheArH_{3,5}), 7.19 - 7.13 (m, 3H, PheArH_{2,4,6}), 7.11 (dd, 1H, J = 5.8, 5.4, EACA-NH), 7.06 (dd, 1H, J = 7.6, 7.2 Hz, D-TrpArH₆), 7.02 - 6.93 (m, 2H, D-TrpArH₂ + D-TrpArH₅), 4.72 (ddd, J = 5.6, 8.4, 13.1 Hz, 1H, TrpH α), 4.28 (ddd, J = 8.6, 8.7, 12.6 Hz, 1H, PheH α), 3.24 - 3.11 (m, 1H, EACA-H ϵ), 3.10 - 2.95 (m, 3H, EACA-H α + TrpH β + PheH β), 2.84 (dd, J = 5.6, 13.1 Hz, 1H, TrpH β), 2.79 (dd, J = 8.7, 12.6 Hz, 1H, PheH β), 2.20 (1H, m, EACA-H α), 1.99 (1H, m, EACA-H α), 1.64 (1H, m, EACA-H γ), 1.49 - 1.40 (2H, m, EACA-H β + EACA-H δ), 1.29 - 1.23 (2H, m, EACA-H γ + EACA-H δ), 0.99 (1H, m, EACA-H β). ¹³C NMR (101 MHz, 8:2 [D₆]DMSO/H₂O) δ 174.1, 172.1, 170.6, 138.7, 136.1, 128.8, 128.2, 127.1, 126.2, 122.9, 121.0, 118.3, 118.2, 111.4, 109.8, 55.4, 53.1, 36.3, 35.5, 34.3, 26.8, 25.6, 22.9, 21.9. ESI MS (m/z) 447.4 [M+H]⁺, calcd for C₂₆H₃₁N₄O₃ 447.2396;

c[ϵ -AHEA-D-Trp-Phe] (JW239)

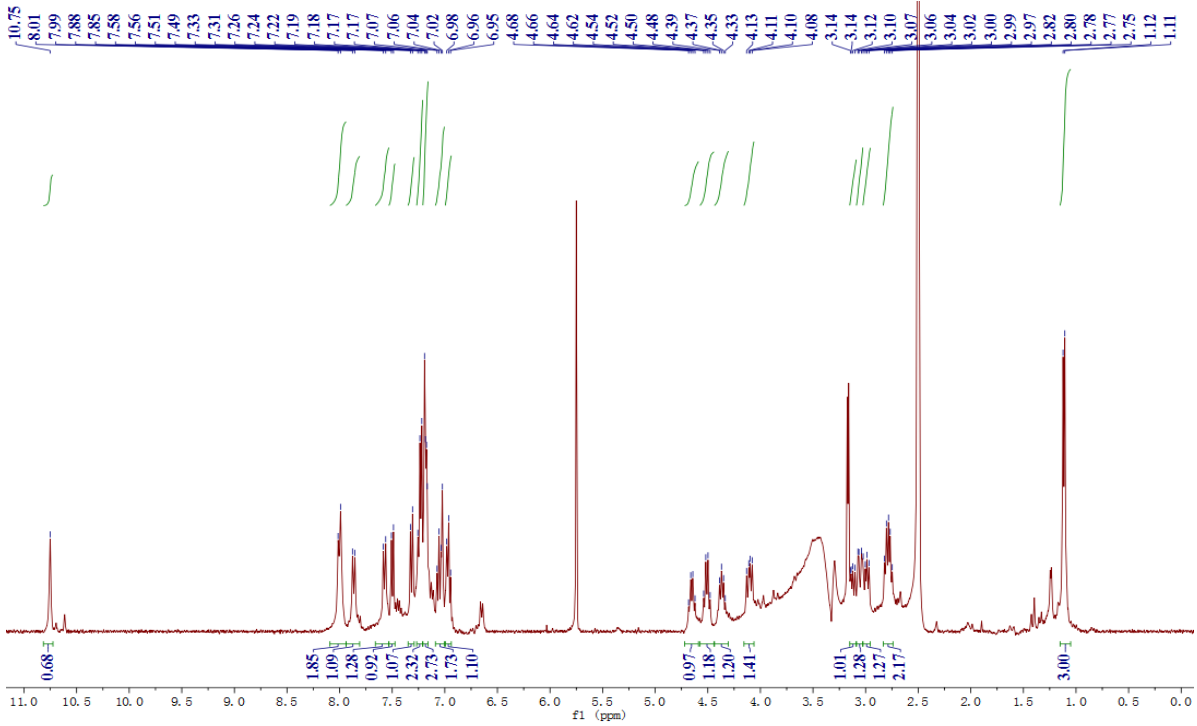
The preparation procedure of JW239 was shown in scheme 4. For the first coupling reaction, firstly, Boc-Phe-OH (1.13 mmol, 343 mg) was dissolved in DCM/DMF (3 mL/1 mL), then HOBt (0.90 mmol, 122 mg) was added and the mixture was stirred for 10 min, followed by adding EDC hydrochloride (0.90 mmol, 173 mg), allylamine (0.90 mmol, 51 mg), triethylamine (1.81 mmol, 251 μ L) in sequence. The mixture was stirred overnight. Afterwards, solvents were removed to obtain an oil-like residue, which was dissolved in 30 mL EA. Then, it was washed with HCl aqueous solution (1 M, 5 mL) and saturated Na₂CO₃ (5 mL) successively. The organic phase was collected and dried over anhydrous Na₂SO₄, and the solvents were removed under vacuum to obtain an oil-like residue. Before coupling the next amino acid, Boc-Phe-allylamine (0.79 mmol, 243 mg) was dissolved in TFA/DCM (1 mL/3 mL) to remove Boc group, and the mixture was stirred for 2 hours to give H-Phe-allylamine. After removing solvents and washing with cold ether to give white powder, H-Phe-allylamine was used directly for next coupling reaction without further purification. For coupling D-Trp-OH into peptide sequence, firstly, Boc-D-Trp-OH (1.13 mmol, 343 mg) was dissolved in DCM/DMF (3 mL/1 mL), then HOBt (1.13 mmol, 153 mg) was added and the mixture was stirred for 10 min, followed by adding EDC hydrochloride (1.03 mmol, 216 mg), H-Phe-allylamine (0.94 mmol, 192 mg), triethylamine (2.26 mmol, 313 μ L) in sequence. The mixture was stirred overnight, and the procedures of work-up and Boc deprotection were as described above. Subsequently, the last coupling reaction was carried out. Firstly, 4-pentenoic acid (1.03 mmol, 104 mg) was dissolved in DCM/DMF (3 mL/1 mL), then HOBt (1.03 mmol, 140 mg) was added and the mixture was stirred for 10 min, followed by adding EDC hydrochloride (1.13 mmol, 198 mg), H-D-Trp-Phe-allylamine (0.86 mmol, 250 mg), triethylamine (2.07 mmol, 287 μ L) in sequence. The mixture was stirred overnight, the procedure of work-up was as described above. Lastly, RCM reaction was performed according to previous work^[27]. To be brief, Grubb's Catalyst1 (8.5% mmol, 10.47 mg) was

added in 20 mL DCM under nitrogen and the mixture was stirred for 10min. Then, 4-pentenoic-D-Trp-Phe-allylamine (0.08 mmol, 60 mg) was dissolved in anhydrous DCM and introduced into the solution containing Grubb's Catalyst prepared above under nitrogen. The mixture was stirred for 30min at rt, then refluxed for 36h. The completion of the reaction was monitored by TLC. After filtration through celite, the solvent of the filtrate was removed under vacuum, and the residue was purified by flash chromatography (Eluent: 50% Chex and 50% EA to 100%EA). ¹H NMR (401 MHz, 8:2 [D₆]DMSO/H₂O) δ 10.70 (s, 1H, D-TrpArH1), 8.92 (d, *J* = 8.5 Hz, 1H, PheNH), 8.26 (d, *J* = 9.3 Hz, 1H, D-TrpNH), 7.47 (d, *J* = 7.8 Hz, 1H, D-TrpArH4), 7.32 (d, *J* = 8.1 Hz, 1H, D-TrpArH7), 7.24 - 7.19 (m, 2H, PheArH3,5), 7.19 - 7.12 (m, 3H, PheArH2,4,6), 7.06 (dd, 1H, *J* = 8.0, 4.0 Hz, D-TrpArH6), 7.02 - 6.92 (m, 2H, D-TrpArH2 + D-TrpArH5), 6.87 (dd, *J* = 8.4, 4.4 Hz, 1H, ε-AHEA-NH), 5.39 (s, 2H, ε-AHEA-Hγ + Hδ), 4.79 (ddd, *J* = 5.6, 8.4, 13.1 Hz, 1H, TrpHα), 4.39 (ddd, *J* = 8.6, 8.7, 12.6 Hz, 1H, PheHα), 3.86 - 3.76 + 3.20 - 3.11 (m, 1H, ε-AHEA-Hε), 3.02 (dd, 1H, *J* = 8.0, 4.0 Hz, PheHβ), 2.98 (dd, 1H, *J* = 14.0, 6.0 Hz, TrpHβ), 2.81 (dd, 1H, *J* = 14.0, 6.0 Hz, TrpHβ), 2.76 (dd, 1H, *J* = 16.0, 8.0 Hz, PheHβ), 2.35 - 2.1 + 2.1 - 1.95 (m, 4H, ε-AHEA-Hα + Hβ). ¹³C NMR (101 MHz, 8:2 [D₆]DMSO/H₂O) δ 172.89, 171.33, 170.94, 138.76, 136.44, 130.96, 129.36, 128.49, 127.78, 127.55, 126.52, 123.14, 121.33, 118.63, 111.68, 110.28, 54.32, 52.42, 35.47, 34.34, 28.81, 27.02. ESI MS (*m/z*) 445.4 [M+H]⁺, calcd for C₂₆H₃₀N₅O₄ 445.2240.

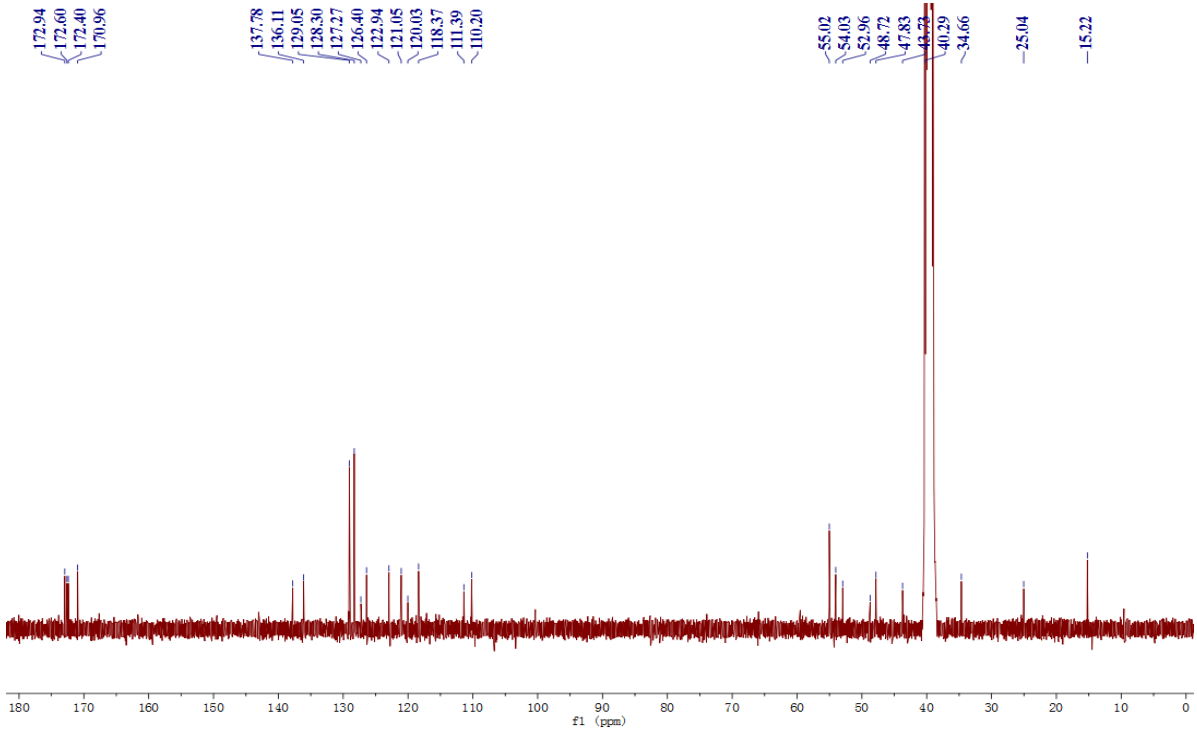
***c*[Gly-D-Trp-Phe-GABA] (RDM1135)**

¹H NMR (401 MHz, 8:2 [D₆]DMSO/H₂O) δ 10.76 (s, 0.25H, D-TrpArH1<), 10.73 (s, 0.75H, D-TrpArH1>), 9.01 (d, *J* = 8.4 Hz, 0.25H, PheNH<), 8.90 (d, *J* = 7.0 Hz, 0.25H, D-TrpNH<), 8.58 (dd, *J* = 5.6 Hz, 0.75H, GlyNH>), 8.43 (d, *J* = 8.7 Hz, 0.75H, D-TrpNH>), 7.54 - 7.47 (m, *J* = 9.6 Hz, 1H, PheNH> + D-TrpArH4<), 7.44 (d, *J* = 7.9 Hz, 0.75H, TrpHα>), 7.40 (dd, *J* = 7.0, 4.8 Hz, 0.75H, GABANH>), 7.35 (d, *J* = 7.9 Hz, 0.25H, D-TrpArH7<), 7.32 (d, *J* = 8.1 Hz, 0.75H, D-TrpH7>), 7.27 (dd, *J* = 6.9 Hz, 0.25H, GlyNH<), 7.25 - 7.11 (m, 5H, PheArH> + PheArH<), 7.11 - 7.02 (m, 1H, D-TrpArH6> + D-TrpArH2<), 7.03 - 6.95 (m, 2H, D-TrpArH5> + D-TrpArH6< + D-TrpArH5< + D-TrpArH2>), 4.56 (m, 0.25H, TrpHα<), 4.46 (dt, *J* = 9.5, 4.7 Hz, 0.75H, PheHα>), 4.41 (dt, *J* = 9.2, 4.4 Hz, 0.75H, TrpHα>), 4.20 (m, 0.25H, PheHα<), 3.85 (dd, *J* = 18.2, 6.3 Hz, 0.25H, GlyHα<), 3.63 - 3.54 (m, 0.25H, GlyHα<), 3.49 (dd, *J* = 5.7 Hz, 1.5H, GlyHα>), 3.46 - 3.37 (m, 1H, GABA Hγ> + TrpHβ<), 3.26 (dd, *J* = 13.9, 4.5 Hz, 0.75H, PheHβ>), 3.20 (dd, *J* = 15.3, 5.0 Hz, 0.75H, TrpHβ>), 3.09 (dd, *J* = 14.1, 3.1 Hz, 0.25H, PheHβ<), 2.95 - 2.86 (m, 1H, GABA Hγ> + TrpHβ<), 2.83 (dd, *J* = 15.2, 5.6 Hz, 0.75H, TrpHβ>), 2.80 - 2.73 (m, 0.25H, PheHβ<), 2.62 (dd, *J* = 13.9, 9.8 Hz, 0.75H, PheHβ>), 2.30 (m, 1.5H, GABA Hα>), 1.87 (m, 0.75H, GABA Hβ>), 1.79 (m, 0.25H, GABA Hβ<), 1.56 (m, 0.75H, GABA Hβ>), 1.43 (m, 0.25H, GABA Hβ<). (> refers to major isomer, < refers to minor isomer). ¹³C NMR (101 MHz, 8:2 [D₆]DMSO/H₂O) δ 174.8, 170.8, 170.2, 170.0, 138.6, 136.1, 129.1, 128.7, 128.2, 128.0, 127.3, 126.0, 122.8, 120.9, 118.3, 118.0, 111.4, 110.7, 53.5, 52.8, 44.0, 40.2, 37.3, 33.6, 25.4, 22.9. ESI MS (*m/z*) 476.4 [M+H]⁺, calcd for C₂₆H₃₀N₅O₄ 476.2298;

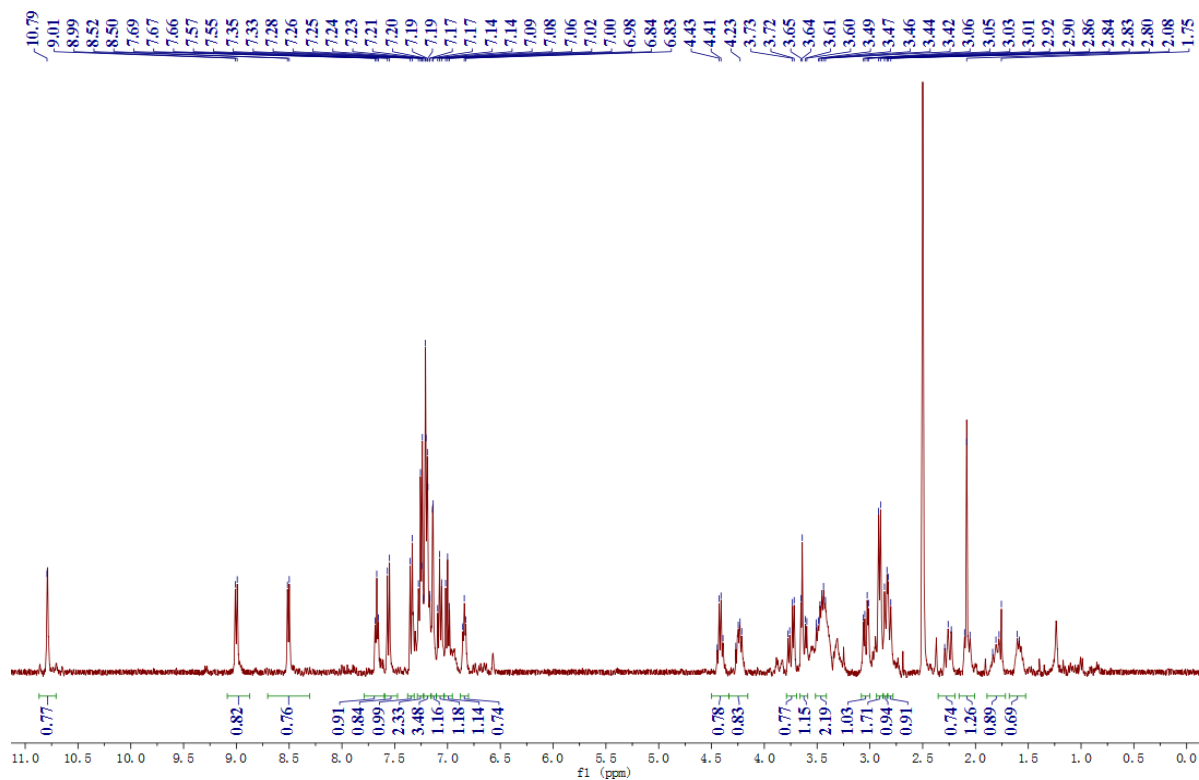
NMR spectra



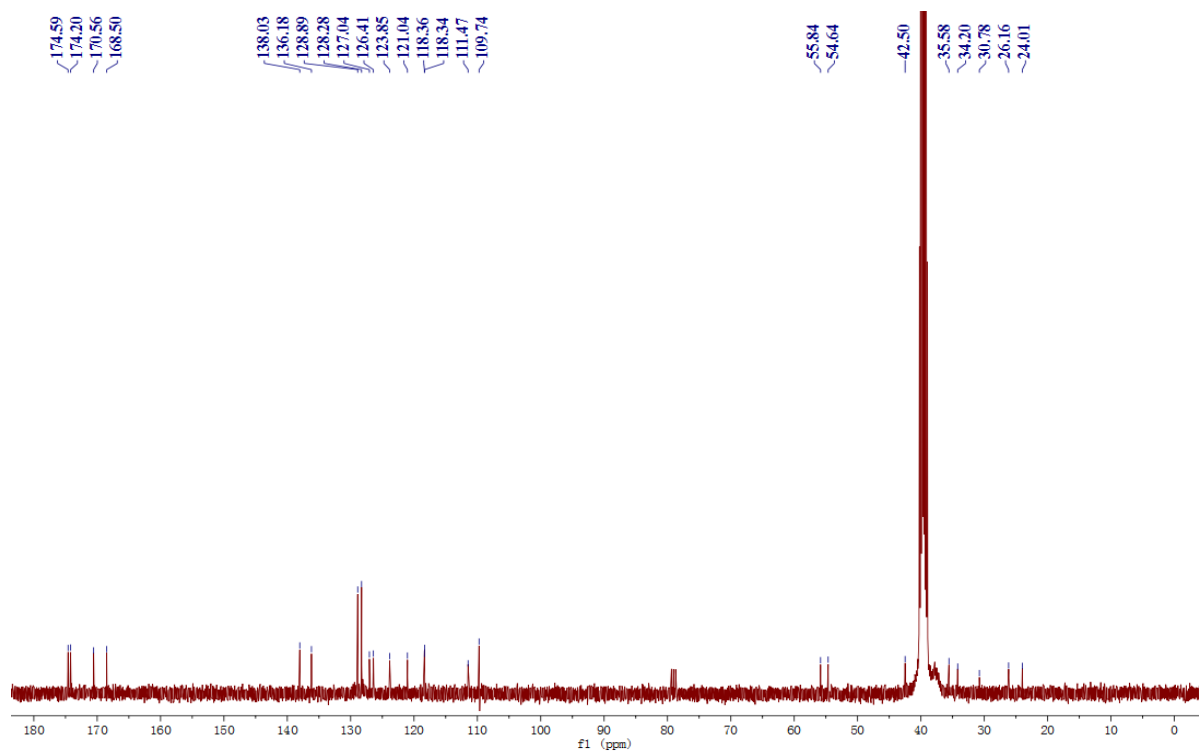
¹H NMR of c[Ala-D-Trp-Phe-Gly](RDM1143)



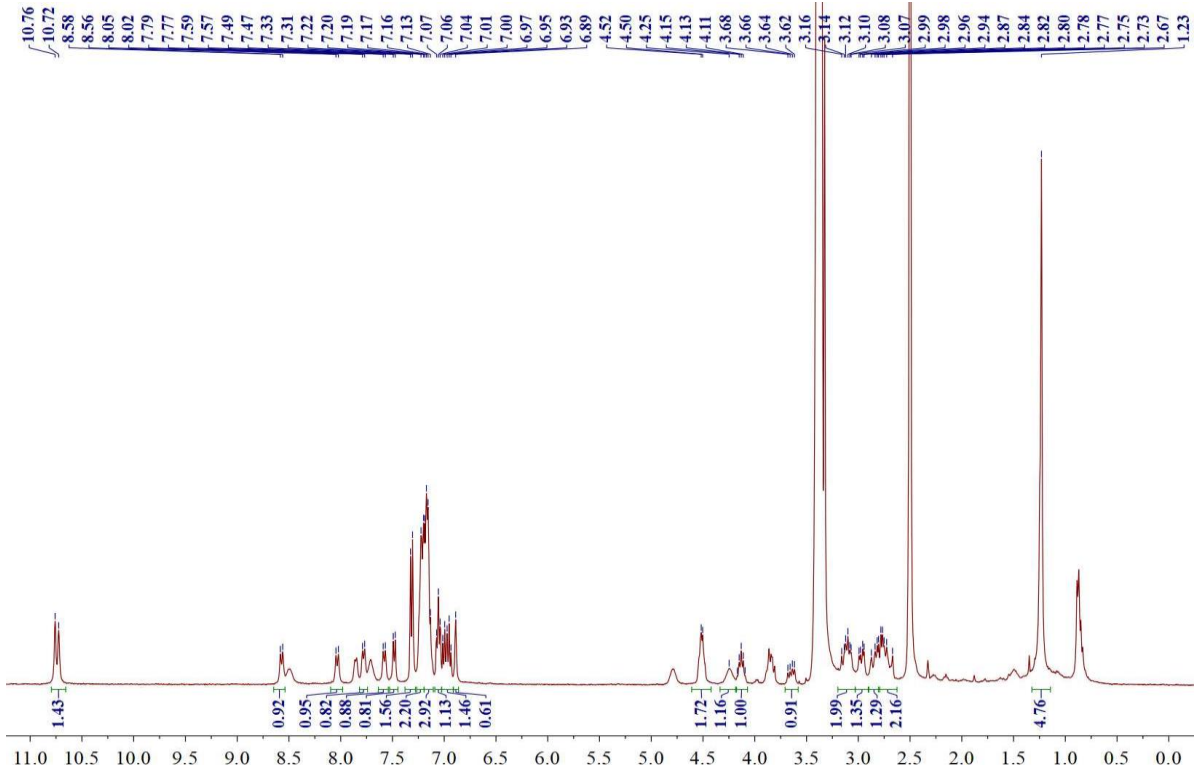
¹³C NMR of c[Ala-D-Trp-Phe-Gly](RDM1143)



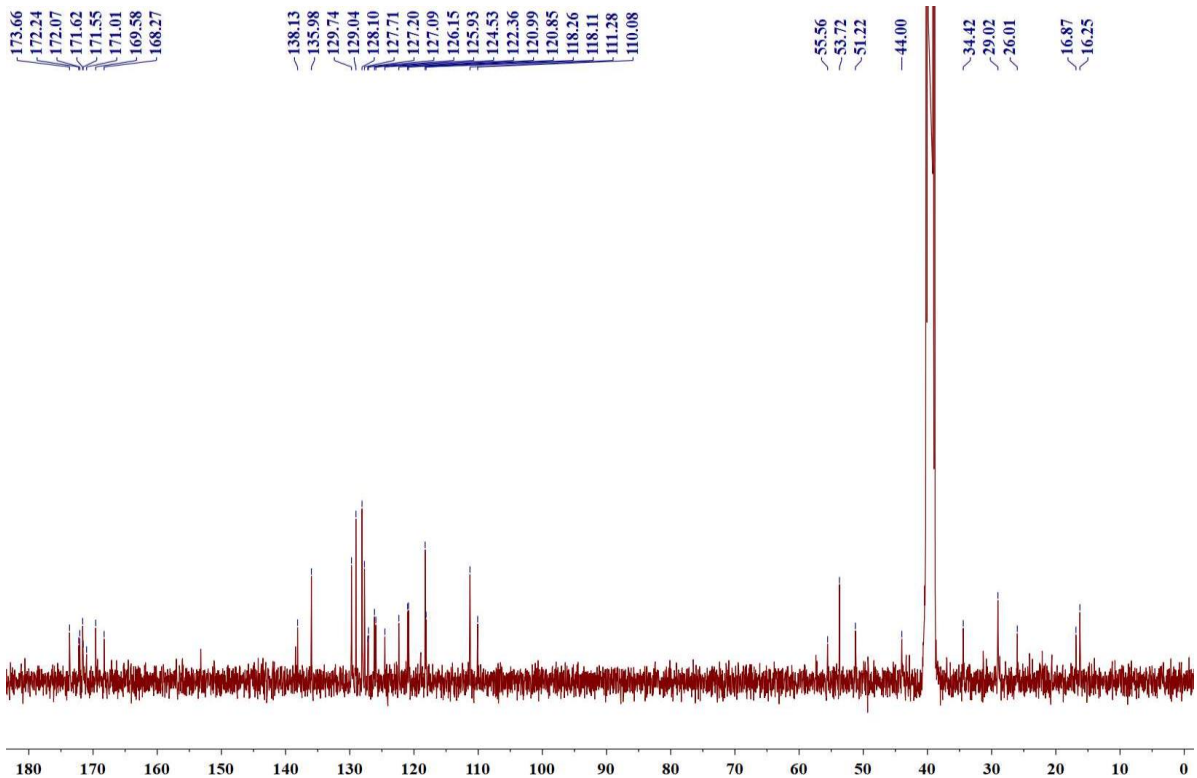
¹H NMR of c[GABA-D-Trp-Phe-Gly] (LOR19org)



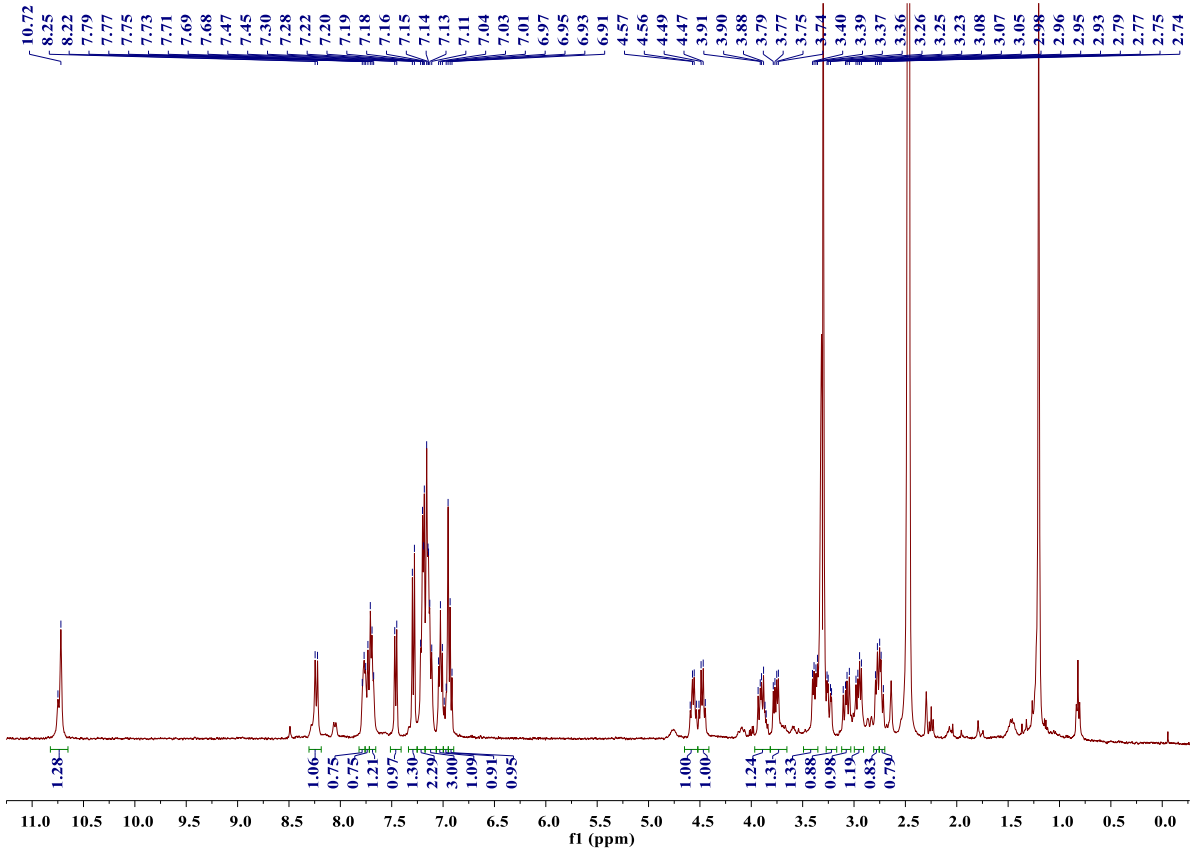
¹³C NMR of c[GABA-D-Trp-Phe-Gly] (LOR19org)



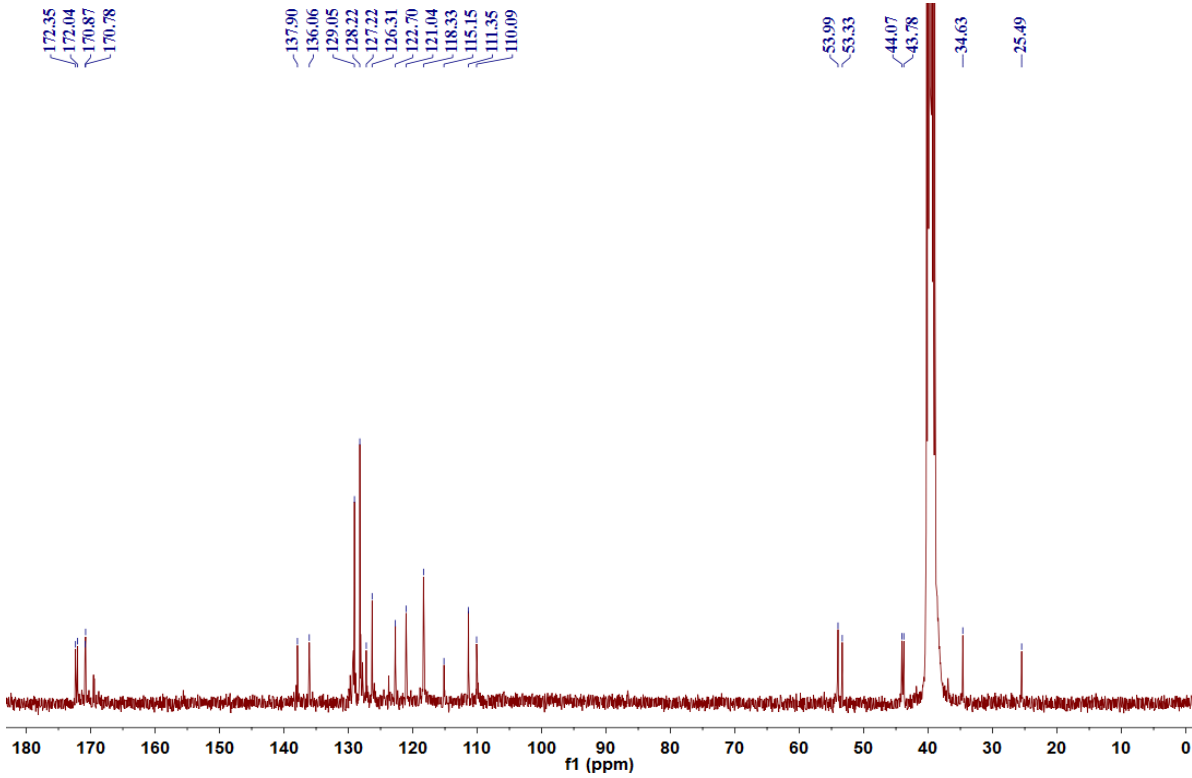
¹H NMR of c[D-Ala-D-Trp-Phe-Gly] (RQ35PP1)



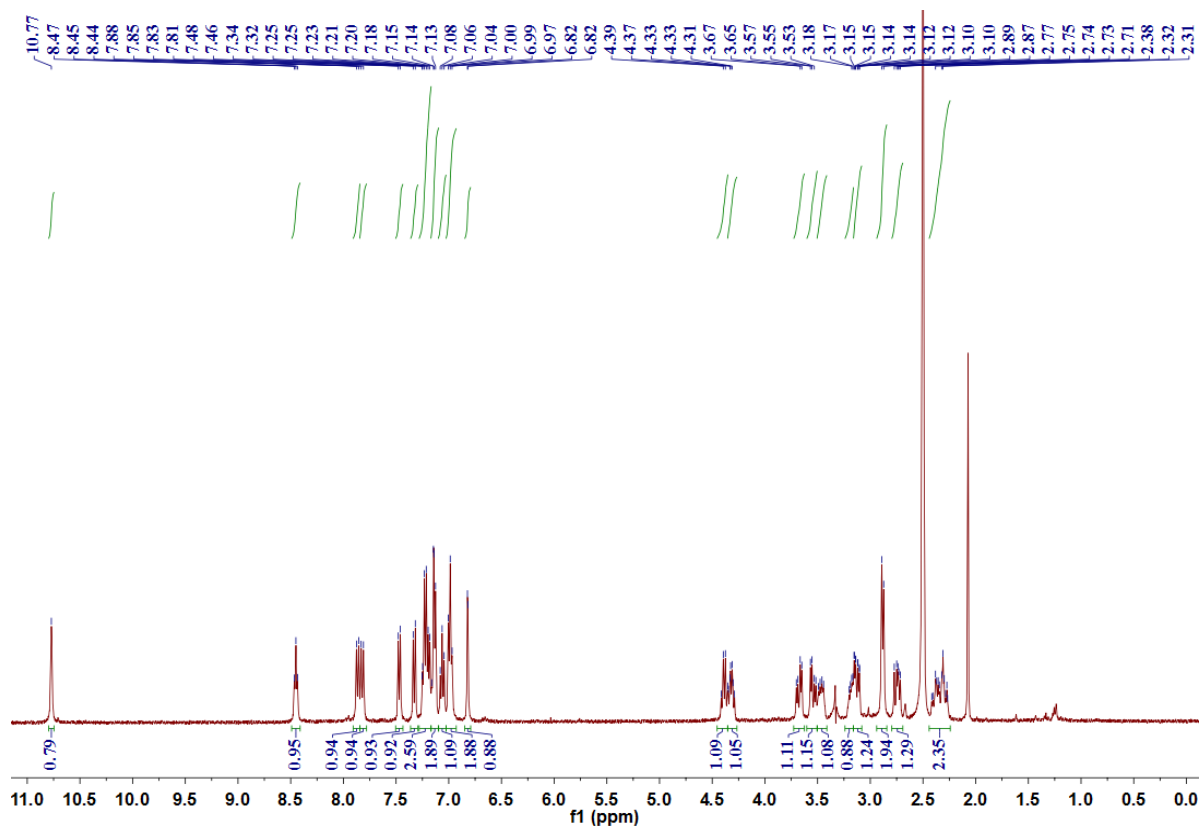
¹³C NMR of c[D-Ala-D-Trp-Phe-Gly] (RQ35PP1)



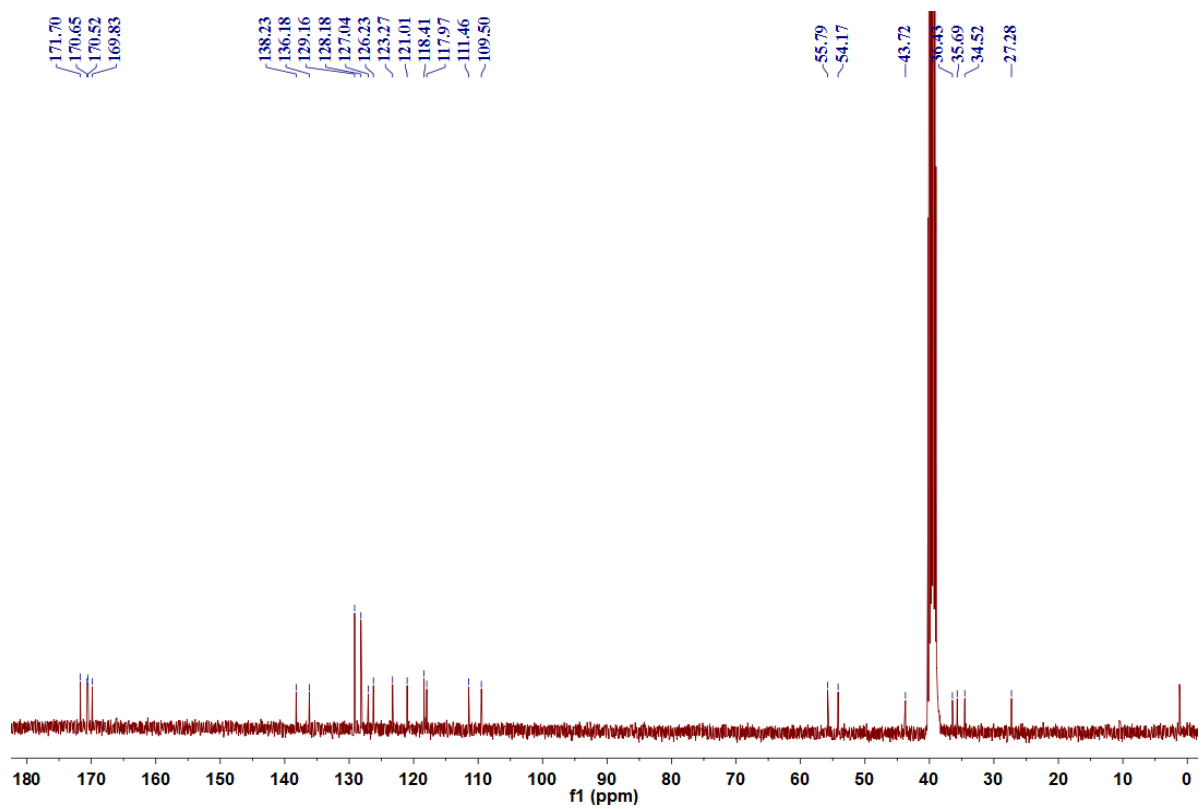
¹H NMR of c[Gly1-D-Trp-Phe-Gly4] (RQ40PP1)



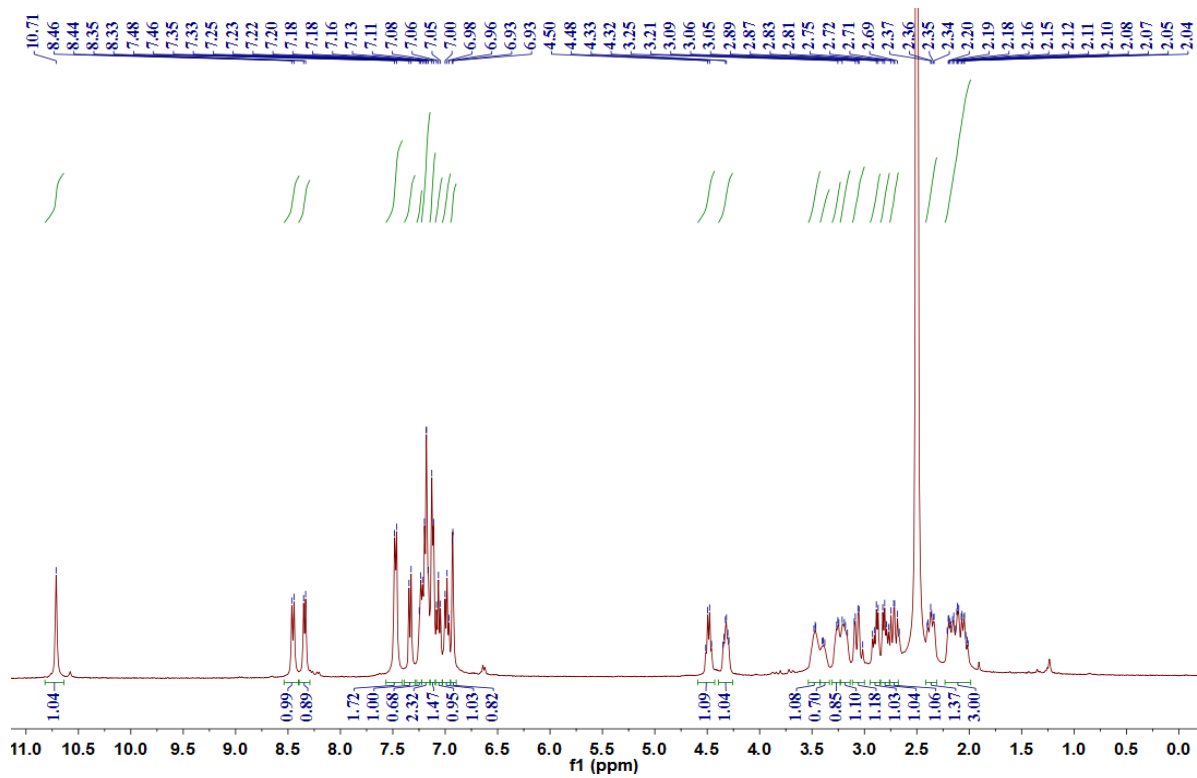
¹³C NMR of c[Gly1-D-Trp-Phe-Gly4] (RQ40PP1)



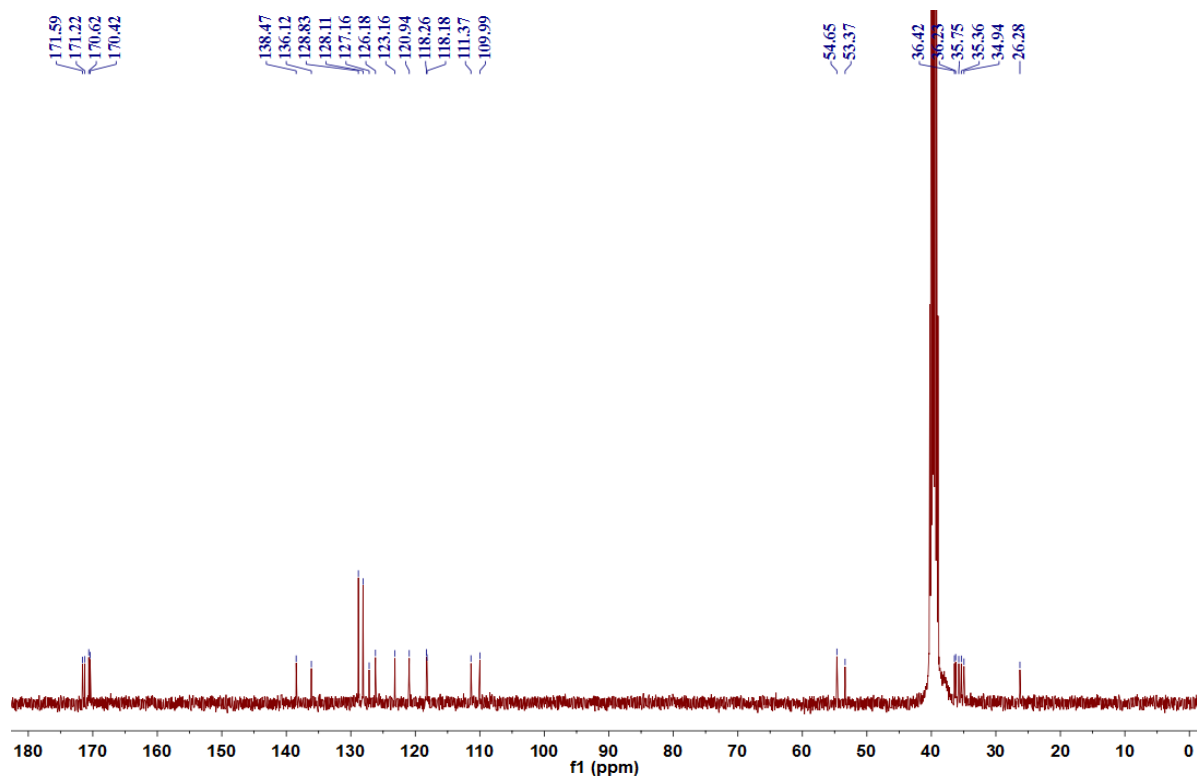
¹H NMR of c[Gly-D-Trp-Phe-βAla] (RDM1125)



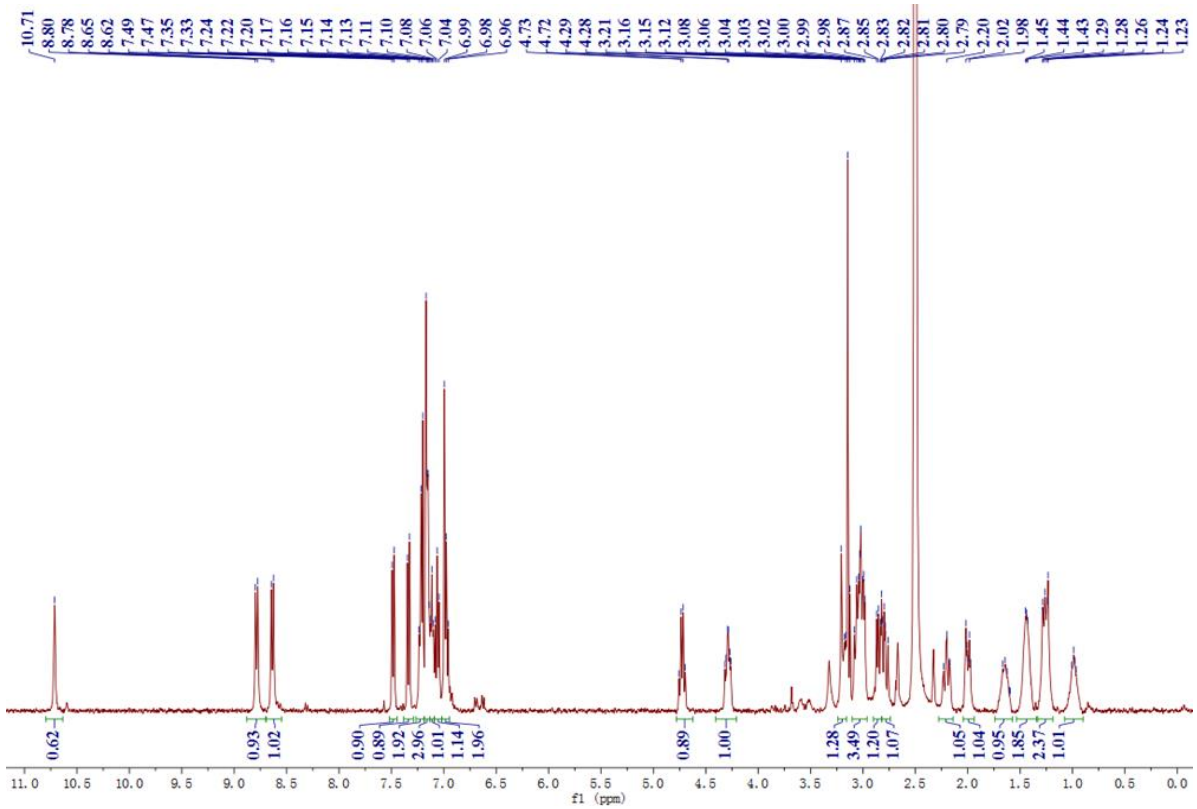
¹³C NMR of c[Gly-D-Trp-Phe-βAla] (RDM1125)



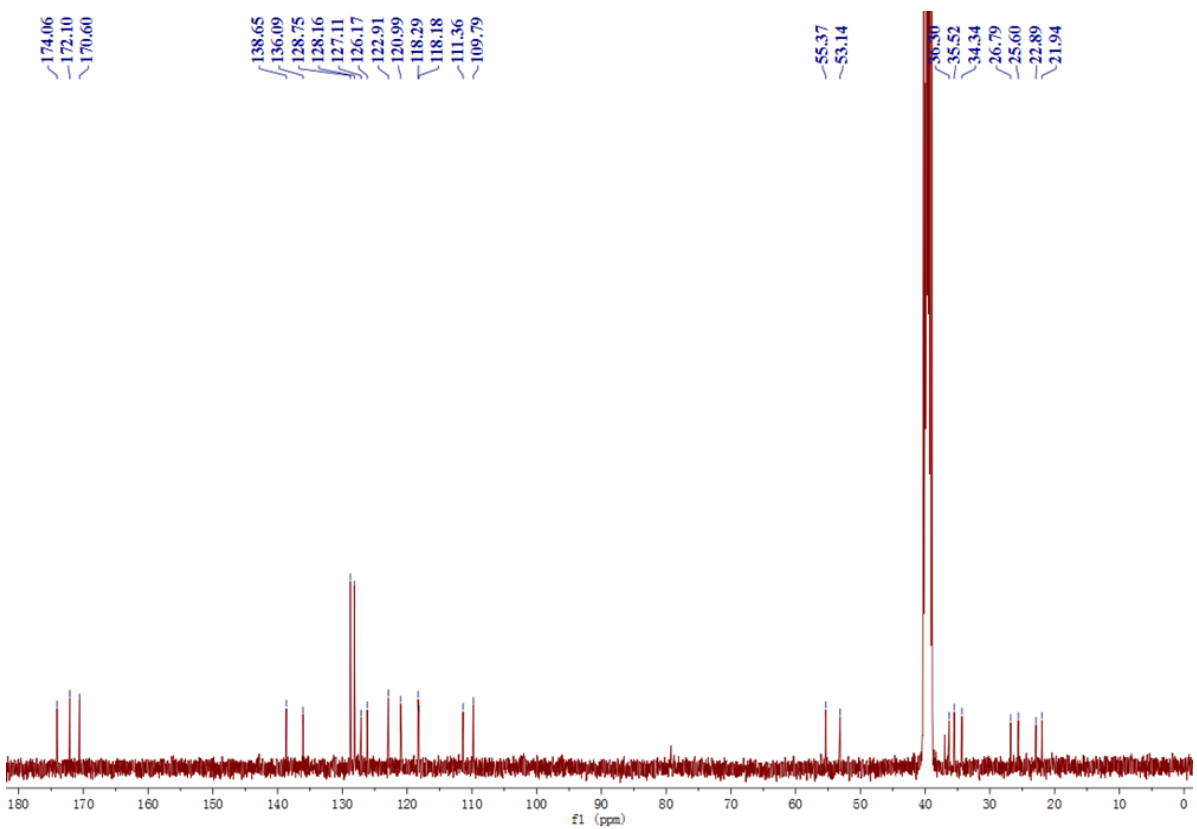
^1H NMR of c[β Ala-D-Trp-Phe- β Ala] (RDM1127)



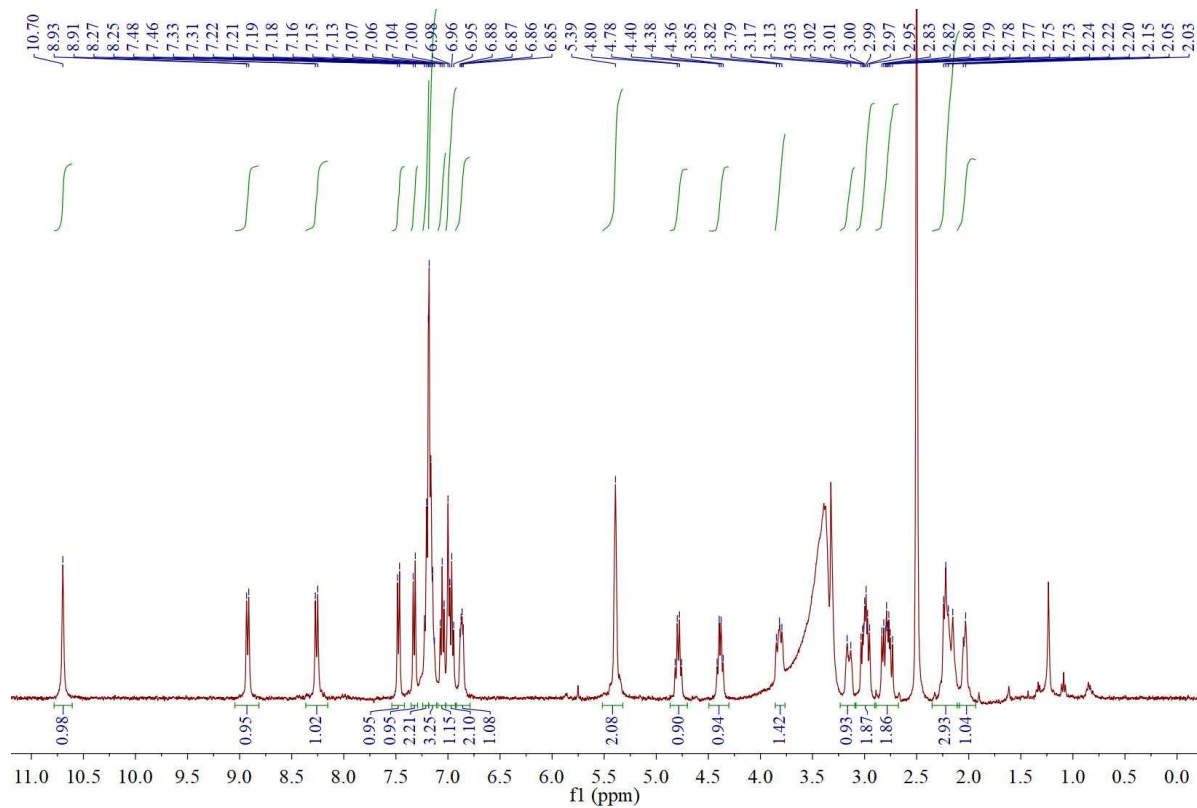
^{13}C NMR of c[β Ala-D-Trp-Phe- β Ala] (RDM1127)



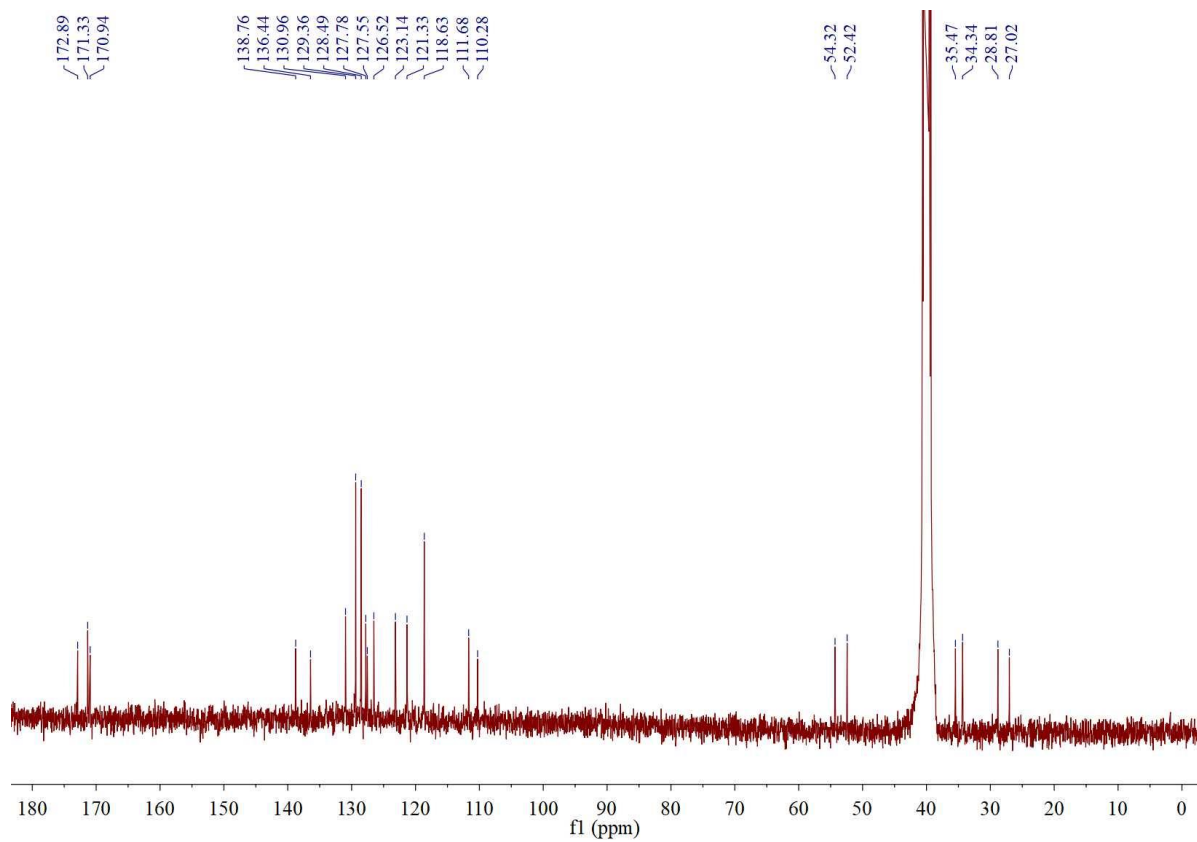
¹H NMR of c[EACA-D-Trp-Phe] (RDM1133)



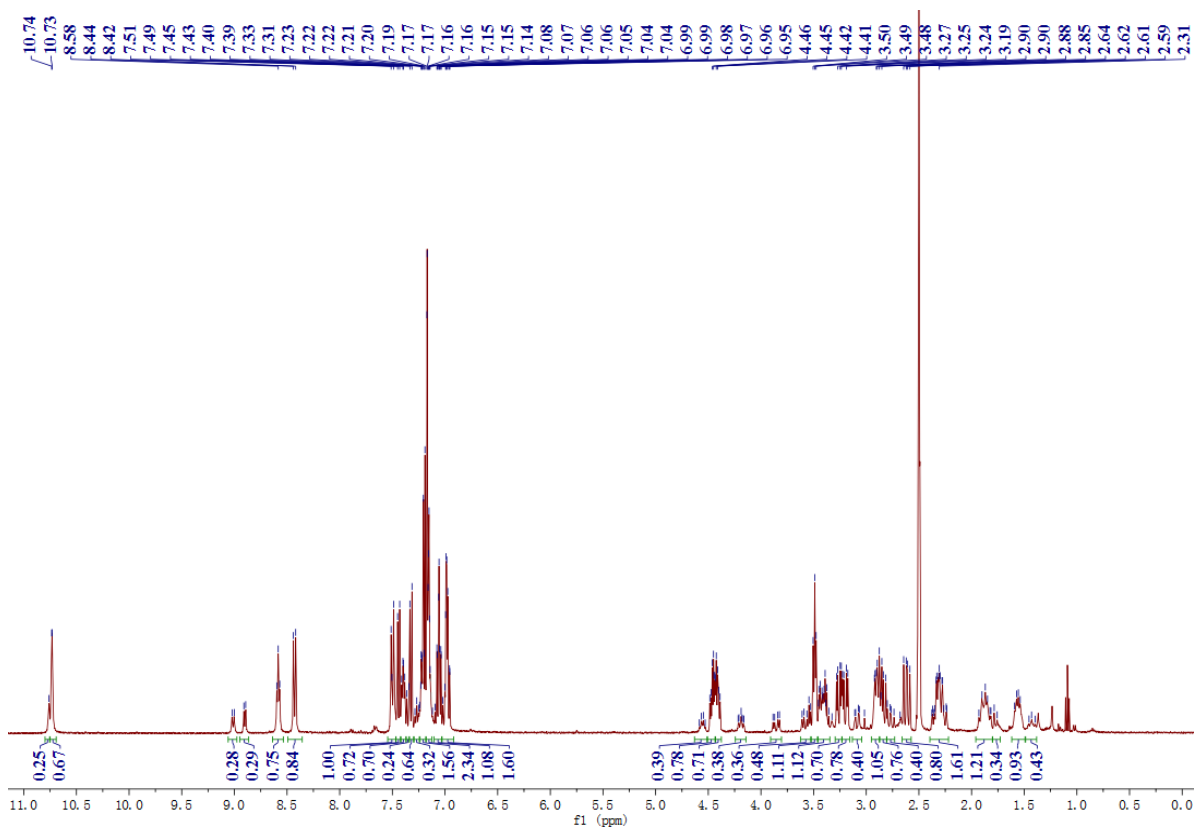
¹³C NMR of c[EACA-D-Trp-Phe] (RDM1133)



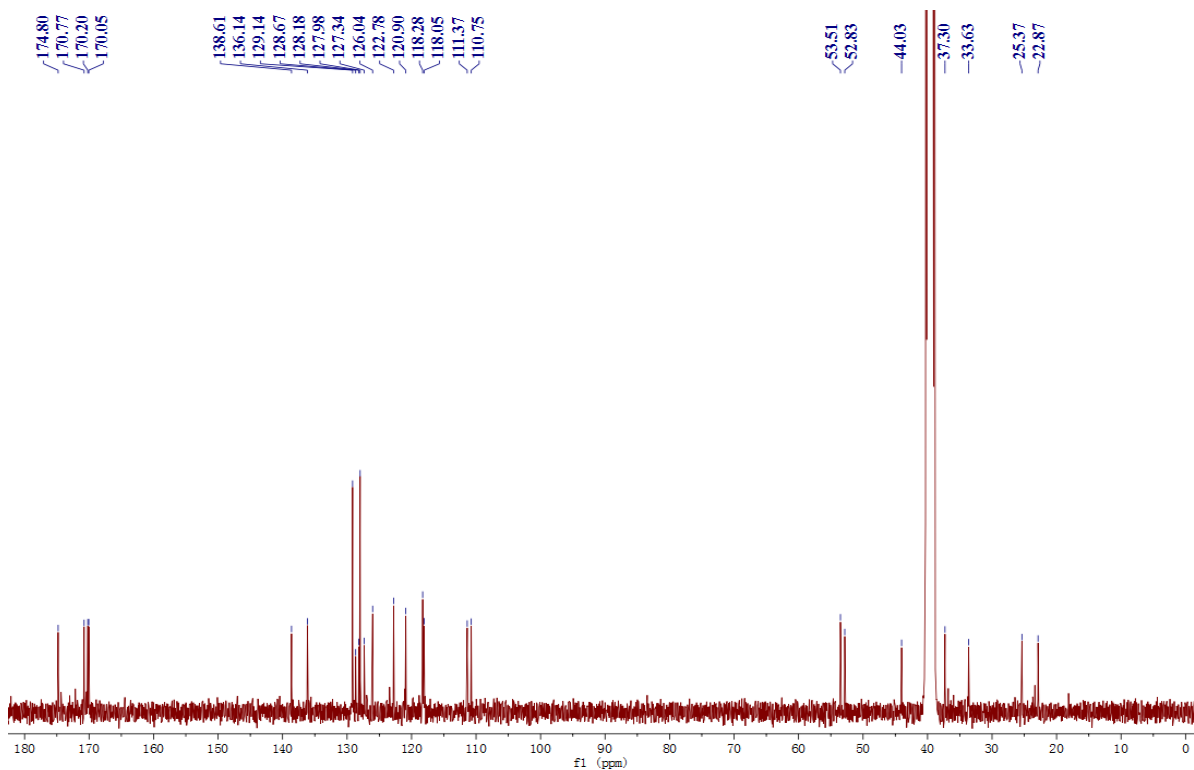
¹H NMR of c[ε-AHEA-D-Trp-Phe] (JW239)



¹³C NMR of c[ε-AHEA-D-Trp-Phe] (JW239)



¹H NMR of c[Gly-D-Trp-Phe-GABA] (RDM1135)



¹³C NMR of c[Gly-D-Trp-Phe-GABA] (RDM1135)

3.3 Variable Temperature NMR, gCOSY and 2D ROESY

Dissolve the samples in 8:2 [D₆] DMSO/H₂O in a 5 mm NMR tube to give the final concentration of 0.01M. Interestingly, the mixture of 8:2 [D₆] DMSO/H₂O was used as an excellent representative of biological environment for analyzing opioid peptides. In addition, since the chemical shifts of non-exchangeable protons within the concentration range of 0.01-0.04M are reproducible, self-association of peptides/peptidomimetics is excluded. The PRESAT program implemented by Varian achieved the suppression of the water peak in the NMR spectrum, and the proton resonance distribution is completed by gCOSY. The VT ¹H NMR experiment was performed in the range of 298-348 K, and the temperature calibration was carried out by ethylene glycol OHCH_n chemical shift separation method. The two-dimensional ROESY experiments were accomplished at rt, phase-sensitive mode, spin-locked field (γb_2) was 2000 Hz, and mixing time was 250 ms. Spectra were processed in the hypercomplex approach and the peak was calibrated with the solvent [D₆]DMSO. The cross-peak intensity was related to the distance (Å): very strong was 2.3, strong was 2.6, medium was 3.0, and weak was 5.0. The intensities of the cross-peaks produced by known protons (e.g. geminal) match these associations, but were discarded. For the case of no $H\alpha(i,i+1)$ ROESY cross peak, all ω bonds are set to 180° (f constant: 16 kcal mol⁻¹ Å⁻²). Using the standard TIP3P model of equilibrium water, the random geometry of each peptide was obtained through high temperature unlimited molecular dynamics simulation. The distances between the protons of these compounds were analyzed by the different intensities of the cross peaks in the 2D ROESY spectra, and then the inferred distances between the protons were used as the constraint, without introducing the hydrogen bond and torsion angle constraints, and set the ω bond to 180°. Then, high-temperature constrained molecular dynamics were performed on the structure with a scaled force field, and then a fully constrained simulation was performed. After cooling the box slowly, the representative conformers with the lowest energy were obtained by rmsd analysis.

3.4 ¹H-¹H ROESY Data

Non-obvious REOSY cross peaks in 8:2 [D₆]DMSO/H₂O; vs = very strong, s = strong, m = medium, w = weak.

c[Phe-Gly-GABA-D-Trp] (LOR19org) ¹H-¹H ROESY

Cross peak	Inten -sity	Cross peak	Inten -sity	Cross peak	Inten -sity
PheNH - PheH β 2.8	s	GlyNH - PheH β 3.0	w	GABANH - TrpH α	w
PheNH - PheH β 3.0	m	GlyNH - GlyH α 3.6	s	PheH α - PheH β 2.8	s
PheNH - PheH α	m	GlyNH - GlyH α 3.7	s	PheH α - PheH β 3.0	s
PheNH - TrpH α	vs	GlyNH - PheH α	s	TrpH α - TrpH β	vs
PheNH - GABANH	ww	GlyNH - TrpH α	w	TrpH α - GABAH γ 3.5	w/m
PheNH - TrpArH2	w	GlyNH - GABANH	s	GABAH γ 3.5 - GABAH β 1.6	s
PheNH - PheArH	s	TrpArH4 - TrpH β	s	GABAH γ 3.5 - GABAH β 1.8	vs
PheNH - TrpArH4	ww	TrpArH4 - TrpH α	s	GABAH γ 3.5 - GABAH α 2.1	s
PheNH - GlyNH	s/m	TrpArH7 - TrpH β	w	GABAH γ 3.5 - GABAH α 2.2	vs
PheNH - TrpH β	ww	PheArH - PheH α	s	GABAH γ 2.8 - GABAH β 1.6	s
TrpNH - GABAH α 2.0	m	GABANH - GABAH β 1.6	w/m	GABAH γ 2.8 - GABAH β 1.8	s
TrpNH - GABAH α 2.2	vs	GABANH - GABAH β 1.8	w/m	GABAH γ 2.8 - GABAH α 2.1	m
TrpNH - TrpH β	vs	GABANH - GABAH α 2.2	ww	GABAH γ 2.8 - GABAH α 2.2	s

TrpNH - TrpH α	m/s	GABANH - GABA γ 2.8	vs	TrpH β - GABA α 2.1	w
TrpNH - GABANH	w	GABANH - GABA γ 3.5	s	GABA α 2.2 - GABA β 1.6	vs
TrpNH - TrpArH2	m	GABANH - GlyH α 3.6	m	GABA α 2.2 - GABA β 1.8	s
TrpNH - TrpArH4	w	GABANH - GlyH α 3.7	m	GABA α 2.1 - GABA β 1.6	m
TrpNH - GlyNH	w/m	GABANH - PheH α	w	GABA α 2.1 - GABA β 1.8	s

c[Gly-D-Trp-Phe- β Ala] (RDM1125) ^1H - ^1H ROESY

Cross peak	Intensity	Cross peak	Intensity
TrpArH1 - PheArH3~5	ww	TrpArH4 - TrpH β \times 2	m
GlyNH - β AlaH α 2.3	m/s	TrpArH5 - TrpH α	w
GlyNH - β AlaH α 2.4	m/s	TrpArH6 - β AlaNH (or TrpArH5)	m(tocsy)
GlyNH - β AlaH β 3.2	w	PheArH2,6 - TrpH β \times 2	w
GlyNH - GlyH α 3.5	m	PheArH2,6 - PheH α	m
GlyNH - GlyH α 3.6	s/vs	PheArH2,6 - PheH β 2.7	s
GlyNH - β AlaNH (or TrpArH5)	ww	PheArH2,6 - PheH β 3.2	m
GlyNH - TrpNH	w/m	β AlaNH (or TrpArH5) - β AlaH α 2.4	w
TrpNH - β AlaH α 2.4	ww	β AlaNH (or TrpArH5) - β AlaH α 2.3	ww
TrpNH - TrpH β \times 2	vs	β AlaNH (or TrpArH5) - PheH β	ww
TrpNH - GlyH α 3.5	w	β AlaNH (or TrpArH5) - β AlaH β 3.6	m/w
TrpNH - GlyH α 3.6	s/vs	β AlaNH (or TrpArH5) - β AlaH β 3.2	m
TrpNH - TrpH α	m(tocsy)	β AlaNH (or TrpArH5) - PheH α	m/s
TrpNH - TrpArH2	w	TrpArH2 - TrpH β \times 2	m/w
TrpNH - β AlaNH (or TrpArH5)	w	TrpArH2 - TrpH α	w
PheNH - β AlaH α 2.4	ww	TrpH α - TrpH β \times 2	s
PheNH - PheH β 2.7	m/s	PheH α - PheH β 2.7	m/w
PheNH - TrpH β \times 2	m	PheH α - PheH β 3.1	m
PheNH - PheH β 3.1	w	β AlaH α 2.4 - β AlaH β 3.2	w
PheNH - PheH α	m(tocsy)	β AlaH α 2.4 - β AlaH β 3.6	m
PheNH - TrpH α	m	β AlaH α 2.3 - β AlaH β 3.2	m
PheNH - β AlaNH (or TrpArH5)	m	β AlaH α 2.3 - β AlaH β 3.6	m/w
PheNH - PheArH2,6	w		

c[β Ala-D-Trp-Phe- β Ala] (RDM1127) ^1H - ^1H ROESY

Cross peak	Intensity	Cross peak	Intensity
TrpArH1 - PheArH3-5	ww	β Ala 4 NH - β Ala 4 H α 2.1	w/ww
PheNH - PheH β 2.7	m	β Ala 4 NH - β Ala 4 H α 2.2	w/ww
PheNH - TrpH β 2.9	ww	β Ala 4 NH - β Ala 4 H β 3.3	m/s
PheNH - PheH β 3.0	w/ww	β Ala 4 NH - β Ala 4 H β 3.4	m/s

PheNH - TrpH α	s	β Ala ⁴ NH - PheH β 2.7	ww
PheNH - TrpArH2	ww	β Ala ⁴ NH - PheH α	m
PheNH - PheArH2,6	m/w	β Ala ⁴ NH - TrpH α	ww
PheNH - β Ala ⁴ NH	m	PheArH3-5 - PheH β 2.7	ww
PheNH - β Ala ¹ NH(or TrpArH4)	ww	PheArH3-5 - PheH β 3.0	ww
PheNH - PheH α	tocsy/m	PheArH2,6 - PheH β 2.7	s/m
TrpNH - β Ala ¹ H α 2.3	w	PheArH2,6 - PheH β 3.0	s/m
TrpNH - β Ala ¹ H α 2.4	s/vs	PheArH2,6 - PheH α	s/m
TrpNH - TrpH β 2.8	s	TrpHArH2 - TrpH β 2.8	m/w
TrpNH - TrpH β 2.9	m	TrpArH2 - TrpH β 2.9	m/w
TrpNH - β Ala ¹ H β 3.2	m	TrpArH2 - PheH α	ww
TrpNH - TrpH α	tocsy/m	TrpArH2 - TrpH α	m
TrpNH - TrpArH2	ww	TrpH α - TrpH β 2.8	s/m
TrpNH - β Ala ⁴ NH	ww	TrpH α - TrpH β 2.9	m
TrpNH - β Ala ¹ NH(or TrpArH4)	ww	PheH α - PheH β 2.7	tocsy/m/w
β Ala ¹ NH(or TrpArH4) - β Ala ⁴ H α 2.1	s	PheH α - PheH β 3.0	m
β Ala ¹ NH(or TrpArH4) - β Ala ⁴ H α 2.2	s	β Ala ¹ H β 3.5 - β Ala ¹ H α 2.3	m/w
β Ala ¹ NH(or TrpArH4) - β Ala ¹ H α 2.3	m/w	β Ala ¹ H β 3.5 - β Ala ¹ H α 2.4	w
β Ala ¹ NH(or TrpArH4) - β Ala ¹ H α 2.4	m/w	β Ala ⁴ H β 3.4 - β Ala ⁴ H α 2.1	m
β Ala ¹ NH(or TrpArH4) - TrpH β 2.8	m/w	β Ala ⁴ H β 3.4 - β Ala ⁴ H α 2.2	m
β Ala ¹ NH(or TrpArH4) - TrpH β 2.9	m/w	β Ala ⁴ H β 3.3 - β Ala ⁴ H α 2.1	m
β Ala ¹ NH(or TrpArH4) - β Ala ¹ H β 3.2	s/m	β Ala ⁴ H β 3.3 - β Ala ⁴ H α 2.2	m
β Ala ¹ NH(or TrpArH4) - β Ala ¹ H β 3.5	s/m	β Ala ¹ H β 3.2 - β Ala ¹ H α 2.3	m
β Ala ¹ NH(or TrpArH4) - TrpH α	m	β Ala ¹ H β 3.2 - β Ala ¹ H α 2.4	m
β Ala ¹ NH(or TrpArH4) - TrpArH5	tocsy/m		

c[ϵ -Ahea-D-Trp-Phe] (JW239) ¹H-¹H ROESY

Cross peak	Intensiy	Cross peak	Intensity	Cross peak	Intensity
PheNH - PheH β 2.7	s	TrpNH - TrpH α	m	AheaNH - AheaH ϵ 3.1	vs
PheNH - PheH β 3.0	m	TrpNH - AheaH γ + AheaH δ	w	AheaNH - AheaH ϵ 3.8	m
PheNH - PheH α	m	TrpArH4 - TrpH β 2.8	s	AheaNH - PheH α	s/vs
PheNH - TrpH α	vs	TrpArH4 - TrpH β 2.9	s	AheaNH - AheaH γ + δ	w/m
PheNH - AheaH γ + δ	ww	TrpArH4 - TrpH α	m	AheaH γ - AheaH β 2.2	m/s
PheNH - AheaNH	w/m	PheArH - PheH β 2.7	vs	AheaH γ - AheaH β 2.1	m/s
PheNH - TrpArH2	w	PheArH - PheH β 3.0	vs	AheaH δ - AheaH ϵ 3.1	m/s
PheNH - PheArH	w	PheArH - PheH α	m/s	AheaH δ - AheaH ϵ 3.8	m
PheNH - TrpArH4	ww	PheArH - TrpArH5	ww	TrpH α - TrpH β 2.8	m
TrpNH - AheH α 2.3	vs	TrpArH2 - TrpH β 2.8	w	TrpH α - TrpH β 2.9	m
TrpNH - TrpH β 2.8	s	TrpArH2 - TrpH β 2.9	ww	PheH α - PheH β 2.7	m

TrpNH - TrpH β 2.9	s	TrpArH2 - TrpH α	m/s	PheH α - PheH β 3.0	m/s
--------------------------	---	-------------------------	-----	----------------------------------	-----

c[Gly-D-Trp-Phe-GABA] (RDM1135) ^1H - ^1H ROESY

Cross peak	Inten-sity	Cross peak	Inten-sity	Cross peak	Inten-sity
GlyNH - GABAH α 2	vs	GABANH - GABAH β 1.9	w	PheH α - PheH β 2.6	m
GlyNH - GlyH α 2	s	GABANH - GABAH α 2	w	PheH α - PheH β 3.3	s
TrpNH - TrpH β 2.9	m/s	GABANH - GABAH γ 2.9	s	TrpH α - TrpH β 2.9	m
TrpNH - GlyH α 2	s	GABANH - GABAH γ 3.4	m	TrpH α - TrpH β 3.2	s
TrpNH - TrpH α	m	GABANH - PheH α	m	GABAH γ 3.4 - GABAH β 1.6	m
TrpNH - PheNH	m	GABANH - PheArH	m/w	GABAH γ 3.4 - GABAH β 1.9	m
PheNH - PheH β 2.6	s	PheArH - PheH β 2.6	vs	GABAH γ 3.4 - GABAH α 2	ww
PheNH - TrpH α	s/vs	PheArH - PheH β 3.3	s	GABAH γ 2.9 - GABAH β 1.6	m/w
PheNH - PheH α	m	PheArH - PheH α	w/m	GABAH γ 2.9 - GABAH α 2	ww
TrpArH4 - TrpH β 2.9	w/m	TrpArH2 - TrpH β 2.9	m/w	GABAH α 2 - GABAH β	m/s
TrpArH4 - TrpH β 3.2	w	TrpArH2 - TrpH β 3.2	w		
TrpArH4 - TrpH α	w/m	TrpArH2 - TrpH α	m		

c[Phe-Gly-Ala-D-Trp] (RDM1143) ^1H - ^1H ROESY

Cross peak	Intensity	Cross peak	Intensity
PheNH - D-TrpH α	m	AlaNH - GlyH α 4.1	m
GlyNH - PheH α	m	AlaNH - GlyNH	w
D-TrpNH - AlaH α	m	D-TrpArH2 - D-TrpH α	w
D-TrpNH - D-TrpH β 3.1	w	PheH β 3.0 - GlyNH	w
AlaNH - AlaMe	w/m		

c[Gly¹-D-Trp-Phe-Gly⁴] (RQ40PP1) ^1H - ^1H ROESY

Cross peak	Intensity	Cross peak	Intensity
PheNH - PheH β 2.7	w	D-TrpArH4 - D-TrpH β 2.8	w
PheNH - D-TrpH α	m	D-TrpArH4 - D-TrpH β 3.1	ww
PheNH - PheArH3,5	w	D-TrpArH4 - D-TrpH α	ww
Gly ⁴ NH - PheH α	m	PheArH2,4,6 - PheH β 2.7	m
Gly ⁴ NH - PheArH2,4,6	w/m	PheArH2,4,6 - PheH β 3.0	m
Gly ⁴ NH - D-TrpArH4	m	D-TrpArH2 - D-TrpH α	w
D-TrpNH - Gly ¹ H α 3.8	m/s	D-TrpH α - Gly ⁴ H α 4.0	m
D-TrpNH - D-TrpArH7	m/s	D-TrpH α - D-TrpArH ₂	ww
Gly ¹ NH - Gly ⁴ H α 4.0	w/m	D-TrpH α - PheArH2,4,6	w

c[Gly1-D-Trp-Phe-Gly4] (RQ35PP1) ¹H-¹H ROESY

Cross peak	Intensity	Cross peak	Intensity	Cross peak	Intensity
PheNH - D-TrpH β	w/m	GlyNH - AlaNH	m/s	D-TrpH α - D-TrpNH	m
PheNH - D-TrpNH	ww	D-TrpNH - D-TrpH7	s	GlyH α 4.1 - AlaMe	ww
PheNH - D-TrpH2	m/w	PheAr3,5 - D-TrpH β 2.7	s	GlyH α 3.6 - D-Trp β 3.1	ww
PheNH - PheAr2,4,6	m	PheAr3,5 - D-TrpH β 3.1	m	PheH β 2.8 - D-TrpH2	w
AlaNH - AlaMe	w	PheAr3,5 - PheH β 2.8	s	PheH β 2.8 - D-TrpH4	w
AlaNH - GlyH α 3.6	m/w	PheAr3,5 - PheH β 3.0	m	PheH β 2.8 - PheNH	w
AlaNH - GlyNH	m/s	PheAr3,5 - PheH α	m		
GlyNH - D-TrpH4	m/w	PheAr3,5 - D-TrpH2	m		

3.5 Human KOR Binding Affinity.

As previously reported [20], displacement binding assays were performed in HEK-293 cells stably expressing human KOR. The human KOR on the cell membrane was measured by the saturation binding assay of [³H] U69,593, and concentration of [³H] U69,593 range of 20 pM to 5 nM. To perform displacement binding assays, HEK-293 cells containing human KOR were combined with 2 nM [³H] U69,593 in a buffer containing 100 mM Tris-HCl and 0.3% BSA at room temperature, with or without cyclic peptides/peptidomimetics (at various concentration, 10⁻¹²-10⁻⁴ M), incubate together for 2 hours. The peptides/peptidomimetics were made into a stock solution (10⁻² M) in EtOH and avoid light. Stock solution was then diluted with assay buffer. The reaction was terminated by filtration with a Whatman GF/C filter presoaked with 0.3% polyethyleneimine, which was washed 3 times with 5 mL of ice-cold 50 mM Tris-HCl buffer (pH 7.4). The captured radioactivity was measured by liquid scintillation spectroscopy. GraphPad Prism was used to fit data from at least three independent experiments through nonlinear regression analysis. K_i values were calculated from IC₅₀ using Cheng-Prusoff equation.

3.6 Assay of Inhibition of cAMP Accumulation for Cyclic Peptides/Peptidomimetics.

The inhibition of cAMP accumulation for cyclic peptides/peptidomimetics was performed in whole HEK-293 cells stably expressing KOR and U87-MG human astrocytoma cells endogenously express hKOR. HEK-293 cells were cultured in MEM, 2 mM Gln, and 1× nonessential amino acids supplemented with 10% fetal bovine serum (FBS, 37°C and 5% CO₂). Cells were placed in a T75 tissue culture flask and split into 24 wells and incubated overnight when most of the cells reached 95-100% confluence. The medium was removed and washed with PBS 3 times when cells reached 85-95% confluence. Then cells were cultured in serum-free medium containing 3-isobutyl-1-methylxanthine (0.5 mM) and 10 μM forskolin. After exposing to U50,488 or cyclic peptides/peptidomimetics (1 pM to 100 μM) at 37°C for 15 minutes, cells were lysed in 0.1 N HCl and scraped off followed by centrifugation (2000 g, 5 min), and the cAMP concentration in the supernatants were determined using the cAMP EIA kit. The assays of inhibition of cAMP accumulation for cyclic peptides/peptidomimetics on U87-MG human astrocytoma cells is similar with on HEK-293 cells. The only difference was the cells growth medium, which was MEM, 10% fetal bovine serum (FBS), 100 units/mL penicillin, 100 μg/mL

streptomycin at 37 °C containing 5% CO₂.

4. Conclusions

In order to screen for novel KOR/MOR/DOR agonists/antagonists with strong receptor affinity, herein, new analogs of CJ-15,208 were synthesized. The inspiration for synthesizing these compounds came from our previous work, namely the peptidomimetic LOR17 (c[Phe-Gly-(beta-Ala)- D-Trp]), which is a selective KOR antagonist ($K_i = 1.19$ nM). The new synthesized analogs maintain the cyclic peptidomimetic structure of LOR17, and Gly² and beta-Ala³ were replaced with other natural/unnatural amino acids to change its flexibility or rigidity in binding to the opioid receptors. From human KOR binding affinity assays in HEK-293/KOR cells and U87-MG cells, it was found that RDM1127 has a strong affinity for the kappa opioid receptor ($K_i = 0.55 \pm 0.04$ nM), but it did not inhibit forskolin-induced cAMP accumulation in either HEK-293/hKOR cells or in U87-MG cells. It should be noted that in the absence of RDM1127, the IC₅₀ value of U50,488 to KOR is 2.1 nM, and U50,488 has an 88% inhibition of forskolin-induced cAMP accumulation. But when 10 μM RDM1127 was coadministered with U50,488, the IC₅₀ value is 1.7 nM, and it only has a 44% inhibition of forskolin-induced cAMP accumulation. In other words, RDM1127 is a KOR antagonist. Another compound that needs to be mentioned is RDM1135WP, which showed a moderate affinity to KOR ($K_i = 102 \pm 3$). KOR reference compounds U50,488 has an IC₅₀ values of 1.2 nM and an E_{max} of 90% in assays of inhibiting forskolin-induced cAMP accumulation in HEK-293/hKOR cells, and has IC₅₀ values of 1.4 nM, and E_{max} of 88% in U87-MG cells. Compared with U50,488, IC₅₀ values of RDM1135WP was 16.6 nM and E_{max} was 32% in assays of inhibiting forskolin-induced cAMP accumulation in HEK-293/hKOR cells. And in U87-MG cells, IC₅₀ value of RDM1135WP was 59.6 nM, and E_{max} was 42%. This means that RDM1135WP is a KOR partial agonist.

References

1. R. Al-Hasani, M.R. Bruchas. Molecular mechanisms of opioid receptor-dependent signaling and behavior. *Anesthesiology* **2011**, *115*, 1363-1381.
2. I.S. Zagon, M.F. Verderame, P.J. McLaughlin. The biology of the opioid growth factor receptor (OGFr). *Brain Res. Rev.* **2002**, *38*, 351-376.
3. H. Machelska, M. O. Celik. Advances in achieving opioid analgesia without side effects. *Front. Pharmacol.* **2018**, *9*, 1388.
4. M. Zielińska, T. B. Haddou, G. Cami-Kobeci, M. Sałaga, A. Jarmuż, M. Padyś, R. Kordek, M. Spetea, S. M. Husbands, J. Fichna Anti-inflammatory effect of dual nociceptin and opioid receptor agonist, BU08070, in experimental colitis in mice. *Eur. J. Pharmacol.* **2015**, *765*, 582-590.
5. P.-E. Lutz, B. L. Kieffer. Opioid receptors: distinct roles in mood disorders. *Trends Neurosci.* **2013**, *36*, 195-206.
6. H. Rawal, B. M. Patel. Opioids in cardiovascular disease: therapeutic options. *J. Cardiovasc. Pharmacol. Ther.* **2018**, *23*, 279-291.
7. P. C. S. Chung, B. L. Kieffer. Delta opioid receptors in brain function and diseases. *Pharmacol. Ther.* **2013**, *140*, 112-120.
8. C. Friesen, I. Hormann, M. Roscher, I. Fichtner, A. Alt, R. Hilger, K.-M. Debatin & E. Miltner. Opioid receptor activation triggering downregulation of cAMP improves effectiveness of anti-cancer drugs in treatment of glioblastoma, *Cell Cycle* **2014**, *13*, 1560-1570.
9. H. Pathan and J. Williams. Basic opioid pharmacology: an update. *Br. J. Pain.* **2012**, *6*, 11-16.
10. X.-T. Chen, P. Pitis, G. Liu, C. Yuan, D. Gotchev, C. L. Cowan, D. H. Rominger, M. Koblish, S. M. DeWire, A. L. Crombie, J. D. Violin, and D. S. Yamashita. Structure-activity relationships and discovery of a G protein biased μ opioid receptor ligand, [(3-methoxythiophen-2-yl)methyl]({2-[(9R)-9-(pyridin-2-yl)-6-oxaspiro-[4.5]decan-9-yl]ethyl})amine (TRV130), for the treatment of acute severe pain. *J. Med. Chem.* **2013**, *56*, 8019-8031

11. A.A Pradhan, M.L. Smith, B.L. Kieffer and C.J. Evans. Ligand-directed signalling within the opioid receptor family. *Br. J. Pharmacol.* **2012**, *167*, 960-969.
12. B. Kivell & T.E. Prisinzano. Kappa opioids and the modulation of pain. *Psychopharmacology* **2010**, *21*, 109-119.
13. T.W. Vanderah. Delta and kappa opioid receptors as suitable drug targets for pain. *Clin. J. Pain*, 2010, *26*, 1.
14. A. Bedini and S. Spampinato. Innovative opioid peptides and biased agonism: novel avenues for more effective and safer analgesics to treat chronic pain. *Curr. Med. Chem.* **2018**, *25*, 3895-3916.
15. L.C. Newman, D.R. Wallace, and C.W. Stevens. Selective opioid agonist and antagonist competition for [3H]-naloxone binding in amphibian spinal cord. *Brain Res.* **2000**, *884*, 184-191.
16. B. de Laat, N. Nabulsi, Y. Huang, S.S. O'Malley, J.C. Froehlich, E.D. Morris & S. Krishnan-Sarin. Occupancy of the kappa opioid receptor by naltrexone predicts reduction in drinking and craving, Jun **2020**, doi: 10.1038/s41380-020-0811-8.
17. G. Bart, J.H. Schluger, L. Borg, A. Ho, J.M. Bidlack, M.J. Kreek. Nalmefene induced elevation in serum prolactin in normal human volunteers: partial kappa opioid agonist activity? *Neuropsychopharmacology* **2005**, *30*, 2254-2262.
18. B. Greenwood-Van Meerveld and K.M Standifer. Methylnaltrexone in the treatment of opioid-induced constipation. *Clin. Exp. Gastroenterol.* **2008**, *1*, 49-58.
19. M. L. Jacobson, C. A. Browne, and I. Lucki. Kappa opioid receptor antagonists as potential therapeutics for stress-related disorders. *Annu. Rev. Pharmacol. Toxicol.* **2020**, *60*, 615-636.
20. T. Saito, H. Hirai, Y.-J. Kim, Y. Kojima, Y. Matsunaga, H. Nishida, T. Sakakibara, O. Suga, T. Sujaku and N. Kojima. CJ-15,208, a Novel Kappa Opioid Receptor Antagonist from a Fungus, *Ctenomyces serratus* ATCC15502. *J. Antibiot.* **2002**, *55*, 847-854.
21. R.E. Dolle, M. Michaut, B. Martinez-Teipel, P.R. Seida, C.W. Ajello, A.L. Muller, R.N. DeHaven, P.J. Carroll. Nascent structure-activity relationship study of a diastereomeric series of kappa opioid receptor antagonists derived from CJ-15,208. *Bioorg. Med. Chem. Lett.* **2009**, *19*, 3647-3650.
22. J.V. Aldrich, S.S. Kulkarni, S.N. Senadheera, N.C. Ross, K.J. Reilley, S.O. Eans, M.L. Ganno, T.F. Murray, and J.P. McLaughlin. Unexpected opioid activity profiles of analogues of the novel peptide kappa opioid receptor ligand CJ-15,208. *ChemMedChem.* **2011**, *6*, 1739-1745.
23. J.V. Aldrich, S.N. Senadheera, N.C. Ross, K.A. Reilley, M.L. Ganno, S.E. Eans, T.F. Murray, and J.P. McLaughlin. Alanine analogues of [D-Trp]CJ-15,208: novel opioid activity profiles and prevention of drug- and stress-induced reinstatement of cocaine-seeking behaviour. *Br. J. Pharmacol.* **2014**, *171*, 3212-3222.
24. R. De Marco, A. Bedini, S. Spampinato, L. Cavina, E. Pirazzoli, and L. Gentilucci. Versatile picklocks to access all opioid receptors: tuning the selectivity and functional profile of the cyclotetrapeptide c[Phe-D-Pro-Phe-Trp] (CJ-15,208). *J. Med. Chem.* **2016**, *59*, 9255-9261.
25. A. Bedini, L. Di Cesare Mannelli, L. Micheli, M. Baiula, G. Vaca, R. De Marco, L. Gentilucci, C. Ghelardini and S. Spampinato. Functional selectivity and antinociceptive effects of a novel KOPr agonist. *Front. Pharmacol.* **2020**, *11*, 188.
26. I.N. Rao, A. Boruah, S.K. Kumar, A.C. Kunwar, A.S. Devi, K. Vyas, K. Ravikumar, and J. Iqbal. Synthesis and conformational studies of novel cyclic peptides constrained into a 3₁₀ helical structure by a heterochiral D-Pro-L-Pro dipeptide template. *J. Org. Chem.* **2004**, *69*, 2181-2184.
27. R. De Marco, A. Bedini, S. Spampinato, L. Comellini, J. Zhao, R. Artali, and L. Gentilucci. Constraining endomorphin-1 by β,α -hybrid dipeptide/heterocycle scaffolds: identification of a novel κ -opioid receptor selective partial agonist. *J. Med. Chem.* **2018**, *61*, 5751-5757

Chapter 5. Review: Integrin-Targeting Peptides for the Design of Functional Cell-Responsive Biomaterials

Integrins are a family of cell surface receptors crucial to fundamental cellular functions such as adhesion, signaling, and viability, deeply involved in a variety of diseases, including the initiation and progression of cancer, of coronary, inflammatory, or autoimmune diseases. The natural ligands of integrins are glycoproteins expressed on the cell surface or proteins of the extracellular matrix. For this reason, short peptides or peptidomimetic sequences that reproduce the integrin-binding motives have attracted much attention as potential drugs. When challenged in clinical trials, these peptides/peptidomimetics let to contrasting and disappointing results. In the search for alternative utilizations, the integrin peptide ligands have been conjugated onto nanoparticles, materials, or drugs and drug carrier systems, for specific recognition or delivery of drugs to cells overexpressing the targeted integrins. Recent research in peptidic integrin ligands is exploring new opportunities, in particular for the design of nanostructured, micro-fabricated, cell-responsive, stimuli-responsive, smart materials.

1. Introduction

In the last 20 years, many studies focused on the implication of integrins in important cell activities, in the signaling from and to the cell, and in a variety of diseases. After the identification of the peptidic recognition sequences to different kinds of integrins, much effort has been dedicated to identifying peptidomimetic ligands with antagonistic properties, especially for cancer therapy, circulatory, or inflammatory diseases. These issues have been widely discussed earlier ^[1-5], and will be not proposed again herein. Despite good initial results *in vitro* and in animal models, clinical trials have not met the expectations. Nevertheless, peptidic integrin ligands still maintain a noteworthy appeal. This review aims at summarizing the more innovative applications of peptide-material conjugates: from nanoparticles (NPs) to new drug delivery systems, to functionalized surfaces, self-assembled monolayers (SAMs) and finally to smart and responsive materials. These conjugates are expected to allow a range of applications in theranostics, disease monitoring, regenerative medicines, and tissue engineering.

2. Integrins Structure and Functions

Integrins are cell adhesion receptors of soluble and insoluble glycoproteins of the extracellular matrix (ECM). These glycoproteins include collagens, fibronectins (FN), vitronectin (VT), laminins, fibrinogen (Fib), as well as cell surface receptors, e.g., the vascular cell adhesion molecule-1 (VCAM-1) and the intercellular adhesion molecule (ICAM). Furthermore, integrins are involved in the assembly of the actin cytoskeleton and signal transduction pathways of biological and cellular functions: cell adhesion, migration, proliferation, cell differentiation, and apoptosis. ^[6]

The integrins are type I heterodimeric transmembrane receptors composed of an α and a β subunits connected by non-covalent bonds. In mammals, 18 α and 8 β subunits have been discovered, and to date are known to combine into 24 distinct heterodimers. In both α and β subunits, a large N-terminal extracellular domain, a single transmembrane domain, and a short C-terminal intracellular cytoplasmic tail, can be identified. The only exception to this rule is the $\beta 4$ subunit, characterized by a long cytoplasmic portion (>1000 residues). ^[7]

The extracellular domain is composed of different highly organized subdomains, well-studied by high-resolution x-ray crystallography. The α subunit is formed by a β -propeller head domain, a thigh domain, and two calf domains. Some mammalian α subunits contain an additional portion called αA or I-domain. This last domain is very important because it contains the “metal-ion-dependent adhesive site” (MIDAS), which is the main domain responsible for ligand binding. When the I-domain is not present in the α subunit, the MIDAS is located inside an I-like domain of the β subunit. The I-like domain, together with a PSI (plexin/semaphorin/integrin) domain, a hybrid domain, four EGF repeats, and a B tail, constitute the β subunit (Figure 1). ^[8]

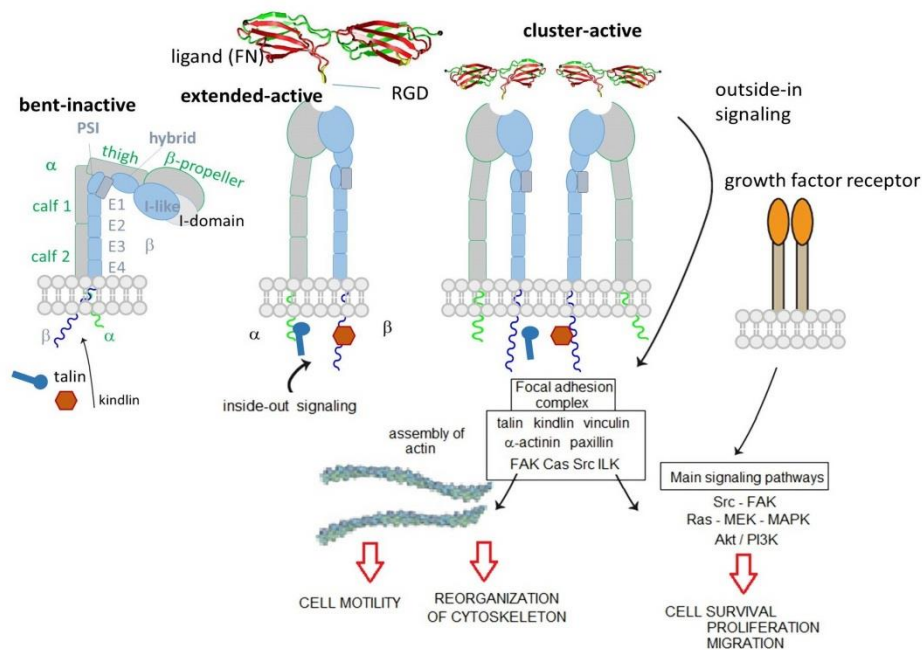


Figure 1. Bent-inactive, and open-active integrin states, and focal adhesions formation that consents outside-in downstream signaling.

The extracellular domain is responsible for ligand binding. Integrins can regulate their modules by shifting from a closed-resting structure to an open one that allows the binding and promotes the activation. The idle state consists of a bent conformation that straightens when the domain receives an impulse from within the cell (inside-out signal). The active conformation exposes the binding site and allows the ligand to connect and to activate the transmission of the signal inside the cell (outside-in signaling). Intracellularly, a large, dynamic multiprotein complex is formed, involving over 150 intracellular proteins, the so-called tight focal adhesions (FA), important for actin cytoskeletal assembly. Actin filaments are reorganized into larger stress fibers leading to further integrin clustering and enhanced matrix binding, allowing integrins to regulate cytoskeleton organization and cell motility. FAs are also responsible for the activation of further downstream signals to control various cellular functions like cell growth, apoptosis, cell proliferation, cell shape, and angiogenesis. In 2017, Springer et al. demonstrate that ultrasensitive integrin activation depends on adaptor binding and cytoskeletal force, which was quantitatively evaluated by measuring the free energy of different conformational states of integrin. [9]

3. Integrin-Related Diseases

As mentioned above, the different integrins are involved in a variety of diseases, including tumor metastasis, tumor invasion, angiogenesis, inflammation, thrombosis, osteoporosis, ocular diseases, restenosis, and autoimmune diseases, i.e., type-1 diabetes (T1D), multiple sclerosis (MS), rheumatoid arthritis (RA), and Crohn's disease. [10,11]

The integrin α IIb β 3 plays a key role in several diseases related to the cardiovascular system, like thrombosis, hemostasis, angina pectoris, and stroke. In particular, this heterodimer is responsible for platelet aggregation and adherence with soluble fibrinogen (Fib). As Fib molecules are bivalent, they can form an integrin-Fib-integrin bridge between adjacent platelets. [12]

Another pathology correlated to integrin α IIb β 3 is restenosis [13,14], i.e., the lumen diameter reduction or re-occlusion after the cardiovascular intervention, angioplasty, or stenting, due to migration of vascular smooth muscle cells (SMCs) towards the site of injury. This migration is critically dependent on the interaction between the integrin receptors highly expressed on the surface of SMCs with extracellular matrix component osteopontin which is upregulated during restenosis.

The integrins of the α 4 family are fundamental to the inflammatory processes, and in particular, α 4 β 1 integrin is crucial for the recruitment of leukocytes. [15] In the proximity of inflammation, the local release of cytokines and chemokines stimulates adjacent endothelial cells to overexpress VCAM-1 on their

vascular surfaces. The consequent production of chemoattractants and the activation of lymphocytes promote a conformational change that triggers integrin clustering along the contact surface. This movement rapidly strengthens integrin-ligand interaction and stops leukocytes rolling in the blood vessel. Once arrested, the immune cells can penetrate the underlying tissue (extravasation/diapedesis).

This process is also at the basis of many autoimmune disorders, including allergy, asthma, psoriasis, and Crohn's disease. These disorders are characterized by an inappropriate inflammatory response against self, which ultimately results in damage to the affected tissue. Autoimmune diseases (AD) such as rheumatoid arthritis, autoimmune encephalomyelitis, and multiple sclerosis (MS), are characterized by $\alpha 4\beta 1$ integrin-mediated invasion of "autoreactive" lymphocytes, while Celiac Disease is characterized by migration of T cells to the gut, guided by $\alpha 4\beta 7$ integrins. ^[16]

Osteoporosis is a degenerative disease characterized by low bone mass and bone degradation with resultant fragility and risk of fracture. Such a condition is caused by an increase in osteoclast differentiation and activity mediated by $\alpha \nu\beta 3$ and $\alpha \nu\beta 5$ integrins. ^[17]

The progression of ocular diseases such as retinopathy of prematurity (ROP), age-related macular degeneration (AMD), and proliferative diabetic neuropathy (PDR), depends on retinal neovascularization. Interaction of $\alpha \nu\beta 3$ and $\alpha \nu\beta 5$ integrins with components of the modified ECM, such as vitronectin, leads to the successful neovascularization of the retinal surface, which eventually extends towards the vitreous region of the eye. ^[18,19]

Furthermore, the engagement of integrins in cell activity, make $\alpha \nu\beta 3$ and other heterodimers like $\alpha \nu\beta 5$, $\alpha 5\beta 1$, $\alpha 6\beta 4$, $\alpha 4\beta 1$, and $\alpha \nu\beta 6$, responsible for development and progression of a large variety of cancers and in tumor angiogenesis. ^[20] Angiogenesis, i.e., the formation of new blood vessels, is a requirement for tumor growth and tumor metastasis. Moreover, the density of the microvasculature at the tumor site has been found to correlate well with the risk of distant metastasis.

4. Peptide and Peptidomimetic Integrin Ligands

Each integrin can bind a variety of ligands; on the other hand, one ligand, either a protein of the ECM or a cell surface adhesion protein, binds to multiple integrin receptors. Recent structure-function analyses of both integrins and their ligands have revealed a similar mode of molecular interaction that explains this promiscuity. In 1984, Pierschbacher and Ruoslahti described the Arg–Gly–Asp (RGD) peptide motif as a minimal integrin recognition sequence within FN. ^[21,22] Later, this tripeptide was found to bind to several other integrins: $\alpha \nu\beta 1$, $\alpha \nu\beta 3$, $\alpha \nu\beta 5$, $\alpha \nu\beta 6$, $\alpha \nu\beta 8$, $\alpha 5\beta 1$, $\alpha 8\beta 1$, and $\alpha \text{IIb}\beta 3$. Other integrins interact with their ligands by recognizing different ligand motif. For instance, $\alpha 4$ integrins ($\alpha 4\beta 1$ and $\alpha 4\beta 7$) recognize Leu–Asp–Val–Pro (LDVP) motif in FN, Leu–Asp–Thr–Ser (LDTS) sequence in the mucosal addressing cell adhesion molecule-1 (MAdCAM-1), and Ile–Asp–Ser (IDS) in VCAM-1.

A systematic study conducted by Kessler and co-workers ^[23], the so-called spatial screening, allowed to investigate the 3D disposition of the pharmacophoric groups of the RGD sequence. In this context, two cyclic molecules emerged: c[RGDfVG] (**1**), an inhibitor of Fib from binding to the integrin $\alpha \text{IIb}\beta 3$ (IC_{50} $\alpha \text{IIb}\beta 3/\text{FB}$ 5.0×10^{-8} M) and c[RGDfV] (**2**), which was shown to prevent the binding of VN to integrin $\alpha \nu\beta 3$ (IC_{50} $\alpha \nu\beta 3/\text{VN}$ 4.9×10^{-8} M). Structure-Activity Relationships (SAR) studies revealed that Val was the less important residue and, because of that, it was replaced or modified. This led to two important molecules, c[RGDfK] (**3**) and c[RGDf-N(Me)V] (**4**). The presence of a Lys allowed linking c[RGDfK] to other molecules or NPs or fluorescent probes, to create drug delivery or diagnostic systems (see next sections). c[RGDf-N(Me)V], or cilengitide, was renowned for its outstanding affinity (but not selectivity) for $\alpha \nu\beta 3$ integrins (IC_{50} 6.5×10^{-10} M) (Figure 2). Further N-methylation yielded c[RG-N(Me)D-f-N(Me)V] (**5**), which showed a slightly decreased affinity for $\alpha \nu\beta 3$ integrins (IC_{50} 5.9×10^{-9} M) but much higher selectivity over $\alpha \nu\beta 5$ and $\alpha 5\beta 1$ integrins. Starting from these cyclic structures, the retro (DGR), inverso (rGd), retro-inverso (dGr), and other peptidomimetic strategies ^[24–26] were extensively adopted (Figure 2).

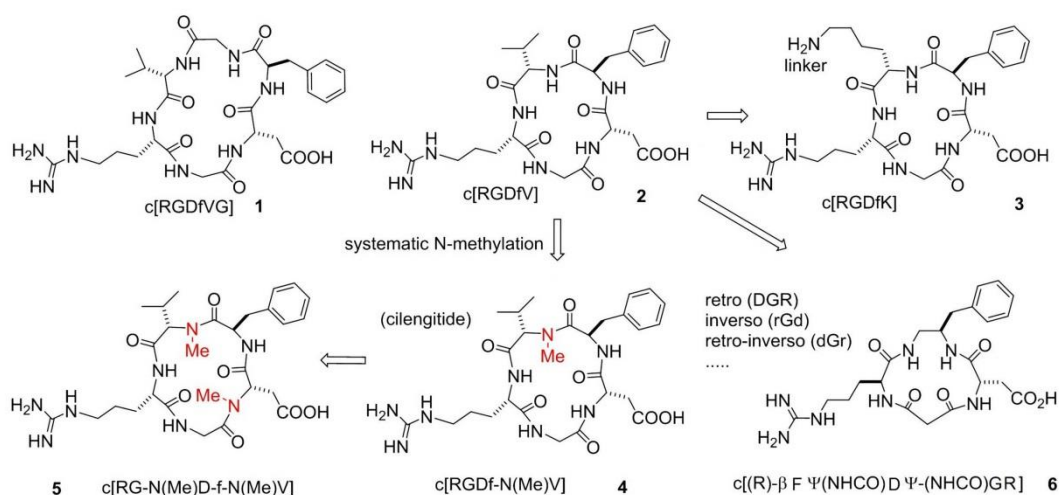


Figure 2. Examples of cyclopeptide integrin ligands: c[RGDFVG], and c[RGDFV], from which derive c[RGDFK], c[RGDF-N(Me)V], and c[(R)- β Phe Ψ (NHCO)Asp Ψ -(NHCO)Gly-Arg].

One meaningful example of peptidomimetic is the cyclotetrapeptide (CTP) c[(R)- β Phe Ψ (NHCO)Asp Ψ -(NHCO)Gly-Arg] (**6**), based on a partially modified retro-inverso (PMRI) variant of a CTP containing a β -amino acid, forming a 13-membered ring (Figure 2). This PMRI-CTP displayed a good activity in inhibiting the $\alpha\beta 3$ integrin-mediated cell adhesion of FN or VN (IC_{50} $\alpha\beta 3$ /FN on SK-MEL-24 cells 1.8×10^{-7} M), as well as the adhesion of FN to the $\alpha 5\beta 1$ integrin (IC_{50} $\alpha 5\beta 1$ /FN on K562 cells 2.4×10^{-8} M). This antagonist significantly inhibited bFGF-induced human endothelial cell tube formation at submicromolar concentrations.^[27] Conformational analysis and Molecular Docking calculations suggested that integrin specificity can be rationalized based on the display of the aromatic side-chain adjacent to Asp.

In the last 20 years, the RGD and other integrin-targeting peptide sequences became the models from which a huge number of peptidomimetics and non-peptides were designed.^[28,29] This wide topic has been adequately reviewed elsewhere;^[2-5,30] hence, it will be not discussed further here. As for cilengitide, for its potent antagonism for pro-angiogenic integrins $\alpha\beta 3$, $\alpha\beta 5$ and $\alpha 5\beta 1$, it became one of the most investigated anticancer peptides in vitro and in vivo. Preclinical in vitro studies confirmed that cilengitide was a potent inhibitor of angiogenesis, and promoted apoptosis in cancer cells obstructing the interaction between integrins and their ECM ligands.^[31,32] Furthermore, numerous in vivo experiments confirmed the previous results supporting the ability of cilengitide to block tumor growth in a dose-dependent fashion [33]. After these promising results, phase I and II trials in solid tumors and glioblastoma started, with cilengitide alone or in combination with radiotherapy and/or chemotherapy with temozolomide.^[34-37] As no dose-limiting toxicities (DLTs) were observed, the CENTRIC EIRTC phase II trial was started, but the latter lead to disappointing results. Cilengitide failed to demonstrate survival advantage and that it had a short plasma half-life. Subsequently, Massabeau, Khalifa, and co-workers^[38] proposed continuous exposure for optimal efficacy. This idea was pursued in a phase I clinical study that combined cilengitide and chemotherapy for stage III NSCLC (non-small cell lung cancer) patients. The results evidenced the safety profile of the administration of cilengitide as continuous infusion and suggested possible future investigations.

Despite of the (so far) failure for cancer treatments, integrin ligands remain privileged tools for other diseases. In particular, ligands that interfere with $\alpha 4$ integrin functions are currently investigated for inflammatory or autoimmune diseases correlated to leukocyte recruitment.^[1,39] BIO1211 (**7**), MPUPA-Leu-Asp-Val-Pro-OH (MPUPA, o-methylphenylureaphenylacetic acid), (Figure 3) is a potent inhibitor of $\alpha 4\beta 1$ integrin,^[40] which unfortunately is readily metabolized in heparinized blood, plasma and rat liver, lung and intestinal homogenates. Starting from the structure of BIO1211, Dattoli et al. designed an $\alpha 4\beta 1$ integrin inhibitor (**8**) containing the pyrrolidine-3-carboxylate (β^2 -Pro) scaffold (Figure 3). The hybrid structure conferred to this compound good enzymatic stability, being degraded of only about 10% in mouse serum after 120 min. The peptidomimetic efficiently inhibited the adhesion of $\alpha 4\beta 1$ integrin-expressing cell to VCAM-1.^[41] The retro-inverso approach was exploited to design BIO1211

peptidomimetics with a dehydro- β -proline core (**9**). The products showed to be effective and selective $\alpha 4\beta 1$ integrin antagonists and displayed IC_{50} values in the nanomolar range in cell adhesion inhibition assays and VCAM-1-induced phosphorylation of extracellular-signal-regulated kinases. Significant activity was observed also toward the homologous integrin $\alpha 4\beta 7$, but not toward the $\beta 1$, $\beta 2$, and $\beta 3$ families.^[42] Subsequently, a mimetic of BIO1211 containing a β^2/α -hybrid Freidinger lactam analog (**10**) was proposed (Figure 3),^[43] i.e., the aminomethylloxazolidine-2,4-dione scaffold (Amo).^[44] Interestingly, this mimetic displayed significant ability to inhibit the adhesion of $\alpha 4\beta 1$ integrin expressing cells (IC_{50} $\alpha 4\beta 1$ /VCAM on Jurkat cells 1.9×10^{-8} M), and remarkable stability in mouse serum.

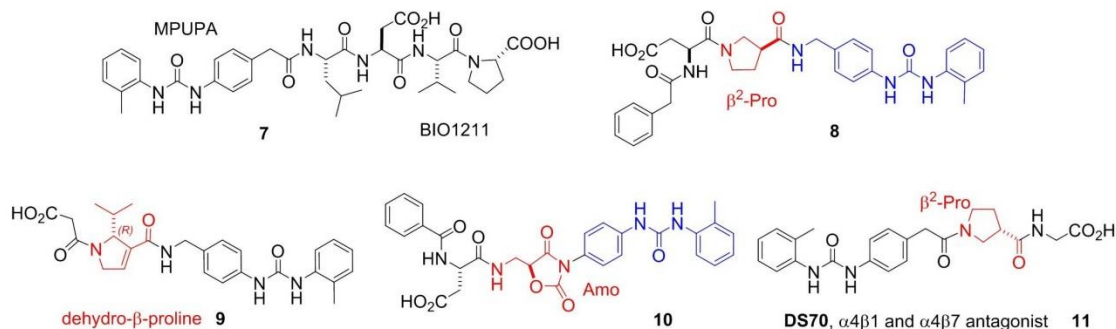


Figure 3. Examples of antagonist integrin ligands.

Finally, Dattoli et al.^[45] reported the α/β hybrid-peptide DS70 (**11**) (Figure 3). The affinity for $\alpha 4\beta 1$ integrin was determined in vitro in the scintillation proximity assay (IC_{50} $\alpha 4\beta 1$ integrin 8.3 nM). Consistently, DS70 reduced Jurkat cell adhesion to VCAM-1 (IC_{50} 5.04 nM) or FN (IC_{50} 4.3 nM). Furthermore, DS70 antagonized VCAM-1-mediated phosphorylation of ERK 1/2 in Jurkat E6.1 cells. Finally, the effects of topical treatment with DS70 on a guinea pig model of allergic conjunctivitis were evaluated, following direct administration in the conjunctival fornix. DS70 dose-dependently reduced clinical aspects of allergic conjunctivitis, conjunctival mast cell and eosinophil infiltration, $\alpha 4$ integrin expression, and levels of mRNAs for IL-1 β , IL-8 (CXCL8), CCL5, and CCL11, thus representing an alternative to antihistamines and mast cell-stabilizing agents.

Addressing Integrins with Agonist Ligands

Even though most of the efforts have been directed to the development of integrin antagonists, the discovery of agonists could represent a new perspective. In recent years, some agonist molecules have been disclosed, targeting different types of integrins. Celik and co-workers^[46] studied the capacity of leukadherin-1 to act as an agonist for $\alpha M\beta 2$, and thus be able to reduce neutrophil migration and inflammatory response. Using the structure of the well-known antagonist TBC3486, Dixon and co-workers^[47] designed and tested in vitro a new $\alpha 4\beta 1$ agonist, with the aim of increase cell retention and so improve progenitor cell therapy. Because previous works have shown that chemotherapy can affect more metastatic melanomas when cells are adherent to ECM instead of suspended. Schwartz and co-workers^[48] tested in vivo the chemotherapeutic drug combined or not with contortrostatin, a disintegrin from snake venom, and proved that stimulate integrin may help the efficacy of chemotherapy and help to reduce tumor growth. As the interaction between $\alpha L\beta 2$ and ICAM-1 plays an important role in the immune responses and leukocytes adhesion, this integrin has been the target of several studies. In particular, small molecule agonists were developed and tested^[49] to demonstrate that stimulation of $\alpha L\beta 2$ integrin facilitates cell signaling.

More recently, β -lactam-based ligands were designed for investigating the structural determinants of agonist vs. antagonist activity.^[50,51] The new ligands (Figure 4) showed nanomolar affinity and selectivity for integrins $\alpha \nu \beta 3$, $\alpha 5\beta 1$, or $\alpha 4\beta 1$, and agonist (**12**, **14**, **17–19**) or antagonist (**13**, **15**, **16**, **20**) activities on integrin-mediated cell adhesion. The best agonist molecules induced significant adhesion of SK-MEL-24 cells and Saos-2 cells as a valuable model for osteoblast adhesion. The latter result could lead to the development of new agents to improve cellular osseointegration and bone regeneration. Molecular modeling and docking studies on $\alpha \nu \beta 3$ or $\alpha 5\beta 1$ integrin supported the notion that ligand carboxylate fixing

to the metal ion-dependent adhesion site in the β -subunit can be sufficient for binding the receptors, while the aryl side chains play a role in determining the selectivity as well as agonism versus antagonism. [52]

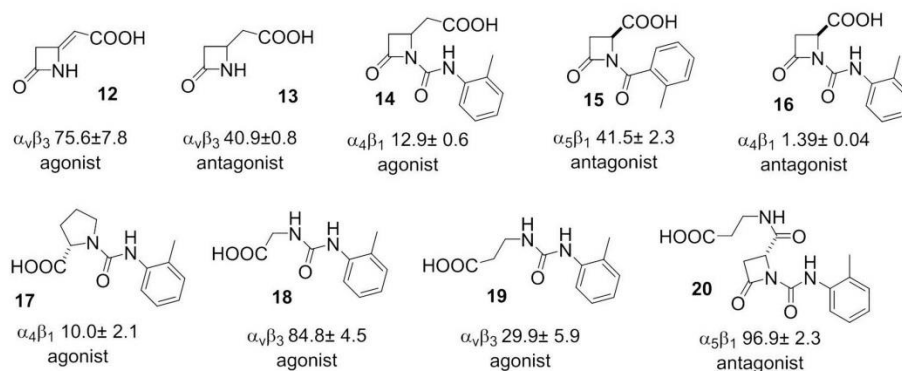


Figure 4. Examples of β -lactam based agonist or antagonist integrin ligands utilized for Structure-Activity Relationships (SAR) and modeling analysis of agonism vs. antagonism; the affinities (nM) for the specified integrins are also shown.

5. Integrin-Targeted Peptide Conjugates

The scarce bioavailability of most anticancer drugs represents a significant obstacle to their efficacy. Besides, most anticancer drugs also show a certain toxicity towards healthy cells. These problems can be solved by coupling the drugs to a carrier to improve its targeted delivery and internalization. There are several advantages for the construction of a carrier system, one of them is the ease of these systems to be internalized via receptor-mediated endocytosis, and thus be able to arrive in regions away from blood vessels, the ones previously impossible to reach. [53] Active and inactive integrins undergo a clathrin-mediated or caveolin-mediated endocytosis-recycling cycle, involved in different processes, such as cell migration, by detaching integrins from the extracellular matrix, integrin recycling and activation of different receptors (Figure 5). [54] Considering this, interest has focused on the construction of RGD conjugates with anticancer drugs, diagnostic probes, NPs, or nanocarriers for cancer therapy or imaging. [2,55,56] All of these drugs are designed to be more effective and reduce collateral damages.

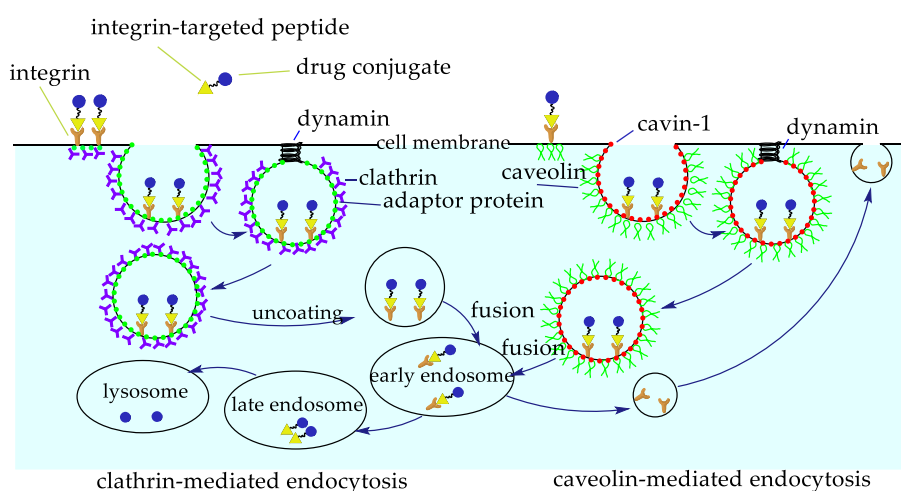


Figure 5. Integrin-targeted internalization of the Arg–Gly–Asp (RGD) peptide-drug conjugates via clathrin or caveolin mediated endocytosis.

Among these approaches, antibody-drug conjugates (ADCs) have met great success. However, they often suffer from limitations ascribable to their dimensions and their possible immunogenicity. [57] Small molecule-drug conjugates (SMDCs) are an alternative approach to ADCs, as they are usually designed to include a drug and a targeting ligand linked by a spacer. [58] To develop tumor-targeting conjugates, it is

suggested to introduce a cleavable bridge, which must be stable in human fluids, while being able to cleave and release the therapeutic payload after penetrating the tumor cells. Most SMDCs are internalized by the cell through receptor-mediated endocytosis; the internalized conjugate is then transferred to the early endosomes or in the lysosomes. As ADCs and SMDCs have been duly reviewed elsewhere, [2,56,58,59] these topics will be not analyzed in detail in this review.

6. Integrin-Targeted NPs

Most NPs used in biomedicine are inorganic, organic, or mixed, particles with dimensions comprised between 1 and 100 nm. Therapeutic NPs can be coupled to diagnostic probes, giving multimodal agents. In particular, the combination of NPs and RGD peptides has been widely explored in cancer and cardiovascular diseases. [2,56]

Nanoparticle delivery systems can be exploited to passively target the tumor and able to penetrate cancer cells, taking advantage of the enhanced permeation and retention (EPR) effect. NPs functionalized with properly disposed of peptide ligands onto the surface can promote the multivalent targeting of integrin receptors. The cargo-bearing NPs approach the receptor-embedded plasma membrane. The ligands bind the recognition domain of the receptors and trigger receptors clustering, and the cargo is internalized for subsequent intracellular trafficking. Binding NP to integrins can activate signaling pathways and subsequently affect cell proliferation, differentiation, or migration. Integrins synergize with other cell surface receptors, such as receptor protein tyrosine kinases, to activate signaling via ERK1/2 cascade. [60] NPs can be adsorbed onto plasma proteins in the bloodstream, then mononuclear phagocyte system may recognize and remove them from circulation. NPs surfaces can be coated with polyethyleneglycols (PEGs), to confer stealth properties with respect to non-specific uptake by the reticuloendothelial system (RES). Pegylation is a widely adopted strategy to increase circulating time in vivo, mostly due to the ability to evading macrophage-mediated uptake and removal from the systemic circulation. In addition, PEG prevents other molecules to bind by steric effects, as well as non-specific binding to proteins and cells. [61] Many protocols have been proposed for NP functionalization. The coupling strategy to be adopted depends on the stability of the NPs, the functional groups, the bioconjugation conditions, and the biomolecule to attach. Besides, depending on the conjugated biomolecule, it is important to control the orientation, so that the biomolecule remains active once conjugated to the NP. Biofunctionalization can be achieved by covalent coupling, including conjugate maleimide to thiols, or the azide-alkyne cycloaddition (CuAAC) reaction catalyzed by copper(I) to introduce functional groups, PEG or proteins. Alternatively, non-covalently physical interactions are also described but compared to covalent functionalization, they show some weaknesses, such as scarce stability, and the unreproducible and uncontrollable amount and orientation of the functionalization. [62]

6.1. Integrin-Targeted Organic NPs

6.1.1. Liposomes

Compared with other drug delivery systems, liposomes loaded with chemotherapeutic agents are supposed to prolong the circulation time in blood, increase the bioavailability and cell uptake. [63] Immuno-liposomes can be utilized to deliver cargos to targeted tissues, avoiding toxicity and side effects to normal tissues, and bio-responsive liposomes are designed for specific tissue targeting and controllable drug delivery. [64] Hydrophobic and hydrophilic molecules are inserted into the lipid bilayer or aqueous compartments, respectively (Figure 6A). This is particularly important for drugs such as paclitaxel (PTX), which is known to induce severe side effects and is practically insoluble in water.

To drive the liposomes towards the desired cells (e.g., cancer cells), preformed liposomes can be modified by conjugation with integrin ligands. [65] More often, integrin targeting liposomes have been prepared using phospholipids carrying integrin ligands. [66] To improve targeting of tumor vasculature, in 2010, Meng et al. prepared PTX-loaded liposomes, carrying RGD peptide and the ATWLPPR sequence, which is the ligand of the VEGF receptor neuropilin-1 (NRP-1). The bimodal liposomes enabled a greater internalization of PTX than either each of two single-targeted liposomes. [67]

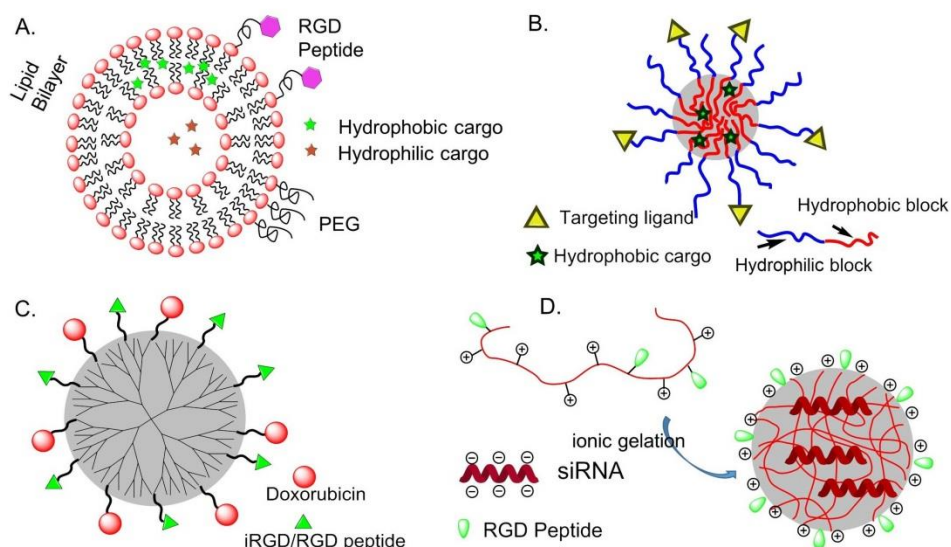


Figure 6. Integrin-targeted organic nanoparticles (NPs). (A) liposomes; (B) polymeric micelles; (C) dendrimers; (D) chitosan NPs.

6.1.2. Polymeric Micelles (PM)

Amphiphilic block or graft copolymers tend to self-assemble in aqueous media giving globular colloidal polymeric micelles (PM). Their core-shell architecture consents to load lipophilic antitumor agents into the hydrophobic core and the outer hydrophilic shell allows NPs to be stable in aqueous solution (Figure 6B). Generally, the copolymers are composed by hydrophobic materials that easily undergo hydrolytic or enzymatic degradation, such as PCL (poly (ϵ -caprolactone)), PLA (poly (lactic acid)), PLGA (poly(lactic-co-glycolic acid)), or temperature or pH variations, whereas PEG is commonly utilized for the hydrophilic segment.^[68]

In 2004, Gao and co-workers first prepared micelles composed of a PEG-PCL block copolymer ending by a maleimide, to which a thiolated-cRGDfK was conjugated. These micelles were able to deliver into SLK tumor cells.^[69] The same authors subsequently prepared RGD-functionalized PEG-PLA micelles loaded with Dox and superparamagnetic iron oxide NPs (SPIONs), for combining therapy and imaging (ultrasensitive MRI).^[70] In these examples, the payload is released upon structure degradation. In some cases, the drug is covalently conjugated to the block copolymer by a hydrazone bond or an amide bond.^[71] RGD-functionalized biocompatible synthetic polymers such as PEG, PLA, PLGA, PLL (poly (lactic lysine)), or natural polymers, chitosan, albumin, collagen, have been utilized to prepare integrin targeting biodegradable polymeric NPs. Drugs such as Paclitaxel, Mitoxantrone, and Fluorouracil can be incorporated in micelles without chemical modification or with conjugation to the polymers. Then, it can be released in a controlled manner by diffusion through the polymer matrix, by polymer degradation.^[72]

6.1.3. Dendrimers

In 2009, Waite et al. found that conjugating cyclic RGD to a poly(amidoamine) (PAMAM) dendrimer enhanced the penetration and delivery of short-interfering RNA (siRNA) through tumors in a manner that depended on the targeting ligand density.^[73]

In 2014, an effective anti-tumor drug delivery system PPCD (PEG-PAMAM-cis-aconityl-DOX) was prepared by covalently bonding or simply mixing the tumor penetrating peptide iRGD (internalizing-RGD, CRGDK/RGPD/EC) and the PAMAM dendrimer. Experiments have shown that it can increase the permeability of the tumor blood vessel and the accumulation of drugs in the tumor tissue (Figure 6C).^[74]

6.1.4. Chitosan

A positively charged chitosan NP is a talented siRNA delivery vehicle because of its advantage in cellular membranes transportation and endocytosis (Figure 6D). In 2010, Sood et al. conjugate RGD peptide to chitosan NP by thiolation reaction for targeted siRNA delivery. This strategy significantly enhanced

siRNA delivery to tumor tissues and vasculature, binding efficiency on $\alpha\text{v}\beta\text{3}$ integrin-expressing tumor cells, and therapeutic efficacy of gene silencing. [75]

6.1.5. Other Organic NPs

Doxorubicin-loaded human serum albumin NPs conjugated with an antibody targeting $\alpha\text{v}\beta\text{3}$ -positive M21 melanoma cells exhibited enhanced cytotoxicity as compared to free doxorubicin. [76] In 2013, splice-switching oligonucleotides (SSOs) was utilized to bond RGD peptide to serum albumin to prepare a nanoconjugate with a diameter of 13 nm. Because of the small size of nanoparticle and grafting of the tumor-targeting peptide, the ability to penetrate receptor-specific cells was 61 times higher than the control. Compared with other siRNA delivery vehicles, this nanoconjugate exhibits the advantages of high loading rate, increment tumor specificity, strong tumor permeability, and high therapeutic oligonucleotide activity. [77]

Poly (cystaminebisacrylamide-diaminohexane) [poly (CBA-DAH)] (CD) is a biodegradable and low-toxic polymer, that was bond to a tumor homing peptide c[RGDfC] by biofunctionalized PEG, c[RGDfC]-PEG-CD shielded on adenovirus (Ad) for reducing cytotoxicity and improving transduction efficiency. This oncolytic Ad expressing short hairpin RNA (shRNA) against interleukin-8 (IL-8) mRNA, after Ad/CD-PEG500-RGD was introduced in HT1080 cells. The expression of IL-8 and VEGF was inhibited and then induce apoptosis. [78]

6.2. Integrin-Targeted Inorganic NPs and QDs

Inorganic NPs of gold, silver semiconductors, magnetic compounds, alloys, silica, etc., display unusual size-dependent optical and/or magnetic properties, drastically different from those of their bulk materials, exploitable for detection and imaging, and the targeting of multifunctional therapeutics. [79]

6.2.1. Silica NPs

Silica NPs as tools to develop targeting probes and drug delivery systems have several advantages over other nanomaterial and self-organized systems. Indeed, silica is photophysically inert, is an intrinsically non-toxic material, and there are many synthetic approaches available to tune these nanosystems in terms of size and functionalization. The luminescence emission of these systems depends on the doping dye so that a large variety of emission properties can be achieved by just choosing the right doping dye(s). The inclusion of dye molecules in rigid matrix-like silica often increases the quantum yield of the dyes and also their photostability, because of the rigidification of dye structure and the protection towards quenching molecules present in the environment. These last two features are of prominent importance to univocally assign the recorded fluorescent signal to the presence of the NPs and to control the local concentration of the cytotoxic compound during the recognition event toward the targeted receptor.

In 2018, Jia et al. generated bifunctional 40 nm-sized silica NPs coated with controlled amounts of the peptides cRGD and ATWLPPR (neuropilin-1 (NRP1), a co-receptor of VEGFR2) and studied their affinity, selectivity and biological activity in HUVECs (Human Umbilical Vein Endothelial Cells). The results supported evidence for a complex cross-talk generated by the binding of the heteromultivalent NPs with $\alpha\text{v}\beta\text{3}$ -integrin and with NRP1. In particular, the NPs exerted dose-dependent pro-survival activity. This study demonstrated the difficulties in designing targeted silica-based NPs for antiangiogenic therapies and the possible risks posed by undesirable side effects. [80]

In 2020, Juthani et al. introduced ultrasmall fluorescent core-shell silica NPs, Cornell prime dots (C' dots), were functionalized with cRGD peptide, and PET (Positron Emission Tomography) labels (^{124}I , ^{89}Zr) to investigate the utility of dual-modality cRGD-C' dots for enhancing accumulation, distribution, and retention (ADR) in a genetically engineered mouse model of glioblastoma (mGBM). The results showed improvements in brain tumor delivery and penetration, as well as enhancement in the ADR, were observed following administration of integrin-targeted C' dots, as compared with a nontargeted control. [81]

6.2.2. Magnetic NPs

In 2009, the Ruoslahti group reported a cyclic peptide combining the tumor-homing RGD sequence with a tissue penetration motif. The homing sequence directs the peptide to the tumor vascular endothelium, while the tissue penetration motif, once activated by a protease, binds to a different receptor (neuropilin-1),

which mediates extravasation and tissue penetration. As a proof of concept, iRGD peptide-linked iron oxide nanoworms could be detected by MRI throughout a tumor once injected *in vivo* to mice.^[82] In 2011, the same group combined two different peptides with the magnetic nanoworms to image and treat mice with glioblastoma, one of the most difficult tumors to treat. While the CGKRG peptide targets the NPs to tumor vascular cells and into their mitochondria, the other peptide acts as a pro-apoptotic drug. By co-injecting these NPs with iRGD, most of the tumors were eradicated or their development delayed in two glioblastoma mouse models.^[83]

PEGylated copolymer-coated iron oxide NPs conjugated with an RGD-containing cyclic peptide c(RGDyK) was administered in a mouse model for targeting $\alpha v \beta 3$ integrins. Successful tumor homing was perceived in a subcutaneous U87MG glioblastoma xenograft model by magnetic resonance imaging (MRI) (Figure 7A).^[84] Similar integrin specific binding was achieved on HUVEC cells by using paramagnetic liposomes conjugated with the cyclic RGD peptide.^[85]

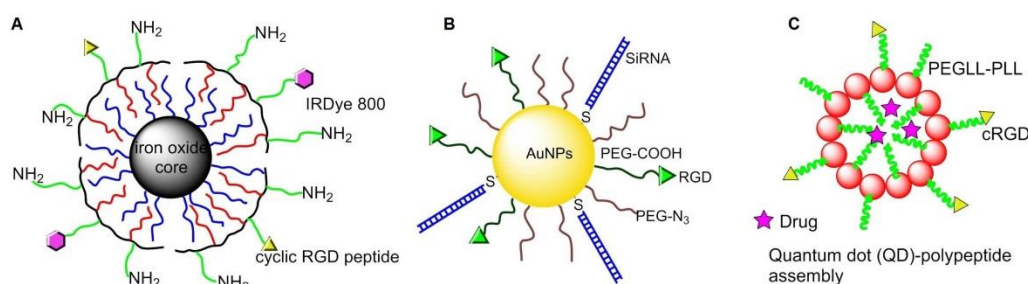


Figure 7. Integrin-targeted inorganic NPs and quantum dots (QDs): (A) magnetic NPs; (B) gold NPs; (C) QDs.

6.2.3. Gold NPs

In 2013, Conde et al. conjugated RGD peptide and thiolated siRNA to PEG-modified Au NPs, making it possible to deliver siRNA to tumor cells and effectively silence target oncogenes, then down-regulate c-Myc oncogene and inhibit tumor growth, as well as prolong the survival time of mice with lung cancer (Figure 7B).^[86] In 2015, Zhang and coworkers bonded c[RGDfK] to PEG-entrapped Au-NPs (Au DENPs-RGD) as a nanoprobe. After intravenous injection into tumor-bearing mice, the NPs accumulated in tumor and were detected by CT imaging.^[87]

6.2.4. Quantum Dots (QDs)

In 2010, Atmaja et al. reported a tunable QD-polypeptide assembly system by self-assembly of QDs and c(RGD)-PEGLL-PLL (Poly (diethylene glycol-L-lysine)-poly (L-lysine)) diblock (Figure 7C). This system entered into the cells by endocytosis, and the cargos were released due to loss of self-assembled electrostatic interactions, allowing simultaneous molecular imaging and drug delivery.^[88]

In 2015, Hu et al. modified the peptide RGD and peptide bombesin (BBN) onto the surface of QDs and then radiolabeled with 4-nitrophenyl-2-¹⁸F-fluoropropionate to synthesize PET/NIRF probe ¹⁸FFP-QD-RGD-BBN. By studying PC-3 cells and prostate tumor-bearing mice with dual-mode PET and NIRF imaging, the biodistribution and tumor targeting of QDs could be determined, and tissue penetration in optical imaging was also improved.^[89]

7. Surfaces and Materials Functionalized with Peptidic Integrin Ligands

Peptide-functionalized surfaces are important both for studying integrin-mediated cell adhesion, growth, spreading and differentiation, and in biomedicine, for implant materials and tissue engineering.^[90] ECM derived peptides or protein fragments that specifically engage integrins were used to functionalize implants and orthopedic biomaterials, to upregulate the formation of osteoblasts, enhance cell adhesion, proliferation, and differentiation.^[91] Different approaches have been developed to promote material surface bioactivation.^[92,93] The mere absorption of the ligands on the surfaces leads to unpredictable, nonspecific, and potentially unstable interactions both with the cells and the material surface. Much better results have been obtained with mechanically and chemically stable linkers. To introduce those linkers

without affecting functions of immobilized-peptides and without interfering other remaining amino acids, a series of chemical reactions have attracted much attention: the palladium-catalyzed or copper-co-catalyzed Suzuki–Miyaura, Sonogashira, and Mizoroki–Heck reaction; the cycloaddition reactions, such as Cu-catalyzed azide-alkyne cycloaddition, Diels–Alder reaction, and Huisgen cycloaddition; the olefin metathesis reaction promoted by Grubbs or Hoveyda–Grubbs catalysts; the Staudinger ligation, utilized in chemical biology for the synthesis of fluorescently labeled nucleosides.^[94] In this context, very recently De Marco et al. developed an expedient synthesis of hybrid peptides containing imidazoline-2-one scaffolds.^[95] The rings were equipped with functional groups capable of selective reactions without perturbing the rest of the structure, for example, the Heck reaction on the allyl group. Potential applications might include the glycosylation, prenylation, PEGylation, biotinylation, or attachment to solid surfaces, SAMs, proteins, or the conjugation with fluorophores or antibodies. Intriguingly, these pseudo-proline heterocycles tend to favor unusual conformations, including the ϵ -turn, a rare secondary structure characterized by an 11-membered 2→4 H-bond going opposite respect to the classic turns.

The interaction between cells and the materials is based on several parameters, among which the density of integrin ligands anchored on the surface of the materials is the most important one. Besides, the spatial distribution of the adhered moieties on the surface is also an indispensable factor, which affects the accessibility of the peptide to the cells. By conjugating the integrin ligand to the surface with different density and spatial arrangement, important insights have been provided into how the organization of the ligands can influence integrin clustering, FA formation, and subsequent adhesion and spreading of cells. In particular, it has been discovered that there is a critical lateral spacing of approximately 60–70 nm between integrin ligands. When the spacing is out of range, integrin clustering and FA formation are hindered, thereby limiting cell attachment and diffusion.^[96] The limitations of spatial distance and peptide arrangement may be related to physiology because ordered structures happen in the native ECM.

7.1. Self-Assembled Monolayers (SAMs)

SAMs of GRGDS peptides on gold were fabricated by using thiolated PEG linkers containing 3 to 6 monomers. An increase in the length of the polyethylene glycol chains resulted in a decrease in Swiss 3T3 fibroblast cell adhesion and spreading, especially for lowest ligand density.^[97] SAMs of cyclic RGD (1 mol%) were further used to investigate the dynamics of cell migration in the presence of a linear RGD antagonist. In a definite concentration range, cell migration speed increased upon increasing the concentration of the antagonist.^[98]

SAMs of RGD peptides were prepared on silicon surfaces with peptide spacing ranging from nanometers to micrometers. The silicon materials were modified with undecenoic acid and mixtures of 1-amino hexa(ethylene oxide) monomethyl ether and 1-amino hexa(ethylene oxide) in various ratios. The alcohol terminus of the hexa(ethylene oxide) was activated to a succinimide ester to consent the pentapeptide RGD to be coupled to the surface. Endothelial cells adhered to and spread on surfaces independently of RGD spacing. However, the formation of FAs was particularly sensitive to the ligand spacing and the optimal spacing for RGD was found to be 44 nm.^[99]

7.2. Interfaces for Studying of Cell Adhesion, Spreading, and Differentiation

To promote cell binding, two domain-peptide ligands were simply absorbed onto gold. One domain is an anchoring domain for AuΦ3 gold binding, and the other is an IKVAV or RGD motif present in ECM proteins as a cell-binding domain. Compared with the sequence containing only the cell-binding domain, the sequence with the anchoring domain had higher adsorption strength, which can induce cell polarization and larger mature FA area. These correspond to the high forces exerted on the interface and they enhance cell interaction with the material.^[100]

In 2009, Garcia et al. prepared supported lipid monolayers (SLMs) directly on octadecyl trichlorosilane-coated substrates. These surfaces were utilized to study the adhesion of hematopoietic progenitor cell lines to a peptide derived from FN.^[101] In 2001, Sackmann and co-workers prepared artificial membrane giant vesicles which incorporated 1–10 mol% of c[RGDfK]-lipopeptide. After seeding, endothelial cells remained adherent and spread on RGD-SLM, while cells remained round on control SLMs.^[102]

Supported lipid bilayers (SLBs) are biological interfaces mimicking cell membrane, with easily tunable characteristics. The head group of the lipids can be functionalized with integrin-binding peptides. In 2017, in Jonkheijm's group, biotinylated 1,2-dioleoyl-*sn*-glycero-3-phosphocholine (biot-DOPC) and 1,2-dipalmitoyl-*sn*-glycero-3-phosphocholine (DPPC) were utilized to obtain ligand-mobile SLBs, which was functionalized with linear biotinylated-RGD thanks to the intermediacy of neutravidin. The resulting RGD-mobile SLBs were employed to study short term cell adhesion and longer-term cell differentiation of human mesenchymal stem cells (hMSCs), and the result showed that cell adhesion and differentiation positively correlated to ligand density and mobility. ^[103]

7.3. Application in Regenerative Medicine and Tissue Engineering

In 2013, Rechenmacher et al. utilized click chemistry to immobilize peptidomimetics of $\alpha 5\beta 1$ - or $\alpha v\beta 3$ -selective RGD peptides on Ti-based materials via phosphonic acid-containing anchoring units, and the resulting surfaces promoted the selective binding of $\alpha 5\beta 1$ - or $\alpha v\beta 3$ -expressing fibroblasts. ^[104] In 2015, Fraioli et al. reported that these Ti-peptide surfaces also allowed the adhesion, proliferation, and differentiation of OB-like cells, hence representing prototypes for implant materials with osteoinductive properties. ^[105]

Track-etched (TE) microporous membranes of polyethylene terephthalate were grafted with GRGDS peptide or peptidomimetic ligands of $\alpha v\beta 3$ integrin, via trifluorotriazine activation. These devices were described by Rémy and his coworkers in 2013 and showed improved adhesion of human endothelial cells under shear stress mimicking arterial conditions. The optimal number of peptide molecules grafted on the surface was about 50 pmol/cm², ^[106] whereas cells were not observed on the surface of non-grafted PET.

Aiming at improving the adhesion of bone-forming osteoblasts at the surface of implants for regenerative medicine, in 1999, Kessler et al. proposed a method for the coating of the implants using integrin-specific ligands. Osteoblasts were found to be effectively bound to the material poly(methyl methacrylate) (PMMA), which anchored the cRGD peptide with N-succinylcysteamide or a 3-sulfanylpropionic acid linkers. ^[107]

The functionalization of collagen scaffolds with RGD ligands that support cellular attachment has been extensively studied by Schussler and his coworkers in 2009, for cardiac tissue engineering in the treatment of diseased myocardium or cardiac malformations. ^[108] In 2012, in the Kilian group, SAMs of cRGD ligands were obtained by conjugating the c[RGDfC]/GRGDSC peptides to Au-SAMs using thiolated tri-(ethylene glycol) linkers. The differentiation of MSCs was affected by the affinity and density of an immobilized ligand for the integrin receptors. As a result, MSCs on monolayers of c[RGDfC]-SAM-Au showed increased expression of osteogenic markers, while cells on monolayers of GRGDSC-SAM-Au expressed early markers of myogenesis at a high density and neurogenesis at a low density of the ligand. ^[109]

7.4. Fabrication Methods of Integrin Ligand Immobilized Nanostructured Surfaces

The random presence of cell adhesive ligands on a material surface alone is not sufficient to elicit a full cell adhesion response, being the nanoscale distribution of these ligands on the surface also critically important. Indeed, to promote the formation of FAs, the integrin receptors must be clustered within the cell membrane. Integrin clustering can be favored by culturing cells on surfaces functionalized with multivalent ligands. A variety of fabrication methods have been developed to control the nanoscale presentation of integrin-binding ligands on biomaterial substrates, including blending, electron beam patterns, photolithography, and nanolithography, electrospinning, 3D printing, etc. ^[110]

7.4.1. Blending Strategy for Surfaces Functionalization

In 2008, Becker and Simon fabricated fibroin and synthetic RGD-containing spidroin (RGD-spidroin) on glass coverslips in different proportions of RGD-spidroin from 0% to 70%. The higher ratio of RGD-spidroin is related to the high content of the β -sheet, which has a positive correlation with film stability and cell adhesion, but an insignificantly negative correlation with differentiation. It was also found that the optimal proportion of RGD-spidroin was 10% for film stability, osteoblast adhesion, and differentiation. ^[111]

In 2014, Yang et al. prepared bio-fibers by blending RGD-containing peptides functionalized mussel adhesion protein (MAP-RGD) into silk fibroin (SF). It was determined that MAP-RGD-SF not only improved the attachment, proliferation, and spread of mammalian cells but also promoted the adhesion of carbohydrates and proteins. Compared with SF, MAP-RGD-SF had high hydrophilicity, biodegradability, and wettability, which made it have greater potential in the application of tissue engineering and regeneration medicine.^[112] In 2018, Janani et al. prepared a 3D porous silk scaffold by blending mulberry silk fibroin protein and RGD-containing non-mulberry silk fibroin protein to develop bioartificial liver constructs. It was found that the blend scaffold increased the density of hepatocyte clusters and retained liver-specific functions for 3 weeks.^[113]

In 2000, Maheshwari et al. reported a Star-shaped polymer containing many PEO arms. The YGRGD attached star-shaped PEO was blended with the unfunctionalized star-shaped polymer covalently tethered on the PEG hydrogel-modified coverslip to independently control the peptide density and spatial distribution of the surface. It was found that NR6 fibroblast cells could only migrate on the YGRGD peptide adhered surfaces (Figure 8A).^[114]

A cRGD-conjugated micellar system was prepared by blending pluronics L121 and F127 to increase docetaxel-loading capacity and particle stability (>1 week). It was also found that the enhancement of cellular uptake improved anticancer activity against U87MG cancer cells, and tumor-targeting accumulation of blending micellar systems in vivo (Figure 8B).^[115]

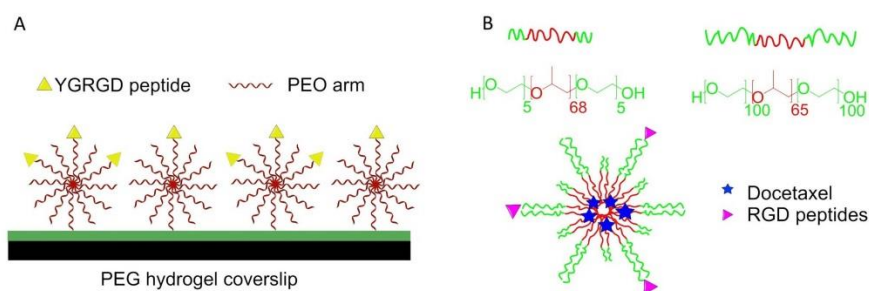


Figure 8. Blending strategy for surface functionalization. (A) Star PEO was blended on the surface. The surface density of star PEO and special distribution of RGD peptides can be controlled. (B) Preparation of cRGD-conjugated tumor-targeting drug delivery platform by blending of L121 and F127 and encapsulating docetaxel.

7.4.2. Electron Beam Fabricated Patterns

In 2007, Rundqvist et al. proposed an electron beam as a high-fidelity approach for surface coating with proteins.^[116] A silicon substrate was coated with protein fibronectin, which was then inactivated by an electron beam. The area exposed to the electron beam lost the ability of Ab binding and cells spreading. The inactivation was dependent on the dose of electron and accelerating voltage. In contrast to the ablation observed in other organic thin films, this patterning approach allowed local inactivation, and the level of protein patterning could be controlled to a single molecule.

Using electron-beam lithography, in 2012, Maynard^[117] functionalized substrates with both Lev-GRGDSPG peptide and basic fibroblast growth factor (bFGF). First, 8-arm PEG-OH was coated on a silicon wafer and passivated by thermal annealing, then a 1:1 blend of PEG-AO (8-arm aminoxy-terminated PEG) and pSS-co-PEGMA (Poly(styrene-4-sulfonate-co-poly(ethylene glycol) methacrylate)) was patterned by electron beam lithography. Finally, GRGDSPG and bFGF were immobilized on the surface. The presence of RGD promoted cell adhesion and the formation of FAs. Compared with the surface containing only RGD, the surface containing both RGD and bFGF increased the cell area of HUVEC (Figure 9).

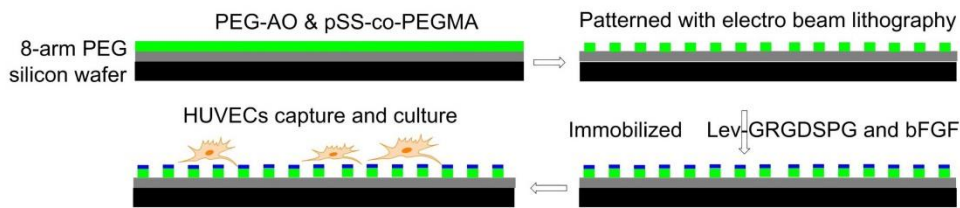


Figure 9. Electron beam lithography. Before immobilizing Lev-GRGDSPG and bFGF on the surface, pSS-co-PEGMA and PEG-AO were coated and cross-linked on passivated silicon wafers. Then HUVEC cells were cultured on the surface.

7.4.3. Photolithography Strategy for Surfaces Functionalization

Using photolithography technology, polydimethylsiloxane (PDMS) microgrooves were prepared in 2017 by Kim and his coworkers and then immobilized by filamentous phages, which were genetically functionalized with RGD peptide. The presence of RGD-phages in PDMS-microgrooves enhanced adhesion, proliferation, and orientation of H9c2 cardiomyocyte, which has application prospects in stent coating materials. ^[118]

In 2017, in the Bilem group, RGD peptide and bone morphogenetic protein (BMP) mimetic peptide were immobilized on glass surfaces by geometrically controlled photolithography patterning. hMSCs osteogenic differentiation-related to the spatial distribution of two different peptides and shape of peptide micropatterns. Compared with the BMP-2 functionalized surface only, the RGD/BMP-2 modified surface could significantly promote hMSC osteogenesis. ^[119] In 2018, the same group described that spatial patterning surfaces of RGD-TAMRA did not change the stemness character of hMSCs, but the presentation of BMP-2-FITC peptide on material surfaces promoted the differentiation of hMSCs into osteoblasts. Triangular and square peptide patterns with an aspect ratio of 1 and 0.7 significantly enhanced hMSCs osteogenesis. ^[120]

In 2011, Using photolithography, RGD-immobilized nanoporous alumina membrane was immobilized with PEG hydrogel micropatterns to construct microwells with different sizes in Koh's lab. Fibroblasts adhered and proliferated in RGD-containing microwells instead of PEG hydrogel walls to form a cellular micropattern. The formation of filopodia and its penetration into nanopores was also observed (Figure 10). ^[121]

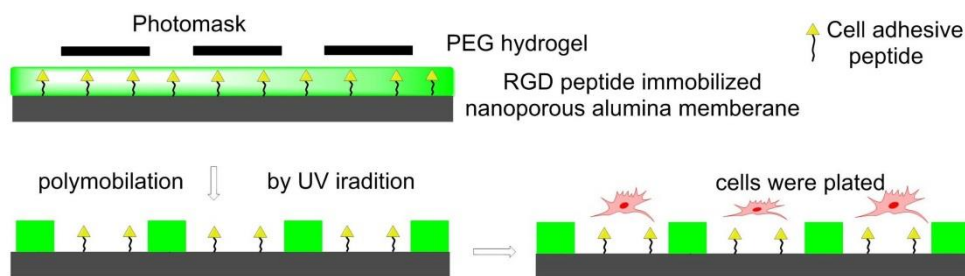


Figure 10. Photolithography strategy for surface functionalization. The photoinitiator-containing gel precursor solution was added on RGD peptides immobilized nanoporous alumina membrane to form a thin layer. Then it was covered by photomask and irradiated by UV light to get polymerization. Fibroblasts cells were seeded in the nanowells.

7.4.4. Nanolithography Strategy for Surfaces Functionalization

A substrate-patterning strategy was based on the self-assembly of diblock copolymer micelles. After the assembly of the Au-dot-containing micelles, the polymer was entirely removed by a gas plasma treatment, which resulted in extended and highly regular Au nanodots, deposited into a nearly perfect hexagonal pattern on substrates such as glass. c[RGDfX] peptides were bound to gold NPs structured surfaces via polyproline, polyethylene glycol, or aminohexanoic acid-containing spacers of different lengths. Changes of the ligand's spacer chemistry and length reveal significant differences in cell adhesion activation and FA formation. An increase in spacer length resulted in an increase in FA density in fibroblasts as well as an

increase in the average cell area. Longer and more hydrophilic spacers induced more stress fiber formation. Short hydrophobic spacers induced the slowest cellular spreading rate; and for all spacers, increasing their length led to an increase in the rate of cell spreading. Polyproline-based peptides demonstrated improved cell adhesion kinetics and FA formation compared with common aminohexanoic acid or polyethylene glycol spacers, correlated to the much higher extension and rigidity of the former. Binding activity was additionally improved, inducing a higher and faster cell spreading, by ligand dimerization, obtained by joining two cRGD peptides with a lysine branch. [122]

In 2014, in Cavalcanti–Adam’s lab, Gold NPs were deposited on β -type Ti-40Nb alloy discs by block copolymer micelle nanolithography and were subsequently functionalized with thiolated cRGD ligands in defined patterns. When seeded with human MSC, these nanostructured discs showed reduced cell heterogeneity, while their adhesion, in terms of cell size and FA formation, was optimized. [123]

In 2013, gold nanopatterns on persistently non-fouling PEG hydrogels were prepared by Wang et al. via block copolymer micelle nanolithography plus transfer nanolithography. Specifically, micelles of amphiphilic block copolymer polystyrene-block-poly(2-vinyl pyridine) (PS-b-P2VP) were reacted with HAuCl_4 to give Au-enriched micellar cores. The process of preparation of a gold nanopattern on glass exploited dip-coating and oxygen plasma, then the Au nanopatterns were transferred from glass to a PEG hydrogel, which was formed via photopolymerization of PEG-diacrylate (DA), and then RGD motifs were grafted onto the gold nanodots to eventually obtain an RGD nanopattern on the surface of a PEG hydrogel. The behaviors of MSCs on diverse pattern nanopacings were examined under a full level of serum, confirming less spreading in the case of nanopacings larger than the critical 70 nm. Osteogenic and adipogenic inductions resulted in higher differentiation extents on patterns of large nanopacings than of small nanopacings (Figure 11). [124]

In 2013, nanodots were fabricated on silicon surfaces by Cheng et al. and modified with RGD peptide by combining nanoimprint lithography technology with surface modification techniques. Square arrays of nanodots were transferred from a silicon mold onto silicon substrates via a polymer mask. These patterns were functionalized with a 3-aminopropyltrimethoxysilane (APDMS) layer subsequently grafted with a cysteine-modified GRGDSPC peptide through a 3-succinimidyl-3-maleimidopropionate (SMP), a heterobifunctional cross-linker. After polymer mask removal, the nonpatterned background was passivated with a cell-repellent PEO-silane layer. These systems were utilized for studies in human mesenchymal stem cell adhesion, differentiation, and induction of FA. [125]

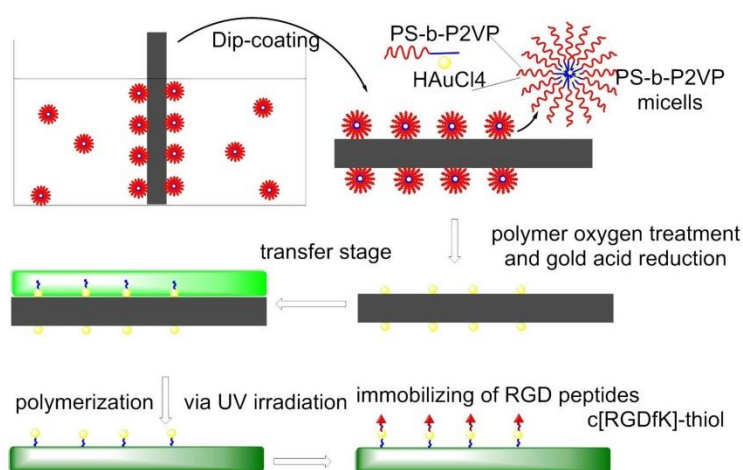


Figure 11. Nanolithography surfaces functionalization. PS-b-P2VP micelles were dip-coated on glass, forming Au-nanopatterned surfaces. c[RGDfK]-thiol was anchored on gold before cell culture.

7.4.5. Electrospinning

In 2016, to mimic ECM structure, a PLGA copolymer immobilized with GRGDY peptide was electrospun by Kim et al. to form nanofibers. PLGA-b-PEG-NH₂ was blended with PLGA as an electrospinning ink to introduce free amino groups, which can be used to functionalize RGD peptides. The polymer concentration and blend ratio influence the characteristics of the nanofiber. Compared with nanofiber

without immobilized RDG peptides, those with RGDs greatly enhanced cell adhesion, spreading, and proliferation (Figure 12).^[126]

In 2014, to challenge the topic of nerve function recovery, Yun et al. prepared electrospun nanofiber scaffolds by electrospinning a mixed solution of RGD-functionalized poly(serinol-hexamethylene urea) (PSHU-RGD) and poly- ϵ -caprolactone (PCL). Compared with laminin-coated surfaces, no cytotoxicity of PSHU-RGD/PCL nanofiber scaffolds was found in the MTT test. PSHU-RGD/PCL not only promoted PC12 cell adhesion and differentiation but also enhanced neurite outgrowth.^[127] In 2018, Madhavan et al. demonstrated that RGD functionalized PSHU/PCL biomaterial could be also used in vascular grafts.^[128] In 2014, to overcome the shortcoming of difficult infiltration of cells into electrospun scaffolds, Jeong et al. proposed that electrospun mats with high porosity, thickness, and small-fiber diameter should be considered. To achieve this purpose, high humidity conditions and ultra-sonication were introduced in the preparation process of RGD-modified alginate mats.^[129] In 2016, Antonova et al. reported that electrospinning of a blend of poly(3-hydroxybutyrate-co-3-hydroxy valerate) (PHBV) and poly(caprolactone) (PCL) gave small-diameter biomaterial grafts for vascular tissue engineering. In the rat's study of grafts implantation, it was found that RGD or VEGF (vascular endothelial growth factor) modified PHBV/PCL grafts promoted endothelialization, collagen production, and primary patency rate.^[130]

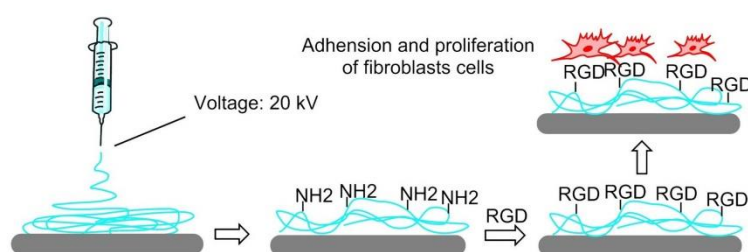


Figure 12. The electrospin strategy for surface functionalization. A mixture of PLGA (poly(lactic-co-glycolic acid)) and PLGA-b-PEI-NH₂ in DMF/THF was electrospun to produce nanofiber with free NH₂-group, which can be used to conjugate RGD peptides. Fibroblasts were used to study cell adhesion, spreading, and proliferation.

7.4.6. 3D Printing

In 2014, Wang et al. reported that filamentous phage can be genetically fused with RGD peptides to the terminal of the major coat protein pVIII, forming RGD-phage nanofibers. A porous bioceramic scaffold was fabricated using 3D printing technology, then it was immersed into a mixture of negatively charged RGD-phage nanofibers and positively charged chitosan, which allowed to stabilize the phage nanofibers. The scaffold seeded with MSCs and implanted into the defect site of rats, and the formation of new bones containing new blood vessels were observed.^[131]

Hydrogel is not suitable for musculoskeletal tissue engineering because of their stiffness. In 2017, Heo et al. found that when cRGD-conjugated gold NPs (RG NPs) were incorporated into the microstructure of 3D printed hydrogel-embedded polylactic acid (PLA), the stiffness can be enhanced to be as strong as native bone tissue. The stiffness could be also modulated to simulate the stiffness of human mandibular condyle. Human adipose-derived stem cells (ADSCs) were encapsulated in reinforced composite hydrogels; it was found that the RGD peptide increased cell adhesion, spreading and proliferation, and osteogenic differentiation (Figure 13).^[132]

Unlike modifications after fabrication, in 2019, Chow et al.^[133] introduced a 3D printing method that used the biodegradable polymers poly(caprolactone) (PCL) pre-functionalized with RGDs or RGEs (control) to modify the surface. Fibroblasts preferred to attach and spread on RGDS (biotin)-PCL fibers rather than RGES (azide)-PCL fibers, and increasing the concentration of RGDS (biotin)-PCL can promote cell adhesion.

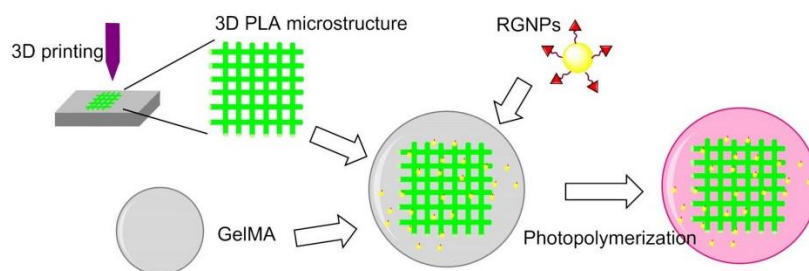


Figure 13. 3D printing for surface functionalization. 3D PLA microstructure was prepared via 3D printing technology; GelMA was obtained by methacrylation of gelatin; peptide-conjugated Gold NPs (RGNPs) were prepared by reduction of chloroauric acid before conjugating RGD peptides.

7.5. Detection of Tumor Cells

Much effort has also been directed to the preparation of RGD-functionalized bioactive surfaces to favor integrin-mediated cell adhesion and growth. For such uses, long contact times between the substrates and the cells are envisaged. Less attention has been paid to the development of RGD-functionalized bioactive surfaces as diagnostic devices to detect cancer cells, for which a fast and yet selective and strong adhesion is preferable. These devices can be exploited for the entrapment and study of circulating tumor cells (CTCs). These are cells that detach from solid primary tumors during metastasis, entering the blood circulation. The importance of CTC counting in cancer diagnostics has grown over the past decades, as their concentration in the blood represents an indicator of tumor invasiveness, allowing monitoring of the therapeutic outcomes of cancer. In 2015, Greco et al. designed an integrin-targeting nanostructured device constituted of patterned SAMs of disk-shaped zeolite L nanocrystals coated with the cyclic integrin ligand c[RGDfK] (**3**) (Figure 14A).^[134]

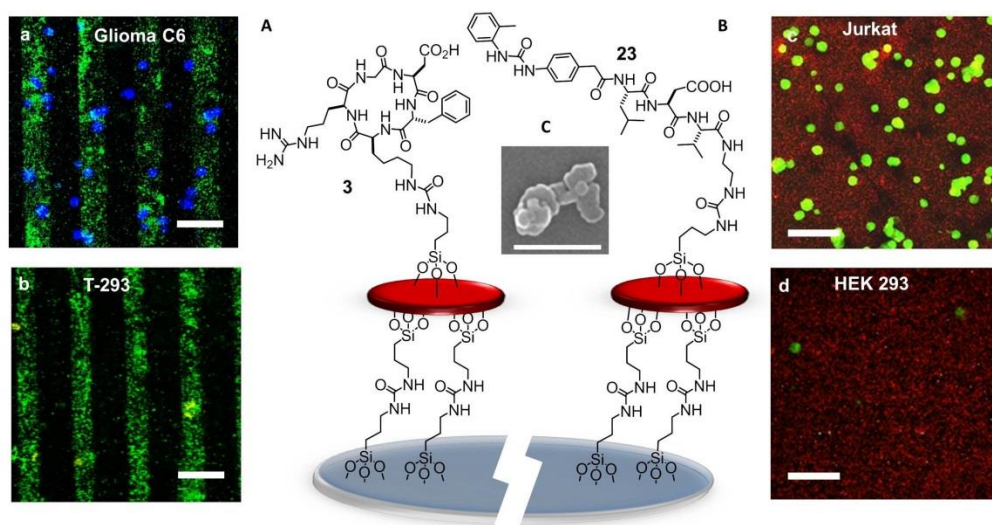


Figure 14. (A) Sketch of c[RGDfK]-zeolite SAM bound onto a glass substrate. Confocal images of the patterned c[RGDfK]-SAM after 30 min incubation with (a) glioma C6 and (b) primary endothelial cells T-293 (scale bar = 100 μ m). (B) Sketch of urea-LDV-zeolite SAM. Confocal microscopy images of urea-LDV-SAM visualized after 15 min incubation with (c) Jurkat cells and (d) HEK-293 cells (scale bar = 50 μ m). (C) SEM image of zeolite L crystals (white bar = 500 nm).

Zeolite SAMs were chosen for the large surface area and the possibility of the high density of superficial functionalization with bioactive molecules, providing a large number of contact points, exploitable for more effective binding to biological systems. Large and ultra-flat disk-shaped zeolite L crystals (about 1000 \times 250 nm) were loaded with the fluorescent dye DXP, and subsequently, their surface was functionalized with an isocyanate linker. Then, the NPs were covalently bound onto the silica plated functionalized with amino groups on the surface, by the formation of urea linkages. Patterning into stripes

was done to better highlight the specific attachment of the cells only on the peptide-functionalized regions of the zeolites. Once prepared, the printed substrate was coupled with the integrin ligand c[RGDfK]. Adhesion experiments were performed with the integrin-expressing cancer cell lines HeLa and Glioma C6. Confocal microscopy (Figure 14a,b) showed that the population of adherent HeLa and Glioma C6 cells was much higher than that of T-293 cells (negative control)

7.6. Ligands other than RGD

The next advances in integrin-binding surfaces are likely to emerge from expanding to other ligands than RGD. For instance, a device for the identification and quantification of the leucocytes expressing active $\alpha 4\beta 1$ integrins could be utilized for monitoring ongoing inflammatory activity. For the detection and counting of leucocytes, attention was turned to peptide-coated SAMs of Zeolite L crystals capable to reproduce the cell adhesive multivalency integrin-ligand interaction at the endothelial surfaces in the proximity of the sites of inflammation.^[135] The SAMs were coated with $\alpha 4\beta 1$ integrin-targeting Gln-Ile-Asp-Ser (QIDS) sequence, the minimal epitope of the natural ligand VCAM-1, or a peptide ligand derived from the $\alpha 4\beta 1$ integrin ligand MPUPA-Leu-Asp-Val (**23**) (Figure 14B), a sequence shared with the potent antagonist BIO1211 (**7**). This peptidomimetic included the minimal epitope of the natural ligand fibronectin (FN), namely the tripeptide LDV, plus the MPUPA moiety at the N-terminus which strongly increased the $\alpha 4\beta 1$ integrin affinity (IC_{50} of urea-LFV = 30 nM). Cell adhesion experiments were performed in Jurkat cells, an immortalized cell line of human T lymphocytes often utilized as prototypic $\alpha 4\beta 1$ integrin-expressing cells. Confocal microscopy revealed that MPUPA-LDV-SAM showed the highest adhesion of Jurkat cells compared to the negative control HEK-293 cells (Figure 14c,d), 1.4×10^4 versus 1.7×10^3 cells/cm².

Peptidomimetic molecules selective for integrin $\alpha v\beta 3$ or $\alpha 5\beta 1$ were utilized for coating bactericidal titanium surfaces reproducing the bactericidal needle-like nanotopography of certain insects' wings. The functionalization increased MSCs adhesion to the surfaces, and the $\alpha v\beta 3$ -selective peptidomimetic-coated materials promoted osteogenesis, while the antibacterial activity of the substrates was maintained when tested on pathogenic *Pseudomonas aeruginosa*.^[136]

β -lactams were also reported to be integrin ligands, especially for integrin $\alpha v\beta 5$, $\alpha 5\beta 1$, or $\alpha 4\beta 1$. To improve human mesenchymal stem cell adhesion and promote the application in tissue engineering and regeneration medicine, β -lactam-based agonist ligands (see also section "Addressing Integrins with Agonist Ligands") were incorporated into poly(L-lactic acid) (PLLA) to form functionalized scaffolds by electrospin technology.^[137]

7.7. Multifunctional Integrin-Targeting Biocompatible Surfaces

The ECM is a multifunctional material with multiple components. Thus, biomaterials need to possess multiple features to recapitulate the essential functionality of these ECM components to satisfy the needs of the cells when they are developed for biomedical applications such as tissue engineering and regenerative medicine. To fulfill this requirement, it is important to not only select a biocompatible material as the fundamental structural component of the ECM mimic but also functionalize this material with a biologically active molecule serving biochemical and biophysical cues. In 2011, Shen et al. reported an engineered biomimetic substrate functionalized with both an FN-derived peptide ligand for $\alpha 5\beta 1$ and a CCN1 (or CYR61, Cysteine-rich angiogenic inducer 61)-derived peptide ligand for $\alpha 6\beta 1$ integrins. The surfaces were prepared by immobilizing cysteine- polypeptide ligands on gold-coated slides and supported efficient early mesodermal differentiation of human embryonic stem cells (hESCs) when cultured in a differentiation medium containing BMP4, while mesodermal differentiation was not induced on substrates functionalized with either ligand alone.^[138]

cRGD and the adhesive peptide sequence PHSRN found in human FN were assembled in a chemically defined and controlled fashion on a peptide-based divalent platform. A Lys-betaAla-Cys sequence was utilized as a branching unit at Lys and as an anchoring group at Cys, to provide a chemoselective, strong and stable binding of the adhesive sequences onto Ti samples. The surfaces coated with the platform of cRGD/PHSRN efficiently supported and promoted good levels of attachment, spreading, proliferation, and differentiation of osteoblast-like cells.^[139]

An RGD peptide and an anti-VEGF aptamer were incorporated through free radical polymerization into a 3D porous PEG hydrogel to develop a dual-functional biomaterial. [140] The data showed that the dual-functional porous hydrogel enhanced the growth and survival of endothelial cells. The integrin ligand promoted the attachment and growth of endothelial cells in the hydrogel, and the antivascular endothelial growth factor aptamer was able to sequester and release VEGF of high bioactivity.

In 2018, Qiao et al. realized a low-fouling polymeric surface-functionalized with nano-clusters of ligands that bind two receptor types which contribute to FA signaling and mechanotransduction, i.e., integrin and syndecan-4 receptors. The clustered surfaces were generated by film casting blends of highly functionalized polymer chains of methyl methacrylate with PEG pendant chains, with non-functionalized polymer chains. The blending strategy created nano-islands of high peptide density. The presence of both ligand types synergistically increased >2-fold the adhesion HUVEC cells and increases the rate of surface endothelialization compared to surfaces functionalized with only one ligand type. Additionally, the mixed population of ligands was shown to regulate endothelial cell migration and induced the appropriate morphological changes (elongation and alignment in the direction of flow), when exposed to laminar shear flow. [141]

8. Nanostructured 2D or 3D Smart Interfaces for Dynamic Cell Adhesion

Recent efforts have been directed towards nanostructured 2D or 3D materials which can be used as smart interfaces to further understand and control the complex interplay of events and interactions occurring within living cells. [96,142] Smart interfaces were triggered according to cellular microenvironment or stimulation outside to study fundamental cell phenomena or achieve precise and controlled drug delivery.

8.1. Thermoresponsive Polymers

In 2008, Ebara et al. proposed a thermoresponsive dish to culture cells, to allow the detachment of the cells by simply reducing the temperature, without digestive enzymes or chelating agents. The temperature-responsive polymer poly (N-isopropyl acrylamide) (PIPAAm) and the cell adhesion peptide Arg–Gly–Asp–Ser (RGDS) were bounded to the surfaces. When the temperature was 37 °C, PIPAAm dehydrated and shrunk, causing the RGD peptide to be exposed, thus consenting cell adhesion. When cells were cultured at 20 °C, the grafted PIPAAm layer was hydrated and expanded, so the RGD peptide was shielded by PIPAAm, inducing cells detachment from the surface (Figure 15). [143] Subsequently, in 2017, Kobayashi et al. reported a system that was optimized by co-immobilization of the Pro–His–Ser–Arg–Asn (PHSRN) peptide found in the 9th type-III repeat of FN, or by the introduction of spacers (PEG, glycine hexamer, streptavidin-biotin). [144]

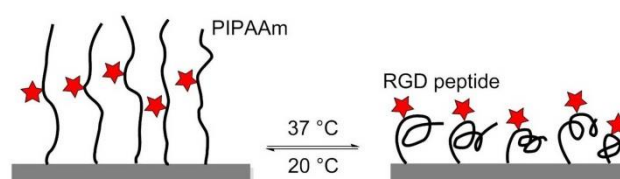


Figure 15. The thermoresponsive PIPAAm polymer undergoes expansion at 20 °C, and the RGD peptide remains hidden into the polymer. At 37 °C, the polymer shrinks and exposes the RGD peptide, promoting cell adhesion.

In 2010, Simnick et al. utilized stimulus-responsive elastin-like diblock copolymers (ELPBCs), i.e., genetically encoded polypeptides composed of a Val–Pro–Gly–Xaa–Gly repeat (Xaa is any amino acid besides Pro), that exhibited inverse phase transition behavior at a specific transition temperature. The ELPBCs were exploited as a scaffold to bind and present the GRGDS peptide, an integrin ligand characterized by low affinity ($IC_{50} = 1$ mM) for the $\alpha\beta_3$ integrin. Despite the low affinity of this ligand, it has been observed that the avidity of K562 human leukemia cells transformed by $\alpha\beta_3$ receptor (K562/ $\alpha\beta_3$) is higher as compared with a wild-type K562 control, through multivalent presentation induced by the thermally triggered self-assembly of the ELPBCs. [145]

8.2. Enzyme-Triggered Polymers

To manage adhesion/cytoskeletal balance and to initiate differentiation of MSCs to prolong cell culture, in 2016, Robert et al. prepared surfaces immobilized by RGD-containing polymer monolayer, which can be enzyme-activated. This surface consisted of RGD peptide or RGE peptide (control), an elastase cleavable dialanine (AA) linker, and steric blocking fluorenylmethyloxycarbonyl (Fmoc) group, or adhesion-reducing PEG. Elastase removed the Fmoc/PEG blocking group exposing RGD and generating cell adhesion and differentiation (Figure 16).^[146]

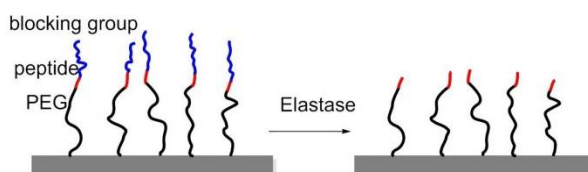


Figure 16. Enzyme-triggered polymers were immobilized on glass. The RGD peptide was blocked by Fmoc, amino acid, or polyethyleneglycol (PEG). Elastase can cleave the blocking group at a specific position thus exposing the RGD peptide, thereby improving cell adhesion.

8.3. Redox-Switchable Polymers

In 2011, Yousaf and co-workers developed a dynamic hide-and-reveal ligand adhesion strategy for controlling substrate adhesiveness for biospecific cell attachment. First, a building block containing both alkyne and oxyamine functional groups was reacted via Huisgen 1,3-cycloaddition with hydroquinone (HQ)-azide linker, which was already immobilized onto the surface. Mild oxidation converted the HQ to benzoquinone (BQ), and the latter gave intramolecular cyclization via oxime chemistry with the oxyamine group on the ligand. Upon application of a reducing potential to the substrate, the oxime bond was cleaved, regenerating the HQ and exposing the linearized RGD ligand. Fibroblast cells were observed with timelapse microscopy; smaller cells were found to migrate faster upon switching from cyclic to linear RGD. Conversely, a higher degree of actin fiber organization and stronger vinculin localization were observed on cyclic RGD (Figure 17).^[147]

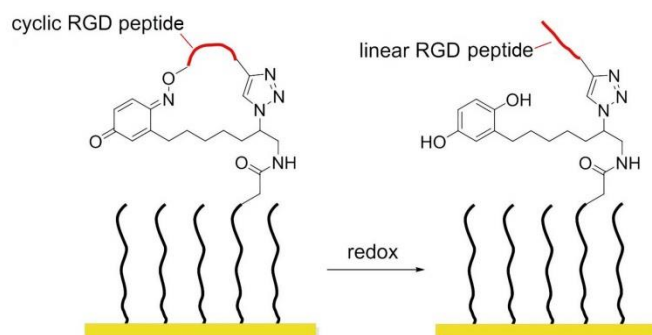


Figure 17. Redox-switchable polymers. In the cyclic form, the RGD sequence is blocked and inactive; after redox, the RGD peptide is exposed.

Later that year, the same author introduced a photo/redox strategy to selectively immobilize ligands in defined areas to control cell adhesion, tissue morphing, and cell migration.^[148] HQs on a SAM were uncaged by UV illumination and then electrochemically converted to BQs, which in turn were reactive toward oxyamine-modified RGD ligands. Adhered fibroblasts were first confined to hydrophobic patterns; after installing RGD ligands, cells migrated from the hydrophobic patterns toward the RGD presenting patterns. When a gradient of RGD ligands was formed, cells were observed to move faster toward lower ligand densities instead of higher ones.

8.4. Potential Responsive Polymers

In 2012, Gooding and coworkers prepared two-component SAMs comprising a protein-resistant ethylene glycol chain containing a charged moiety at its distal end, and a terminated RGD component on which

cellular adhesion receptors, integrins can bind. The electro-switchable surfaces were able to control cell adhesion under different electrical potential. In one case, the surface was constituted by an RGD and hexa(ethylene glycol)-sulfonate species (EG6) mixed SAM that promoted cell adhesion under a positive potential (+0.3 V), while in the other case the surface comprises an RGD and EG5-ammonium mixed SAM that prevents cell adhesion at the same positive potential^[149] while promoting cell adhesion at negative potentials (−0.3 V).

A switchable SAMs based on electrochemical potentials was reported by Zhang and his coworkers in 2015.^[150] Reversible modulation of cell adhesion/migration based on switch of potential because of transformation between linear RGD and cyclic RGD. Two-component SAMs were formed on a gold surface. One of them consisted of cysteine, an ethylene glycol, and an RGD peptide (Me_3N^+)-KRGDK with a positively charged quaternary ammonium group. The other one was a thiol group headed tetra ethylene glycol (TEG) for preventing nonspecific cell adhesions. When the surface was positively charged (+0.3), the distal end of RGD-NMe₃ with positive charge were repelled by electrostatic repulsion, to form a linear RGD domain capable to interact with cells. On the contrary, under a negative potential (−0.3 V), the (Me_3N^+)-KRGDK component was hidden into the TEG due to the electrostatic attraction (Figure 18).

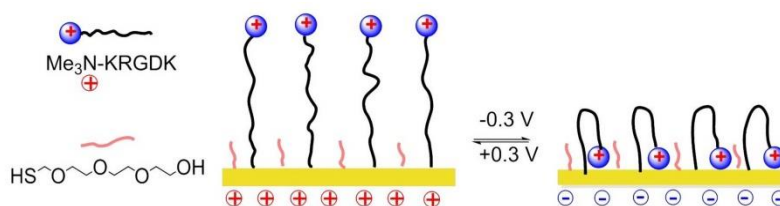


Figure 18. Potential responsive polymers on the Au surface. When the surface is positively charged, positively charged RGD-containing molecule (Me_3N^+)-KRGDK is extended, and the RGD peptide is exposed and active. When the surface is negatively charged, (Me_3N^+)-KRGDK is hidden.

8.5. Photo Responsive Polymers

In 2013, Surfaces modified with photo-activable adhesion peptides were designed by Salierno et al. as platforms for advanced cell migration studies. The surfaces were functionalized with the 3-(4,5-dimethoxy-2-nitrophenyl) butan-2-ol (DMNPB) modified peptide c[RGD(DMNPB)fK]. Cell attachment and migration were independently triggered by subsequent light exposure steps. Indeed, RGD adhesive patterns were generated after irradiation to cleave the Asp-DMNPB ester in specific areas. Subsequent cell seeding gave monolayer formation onto the exposed zones, and a second irradiation step activated further migration.^[151]

In 2018, Wiemann et al. reported that in the presence of methyl violet (MV^{2+}), the photo-convertible arylazopyrazole (AAP) derivative could be encapsulated in cucurbit [8] uril (CB [8]) to form a hetero ternary photoswitchable complex. Under the irradiation of light with a wavelength of 365 or 520 nm, AAP was transformed from E- to Z-isomer or vice versa, and the Z isomer caused the dissociation of the complex. When the Arg-Gly-Asp-AAP (AAP-RGD) peptide (**24**) was attached to a CB[8]/ MV^{2+} complex bounded biologically active surface, cell adhesion, and release could be controlled by UV radiation (Figure 19).^[152]

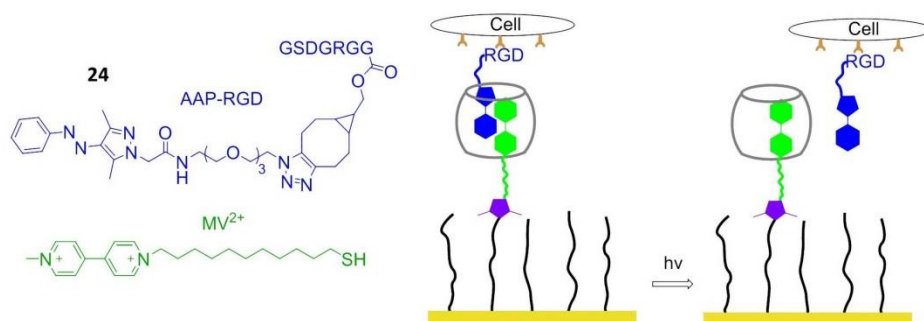


Figure 19. Photo-responsive polymers. AAP-RGD is isomerized from E- to Z-isomer under UV irradiation at 365 nm, resulting in dissociation of AAP-RGD from MV²⁺/AAP-RGD/CB [8] complex. When AAP-RGD is irradiated at 520 nm, the E-isomer is reobtained, and the MV²⁺/AAP-RGD/CB [8] complex can reform.

8.6. Electrochemically Controlled Polymers

Cucurbit [8] uril (CB [8]), a macrocyclic host molecule capable of binding two aromatic guest molecules simultaneously, was utilized for the preparation of electrochemically controlled noncovalent functionalized cell-adhesive surfaces. One guest was Trp–Gly–Gly (WGG)-RGDS, the second one was electroactive viologen modified with an alkyl thiol group to provide a bond with gold slides. The ternary WGG-viologen-CB [8] complex containing the RGDS ligand to recognize integrin receptors and mediate cell adhesion. Subsequently, electrochemical reduction of viologen leads to the release of the peptide and subsequent detachment of cells from the slides (Figure 20).^[153]

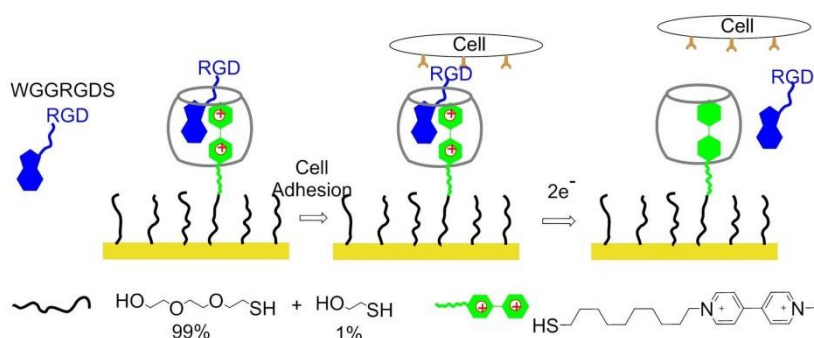


Figure 20. Electrochemically controlled polymers on the surface. The WGG-viologen-CB [8] complex is immobilized on the gold surface when viologen gets 2 electrons, and WGG-RGDS is released from the complex.

8.7. Dynamically Competitive Polymers

In 2013, Stupp and coworkers grafted β -cyclodextrin (β -CD) to alginate, a well-known non-spreading surface for 3T3 fibroblasts, and the CD-alginate was stamped to glass. The addition of soluble 1-naphthoic acid-pentaglycine (G5) linker-RGDS guest molecules to the culture media induced FA formation and cell spreading thanks to the naphthyl host-CD guest interactions. The spreading of cells on the substrate was reversed by the addition of adamantane-RGES, which are competitive guest molecules, supporting that the expressed cue on this artificial ECM can be controlled dynamically (Figure 21).^[154]

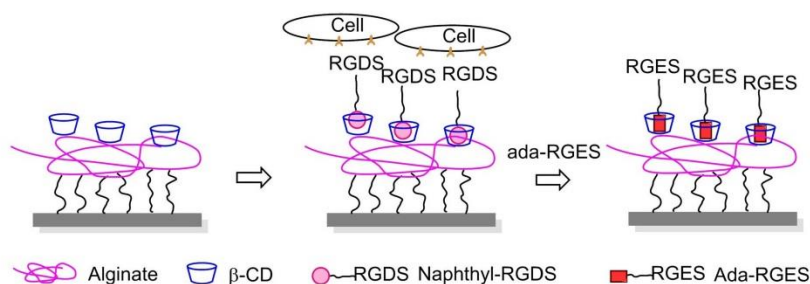


Figure 21. Dynamically competitive polymers. Guest molecular naphthyl-RGDS is captured by β -CD, which is grafted on alginate. Cell adhesion and spreading can be controlled dynamically because the addition of Ada-RGES can reverse cell adhesion due to it competed with naphthyl-RGDS to form a complex with β -CD.

8.8. Dynamically Controlled Smart Interfaces for 3D Cell Culture

The dynamic cell-instructive biointerfaces represent a newly proposed concept as smart interfaces, aimed at mimicking native 3D microenvironment that surround encapsulated cells to implementation of

sufficient complexity and dynamism to instruct cells toward a certain behavior. Multiple 3D biomaterial strategies have been developed based on synthetic polymers and natural ECM (e.g., proteins and polysaccharides). Advanced 3D dynamic cell-culture platforms for regenerative medicine applications took advantage of nondegradable PEG hydrogels.

In 2009, Kloxin et al. exploited photodegradable linkages to locally modify the chemical environment within a hydrogel. A biofunctional acrylic monomer containing the adhesion peptide RGDS was attached to a photodegradable acrylate. The monomer was polymerized into a nondegradable PEG gel. The chemical composition of the resulting poly(acrylate)-PEG 3D material was controlled with light exposure by photolytic release of the tethered biomolecule RGDS. hMSCs were encapsulated until the presentation of RGDS was temporally altered by photocleavage of RGDS from the gel on day 10 in culture. RGDS presentation maintained hMSC viability within PEG-based gels while RGDS photolytic removal directed hMSC chondrogenic differentiation, indicating that the cells responded to the chemical change in their environment (Figure 22A).^[155]

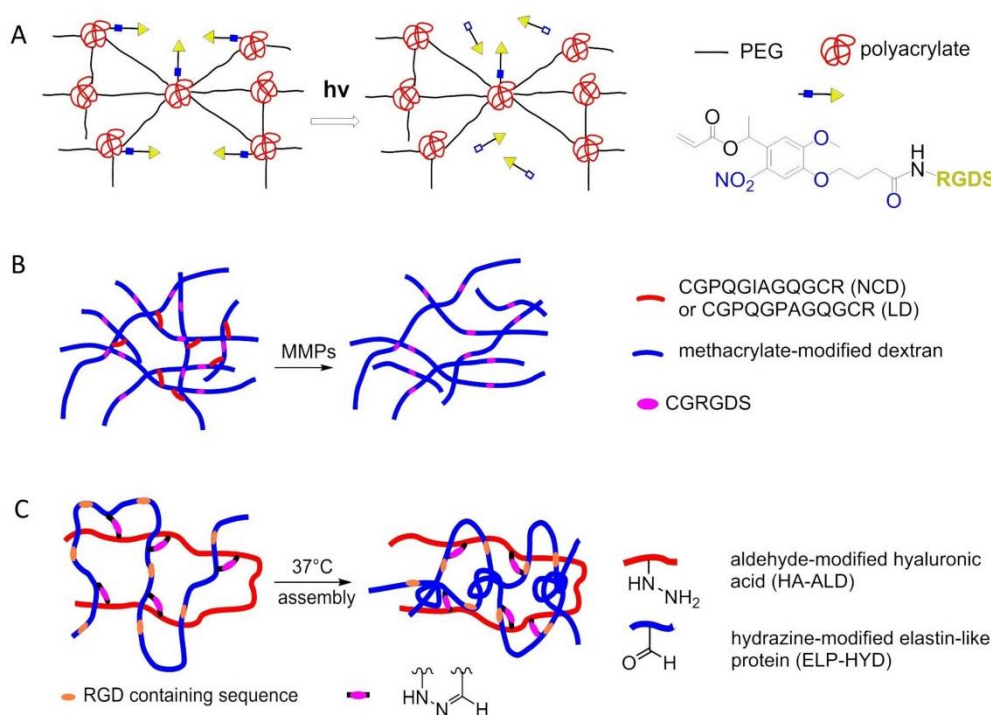


Figure 22. Smart interfaces for 3D cell culture. (A) Poly(acrylate)-PEG 3D gel containing RGD peptide and photocleavable domain. (B) ELP-HA hydrogel containing RGD sequence. (C) DexMA hydrogels functionalized RGD peptide.

In 2017, Trappmann et al. introduced 3D hydrogels of methacrylated dextran (DexMA) functionalized with RGD and crosslinked with collagen-derived peptides that can be cleaved enzymatically by cell-secreted matrix metalloproteinases (MMPs), have been used in the context of an *in vitro* study of angiogenic sprouting (Figure 22B).^[156] Another strategy to introduce dynamicity to hydrogel design is to make use of covalent bonds that can be formed, broken, and reformed under equilibrium conditions. In the same year, Heilshorn and co-workers introduced a thermoresponsive engineered elastin-like protein (ELP), incorporated with a cell-adhesive RGD sequence, to develop a novel dual-crosslinked adaptable hydrogel with improved material properties for injectable cell delivery. A mixture of hydrazine-modified ELP (ELP-HYD) and aldehyde-modified hyaluronic acid (HA-ALD) macromers was used at room temperature to induce the first gelation. Upon heating to physiological temperatures, mechanical properties of the hydrogel improved, enabling easy injectability of encapsulated hMSCs (Figure 22C).^[157]

9. Conclusions

This paper aimed at presenting the more recent uses of integrin-targeting peptides for biofunctionalization of diverse bulk materials or nanomaterials. Micelles, dendrimers, paramagnetic liposomes, chitosan NPs,

silicon NPs, Au NPs, iron oxide NPs, quantum dots (QDs), etc. have found applications not only to deliver anti-tumor drugs, but also as diagnostic probes, or to deliver proteins and siRNA, for the detection and treatment of tumors and other severe diseases. Besides, using appropriate linkers, integrin-targeting peptides can be anchored onto a variety of organic or inorganic nanomaterials, surfaces, or polymers, etc., by forming covalent or non-covalent bonds. Interestingly, cleavable covalent bonds or non-covalent interactions have been utilized to deliver cargos more precisely under the stimulation of certain conditions. More recently, the peptides have been combined with smart materials to obtain thermally-responsive, redox-controlled, light-sensitive, potential-controlled, smart nanomaterials for controlling cell adhesion. Host-guest interaction molecules can be exploited to realize light or chemically regulated, reversible cell adhesion. In summary, these peptide-material conjugates might consent applications ranging from fundamental cellular studies to oncology diagnostics, orthopedic biomaterials, regenerative medicine, tissue engineering, and other fields.

So far, the large majority of the peptide-functionalized materials are utilized as integrin-targeting molecules cyclic or linear peptides containing the RGD sequence. In perspective, other integrin-binding sequences such as the LDV, QIDS, etc., as well as recently discovered agonist ligands, are expected to gain increasing attention in the next future.

The work described in this chapter has already been published in *Biomedicines* with slight modification and has been reproduced here with the permission of the copyright holder.

Zhao, Junwei; Santino, Federica; Giacomini, Daria; Gentilucci, Luca. 2020. "Integrin-Targeting Peptides for the Design of Functional Cell-Responsive Biomaterials" *Biomedicines* 8, no. 9: 307. <https://doi.org/10.3390/biomedicines8090307>

References

1. Baiula, M.; Spampinato, S.; Gentilucci, L.; Tolomelli, A. Novel ligands targeting $\alpha 4\beta 1$ integrin: Therapeutic applications and perspectives. *Front. Chem.* **2019**, *7*, 489.
2. Danhier, F.; Le Breton, A.; Pr at, V. RGD-based strategies to target $\alpha \beta 3$ integrin in cancer therapy and diagnosis. *Mol. Pharm.* **2012**, *9*, 2961–2973.
3. De Marco, R.; Tolomelli, A.; Juaristi, E.; Gentilucci, L. Integrin ligands with α/β -hybrid peptide structure: Design, bioactivity, and conformational aspects. *Med. Res. Rev.* **2016**, *36*, 389–424.
4. Curley, G.P.; Blum, H.; Humphries, M.J. Integrin antagonists. *Cell. Mol. Life Sci.* **1999**, *56*, 427–441.
5. Auzzas, L.; Zanardi, F.; Battistini, L.; Burreddu, P.; Carta, P.; Rassu, G.; Curti, C.; Casiraghi, G. Targeting $\alpha \beta 3$ integrin: Design and applications of mono- and multifunctional RGD-based peptides and semipeptides. *Curr. Med. Chem.* **2010**, *17*, 1255–1299.
6. Humphries, J.D.; Byron, A.; Humphries, M.J. Integrin ligands at a glance. *J. Cell Sci.* **2006**, *119*, 3901–3903.
7. Campbell, I.D.; Humphries, M.J. Integrin structure, activation and interaction. *Cold Spring Harb. Perspect. Biol.* **2011**, *3*, a004994.
8. Zent, R.; Pozzi, A. *Cell-Extracellular Matrix Interaction in Cancer*; Springer: New York, NY, USA, 2010.
9. Li, J.; Springer, T.A. Integrin extension enables ultrasensitive regulation by cytoskeletal force. *Proc. Natl. Acad. Sci. USA* **2017**, *114*, 4685–4690.
10. Hillis, G.S.; MacLeod, A.M. Integrins and disease. *Clin. Sci.* **1996**, *91*, 639–650.
11. Winograd-Katz, S.E.; Fassler, R.; Geiger, B.; Legate, K.R. The integrin adhesome: From genes and proteins to human disease. *Nat. Rev. Mol. Cell Biol.* **2014**, *15*, 273–288.
12. Ni, H.; Freedman, J. Platelets in hemostasis and thrombosis: Role of integrins and their ligands. *Transfus. Apher. Sci.* **2003**, *28*, 257–264.
13. Topol, E.J.; Califf, R.M.; Weisman, H.F.; Ellis, S.G.; Tcheng, J.E.; Worley, S.; Ivanhoe, R.; George, B.S.; Fintel, D.; Weston, M.; et al. Randomised trial of coronary intervention with antibody against platelet IIb/IIIa iritegrin for reduction of clinical restenosis: Results at six months. *Lancet* **1994**, *343*, 881–886.
14. Chico, T.J.A.; Chamberlain, J.; Gunn, J.; Arnold, N.; Bullens, S.L.; Gadek, T.R.; Francis, S.E.; Bunting, S.; Horton, M.; Shepherd, L.; et al. Effect of selective or combined inhibition of integrins $\alpha \text{IIb}\beta 3$ and $\alpha \beta 3$ on thrombosis and neointima after oversized porcine coronary angioplasty. *Circulation* **2001**, *103*, 1135–1141.

15. Herter, J.; Zarbock, A. Integrin regulation during leukocytes recruitment. *J. Immunol.* **2013**, *190*, 4451–4457
16. von Andrian, U.H.; Engelhardt, B. Alpha(4) integrins as therapeutic targets in autoimmune disease. *N. Engl. J. Med.* **2003**, *348*, 68–72.
17. Teitelbaum, S.L. Osteoporosis and integrins. *J. Bone Miner. Metab.* **2000**, *18*, 344–349.
18. Friedlander, M.; Theesfeld, C.L.; Sugita, M.; Fruttiger, M.; Thomas, M.A.; Chang, S.; Cheresch, D.A. Involvement of integrins $\alpha v \beta 3$ and $\alpha v \beta 5$ in ocular neovascular diseases. *Proc. Natl. Acad. Sci. USA* **1996**, *93*, 9764–9769.
19. Lee, J.; Kim, K.E.; Choi, D.K.; Jang, J.Y.; Jung, J.J.; Kiyonari, H.; Shioi, G.; Chang, W.; Suda, T.; Mochizuki, N.; et al. Angiopoietin-1 guides directional angiogenesis through integrin $\alpha v \beta 5$ signaling for recovery of ischemic retinopathy. *Sci. Transl. Med.* **2013**, *5*, 203ra127.
20. Avraamides, C.J.; Garmy-Susini, B.; Varnier, J.A. Integrins in angiogenesis and lymphangiogenesis. *Nat. Rev. Cancer* **2008**, *8*, 604–617.
21. Ruoslahti, E.; Pierschbacher, M.D. Arg-Gly-Asp: A versatile cell recognition signal. *Cell* **1986**, *44*, 517–518.
22. Ruoslahti, E.; Pierschbacher, M.D. New perspectives in cell adhesion: RGD and integrins. *Science* **1987**, *238*, 491–497.
23. Haubner, R.; Gratias, R.; Diefenbach, B.; Goodman, S.L.; Jonczyk, A.; Kessler, H. Structural and functional aspects of RGD-containing cyclic pentapeptides as highly potent and selective integrin $\alpha v \beta 3$ antagonists. *J. Am. Chem. Soc.* **1996**, *118*, 7461–7472.
24. Gentilucci, L.; De Marco, R.; Cerisoli, L. Chemical modifications designed to improve peptide stability: Incorporation of non-natural amino acids, pseudo-peptide bonds, and cyclization. *Curr. Pharm. Des.* **2010**, *16*, 3185–3203.
25. Gentilucci, L.; Tolomelli, A.; Squassabia, F. Peptides and peptidomimetics in medicine, surgery and biotechnology. *Curr. Med. Chem.* **2006**, *13*, 2449–2466.
26. Gentilucci, L.; Tosi, P.; Bauer, A.; De Marco, R. Modern tools for the chemical ligation and synthesis of modified peptides and proteins. *Future Med. Chem.* **2016**, *8*, 2287–2304.
27. Gentilucci, L.; Cardillo, G.; Spampinato, S.; Tolomelli, A.; Squassabia, F.; De Marco, R.; Bedini, A.; Baiula, M.; Belvisi, L.; Civera, M. Antiangiogenic effect of dual/selective $\alpha 5 \beta 1 / \alpha v \beta 3$ integrin antagonists designed on partially modified retro-inverso cyclotetrapeptide mimetics. *J. Med. Chem.* **2010**, *53*, 106–118.
28. Tolomelli, A.; Gentilucci, L.; Mosconi, E.; Viola, A.; Dattoli, S.D.; Baiula, M.; Spampinato, S.; Belvisi, L.; Civera, M. Development of isoxazoline-containing peptidomimetics as dual $\alpha v \beta 3$ and $\alpha v \beta 5$ integrin ligands. *ChemMedChem* **2011**, *6*, 2264–2272.
29. Tolomelli, A.; Baiula, M.; Belvisi, L.; Viola, A.; Gentilucci, L.; Troisi, S.; Dattoli, S.D.; Spampinato, S.; Civera, M.; Juaristi, E.; et al. Modulation of $\alpha v \beta 3$ - and $\alpha 5 \beta 1$ -integrin-mediated adhesion by dehydro- β -amino acids containing peptidomimetics. *Eur. J. Med. Chem.* **2013**, *66*, 258–268.
30. De Marco, R.; Mazzotti, G.; Greco, A.; Gentilucci, L. Heterocyclic scaffolds in the design of peptidomimetic integrin ligands: Synthetic strategies, structural aspects, and biological activity. *Curr. Top. Med. Chem.* **2016**, *16*, 343–359.
31. Mitjans, F.; Meyer, T.; Fittschen, C.; Goodman, S.; Jonczyk, A.; Marshall, J.F.; Reyes, G.; Piulats, J. In Vivo therapy of malignant melanoma by means of antagonists of αv integrins. *Int. J. Cancer* **2000**, *87*, 716–723.
32. Lomonaco, S.L.; Finnis, S.; Xiang, C.; Lee, H.K.; Jiang, W.; Lemke, N.; Rempel, S.A.; Mikkelsen, T.; Brodie, C. Cilengitide induces autophagy-mediated cell death in glioma cells. *Neuro-oncology* **2011**, *13*, 857–865.
33. Taga, T.; Suzuki, A.; Gonzalez-Gomez, I.; Gilles, F.H.; Stins, M.; Shimada, H.; Barsky, L.; Weinberg, K.I.; Laug, W.E. Alpha(v)-integrin antagonist EMD 121974 induces apoptosis in brain tumor cells growing on vitronectin and tenascin. *Int. J. Cancer* **2002**, *98*, 690–697.
34. Nabors, L.B.; Mikkelsen, T.; Rosenfeld, S.S.; Hochberg, F.; Akella, N.S.; Fisher, J.D.; Cloud, G.A.; Zhang, Y.; Carson, K.; Wittemer, S.M.; et al. Phase I and correlative biology study of cilengitide in patients with recurrent malignant glioma. *J. Clin. Oncol.* **2007**, *25*, 1651–1657.
35. MacDonald, T.J.; Stewart, C.F.; Kocak, M.; Goldman, S.; Ellenbogen, R.G.; Phillips, P.; Lafond, D.; Poussaint, T.Y.; Kieran, M.W.; Boyett, J.M.; et al. Phase I clinical trial of cilengitide in children with refractory brain tumors: Pediatric brain tumor consortium study PBTC-012. *J. Clin. Oncol.* **2008**, *26*, 919–924.
36. Fink, K.; Mikkelsen, T.; Nabors, L.B.; Ravin, P.; Plotkin, S.R.; Schiff, D.; Hicking, C.; Picard, M.; Reardon, D.A. Long-term effects of cilengitide, a novel integrin inhibitor, in recurrent glioblastoma: A randomized phase IIa study. *J. Clin. Oncol.* **2010**, *28*, 15.
37. Gilbert, M.R.; Kuhn, J.; Lamborn, K.R.; Lieberman, F.; Wen, P.Y.; Mehta, M.; Cloughesy, T.; Lassman, A.B.; Deangelis, L.M.; Chang, S.; et al. Cilengitide in patients with recurrent glioblastoma: The results of NABTC 03-02, a phase II trial with measures of treatment delivery. *J. Neurooncol.* **2012**, *106*, 147–153.
38. Massabeau, C.; Khalifa, J.; Filleron, T.; Modesto, A.; Bigay-Gamé, L.; Plat, G.; Dierickx, L.; Aziza, R.; Rouquette, I.; Gomez-Roca, C.; et al. Continuous infusion of cilengitide plus chemoradiotherapy for patients with stage III non-small-cell

- lung cancer: A phase I study. *Clin. Lung Cancer* **2018**, *19*, e277–e285.
39. Yang, G.X.; Hagmann, W.K. VLA-4 antagonists: Potent inhibitors of lymphocyte migration. *Med. Res. Rev.* **2003**, *23*, 369–392.
 40. Lin, K.C.; Ateeq, H.S.; Hsiung, S.H.; Chong, L.T.; Zimmerman, C.N.; Castro, A.; Lee, W.C.; Hammond, C.E.; Kalkunte, S.; Chen, L.L.; et al. Selective, tight-binding inhibitors of integrin $\alpha 4\beta 1$ that inhibit allergic airway responses. *J. Med. Chem.* **1999**, *42*, 920–934.
 41. Dattoli, S.D.; De Marco, R.; Baiula, M.; Spampinato, S.; Greco, A.; Tolomelli, A.; Gentilucci, L. Synthesis and assay of retro- $\alpha 4\beta 1$ integrin-targeting motifs. *Eur. J. Med. Chem.* **2014**, *12*, 225–232.
 42. Tolomelli, A.; Baiula, M.; Viola, A.; Ferrazzano, L.; Gentilucci, L.; Dattoli, S.D.; Spampinato, S.; Juaristi, E.; Escudero, M. Dehydro- β -proline containing $\alpha 4\beta 1$ integrin antagonists: Stereochemical recognition in ligand-receptor interplay. *ACS Med. Chem. Lett.* **2015**, *6*, 701–706.
 43. De Marco, R.; Mazzotti, G.; Dattoli, S.D.; Baiula, M.; Spampinato, S.; Greco, A.; Gentilucci, L. 5-Aminomethylloxazolidine-2,4-dione hybrid $\alpha\beta$ -dipeptide scaffolds as inducers of constrained conformations: Applications to the synthesis of integrin antagonists. *Biopolymers* **2015**, *104*, 636–649.
 44. Greco, A.; Tani, S.; De Marco, R.; Gentilucci, L. Synthesis and analysis of the conformational preferences of 5-aminomethylloxazolidine-2,4-dione scaffolds: First examples of $\beta(2)$ - and $\beta(2,2)$ -homo-freidinger lactam analogues. *Chem. Eur. J.* **2014**, *20*, 13390–13404.
 45. Dattoli, S.D.; Baiula, M.; De Marco, R.; Bedini, A.; Anselmi, M.; Gentilucci, L.; and Spampinato, S. DS-70, a novel and potent $\alpha 4$ integrin antagonist, is an effective treatment for experimental allergic conjunctivitis in guinea pigs. *Br. J. Pharmacol.* **2018**, *175*, 3891–3910.
 46. Celik, E.; Faridi, M.H.; Kumar, V.; Deep, S.; Moy, V.T.; Gupta, V. Agonist leukadherin-1 increases CD11b/CD18-dependent adhesion via membrane tethers. *Biophys. J.* **2013**, *105*, 2517–2527.
 47. Vanderslice, P.; Biediger, R.J.; Woodside, D.G.; Brown, W.S.; Khounlo, S.; Warier, N.D.; Gundlach, C.W.; Caivano, A.R.; Bornmann, W.G.; Maxwell, D.S.; et al. Small molecule agonist of very late antigen-4 (VLA-4) integrin induces progenitor cell adhesion. *J. Biol. Chem.* **2013**, *288*, 19414–19428.
 48. Schwartz, M.A.; McRoberts, K.; Coyner, M.; Andarawewa, K.L.; Frierson, H.F.; Sanders, J.M.; Swenson, S.; Markland, F.; Conaway, M.R.; Theodorescu, D. Integrin agonists as adjuvants in chemotherapy for melanoma. *Clin. Cancer Res.* **2008**, *14*, 6193–6197.
 49. Yang, W.; Carman, C.V.; Kim, M.; Salas, A.; Shimaoka, M.; Springer, T.A. A small molecule agonist of an integrin, $\alpha L\beta 2$. *J. Biol. Chem.* **2006**, *281*, 37904–37912.
 50. Galletti, P.; Soldati, R.; Pori, M.; Durso, M.; Tolomelli, A.; Gentilucci, L.; Dattoli, S.D.; Baiula, M.; Spampinato, S.; Giacomini, D. Targeting integrins $\alpha v\beta 3$ and $\alpha 5\beta 1$ with new β -lactam derivatives. *Eur. J. Med. Chem.* **2014**, *83*, 284–293.
 51. Baiula, M.; Galletti, P.; Martelli, G.; Soldati, R.; Belvisi, L.; Civera, M.; Dattoli, S.D.; Spampinato, S.M.; Giacomini, D. New β -lactam derivatives modulate cell adhesion and signaling mediated by RGD-binding and leukocyte integrins. *J. Med. Chem.* **2016**, *59*, 9721–9742.
 52. Martelli, G.; Baiula, M.; Caligiana, A.; Galletti, P.; Gentilucci, L.; Arta, R.; Spampinato, S.; Giacomini, D. Could dissecting the molecular framework of β -lactam integrin ligands enhance selectivity? *J. Med. Chem.* **2019**, *62*, 10156–10166.
 53. Majumder, P. Integrin-Mediated delivery of drugs and nucleic acids for anti-angiogenic cancer therapy: Current landscape and remaining challenges. *Bioengineering* **2018**, *5*, 76.
 54. Bridgewater, R.E.; Norman, J.C.; Caswell, P.T. Integrin trafficking at a glance. *J. Cell Sci.* **2012**, *125*, 3695–3701.
 55. Temming, K.; Schiffelers, R.M.; Molemad, G.; Kok, R.J. RGD-based strategies for selective delivery of therapeutics and imaging agents to the tumour vasculature. *Drug Resist. Updat.* **2005**, *8*, 381–402.
 56. Arosio, D.; Casagrande, C.; Manzoni, L. Integrin-mediated drug delivery in cancer and cardiovascular diseases with peptide-functionalized nanoparticles. *Curr. Med. Chem.* **2012**, *19*, 3128–3151.
 57. Pysz, I.; Jackson, P.J.M.; Thurston, D.E. Introduction to antibody-drug conjugates (ADCs). In *Cytotoxic Payloads for Antibody-Drug Conjugates*; Thurston, D.E., Jackson, P.J.M., Eds.; Royal Society of Chemistry: London, UK, 2019.
 58. Dal Corso, A.; Pignataro, L.; Belvisi, L.; Gennari, C. Alpha(v)beta(3) Integrin-targeted peptide/peptidomimetic-drug conjugates: In-Depth analysis of the linker technology. *Curr. Top. Med. Chem.* **2016**, *16*, 1–16.
 59. Zhuang, C.; Guan, X.; Ma, H.; Cong, H.; Zhang, W.; Miao, Z. Small molecule-drug conjugates: A novel strategy for cancer-targeted treatment. *Eur. J. Med. Chem.* **2019**, *163*, 883–895.
 60. Xu, S.; Olenyuk, B.Z.; Okamoto, C.T.; Hamm-Alvarez, S.F. Targeting receptor-mediated endocytotic pathways with nanoparticles: Rationale and advances. *Adv. Drug Deliv. Rev.* **2013**, *65*, 121–138.
 61. Suk, J.S.; Xu, Q.G.; Kim, N.; Hanes, J.; Ensign, L.M. Glycation as a strategy for improving nanoparticle-based drug and

- gene delivery. *Adv. Drug Deliv. Rev.* **2016**, *99*, 28–51.
62. Spicer, C.D.; Pashuck, E.T.; Stevens, M.M. Achieving controlled biomolecule-biomaterial conjugation. *Chem. Rev.* **2018**, *118*, 7702–7743.
63. Gabizon, A.; Papahadjopoulos, D. Liposome formulations with prolonged circulation time in blood and enhanced uptake by tumors. *Proc. Natl. Acad. Sci. USA* **1988**, *85*, 6949–6953.
64. Madni, A.; Sarfraz, M.; Rehman, M.; Ahmad, M.; Akhtar, N.; Ahmad, S.; Tahir, N.; Ijaz, S.; Al-Kassas, R.; Lobenberg, R. Liposomal drug delivery: A versatile platform for challenging clinical applications. *J. Pharm. Pharm. Sci.* **2014**, *17*, 401–426.
65. Schiffler, R.M.; Koning, G.A.; ten Hagen, T.L.M.; Fens, M.H.A.M.; Schraa, A.J.; Janssen, A.P.C.A.; Kok, R.J.; Molema, G.; Storm, G. Antitumor efficacy of tumor vasculature-targeted liposomal doxorubicin. *J. Control. Release* **2003**, *91*, 115–122.
66. Bianchini, F.; De Santis, A.; Portioli, E.; Krauss, I.R.; Battistini, L.; Curti, C.; Peppicelli, S.; Calorini, L.; D'Errico, G.; Zanardi, F.; et al. Integrin-Targeted AmpRGD sunitinib liposomes as integrated antiangiogenic tools. *Nanomedicine* **2019**, *18*, 135–145.
67. Meng, S.; Su, B.; Li, W.; Ding, Y.; Tang, L.; Zhou, W.; Song, Y.; Li, H.; Zhou, C. Enhanced antitumor effect of novel dual-targeted paclitaxel liposomes. *Nanotechnology* **2010**, *21*, 1–7.
68. Manavitehrani, I.; Fathi, A.; Badr, H.; Daly, S.; Shirazi, A.N.; Dehghani, F. Biomedical applications of biodegradable polyesters. *Polymers* **2016**, *8*, 20.
69. Nasongkla, N.; Shuai, X.; Ai, H.; Weinberg, B.D.; Pink, J.; Boothman, D.A.; Gao, J. cRGD-functionalized polymer micelles for targeted doxorubicin delivery. *Angew. Chem. Int. Ed.* **2004**, *43*, 6323–6327, doi:10.1002/anie.200460800.
70. Nasongkla, N.; Bey, E.; Ren, J.; Ai, H.; Khemtong, C.; Guthi, J.S.; Chin, S.F.; Sherry, A.D.; Boothman, D.A.; Gao, J. Multifunctional polymeric micelles as cancer-targeted, MRI-ultrasensitive drug delivery systems. *Nano Lett.* **2006**, *6*, 2427–2430.
71. Xiong, X.B.; Ma, Z.; Lai, L.; Lavasanifar, A. The therapeutic response to multifunctional polymeric nano conjugates in the targeted cellular and subcellular delivery of doxorubicin. *Biomaterials* **2010**, *31*, 757–768.
72. Danhier, F.; Vroman, B.; Lecouturier, N.; Crockart, N.; Pourcelet, V.; Freichels, H.; Jérôme, C.; Marchand-Brynaert, J.; Feron, O.; Préat, V. Targeting of tumor endothelium by RGD-grafted PLGA-nanoparticles loaded with Paclitaxel. *J. Control. Release* **2009**, *140*, 166–173.
73. Waite, C.L.; Roth, C.M. PAMAM-RGD conjugates enhance siRNA delivery through a multicellular spheroid model of malignant glioma. *Bioconjugate Chem.* **2009**, *20*, 1908–1916.
74. Wang, K.; Zhang, X.F.; Liu, Y.; Liu, C.; Jiang, B.H.; Jiang, Y.Y. Tumor penetrability and anti-angiogenesis using iRGD-mediated delivery of doxorubicin-polymer conjugates. *Biomaterials* **2014**, *35*, 8735–8747.
75. Han, H.D.; Mangala, L.S.; Lee, J.W.; Shahzad, M.M.; Kim, H.S.; Shen, D.; Nam, E.J.; Mora, E.M.; Stone, R.L.; Lu, C.; et al. Targeted gene silencing using RGD-labeled chitosan nanoparticles. *Clin. Cancer Res.* **2010**, *16*, 3910–3922.
76. Wagner, S.; Rothweiler, F.; Anhorn, M.G.; Sauer, D.; Riemann, I.; Weiss, E.C.; Katsen-Globa, A.; Michaelis, M.; Cinatl Jr., J.; Schwartz, D.; et al. Enhanced drug targeting by attachment of an anti αv integrin antibody to doxorubicin loaded human serum albumin nanoparticles. *Biomaterials* **2010**, *31*, 2388–2398.
77. Ming, X.; Carver, K.; Wu, L. Albumin-Based nanoconjugates for targeted delivery of therapeutic oligonucleotides. *Biomaterials* **2013**, *34*, 7939–7949.
78. Kim, J.; Nam, H.Y.; Kim, T.I.; Kim, P.H.; Ryu, J.; Yun, C.O.; Kim, S.W. Active targeting of RGD-conjugated bioreducible polymer for delivery of oncolytic adenovirus expressing shRNA against IL-8 mRNA. *Biomaterials* **2011**, *32*, 5158–5166.
79. Conde, J.; Dias, J.T.; Grazú, V.; Moros, M.; Baptista, P.V.; de la Fuente, J.M. Revisiting 30 years of biofunctionalization and surface chemistry of inorganic nanoparticles for nanomedicine. *Front. Chem.* **2014**, *2*, 1–27.
80. Jia, T.; Choi, J.; Ciccione, J.; Henry, M.; Mehdi, A.; Martinez, J.; Eymen, B.; Subra, G.; Coll, J.L. Heteromultivalent targeting of integrin $\alpha v \beta 3$ and neuropilin 1 promotes cell survival via the activation of the IGF-1/insulin receptors. *Biomaterials* **2018**, *155*, 64–79.
81. Juthani, R.; Madajewski, B.; Yoo, B.; Zhang, L.; Chen, P.M.; Chen, F.; Turker, M.Z.; Ma, K.; Overholtzer, M.; Longo, V.A.; et al. Ultrasmall core-shell silica nanoparticles for precision drug delivery in a high-grade malignant brain tumor model. *Clin. Cancer Res.* **2020**, *26*, 147–158.
82. Sugahara, K.N.; Teesalu, T.; Karmali, P.P.; Kotamraju, V.R.; Agemy, L.; Girard, O.M.; Hanahan, D.; Mattrey, R.F.; Ruoslahti, E. Tissue-Penetrating delivery of compounds and nanoparticles into tumors. *Cancer Cell* **2009**, *16*, 510–520.
83. Agemy, L.; Friedmann-Morvinski, D.; Kotamraju, V.R.; Roth, L.; Sugahara, K.N.; Girard, O.M.; Mattrey, R.F.; Verma, I.M.; Ruoslahti, E. Targeted nanoparticle enhanced proapoptotic peptide as potential therapy for glioblastoma. *Proc. Natl.*

Acad. Sci. USA **2011**, *108*, 17450–17455.

84. Chen, K.; Xie, J.; Xu, H.; Behera, D.; Michalski, M.H.; Biswal, S.; Wang, A.; Chen, X. Triblock copolymer coated iron oxide nanoparticle conjugate for tumor integrin targeting. *Biomaterials* **2009**, *30*, 6912–6919.
85. Kluza, E.; van der Schaft, D.W.; Hautvast, P.A.; Mulder, W.J.; Mayo, K.H.; Griffioen, A.W.; Strijkers, G.J.; Nicolay, K. Synergistic targeting of $\alpha\beta 3$ integrin and galectin-1 with heteromultivalent paramagnetic liposomes for combined MR imaging and treatment of angiogenesis. *Nano Lett.* **2010**, *10*, 52–58.
86. Conde, J.; Tian, F.; Hernandez, Y.; Bao, C.; Cui, D.; Janssen, K.P.; Ibarra, M.R.; Baptista, P.V.; Stoeger, T.; de la Fuente, J.M. In vivo tumor targeting via nanoparticle-mediated therapeutic siRNA coupled to inflammatory response in lung cancer mouse models. *Biomaterials* **2013**, *34*, 7744–7753.
87. Li, K.G.; Zhang, Z.L.; Zheng, L.F.; Liu, H.; Wei, W.; Li, Z.Y.; He, Z.Y.; Larson, A.C.; Zhang, G.X. Arg-Gly-Asp-D-Phe-Lys peptide-modified PEGylated dendrimer-entrapped gold nanoparticles for targeted computed tomography imaging of breast carcinoma. *Nanomedicine* **2015**, *10*, 2185–2197.
88. Atmaja, B.; Lui, B.H.; Hu, Y.H.; Beck, S.E.; Frank, C.W.; Cochran, J.R. Targeting of cancer cells using quantum dot-polypeptide hybrid assemblies that function as molecular imaging agents and carrier systems. *Adv. Funct. Mater.* **2010**, *20*, 4091–4097.
89. Hu, K.Z.; Wang, H.L.; Tang, G.H.; Huang, T.T.; Tang, X.L.; Liang, X.; Yao, S.B.; Nie, D.H. In vivo cancer dual-targeting and dual-modality imaging with functionalized quantum dots. *J. Nucl. Med.* **2015**, *56*, 1278–1284.
90. Hirano, Y.; Mooney, D.J. Peptide and protein presenting materials for tissue engineering. *Adv. Mater.* **2004**, *16*, 17–25.
91. Shekaran, A.; García, A.J. Extracellular matrix-mimetic adhesive biomaterials for bone repair. *J. Biomed. Mater. Res. A* **2011**, *96*, 261–272.
92. Meyers, S.R.; Grinstaff, M.W. Biocompatible and bioactive surface modifications for prolonged in vivo efficacy. *Chem. Rev.* **2012**, *112*, 1615–1632.
93. Elbert, D.L.; Hubbell, J.A. Surface treatments of polymers for biocompatibility. *Annu. Rev. Mater. Sci.* **1996**, *26*, 365–394.
94. Spicer, C.D.; Davis, B.G. Selective chemical protein modification. *Nat. Commun.* **2014**, *5*, 4740–4753.
95. De Marco, R.; Zhao, J.; Greco, A.; Ioannone, S.; Gentilucci, L. In-Peptide synthesis of imidazolidin-2-one scaffolds, equippable with proteinogenic or taggable/linkable side chains, general promoters of unusual secondary structures. *J. Org. Chem.* **2019**, *84*, 4992–5004.
96. Mendes, P.M. Cellular nanotechnology: Making biological interfaces smarter. *Chem. Soc. Rev.* **2013**, *42*, 9207–9218.
97. Houseman, B.T.; Mrksich, M. The microenvironment of immobilized Arg-Gly-Asp peptides is an important determinant of cell adhesion. *Biomaterials* **2001**, *22*, 943–955.
98. Shabbir, S.H.; Eisenberg, J.L.; Mrksich, M. An inhibitor of a cell adhesion receptor stimulates cell migration. *Angew. Chem. Int. Ed.* **2010**, *49*, 7706–7709.
99. Le Saux, G.; Magenau, A.; Gunaratnam, K.; Kilian, K.A.; Böcking, T.; Gooding, J.J.; Gaus, K. Spacing of integrin ligands influences signal transduction in endothelial cells. *Biophys. J.* **2011**, *101*, 764–773.
100. Cosenza, C.; Lettera, V.; Causa, F.; Scognamiglio, P.L.; Battista, E.; Netti, P.A. Cell mechanosensory recognizes ligand compliance at biomaterial interface. *Biomaterials* **2016**, *76*, 282–291.
101. Garcia, A.S.; Dellatore, S.M.; Messersmith, P.B.; Miller, W.M. Effects of supported lipid monolayer fluidity on the adhesion of hematopoietic progenitor cell lines to fibronectin-derived peptide ligands for $\alpha 5\beta 1$ and $\alpha 4\beta 1$ integrins. *Langmuir* **2009**, *25*, 2994–3002.
102. Marchi-Artzner, V.; Lorz, B.; Hellerer, U.; Kantlehner, M.; Kessler, H.; Sackmann, E. Selective adhesion of endothelial cells to artificial membranes with a synthetic RGD-lipopeptide. *Chem. Eur. J.* **2001**, *7*, 1095–1101.
103. Koçer, G.; Jonkheijm, P. Guiding hMSC adhesion and differentiation on supported lipid bilayers. *Adv. Healthc. Mater.* **2017**, *6*, 1600862.
104. Rechenmacher, F.; Neubauer, S.; Mas-Moruno, C.; Dorfner, P.M.; Polleux, J.; Guasch, J.; Conings, B.; Boyen, H.G.; Bochen, A.; Sobahi, T.R.; et al. A molecular toolkit for the functionalization of titanium-based biomaterials that selectively control integrin-mediated cell adhesion. *Chem. Eur. J.* **2013**, *19*, 9218–9223.
105. Fraioli, R.; Rechenmacher, F.; Neubauer, S.; Manero, J.M.; Gil, J.; Kessler, H.; Mas-Moruno, C. Mimicking bone extracellular matrix: Integrin-binding peptidomimetics enhance osteoblast-like cells adhesion, proliferation and differentiation on titanium. *Colloids Surf. B Biointerfaces* **2015**, *128*, 191–200.
106. Rémy, M.; Bareille, R.; Rerat, V.; Bourget, C.; Marchand-Brynaert, J.; Bordenave, L. Polyethylene terephthalate membrane grafted with peptidomimetics: Endothelial cell compatibility and retention under shear stress. *J. Biomater. Sci. Polym. Ed.* **2013**, *24*, 269–286.
107. Kantlehner, M.; Finsinger, D.; Meyer, J.; Schaffner, P.; Jonczyk, A.; Diefenbach, B.; Nies, B.; and Kessler, H.

- Selective RGD mediated adhesion of osteoblasts at surfaces of implants. *Angew. Chem. Int. Ed.* **1999**, *38*, 560–562.
108. Schussler, O.; Coirault, C.; Louis-Tisserand, M.; Al-Chare, W.; Oliviero, P.; Menard, C.; Michelot, R.; Bochet, P.; Salomon, D.R.; Chachques, J.C.; et al. Use of Arginine-Glycine-Aspartic acid adhesion peptides coupled with a new collagen scaffold to engineer a myocardium-like tissue graft. *Nat. Clin. Pract. Cardiovasc. Med.* **2009**, *6*, 240–249.
109. Kilian, K.A.; Mrksich, M. Directing stem cell fate by controlling the affinity and density of ligand-receptor interactions at the biomaterials interface. *Angew. Chem. Int. Ed.* **2012**, *51*, 4891–4895.
110. Karimi, F.; O'Connor, A.J.; Qiao, G.G.; Heath, D.E. Integrin clustering matters: A review of biomaterials functionalized with multivalent integrin-binding ligands to improve cell adhesion, migration, differentiation, angiogenesis, and biomedical device integration. *Adv. Healthc. Mater.* **2018**, *7*, 1701324.
111. Morgan, A.W.; Roskov, K.E.; Lin-Gibson, S.; Kaplan, D.L.; Becker, M.L.; Simon, C.G. Characterization and optimization of RGD-containing silk blends to support osteoblastic differentiation. *Biomaterials* **2008**, *29*, 2556–2563.
112. Yang, Y.J.; Kwon, Y.; Choi, B.H.; Jung, D.; Seo, J.H.; Lee, K.H.; Cha, H.J. Multifunctional adhesive silk fibroin with blending of RGD bioconjugated mussel adhesive protein. *Biomacromolecules* **2014**, *15*, 1390–1398.
113. Janani, G.; Nandi, S.K.; Mandal, B.B. Functional hepatocyte clusters on bioactive blend silk matrices towards generating bioartificial liver constructs. *Acta Biomater.* **2018**, *67*, 167–182.
114. Maheshwari, G.; Brown, G.; Lauffenburger, D.A.; Wells, A.; Griffith, L.G. Cell adhesion and motility depend on nanoscale RGD clustering. *J. Cell Sci.* **2000**, *113*, 1677–1686.
115. Lim, C.; Moon, J.; Sim, T.; Hoang, N.H.; Won, W.R.; Lee, E.S.; Youn, Y.S.; Choi, H.G.; Oh, K.; Oh, K.T. Cyclic RGD-conjugated Pluronic® blending system for active, targeted drug delivery. *Int. J. Nanomed.* **2018**, *13*, 4627–4639.
116. Rundqvist, J.; Mendoza, B.; Werbin, J.L.; Heinz, W.F.; Lemmon, C.; Romer, L.H.; Haviland, D.B.; Hoh, J.H. High fidelity functional patterns of an extracellular matrix protein by electron beam-based inactivation. *J. Am. Chem. Soc.* **2007**, *129*, 59–67.
117. Kolodziej, C.M.; Kim, S.H.; Broyer, R.M.; Saxer, S.S.; Decker, C.G.; Maynard, H.D. Combination of integrin-binding peptide and growth factor promotes cell adhesion on electron-beam-fabricated patterns. *J. Am. Chem. Soc.* **2012**, *134*, 247–255.
118. Kim, Y.; Kwon, C.; Jeon, H. Genetically engineered phage induced selective H9c2 cardiomyocytes patterning in PDMS microgrooves. *Materials* **2017**, *10*, 973.
119. Bilem, I.; Chevallier, P.; Plawinski, L.; Sone, E.D.; Durrieu, M.C.; Laroche, G. Interplay of geometric cues and RGD/BMP-2 crosstalk in directing stem cell fate. *ACS Biomater. Sci. Eng.* **2017**, *3*, 2514–2523.
120. Bilem, I.; Plawinski, L.; Chevallier, P.; Ayela, C.; Sone, E.D.; Laroche, G.; Durrieu, M.C. The spatial patterning of RGD and BMP-2 mimetic peptides at the subcellular scale modulates human mesenchymal stem cells osteogenesis. *J. Biomed. Mater. Res. A* **2018**, *106*, 959–970.
121. Lee, H.J.; Kim, D.N.; Park, S.; Lee, Y.; Koh, W.G. Micropatterning of a nanoporous alumina membrane with poly(ethylene glycol) hydrogel to create cellular micropatterns on nanotopographic substrates. *Acta Biomater.* **2011**, *7*, 1281–1289.
122. Pallarola, D.; Bochen, A.; Boehm, H.; Rechenmacher, F.; Sobahi, T.R.; Spatz, J.P.; Kessler, H. Interface immobilization chemistry of cRGD-based peptides regulates integrin mediated cell adhesion. *Adv. Funct. Mater.* **2014**, *24*, 943–956.
123. Medda, R.; Helth, A.; Herre, P.; Pohl, D.; Rellinghaus, B.; Perschmann, N.; Neubauer, S.; Kessler, H.; Oswald, S.; Eckert, J.; et al. Investigation of early cell-surface interactions of human mesenchymal stem cells on nanopatterned β -type titanium-niobium alloy surfaces. *Interface Focus* **2014**, *4*, 20130046.
124. Wang, X.; Yan, C.; Ye, K.; He, Y.; Li, Z.; Ding, J. Effect of RGD nanospacing on differentiation of stem cells. *Biomaterials* **2013**, *34*, 2865–2874.
125. Cheng, Z.A.; Zouani, O.F.; Glinel, K.; Jonas, A.M.; Durrieu, M.C. Bioactive chemical nanopatterns impact human mesenchymal stem cell fate. *Nano Lett.* **2013**, *13*, 3923–3929.
126. Kim, T.G.; Park, T.G. Biomimicking extracellular matrix: Cell adhesive RGD peptide modified electrospun poly(D, L-lactic-co-glycolic acid) nanofiber mesh. *Tissue Eng.* **2006**, *12*, 221–33.
127. Yun, D.H.; Famili, A.; Lee, Y.M.; Jenkins, P.M.; Freed, C.R.; Park, D. Biomimetic poly(serinol hexamethylene urea) for promotion of neurite outgrowth and guidance. *J. Biomater. Sci. Polym. Ed.* **2014**, *25*, 354–369.
128. Madhavan, K.; Frid, M.G.; Hunter, K.; Shandas, R.; Stenmark, K.R.; Park, D. Development of an electrospun biomimetic polyurea scaffold suitable for vascular grafting. *J. Biomed. Mater. Res. Part. B Appl. Biomater.* **2018**, *106*, 278–290.
129. Jeong, S.I.; Burns, N.A.; Bonino, C.A.; Kwon, I.K.; Khan, S.A.; Alsborg, E. Improved cell infiltration of highly porous D nanofibrous scaffolds formed by combined fiber-fiber charge repulsions and ultra-sonication. *J. Mater. Chem. B* **2014**, *2*,

8116–8122.

130. Antonova, L.V.; Seifalian, A.M.; Kutikhin, A.G.; Sevostyanova, V.V.; Matveeva, V.G.; Velikanova, E.A.; Mironov, A.V.; Shabaev, A.R.; Glushkova, T.V.; Senokosova, E.A.; et al. Conjugation with RGD peptides and incorporation of vascular endothelial growth factor are equally efficient for biofunctionalization of tissue-engineered vascular grafts. *Int. J. Mol. Sci.* **2016**, *17*, 1920.
131. Wang, J.L.; Yang, M.Y.; Zhu, Y.; Wang, L.; Tomsia, A.P.; Mao, C.B. Phage nanofibers induce vascularized osteogenesis in D printed bone scaffolds. *Adv. Mater.* **2014**, *26*, 4961–4966.
132. Heo, D.N.; Castro, N.J.; Lee, S.J.; Noh, H.; Zhu, W.; Zhang, L.G. Enhanced bone tissue regeneration using a D printed microstructure incorporated with hybrid nano hydrogel. *Nanoscale* **2017**, *9*, 5055–5062.
133. Camacho, P.; Busari, H.; Seims, K.B.; Schwarzenberg, P.; Dailey, H.L.; Chow, L.W. D printing with peptide-polymer conjugates for single-step fabrication of spatially functionalized scaffolds. *Biomater. Sci.* **2019**, *7*, 4237–4247.
134. Greco, A.; Maggini, L.; De Cola, L.; De Marco, R.; and Gentilucci, L. Diagnostic implementation of fast and selective integrin-mediated adhesion of cancer cells on functionalized zeolite L monolayers. *Bioconjugate Chem.* **2015**, *26*, 1873–1878.
135. De Marco, R.; Greco, A.; Calonghi, N.; Dattoli, S.D.; Baiula, M.; Spampinato, S.; Picchetti, P.; De Cola, L.; Anselmi, M.; Cipriani, F.; et al. Selective detection of $\alpha 4\beta 1$ integrin (VLA-4)-expressing cells using peptide-functionalized nanostructured materials mimicking endothelial surfaces adjacent to inflammatory sites. *Pept. Sci.* **2018**, *110*, e23081.
136. Fraioli, R.; Tsimbouri, P.M.; Fisher, L.E.; Nobbs, A.H.; Su, B.; Neubauer, S.; Rechenmacher, F.; Kessler, H.; Ginebra, M.P.; Dalby, M.J.; et al. Towards the cell-instructive bactericidal substrate: Exploring the combination of nanotopographical features and integrin selective synthetic ligands. *Sci. Rep.* **2017**, *7*, 16363.
137. Martelli, G.; Bloise, N.; Merlettini, A.; Bruni, G.; Visai, L.; Focarete, M.L.; Giacomini, D. Combining biologically active β -lactams integrin agonists with poly(L-lactic acid) nanofibers: Enhancement of human mesenchymal stem cell adhesion. *Biomacromolecules* **2020**, *21*, 1157–1170.
138. Liu, Y.; Wang, X.; Kaufman, D.S.; Shen, W. A synthetic substrate to support early mesodermal differentiation of human embryonic stem cells. *Biomaterials* **2011**, *32*, 8058–8066.
139. Mas-Moruno, C.; Fraioli, R.; Albericio, F.; Manero, J.M.; Gil, F.J. Novel peptide-based platform for the dual presentation of biologically active peptide motifs on biomaterials. *ACS Appl. Mater. Interfaces* **2014**, *6*, 6525–6536.
140. Zhao, N.; Battig, M.R.; Xu, M.; Wang, X.; Xiong, N.; Wang, Y. Development of a dual-functional hydrogel using RGD and anti-VEGF aptamer. *Macromol. Biosci.* **2017**, *17*, 1700201.
141. Karimi, F.; Thombare, V.J.; Hutton, C.A.; O'Connor, A.J.; Qiao, G.G.; Heath, D.E. Beyond RGD; nanoclusters of syndecan- and integrin-binding ligands synergistically enhance cell/material interactions. *Biomaterials* **2018**, *187*, 81–92.
142. Koçer, G.; Jonkheijm, P. About chemical strategies to fabricate cell-instructive biointerfaces with static and dynamic complexity. *Adv. Healthc. Mater.* **2018**, *7*, 1701192.
143. Ebara, M.; Yamato, M.; Aoyagi, T.; Kikuchi, A.; Sakai, K. and Okano, T. A novel approach to observing synergy effects of PHSRN on integrin-RGD binding using intelligent surfaces. *Adv. Mater.* **2008**, *20*, 3034–3038.
144. Kobayashi, J.; Yamato, M.; Okano, T. On-Off affinity binding modulation on thermoresponsive polymer-grafted surfaces for capture and release of proteins and cells. *J. Biomater. Sci. Polym. Ed.* **2017**, *28*, 939–957.
145. Simnick, A.J.; Valencia, C.A.; Liu, R.; Chilkoti, A. Morphing low-affinity ligands into high-avidity nanoparticles by thermally triggered self-assembly of a genetically encoded polymer. *ACS Nano* **2010**, *4*, 2217–2227.
146. Roberts, J.N.; Sahoo, J.K.; McNamara, L.E.; Burgess, K.V.; Yang, J.L.; Alakpa, E.V.; Anderson, H.J.; Hay, J.; Turner, L.A.; Yarwood, S.J.; et al. Dynamic surfaces for the study of mesenchymal stem cell growth through adhesion regulation. *ACS Nano* **2016**, *10*, 6667–6679.
147. Lamb, B.M.; Yousaf, M.N. Redox-Switchable surface for controlling peptide structure. *J. Am. Chem. Soc.* **2011**, *133*, 8870–8873.
148. Luo, W.; Yousaf, M.N. Tissue morphing control on dynamic gradient surfaces. *J. Am. Chem. Soc.* **2011**, *133*, 10780–10783.
149. Ng, C.C.A.; Magenau, A.; Ngalim, S.H.; Ciampi, S.; Chockalingham, M.; Harper, J.B.; Gaus, K.; Gooding, J.J. Using an electrical potential to reversibly switch surfaces between two states for dynamically controlling cell adhesion. *Angew. Chem. Int. Ed.* **2012**, *51*, 7706–7710.
150. Li, J.; Lei, Y.F.; Sun, C.L.; Zheng, W.F.; Jiang, X.Y.; Zhang, H.L. Rationally designed peptide interface for potential modulated cell adhesion and migration. *Adv. Mater. Interfaces* **2015**, *2*, 1500335.
151. Salierno, M.J.; García, A.J.; del Campo, A. Photo-Activatable surfaces for cell migration assays. *Adv. Funct. Mater.* **2013**, *23*, 5974–5980.
152. Wiemann, M.; Niebuhr, R.; Juan, A.; Cavatorta, E.; Ravoo, B.J.; Jonkheijm, P. Photo-Responsive bioactive surfaces

- based on cucurbit[8]uril-mediated host–guest interactions of arylazopyrazoles. *Chem. Eur. J.* **2018**, *24*, 813–817.
153. An, Q.; Brinkmann, J.; Huskens, J.; Krabbenborg, S.; de Boer, J.; Jonkheijm, P. A supramolecular system for the electrochemically controlled release of cells. *Angew. Chem. Int. Ed.* **2012**, *51*, 12233–12237.
154. Boekhoven, J.; Rubert Pérez, C.M.; Sur, S.; Worthy, A.; Stupp, S.I. Dynamic display of bioactivity through host-guest chemistry. *Angew. Chem. Int. Ed.* **2013**, *52*, 12077–12080.
155. Kloxin, A.M.; Kasko, A.M.; Salinas, C.N.; Anseth, K.S. Photodegradable hydrogels for dynamic tuning of physical and chemical properties. *Science* **2009**, *324*, 59–63.
156. Trappmann, B.; Baker, B.M.; Polacheck, W.J.; Choi, C.K.; Burdick, J.A.; Chen, C.S. Matrix degradability controls multicellularity of D cell migration. *Nat. Commun.* **2017**, *8*, 371.
157. Wang, H.; Zhu, D.; Paul, A.; Cai, L.; Enejder, A.; Yang, F.; Heilshorn, S.C. Covalently adaptable elastin-like protein-hyaluronic acid (ELP-HA) hybrid hydrogels with secondary thermoresponsive crosslinking for injectable stem cell delivery. *Adv. Funct. Mater.* **2017**, *27*, 1605609.

Chapter 6. Integrin-Targeting Dye-Doped PEG-Shell/Silica-Core Nanoparticles Mimicking the Proapoptotic Smac/DIABLO Protein.

Cancer cells demonstrate elevated expression levels of inhibitor of apoptosis proteins (IAPs), contributing to tumor cell survival, disease progression, chemo-resistance, and poor prognosis. Smac/DIABLO is a mitochondrial protein that promotes apoptosis by neutralizing members of the IAP family. Herein we describe the preparation and *in vitro* validation of a synthetic mimic of Smac/DIABLO, based on a fluorescent PEG-coated silica-core nanoparticle (NP) carrying a Smac/DIABLO-derived pro-apoptotic peptide and a tumor-homing integrin peptide ligand. At low μM concentration, the NPs showed significant toxicity towards A549, U373, and HeLa cancer cells, modest toxicity towards other integrin-expressing cells, correlated to integrin-mediated cell uptake and consequent highly increased levels of apoptotic activity, without perturbing non integrin-expressing cells.

1. Introduction

Apoptosis, or programmed cell death, is an essential process in homeostasis of multicellular organisms. It initiates through either the extrinsic death receptor pathway or the intrinsic mitochondrial signaling pathway, but both culminate with the activation of Cysteine ASPartic acid-specific proteASES (CASPASES), enzymes that degrade specific substrates implied in fundamental cellular processes. In mammals, caspases-3, -7 and -9 activity is regulated by the inhibitor of apoptosis proteins (IAPs).^[1,2] The mammalian IAP family includes eight members, all of which share the family-defining baculovirus IAP repeat (BIR) domain at the N-terminal end of the protein.^[3] BIRs are protein-interacting modules with distinct binding properties, necessary for the anti-apoptotic activity.^[4,5,6]

Strict regulation of apoptosis is involved in many human diseases.^[7] Tumorigenic cells exhibit significantly elevated expression levels of IAPs, resulting in the elusion of apoptosis, one of the defining hallmarks of cancer, and an underlying cause of therapeutic resistance.^[8] IAP-mediated caspase inhibition is depressed by the second mitochondria-derived activator (Smac)/direct inhibitor of apoptosis-binding protein with low pI (DIABLO), a mitochondrial protein that is translocated to the cytoplasm in apoptotic conditions.^[9] Structural analysis proved that the N-terminal sequence of Smac/DIABLO is essential for its function in interaction with BIR domain of IAP.^[10] As a consequence, peptides derived from the N-terminal sequence of Smac/DIABLO may represent attractive anticancer molecules.

In general, native peptides show too scarce stability and bioavailability to consent therapeutic or diagnostic applications.^[11, 12] To increase cellular uptake, the native 7-residue N-terminus of Smac/DIABLO (SmacN7) was bonded to a cell membrane permeable octaArg peptide (R8). The resulting SmacN7-R8 was able to induce the apoptosis of human nonsmall lung cancer (NSCLC) cells H460.^[13] More recently, peptidomimetics^[12] of the N-terminus of Smac/DIABLO have been designed and tested for higher stability and bioavailability, including retro-inverso,^[14] C-naphthyl substituted,^[15] and aza-peptides.^[16]

Nanoparticles (NPs) provide extraordinary opportunities as nanocarriers, due to prolonged circulation time and both passive and active targeting abilities towards cancerous tissues/cells. Seneci et al. reported non-covalent and covalent super paramagnetic iron oxide NPs (SPIONs)-Smac/DIABLO mimetic nano-conjugates. Unfortunately, the nanoconjugates were almost inactive in assays against breast cancer cells MDA-MB-231, ovarian carcinoma IGROV-1, cervical cancer HeLa cells.^[17] Li et al. prepared a

SmacN7-conjugated polymer containing the cell penetrating R8 peptide and four hydrophobic tails. The Smac-conjugated polymer could self-assemble giving NPs in aqueous environment. At high concentrations ($>10 \mu\text{M}$), the Smac-NPs elicited a measurable effect in MDA-MB-231 and H460 cells. The NPs have been also used as a drug delivery system to load doxorubicine (DOX) for combination therapy the DOX-loaded nanoparticles exhibited higher cellular uptake and antitumor effect.^[18] The tumor-targeting precision of drugs,^[19,20] NPs,^[21,22] polymers,^[23] biomaterials,^[24] or nanostructured materials,^[25,26] can be strongly improved by conjugation with peptide ligands addressing integrin receptors overexpressed by cancer cells.^[27,28] In fact, the integrin family of cell adhesion receptors regulates a diverse array of cellular functions crucial to the initiation, progression and metastasis of solid tumors, making them an appealing target for cancer therapy.^[29] For this reason, Gennari et al. connected a cyclo Arg-Gly-Asp (cRGD) ligand of the integrins $\alpha\beta3$ and $\alpha\beta5$ to mimetics of Smac/DIABLO. *In vitro*, the conjugates showed moderate synergistic/enhanced cytotoxic effects towards IGROV-1 cells.^[30] In this context, we designed nanosystems mimicking the Smac/DIABLO protein, based on inorganic fluorescent NPs coated with a biocompatible organic shell, functionalized with a Smac/DIABLO-derived peptide, and/or a tumor-homing integrin ligand peptide. The cytotoxicity, pro-apoptotic efficacy, and cellular uptake, have been determined for the peptide-NPs in diverse cells. Particularly, the role of integrin-mediated cell uptake was investigated by confocal microscopy.

2. Results

2.1 Chemistry.

Monodispersed fluorescent silica-core PEG-shell NPs (PEG, polyethylene glycol) functionalized with azide moieties and incorporating the dye rhodamine B triethoxysilane (RhB-TES),^[31] (Figure 1A), were expediently obtained by means of a direct micelles assisted method.^[32] These nanostructures were formed by the condensation of the silica precursor tetraethyl orthosilicate (TEOS) in aqueous acid environment in the presence of co-aggregates composed by a 10:1 mixture of the tri-block surfactant copolymer Pluronic® F127 (PF127) and its diazide derivative PF127-(N₃)₂.^[33] The condensation of RhB-TES within the silica core of the NP conferred the desired fluorescent properties to this nanosystem, preventing also the leaching of the fluorophore in the external environment. Transmission electron microscopy (TEM) images showed a silica core diameter $d_c = (10 \pm 2)$ nm, while the hydrodynamic diameter measured by dynamic light scattering (DLS) was $d_H = 22 \pm 0.5$ nm (PDI = 0.10) (Figure 1B-D), confirming the core/shell type architecture of the resulting NPs-N₃.

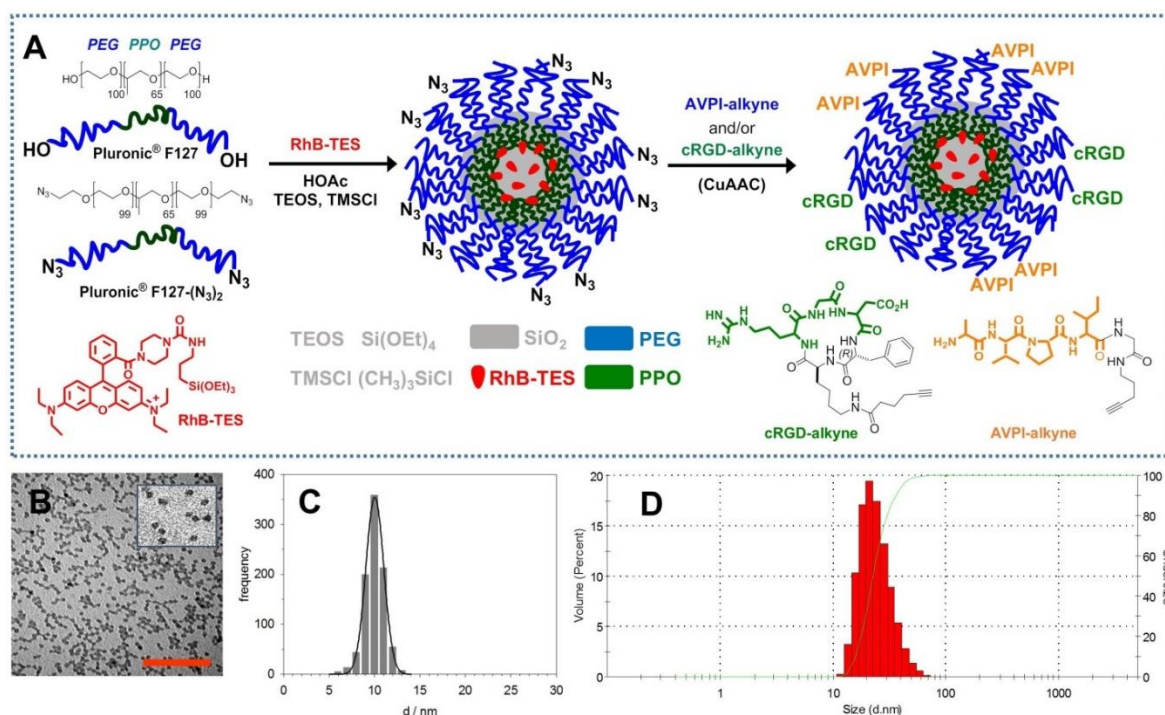


Figure 1. (A) Molecular components involved in the synthesis of nanoparticles NPs-N₃, and functionalization scheme with peptides AVPI-alkyne and/or cRGD-alkyne for the preparation of AVPI-NPs, cRGD-NPs and AVPI/cRGD-NPs. Morphological characterization of NPs-N₃: (B) TEM images of NP-N₃ (scale bar = 100 nm) and (C) TEM distribution of the diameters (nm). (D) Hydrodynamic diameters distribution by volume of NP-N₃ determined by DLS (water, 25°C).

The NPs-N₃ were derivatized by copper (I) catalyzed azide-alkyne cycloaddition (CuAAC) with either the peptide-alkyne H-Ala-Val-Pro-Ile-Gly-pent-4-yn-1-amine (AVPI-alkyne), containing the pro-apoptotic Smac/DIABLO-derived sequence AVPI,^[10] or the integrin-targeting cyclopeptide-alkyne c[Arg-Gly-Asp-D-Phe-Lys(hex-5-ynamide)] (cRGD-alkyne),^[34] or with a 1:1 mixture of both. These reactions gave AVPI-NPs, cRGD-NPs, or AVPI/cRGD-NPs, respectively. DLS indicated the effectiveness of the conjugation reaction, since the volume distribution after the conjugation reaction increased to 28 nm, compared to the pristine NP-N₃ (Figure 6-8).

Adapting reported procedures,^[35] the number of NP-bonded AVPI molecules was estimated by fluorimetric quantitation with fluorescamine (an amine reactive fluorogenic tracer), against a standard calibration curve obtained with PEG-amine/fluorescamine (λ_{ex} 390 nm, λ_{em} 480 nm). An aliquot of AVPI-NP suspension (25 μ L, 29 mM) was treated with fluorescamine, and the relative fluorescence intensity measured allowed to estimate 7.8 ± 1 peptides/NP.

Alternatively, NPs functionalization was appraised by the fluorimetric quantitation of the dansyl group after CuAAC reaction with dansyl-AVPI-alkyne, against a calibration curve obtained with unconjugated dansyl-AVPI-alkyne (λ_{ex} 340 nm, λ_{em} 477 nm). Consistent with the fluorescamine method, this test gave 9.3 ± 1 dansyl-AVPI/NP, and gave us the possibility to measure the amount of dansyl-AVPI bounded to a sample obtained by CuAAC reaction with a 1:1 mixture of dansyl-AVPI-alkyne and cRGD-alkyne. For this sample, an average number of 4.8 ± 1 dansyl-AVPI/NP was determined, indicating by difference that cRGD-alkyne reacted *circa* to the same extent.

2.2 Cytotoxicity of the Peptide-NPs.

The *in vitro* cell growth inhibitory efficacy was determined for the NPs and the unconjugated AVPI peptide, by incubating the A549, U-373, HeLa, Huvec, and fibroblast cells, with increasing concentrations of the compounds (0.1, 1.0, 3.0 μM) for 48 h. Cell viability is reported in Figure 2A; in general, all the combinations tested were ineffective at the conc. of 0.1 μM , therefore these data have been omitted. As expected, the simple peptide AVPI did not show any toxicity (data not shown), plausibly due to poor-to-null intracellular uptake.^[18] The NP-N₃ appeared well tolerated, since no detectable decrease in viability was observed after 48 h.

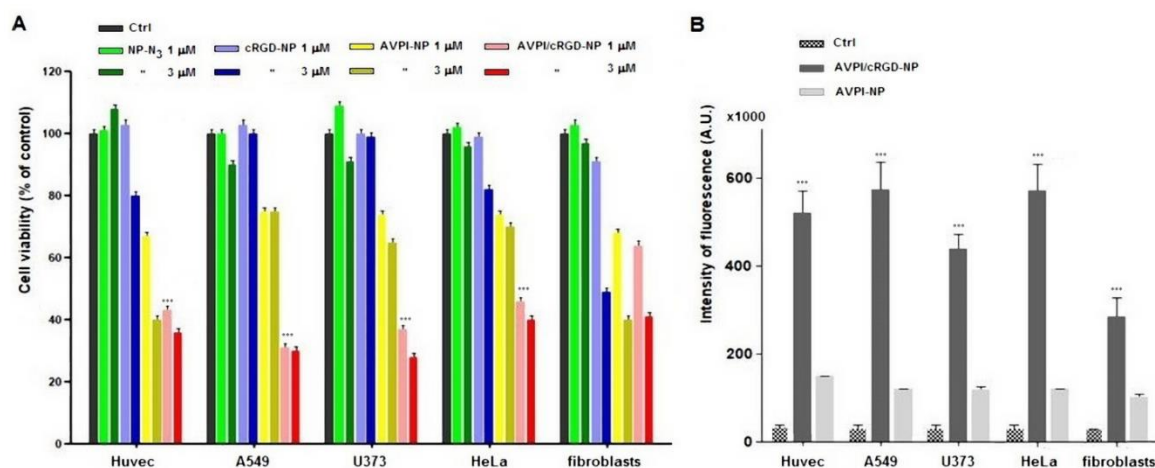


Figure 2. (A) Cell viability of peptide-NPs as % of control cells. Bars represent the mean \pm SD from two independent experiments ($n = 2$), each performed in triple. (B) Caspase-9 levels after 6 h of incubation with either 1 μM AVPI/cRGD-NPs or AVPI-NPs. Bars indicate the increase in activity of treated cells compared to the control. Data are reported as mean \pm SD from at least three independent experiments. *** $p < 0.001$.

As for the peptide-NPs, 1 μM cRGD-NPs showed very little toxicity, and modest toxicity when the concentration was increased to 3 μM . At the concentration of 1 μM , AVPI-NPs induced a decrease of viability in A549, U373 and HeLa cells of about 25%, and 33% in Huvec and fibroblast cells. At the concentration of 3 μM the AVPI-NPs showed much higher toxicity against Huvec and fibroblasts, reducing viability by 60%, while the effect was lower in U373, A549, and HeLa cells, decreasing vitality by 37% and 30%, respectively. In contrast, 1 μM AVPI/cRGD-NPs significantly inhibited the proliferation of A549, U373, HeLa, Huvec cells of about 60%, and a comparatively lower effect towards fibroblasts. Increasing the concentration of AVPI/cRGD-NPs to 3 μM led in general to higher toxicity, while the exclusion of A549 cells for which the toxicity remained the same.

2.3 Caspase-9 Activity.

The activity of caspase-9^[9] was assayed by a fluorimetric method in A549, U373, HeLa, Huvec, and fibroblast cells treated with 1 μM peptide-NPs for 6 h (Figure 2B). The AVPI-NPs gave a moderate but well measurable increase of activity, about 4-fold as compared to untreated control cells. On the other hand, AVPI/cRGD-NPs showed a > 40 -fold increase towards A549 and HeLa cells, Huvec, U373, and a comparatively lower 10-fold increase in activity in fibroblasts.

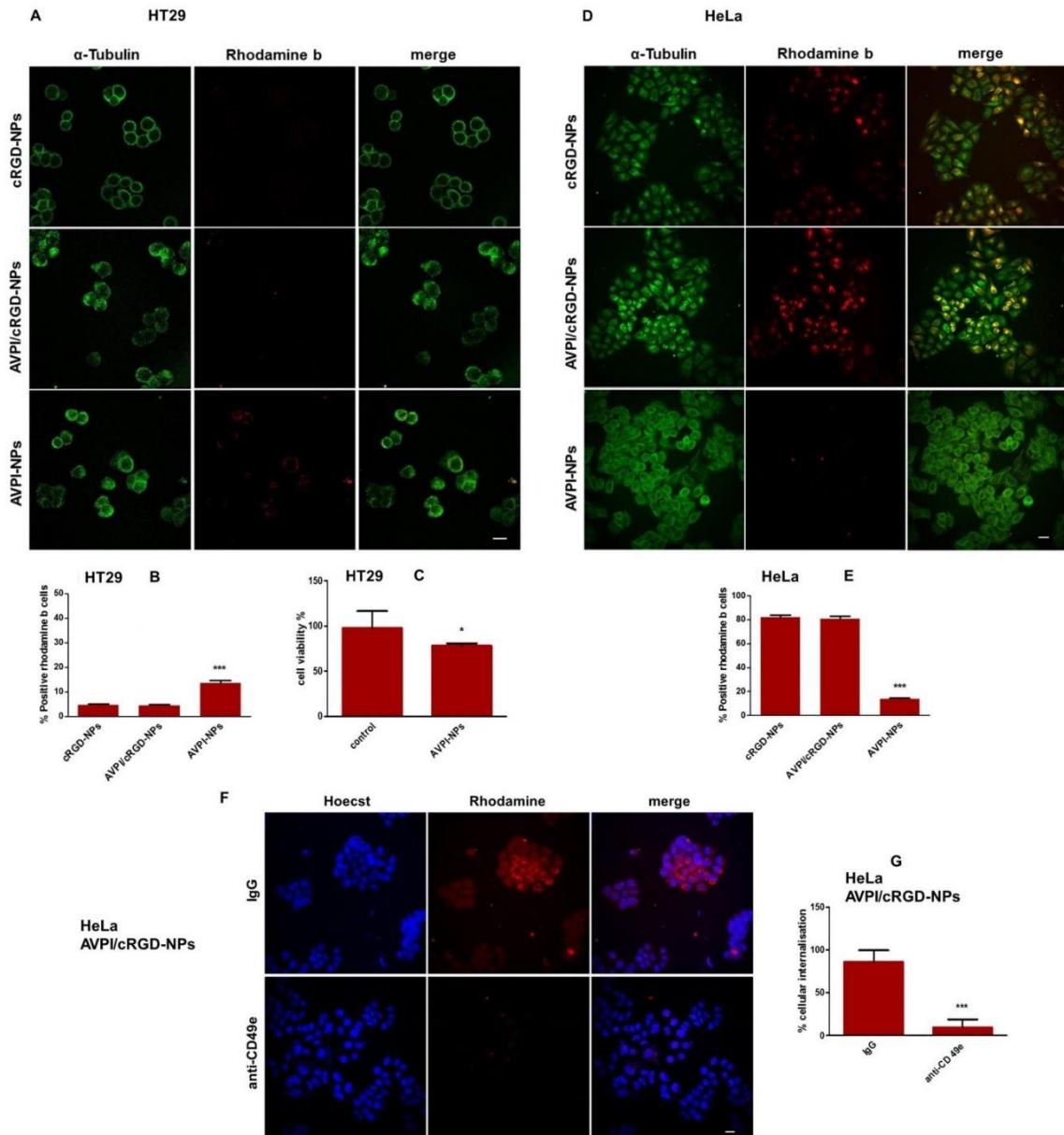


Figure 3. Fluorescence microscopy of cells after 1h of treatment with fluorescent peptide-RhB-NPs (red) and then counterstained with anti α -tubulin antibody (green) to visualize the cytoskeleton. (A) HT29 cells. Photographs were taken at 60 \times magnification, bar = 20 μ m. (B) Positive RhB HT29 cells %, error bars represent SD (n = 15 imaging fields), *** $p < 0.001$. (C) HT29 cell viability % in the presence of AVPI-NPs; data represent mean \pm SD (n = 6). * $p < 0.05$. (D) HeLa cells. Photographs were taken at 40 \times magnification. Bar 20 μ m. (E) Positive RhB HeLa cells %, error bars represent SD (n = 15 imaging fields), *** $p < 0.001$. (F) HeLa cells were treated or not with an anti-CD49e antibody or control IgG for 1 h, then incubated with fluorescent AVPI/cRGD-NPs (red) and then counterstained with Hoechst33342 dye (blue, Hoechst33342 = 2'-(4-Ethoxyphenyl)-5-(4-methyl-1-piperazinyl)-2,5'-bi-1H-benzimidazole trihydrochloride) to visualize the nuclei. Photographs were taken at 40 \times magnification. (G) HeLa cells internalization %, error bars represent SD (n = 15 imaging fields), bar = 20 μ m, *** $p < 0.001$.

2.4 Cellular Uptake of Peptide-NPs.

The internalization of the fluorescent peptide-NPs was observed by confocal microscopy in HeLa ($\alpha 5$ subunit positive),^[36] and in HT29 ($\alpha 5$ subunit negative) cells.^[37,38] In control HT29 cells, the internalization of AVPI-NPs was modest, and that of cRGD-NPs and AVPI/cRGD-NPs was very poor, as shown by the low fluorescent signal in the cytoplasm (Figure 3A,B). By contrast, HeLa cells exposed to cRGD-NPs and AVPI/cRGD-NPs, but not AVPI-NPs, gave a similar, very high number of fluorescent positive cells (Figure 3D,E). The scarce internalization of AVPI-NPs was consistent with the modest decrease of viability in HT29 (about 20%, Figure 3C) and HeLa (approx. 25%, Figure 2A) cells.

The merge of the images of HeLa treated with cRGD-NPs or AVPI/cRGD-NPs showed some cells colored in yellow/orange, but this observation was not indicative of colocalization between RhB and α -tubulin. In fact, these interactions have been quantified by analyzing the correlation and/or the overlap between images, using the Pearson's and Manders' coefficients, respectively.

Finally, the cells were pre-incubated with anti-CD49e antibody or mouse immunoglobulin G (IgG) antibody prior to exposure to AVPI/cRGD-NPs (Figure 3F). Microscopic observations showed that, in the presence of the antibody, the internalization was considerably reduced, as compared to cells incubated in the presence of the control IgG (Figure 3G).

3. Discussion

The aim of our study was to develop fluorescent probes with sufficient brightness, able to selectively sustain a long-term interaction with cellular receptors in dilute conditions. High brightness, low in vivo toxicity, and ease of functionalization with pharmacologically active biomolecules make fluorescent silica-based NPs attractive platforms for diagnostic and theranostic applications in cancer.^[39] Hence, we prepared dye-doped silica NPs surrounded by an outer shell of the biocompatible polymer PEG, which is expected to increase NP dispersion in physiological conditions (Figure 1A) and to oppose the uptake by the reticuloendothelial system.^[40,41] The covalent inclusion of the RhB derivative was adopted to prevent dye leaking in the external environment, a behavior that can affect the signal-to-noise ratio during optical imaging experiments. The influence of “minimal leakage” of fluorescent dyes from NPs or nanosystems on the overall fluorescent signal recorded during real experiments with cells is often a very difficult variable to quantify. For this reason, we preferred to circumvent this problem by the covalent linking of the dye to the NP silica core.

To avoid the leakage of the dye and of the cytotoxic compound, the NPs covalently embedded RhB-TES in their core, and the azide termini of PEG were exploited for the covalent functionalization with peptide-alkyne partners. We designed the sequence H-Ala-Val-Pro-Ile-Gly-pent-4-yn-1-amine (AVPI-alkyne); the AVPI N-terminal tetrapeptide of Smac/DIABLO maintains a binding affinity for IAP BIR of 0.5 μ M,^[10] while Gly and the C5 amine served as spacers. The cRGD-alkyne sequence was designed on the basis on the well-known Kessler's $\alpha 5\beta 1$ integrin ligand c[Arg-Gly-Asp-D-Phe-Lys] (c[RGDfK]).³⁴ It is well known that simple peptides, such as the AVPI and RGD sequences, delivered to the body are subject to enzymatic degradation and are poorly permeable through biological membranes. Nevertheless, inorganic NP carriers can support the transport of peptides by protecting them from environmental conditions while maintaining their stability.^[42,43]

The stability of the NPs was previously tested under different pseudo physiological and in vivo experimental situations. Pluronic®F127/silica-core/PEG-shell NPs, doped with RhB and/or polymethine cyanine dye, demonstrated outstanding stability in the presence of phosphate-buffered saline and bovine serum albumin (PBS/BSA).^[44] These NPs were tested in small animals for in vivo total-body imaging and

intravital 3D imaging, giving well detectable signals for hours after injection. The same silica-core/PEG-shell NPs, doped with cyanine 7 dye, were subcutaneously injected in animals, and the in vivo fluorescence signal in the right axillary lymph node was detected for at least 8 h.^[45]

The cytotoxicity of the resulting peptide-NPs was evaluated in A549, U-373, HeLa, Huvec, and fibroblast cells. Compared to AVPI-NPs, the dual functionalized AVPI/cRGD-NPs showed much higher toxicity already at the concentration of 1 μ M towards the cancer cells, and reduced toxicity towards fibroblasts. To understand whether the peptide-NPs restored apoptotic cancer cell death, the activity of caspase-9 was measured. While AVPI-NPs gave a moderate increase of caspase activity, AVPI/cRGD-NPs showed a > 40-fold increase in A549, HeLa, Huvec, U373, and a comparatively lower effect in fibroblasts.

The much higher apoptotic effect of AVPI/cRGD-NPs over AVPI-NPs towards cancer cells appeared clearly correlated to integrin-mediated cellular uptake. The internalization of the peptide-NPs was observed in HeLa (α 5 subunit positive), and in control HT29 (α 5 subunit negative) cells. cRGD-NPs and AVPI/cRGD-NPs showed much higher internalization in HeLa cells (Figure 3D,E) than AVPI-NPs, likely mediated by the interaction between the RGD peptides and the integrin receptors. This observation was supported by the almost negligible uptake of both RGD-NPs and AVPI/cRGD-NPs in the HT29 cell line not expressing α 5 subunit (Figure 3A). To confirm that the uptake of AVPI/cRGD NPs was integrin-mediated, exclusion studies were carried out by incubating the cells with anti-CD49e antibody or mouse IgG antibody prior to exposure to AVPI/cRGD-NPs. Microscopic observations showed that, in the presence of anti-CD49e, the internalization was strongly reduced, as compared to cells incubated in the presence of the control IgG (Figure 3F).

4. Conclusions.

In this work, we have described synthetic NPs mimicking the proapoptotic protein Smac/DIABLO, constituted by a fluorescent silica core doped with RhB, coated with a PEG shell, carrying in turn the AVPI peptide and/or a tumor-homing cRGD peptide. The bifunctional AVPI/RGD-NPs showed superior toxicity towards cancer cells, correlated to increased levels of caspase activity, plausibly due to efficient integrin-mediated transport into cells, as shown by confocal microscopy, and modest toxicity towards non-integrin expressing cells. In perspective, these Smac/DIABLO-mimetic nanosystems can find applications in the treatment of cancer, and thanks to the combination with the fluorescent dye can provide new insight into integrin-mediated internalization.

5. Experimental Procedures

5.1 General Methods.

Standard chemicals, including protected amino acids, were purchased from commercial sources and used without further purification. Peptide purity was assessed by analytical RP HPLC performed on a 1100 series apparatus (Agilent). Method A: RP XSelect Peptide CSH C18 column (Waters), 4.6 mm \times 100 mm, pore size 130Å, particle size 3.5 μ m; mobile phase: from 9:1 H₂O/0.1% TFA//CH₃CN/0.1% TFA to 2:8 H₂O/0.1% TFA//CH₃CN/0.1% TFA, in 20 min at a flow rate of 1.0 mL/min, followed by 10 min at the same composition. Method B: for fully protected peptide intermediates, the same chromatographic system was used with the exclusion of TFA in the mobile phase. Peptide isolation was performed by preparative RP HPLC performed on an 1100 series apparatus (Agilent), using a XSelect Peptide CSH C18 OBD column (Waters), 130Å, 5 μ m, 19 mm \times 150 mm; mobile phase: from 7:3 H₂O/0.1% TFA//CH₃CN/0.08% TFA to 2:8 H₂O/0.1% TFA//CH₃CN/0.08% TFA, in 10 min at a flow rate of 10 mL/min. MS (ESI)

analysis was performed using a MS single quadrupole HP 1100 MSD detector (Agilent), with a drying gas flow of 12.5 L/min, nebulizer pressure 30 psig, drying gas temp. 350 °C, capillary voltage 4500 (+) and 4000 (-), scan 50-2600 amu. The synthetic procedures by MW irradiation were performed with a Microwave Labstation for Synthesis (Micro-SYNTH) equipped with a built-in ATC-FO advanced fiber-optic automatic temperature control. Fluorescence measurements were performed with a LS-55 Fluorescence Spectrometer (Perkin Elmer) and quartz cuvettes, optical path length 1 cm. DLS measurements were performed with a Zetasizer Nano ZS (Malvern), He-Ne laser 633 nm, Max 4 mW, using polystyrene cuvettes (optical path length 1 cm). Confocal images were obtained with a C1s confocal laser-scanning microscope (Nikon), equipped with a PlanApo 60X or 40X, oil immersion lens (Nikon).

5.2 Solid-Phase Synthesis of *H-Asp(OtBu)-D-Phe-Lys(Cbz)-Arg(Mtr)-Gly-OH* (*Mtr* = 4-methoxy-2,3,6-trimethylbenzenesulphonyl)

H-Gly-preloaded 2-chlorotrityl resin (0.5 g, Gly loading 1.1 mmol/g resins) was swollen in dichloromethane (DCM, 785 mL) for 10 min before use. Fmoc-amino acid (Fmoc- = fluorenylmethoxycarbonyl-, 2 equiv.) carrying orthogonal protecting groups at the side chains, *N,N,N',N'*-tetramethyl-*O*-(1*H*-benzotriazol-1-yl)uronium hexafluorophosphate (TBTU, 2 equiv.), 1-hydroxybenzotriazole (HOBt, 2 equiv.), *N,N*-diisopropylethylamine (DIPEA, 4 equiv.), were added to the resin and the mixture was allowed to react for 10 min under MW irradiation (50 W, keeping internal temperature at 50 °C). The resin was washed 3 times with dimethylformamide (DMF, 5 mL), MeOH (5 mL), DCM (5 mL). Coupling efficacy was monitored using the Kaiser test. Fmoc deprotection was carried out by treatment with 20% piperidine/DMF (5 mL) for 2 min under MW irradiation (40 W). The procedure was repeated, and after that, the resin was washed 3 times in sequence with DMF (5 mL), MeOH (5 mL), DCM (5 mL). For peptide cleavage, the peptidyl resin was treated with AcOH/TFE/DCM (1:1:4 v/v/v, 15 mL) under stirring for 90 min at rt. The resulting mixture was filtered, and the resin was washed in sequence with 10% TFA in Et₂O (5 ml), CH₂Cl₂ (5 ml) and MeOH (5 ml). The filtrate and the washes were collected, and the organic solvents were removed under reduced pressure. The resulting residue was suspended in ice-cold Et₂O, and the crude solid that precipitated was collected by centrifugation. The product was obtained as a waxy solid; 78% yield, 80% pure according to analytical RP HPLC (Method A, general methods), *R*_t = 6.71 min. MS (ESI): *m/z* calc. 1023.47, found: 512.8 [M+2H]²⁺, 1024.4 [M+H]⁺.

5.3 Synthesis of *c[Arg(Mtr)-Gly-Asp(OtBu)-D-Phe-Lys(Cbz)]* (*Cbz* = carbobenzyloxy).

The crude linear peptide was dissolved in DMF (10 mL), and submitted to cyclization in the presence of NaHCO₃ (15 equiv.) under pseudo high dilution conditions, by adding a solution of DPPA (3 equiv.) in DMF (10 mL) over 12 h by means of a temporized syringe, and the mixture was stirred for additional 6 h. Then the solvent was distilled under reduced pressure, the residue was suspended in water (5 mL), and extracted 3 times with EtOAc (20 mL). The solvent was removed at reduced pressure, and the cyclopeptide was utilized without further purification. 67% Yield, 75% pure according to analytical RP HPLC (Method B, general methods), *R*_t = 9.68 min. MS (ESI): *m/z* calcd. 1005.46; found: 1006.2 [M+H]⁺, 1028.2 [M+Na]⁺.

5.4 Synthesis of *c[Arg(Mtr)-Gly-Asp(OtBu)-D-Phe-Lys(alkyne)]*.

The Cbz protecting group at Lys of *c[Arg(Mtr)-Gly-Asp(OtBu)-D-Phe-Lys(Cbz)]* was removed by catalytic hydrogenation over Pd/C in MeOH (20 mL) at rt for 3 h. After filtration of the catalyst over celite®, the solvent was distilled at reduced pressure.

The εNH₂ amine of Lys was derivatized with 5-hexynoic acid (1.2 equiv) in 1:2 DMF/DCM (15 mL) in the presence of HOBt/TBTU/DIPEA (2:2:4 equiv.) under MW (50W, internal temperature 50°C) for 15 min. The organic solvent was removed under reduced pressure, the residue was diluted with EtOAc (50 mL), and the organic phase was washed with a 1M HCl (7 mL) and saturated NaHCO₃ (7 mL). The organic solvent was removed under reduced pressure and the product was isolated as a waxy solid. 98% Yield, 68% pure by analytical RP HPLC (Method B, general methods), *R*_t = 8.5 min. MS (ESI): *m/z* calcd. 965.47; found: 966.4 [M+H]⁺.

5.5 Synthesis of *c[Arg-Gly-Asp-D-Phe-Lys(alkyne)]* (*cRGD-alkyne*).

The final peptide side-chain deprotection was carried out by treatment of *c[Arg(Mtr)-Gly-Asp(OtBu)-D-Phe-Lys(alkyne)]* with TFA/thioanisole/phenol/triisopropylsilane (7:1:1:1 v/v, 10 mL) at rt for 8 h. Then the organic solvent was removed under reduced pressure, giving a white solid. The cyclopeptide-alkyne was isolated by preparative RP HPLC (general methods). 85% yield, 94% pure by analytical RP HPLC (Method A, general methods), *R*_t = 1.73 min. MS (ESI): *m/z* calcd. 697.35; found: 349.6 [M+2H]²⁺, 698.2 [M+H]⁺.

5.6 Synthesis of *Boc-Ala-Val-Pro-Ile-Gly-OH*.

The linear Boc-protected pentapeptide was synthesized by solid phase peptide synthesis (SPPS) on a H-Gly-preloaded 2-chlorotrityl resin according to the general procedure describe above, using Boc-Ala-OH for final coupling reaction. The chloranil test was utilized for monitoring the coupling between Fmoc-Val-OH and H-Pro-Ile-Gly-resin. Final peptide cleavage from the resin support with AcOH/TFE/DCM as described above, gave a white solid. 73% Yield, 85% pure by analytical RP HPLC (Method A, general methods), *R*_t = 5.22 min. MS (ESI): *m/z* calcd. 555.33; found: 556.2 [M+H]⁺.

5.7 Synthesis of *Boc-Ala-Val-Pro-Ile-Gly-pent-4-yn-1-amine*.

The peptide *Boc-Ala-Val-Pro-Ile-Gly-OH* was solubilized in 1:2 DMF/DCM (15 mL), and HOBt/TBTU/DIPEA (2:2:4 equiv.) and 4-pentyn-1-amine (1.2 equiv.) were added to the solution. The reaction was carried out under MW radiation for 15 min (50 W, internal temperature 50°C). EtOAc (50 mL) was added and the organic phase was washed with 1M HCl (5 mL) and saturated NaHCO₃ (5 mL). The organic phase was removed under reduced pressure and the product was obtained as a yellowish oil. 75% yield, 80% pure by analytical RP HPLC (Method B, general methods), *R*_t = 7.24 min. MS (ESI): *m/z* calcd. 620.39; found: 621.2 [M+H]⁺, 643.2 [M+Na]⁺.

5.8 *Dansyl-AVPI-alkyne*.

Dansyl-Ala-Val-Pro-Ile-Gly-pent-4-yn-1-amine was obtained by the same procedure, using the commercially available dansyl-Ala-OH.

5.9 *H-Ala-Val-Pro-Ile-Gly-pent-4-yn-1-amine* (*AVPI-alkyne*).

The peptide *Boc-AVPI-alkyne* was treated with TFA/DCM (1:3 v/v, 4 mL) at rt for 25 min. The procedure was repeated, then the organic solvents were removed under reduced pressure. The product was isolated by preparative RP HPLC (general methods). 78% yield, 93 % pure according to analytical RP HPLC

(Method A, General methods), $R_t = 2.3$ min. MS (ESI): m/z calcd. 520.34; found: 521.2 $[M+H]^+$, 543.2 $[M+Na]^+$.

5.10 Dimesylate Derivative of Pluronic®F127.

Prior to use, BASF Pluronic®F127 (PF127) surfactant (12.6 g, 1.0 mol, 1.0 equiv.) was dried by azeotropic distillation at low pressure in toluene, and was solubilized in anhydrous DCM (50 mL). This solution was cooled to 0°C and kept under an inert N₂ atmosphere, after that triethylamine (280 µL, 2.0 mmol, 2.0 equiv.) and methanesulfonyl chloride (155 µL, 2.0 mmol, 2.0 equiv.) were added. The reaction mixture was kept under stirring at 0°C under inert atmosphere for 3h and then at rt overnight. The dispersion was filtered, the organic layer was distilled under reduced pressure, and the residue was dried under high vacuum (quantitative yield).^[46]

5.11 Diazide Derivative of PF127, PF127-(N₃)₂.

To a suspension of dimesylate-PF127 (10.2 g, 0.8 mmol, 1.0 equiv.) in CH₃CN (50 mL), sodium azide (156 mg, 2.4 mmol, 4.0 equiv.) was added and the reaction mixture was allowed to stir under reflux for 48 h. Subsequently, the solvent was removed under reduced pressure. The obtained solid was dispersed in 5% NaHCO₃ (10 mL) and the solution was then saturated with solid NaCl. This mixture was extracted four times with DCM (4 × 10 mL). The combined organic phases were dried over Na₂SO₄, filtered and evaporated at reduced pressure, affording a white solid (>95% yield).

5.12 PEG-Shell/Silica-Core NPs.

PF127 (200 mg), PF127-(N₃)₂ (20 mg), and RhB-TEOS (4.0 mg) were solubilized in DCM (2 mL) in a 20 mL glass scintillation vial. The organic solvent was evaporated from the homogeneous solution, and the solid residue was subsequently dried under vacuum at rt. The resulting solid mixture was solubilized at 25°C while stirring in a 1 M AcOH/0.85 M NaCl solution (3.2 mL) for 1h. Subsequently, TEOS (350 µL) was added after 3h of stirring, then followed TMSCl (40 µL) was added. The mixture was kept under stirring for 48 h at 25 °C. The NPs were purified by dialysis against water at rt using cellulose dialysis tubing (Sigma, mw cutoff >12 kDa, avg. diameter 33 mm), and the solution was finally diluted to a total volume of 3.5 mL with water to the final NPs concentration 29 µM.

5.13 Peptide Conjugation to NPs by CuAAC.

A fragment of copper wire (1 cm) was polished in 10% HNO₃ for 2 min, then it was rinsed with water and acetone and dried, then it was introduced in a glass vial containing a dispersion of NPs (500 µL, 29 µM in water) in Tris buffer (1.5 mL, 200 mM in bidist. H₂O, pH 8). Subsequently, CuSO₄ solution (6 µL, 2 mM in bidist. H₂O), sodium 4,4'-(1,10-phenanthroline-4,7-diyl)dibenzenesulfonate (12 µL, 2 mM in bidist. H₂O) and the peptide-alkyne (50 µL, 53 mM in dimethylsulfoxide (DMSO)) were added. The obtained homogeneous mixture was stirred for 3 days at rt. The NPs were purified via size-exclusion chromatography (SEC) on Sephadex® G-25 gel (dry bead size 20-80 µm, fractionation range 1000-5000 Da) using bidist. water as eluent and finally diluted with bidist. water to obtain a final NP concentration of 3 µM. The NPs were stored at 4°C.

5.14 Cell Lines and Culture Conditions.

Human umbilical vein endothelial cells (Huvec), adenocarcinomic *human* alveolar basal epithelial cells (A549), human glioblastoma (U373) and human fibroblasts were obtained from ThermoFisher. The human

cervical carcinoma (HeLa) cells and human colon cancer (HT29) cells were obtained from ATCC. Cells were grown in RPMI 1640 medium (Labtek Eurobio, Milan, Italy), supplemented with 10% FCS (Euroclone, Milan, Italy) and 2mM L-glutamine (Sigma-Aldrich, Milan, Italy), at 37°C and 5% CO₂ atmosphere. Cells were seeded at 20×10^4 cells/cm² in plastic wells (Orange Scientific, Braine l'Alleud, Belgium). The cells were detached by trypsin-EDTA solution (0.115 w/v % trypsin and 0.02 w/v % EDTA) (Sigma-Aldrich, Milan, Italy), and then rinsed and re-suspended in the corresponding medium.

5.15 Cell Viability Assays.

The cytotoxicity of peptide-NPs was evaluated using the cell viability 3-(4,5-dimethylthiazol-2-yl)-5-(3-carboxymethoxyphenyl)-2-(4-sulfophenyl)-2H-tetrazolium (MTS) assay CellTiter 96® AQueous One Solution Cell Proliferation Assay (Promega), according to the manufacturer's instructions. Cells were seeded (1.5×10^4 cells/well) and cultured for 48 h. The primary growth medium was replaced by fresh medium, containing NPs at the concentrations of 0.1, 1.0, 3.0 μM. After 48 h, PBS (100 μL) was supplemented with MTS solution (20 μL/well), incubated for 2 h, and then the absorbance was recorded at 570 nm with a 96-well plate reader. Data were analyzed by Prism GraphPad software and expressed as % of controls (untreated cells).

5.16 Apoptosis.

1.0×10^4 cells/well were incubated with the peptides-NPs at the concentration of 1 μM for 6 h. The apoptotic process onset was evaluated by the Caspase-Glo® 9 assay (Promega), according to the manufacturer's instructions. After 30 min the luminescence was measured using a Synergy HT microplate reader (Biotek).

5.17 Cell Internalization.

HT29 and HeLa cells were grown on sterile glass coverslips for 48h and then treated with 1 μM peptide-NPs for 1 h. Cells were washed (3×) with PBS and fixed in 500 μL of 3% paraformaldehyde. Glass slides were washed twice with 1 mL of PBS-Gly 0.1 M (Merck) and washed twice again with 1 mL of PBS-BSA 1% (Merck). Samples were first incubated with mouse anti-α-tubulin primary antibody (BioLegend, San Diego, CA) for 1 h in agitation at rt. Samples were washed again twice with 1 mL of PBS-BSA 1% and then incubated with anti-mouse fluorescein isothiocyanate (FITC)-conjugated secondary antibody (ThermoFisher Scientific, Waltham, MA) for 1 h at rt. Finally, specimens were embedded in Mowiol and analyzed by confocal microscopy. The visualization and quantification of cells that internalized the RhB-NPs were performed using ImageJ (NIH, USA).

5.18 Competition Experiments.

HeLa cells were seeded on sterile glass coverslips for 48h. Then cells were first pre-exposed to IgG isotype or anti-CD49e antibody for 1 h and then incubated with 1μM peptide-NP for 1h. Cells were stained with Hoechst33342 (ThermoFisher) and specimens were analysed by confocal microscopy as described above. The number of cells showing intracellular red fluorescence was expressed as % of the total cells, counterstained with Hoechst33342.

5.19 Determination of NPs Peptide Functionalization.

For fluorimetric quantitative analysis of peptides' primary amines on the NP surface, a PEG-amine (750 Da) standard calibration curve was established. 2.5 mL DMSO and 500 μL of fluorescamine solution

(0.264 mM in DMSO) were introduced in a UV/Vis glass cuvette. Then the fluorescence measurements with individual different quantities of PEG-diamine stock solution were conducted. The PEG-amine stock solution (0.675 mM in DMSO) was added at each individual measurement to obtain the following concentrations in the cuvette: 5.94 μ M, 3.76 μ M, 1.78 μ M. After 8 min of the PEG-amine stock solution addition, the fluorescent signal was recorded (λ_{exc} 390 nm, λ_{em} 480 nm). To quantify peptide functionalization, a sample of AVPI-NP conjugate (25 μ L, 30 μ M) was analyzed in the cuvette. According to the sample measurement, a peptide number of 7.8 ± 1 per NP was calculated.^[47]

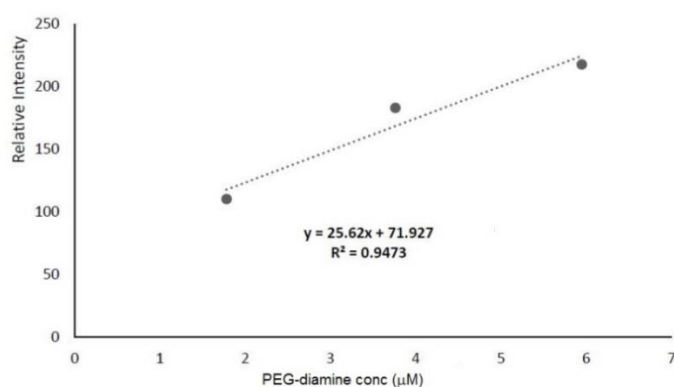


Figure 4. Calibration curve of the fluorescence intensity at λ 480 nm (λ_{exc} 390 nm) vs the concentration of PEG-NH₂/fluorescamine standard solutions, constructed to measure the number of peptides/NP by titration with fluorescamine.

5.20 Quantification of Dansyl-AVPI-NP.

The NP-N₃ (29 mM, 500 μ L) were reacted with dansyl-AVPI-alkyne or with a 1:1 mixture of dansyl-AVPI-alkyne and cRGD-alkyne, by CuAAC as described above. In short, NP-N₃ (500 μ L, 29 μ M) were diluted with Tris buffer (1.5 mL, 200 mM, Tris = tris(hydroxymethyl)aminomethane), and CuSO₄ aqueous solution (6 μ L, 2 mM), sodium 4,4'-(1,10-phenanthroline-4,7-diyl)dibenzenesulfonate (12 μ L, 2 mM), dansyl-AVPI-alkyne (50 μ L, 53 mM in DMF), and polished copper wire, were added under inert atmosphere, and the mixture (final volume 2106 μ L) was stirred for 48h. The suspension was filtered with a 200 nm filter, and 400 μ L of the filtrate was diluted to 5000 μ L before purification by SEC using phosphate buffer (10 mM, pH 7.4), containing 1 mM EDTA. After purification, the concentration of dansyl-AVPI-NP in solution was determined directly by fluorometric quantification against a calibration curve obtained by measuring the fluorescence intensity of standard solutions of dansyl-AVPI in the concentration range 1-9 mM. (λ_{exc} 340 nm, λ_{em} 477 nm). The calculation indicated a number of 9.3 ± 1 dansyl-AVPI peptides per NP. The CuAAC functionalization of the NP-N₃ (500 μ L, 29 μ M) was repeated with a 1:1 mixture of dansyl-AVPI-alkyne (12.8 μ L, 53 mM in DMF), and cRGD-alkyne (12.8 μ L, 53 mM in DMF). Fluorometric quantification indicated a number of dansyl-AVPI peptide/NP of 4.8. This number is suggestive of a circa 1:1 dansyl-AVPI/cRGB ratio, consistent to a very similar chemical reactivity for dansyl-AVPI-alkyne and cRGB-alkyne during CuAAC coupling.

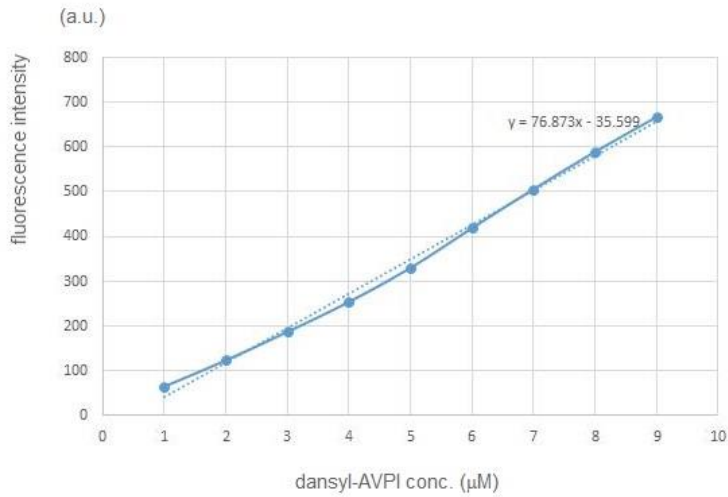


Figure 5. Calibration curve of the fluorescence intensity at λ 477 nm (λ_{ex} 340 nm) vs the concentration of dansyl-AVPI peptide standard solutions, constructed to determine the number of dansyl-AVPI/NP.

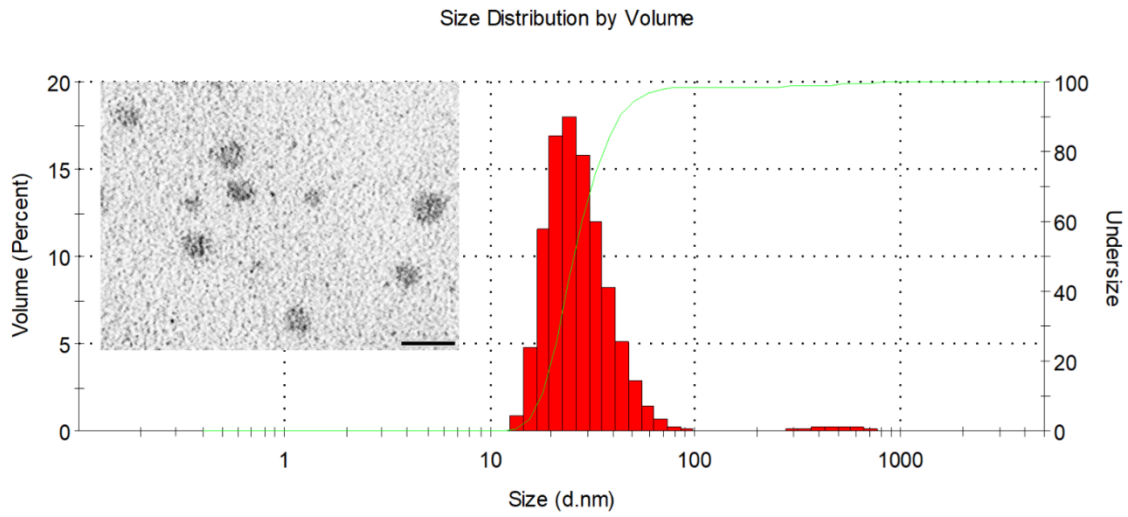


Figure 6. DLS hydrodynamic size distribution by volume (water, 25°C) and representative TEM image of AVPI-NPs (scale bar 20 nm).

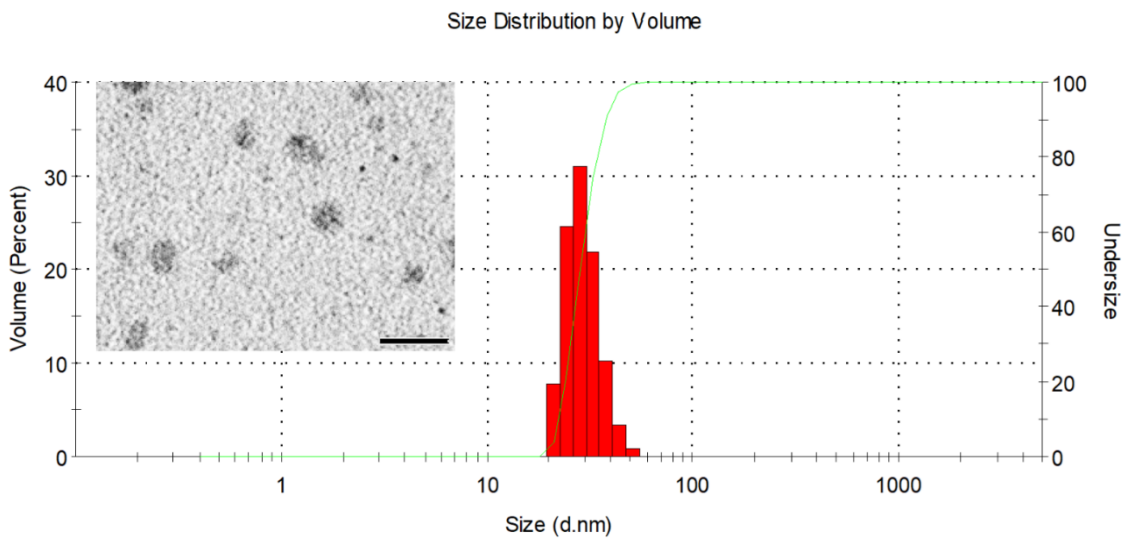


Figure 7. DLS hydrodynamic size distribution by volume (water, 25°C) and representative TEM image of cRGB-NPs (scale bar 20 nm).

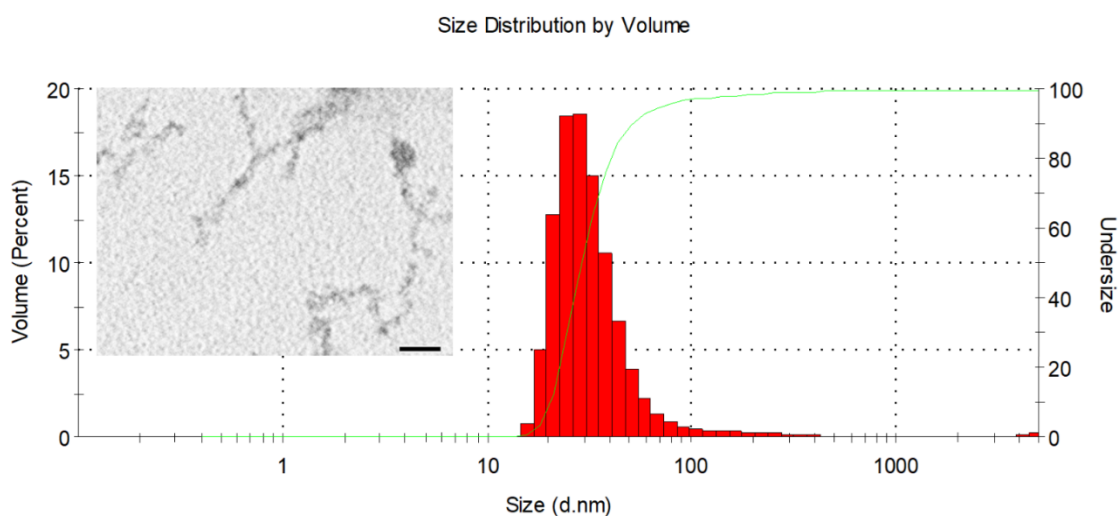


Figure 8. DLS hydrodynamic size distribution by volume (water, 25°C) and representative TEM image of AVPI/cRGD-NPs (scale bar 20 nm).

Table 1. Summary of the hydrodynamic diameter data (water, 25°C) for the samples presented in this work.

Sample	d _H (by volume) / nm	d _H (standard deviation) / nm	Polydispersion Index (PDI)
NP-N ₃	22	0.5	0.10
AVPI-NPs	28	2	0.38
cRGD-NPs	29	4	0.29
AVPI/cRGD-NPs	28	2	0.40

The work described in this chapter has already been published in *Nanomaterials* with slight modification and has been reproduced here with the permission of the copyright holder.

De Marco, Rossella; Rampazzo, Enrico; **Zhao, Junwei**; Prodi, Luca; Paolillo, Mayra; Picchetti, Pierre; Gallo, Francesca; Calonghi, Natalia; Gentilucci, Luca. 2020. "Integrin-Targeting Dye-Doped PEG-Shell/Silica-Core Nanoparticles Mimicking the Proapoptotic Smac/DIABLO Protein" *Nanomaterials* 10, no. 6: 1211. <https://doi.org/10.3390/nano10061211>.

References

1. Crook, N.E.; Clem, R.J.; Miller, L.K. *J. Virol.* **1993**, *67*, 2168-2174.
2. Kocab, A.J.; Duckett, C.S. Inhibitor of apoptosis proteins as intracellular signalling intermediates. *FEBS J.* **2016**, *283*, 221-231.

-
3. Berthelet, J.; Dubrez, L. Regulation of apoptosis by inhibitors of apoptosis (IAPs). *Cells* **2013**, *2*, 163-187.
 4. Eckelman, B.P.; Drag, M.; Snipas S.J.; Salvesen G.S. The mechanism of peptide-binding of IAP BIR domains. *Cell Death Differ.* **2008**, *15*, 920.
 5. Deveraux, Q.L.; Takahashi, R.; Salvesen, G.S.; Reed, J.C. X-linked IAP is a direct inhibitor of cell-death proteases. *Nature* **1997**, *388*, 300-304.
 6. Cossu, F.; Milani, M.; Mastrangelo, E.; Lecis, D. Targeting the BIR domains of inhibitor of apoptosis (IAP) proteins in cancer treatment. *Comput. Struct. Biotechnol. J.* **2019**, *17*, 142-150.
 7. Mohamed, M.S.; Bishr, M.K.; Almutairi, F.M.; Ali, A.G. 2017 Inhibitors of apoptosis: clinical implications in cancer. *Apoptosis* **22**, 1487-1409.
 8. Rathore, R.; McCallum, J.E.; Varghese, E.; Florea, A.M.; Büsselber, D. Overcoming chemotherapy drug resistance by targeting inhibitors of apoptosis proteins (IAPs). *Apoptosis* **2017**, *22*, 898-819.
 9. Du, C.; Fang, M.; Li, Y. Li.; L, Wang, X. Smac, a mitochondrial protein that promotes cytochrome c-dependent caspase activation by eliminating IAP inhibition. *Cell* **2000**, *102*, 33-42.
 10. Wu, G.; Chai, J.; Suber, T.L.; Wu, J.W.; Du, C.; Wang, X.; Shi, Y. Structural basis of IAP recognition by Smac/DIABLO. *Nature* **2000**, *408*, 1008-1012.
 11. Gentilucci, L.; Tolomelli, A.; Squassabia, F. Peptides and peptidomimetics in medicine, surgery and biotechnology. *Curr. Med. Chem.* **2006**, *13*, 2449-2466.
 12. Gentilucci, L.; De Marco, R.; Cerisoli, L. Chemical modifications designed to improve peptide stability: incorporation of non-natural amino acids, pseudo-peptide bonds, and cyclization. *Curr. Pharm. Des.* **2010**, *16*, 3185-3203.
 13. Yang, L.; Mashima, T.; Sato, S.; Mochizuki, M.; Sakamoto, H.; Yamori, T.; Oh-Hara, T.; Tsuruo, T. Predominant suppression of apoptosome by inhibitor of apoptosis protein in non-small cell lung cancer H460 cells: therapeutic effect of a novel polyarginine conjugated Smac peptide. *Cancer Res.* **2003**, *63*, 831-837.
 14. Hossbach, J.; Michalsky, E.; Henklein, P.; Jaeger, M.; Daniel, P.T.; Preissner, R. Inhibiting the inhibitors: retro-inverso Smac peptides. *Peptides* **2009**, *30*, 2374-2379.
 15. Ardecky, R.J.; Welsh, K.; Finlay, D.; Lee, P.S.; González-López, M.; Ganji, S.R.; Ravanan, P.; Mace, P.D.; Riedl, S.J.; Vuori, K. et al. Design, synthesis and evaluation of inhibitor of apoptosis protein (IAP) antagonists that are highly selective for the BIR2 domain of XIAP. *Bioorg. Med. Chem. Lett.* **2013**, *23*, 4253-4257.
 16. Bourguet, C.B.; Boulay, P.L.; Claing, A.; Lubell, W.D. Design and synthesis of novel azapeptide activators of apoptosis mediated by caspase-9 in cancer cells. *Bioorg. Med. Chem. Lett.* **2014**, *24*, 3361-3365.
 17. Seneci, P.; Rizzi, M.; Ballabio, L.; Lecis, D.; Conti, A.; Carrara, C.; Licandro, E. SPION-Smac mimetic nano-conjugates: Putative pro-apoptotic agents in oncology. *Bioorg. Med. Chem. Lett.* **2014**, *24*, 2374-2378.
 18. Li, M.; Liu, P.; Gao, G.; Deng, J.; Pan, Z.; Wu, X.; Xie, G.; Yue, C.; Cho, C.H.; Ma, Y. et al. Smac therapeutic peptide nanoparticles inducing apoptosis of cancer cells for combination chemotherapy with Doxorubicin. *ACS Appl. Mater. Interfaces* **2015**, *7*, 8005-8012.
 19. Arosio, D.; Manzoni, L.; Corno, C.; Perego, P. Integrin-targeted peptide- and peptidomimetic-drug conjugates for the treatment of tumors. *Recent Pat. Anti-Canc.* **2017**, *12*, 148-168.
 20. Borbély, A.; Figueras, E.; Martins, A.; Boderó, L.; Raposo Moreira Dias, A.; López Rivas, P.; Pina, A.; Arosio, D.; Gallinari, P.; Frese, M. et al. Conjugates of cryptophycin and RGD or isoDGR peptidomimetics for targeted drug delivery. *ChemistryOpen* **2019**, *8*, 737-742.
 21. Conde, J.; Tian, F.; Hernández, Y.; Bao, C.; Cui, D.; Janssen, K.P.; Ibarra, M.R.; Baptista, P.V.; Stoeger, T.; de la Fuente, J.M. *In vivo* tumor targeting via nanoparticle-mediated therapeutic siRNA coupled to inflammatory response in lung cancer mouse models. *Biomaterials* **2013**, *34*, 7744-7753.

-
22. Duro-Castano, A.; Gallon, E.; Decker, C.; Vicent, M.J. Modulating angiogenesis with integrin-targeted nanomedicines. *Adv. Drug. Deliv. Rev.* **2017**, *119*, 101-119.
23. Duret, D.; Grassin, A.; Henry, M.; Jacquet, T.; Thoreau, F.; Denis-Quanquin, S.; Coll, J.L.; Boturyn, D.; Favier, A.; Charreyre, M.T. Polymultivalent polymer-peptide cluster conjugates for an enhanced targeting of cells expressing $\alpha\beta 3$ integrins. *Bioconjug. Chem.* **2017**, *28*, 2241-2245.
24. Mas-Moruno, C.; Fraioli, R.; Rechenmacher, F.; Neubauer, S.; Kapp, T.G.; Kessler, H. $\alpha\beta 3$ - or $\alpha 5\beta 1$ -Integrin-selective peptidomimetics for surface coating. *Angew. Chem. Int. Ed.* **2016**, *55*, 7048-7067.
25. Greco, A.; Maggini, L.; De Cola, L.; De Marco, R.; Gentilucci, L. Diagnostic implementation of fast and selective integrin-mediated adhesion of cancer cells on functionalized Zeolite L Monolayers. *Bioconjug. Chem.* **2015**, *26*, 1873-1878.
26. De Marco, R.; Greco, A.; Calonghi, N.; Dattoli, S.D.; Baiula, M.; Spampinato, S.; Picchetti, P.; De Cola, L.; Anselmi, M.; Cipriani, F. et al. Selective detection of $\alpha 4\beta 1$ integrin (VLA-4)-expressing cells using peptide-functionalized nanostructured materials mimicking endothelial surfaces adjacent to inflammatory sites. *Peptide Science* **2018**, *110*, e23081.
27. Nieberler, M.; Reuning, U.; Reichart, F.; Notni, J.; Wester, H.J.; Schwaiger, M.; Weinmüller, M.; Räder, A.; Steiger, K.; Kessler, H. Exploring the Role of RGD-Recognizing Integrins in Cancer. *Cancers* **2017**, *9*, pii: E116.
28. Katsamakas, S.; Chatzisideri, T.; Thysiadis, S.; Sarli, V. RGD-mediated delivery of small-molecule drugs. *Future Med. Chem.* **2017**, *9*, 579-604.
29. Desgrosellier, J.S.; Cheresh, D.A. Integrins in cancer: biological implications and therapeutic opportunities. *Nat. Rev. Cancer* **2010**, *10*, 9-22.
30. Mingozzi, M.; Manzoni, L.; Arosio, D.; Dal Corso, A.; Manzotti, M.; Innamorati, F.; Pignataro, L.; Lecis, D.; Delia, D.; Seneci, P. et al. Synthesis and biological evaluation of dual action cyclo-RGD/SMAC mimetic conjugates targeting $\alpha\beta 3/\alpha\beta 5$ integrins and IAP proteins. *Org. Biomol. Chem.* **2014**, *12*, 3288-3202.
31. Rampazzo, E.; Bonacchi, S.; Juris, R.; Montalti, M.; Genovese, D.; Zaccheroni, N.; Prodi, L.; Rambaldi, D. C.; Zattoni, Andrea C.; Reschiglian, P. Energy transfer from silica core-surfactant shell nanoparticles to hosted molecular fluorophores. *J. Phys. Chem. B*, **2010**, *114*, 14605-14613.
32. Valenti, G.; Rampazzo, E.; Bonacchi, S.; Khajvand, T.; Juris, R.; Montalti, M.; Marcaccio, M.; Paolucci, F.; Prodi, L. A versatile strategy for tuning the color of electrochemiluminescence using silica nanoparticles. *Chem. Commun.* **2012**, *48*, 4187-4189.
33. Rampazzo, E.; Bonacchi, S.; Juris, R.; Genovese, D.; Prodi, L.; Zaccheroni, N.; Montalti, M. Dual-mode, anisotropy-encoded, ratiometric fluorescent nanosensors: Towards multiplexed detection. *Chem. Eur. J.* **2018**, *24*, 16743-16746.
34. Haubner, R.; Finsinger, D.; Kessler, H. Stereoisomeric peptide libraries and peptidomimetics for designing selective inhibitors of the $\alpha\beta 3$ integrin for a new cancer therapy. *Angew. Chem. Int. Ed.* **1997**, *36*, 1374-1389.
35. Adamou, R.; Coly, A.; Douabalé, S.E.; Saleck, M.L.; Gaye-Seye, M. D.; Tine, A. Fluorimetric determination of histamine in fish using micellar media and fluorescamine as labelling reagent. *J. Fluoresc.* **2005**, *15*, 679-688.
36. Parolin, C.; Frisco, G.; Foschi, C.; Giordani, B.; Salvo, M.; Vitali, B.; Marangoni, A.; Calonghi, N. *Lactobacillus crispatus* BC5 interferes with chlamydia trachomatis infectivity through integrin modulation in cervical cells. *Front. Microbiol.* **2018**, *9*, 2630.
37. Kemperman, H.; Wijnands, Y.M.; Roos, E. αV Integrins on HT-29 colon carcinoma cells: Adhesion to fibronectin is mediated solely by small amounts of $\alpha V\beta 6$, and $\alpha V\beta 5$ is codistributed with actin fibers. *Exp. Cell Res.* **1997**, *234*, 156-164.

-
38. Schmidt, R.; Streit, M.; Kaiser, R.; Herzberg, F.; Schirner, M.; Schramm, K.; Kaufmann, C.; Henneken, M.; Schäfer-Korting, M.; Thiel, E. et al. *De novo* expression of the $\alpha 5\beta 1$ -fibronectin receptor in HT29 colon-cancer cells reduces activity of c-src. Increase of c-src activity by attachment on fibronectin. *Int. J. Cancer* **1998**, *76*, 91-98.
39. Bonacchi, S.; Genovese, D.; Juris, R.; Montalti, M.; Prodi, L.; Rampazzo, E.; Zaccheroni, N. Luminescent silica nanoparticles: extending the frontiers of brightness. *Angew. Chem. Int. Ed.* **2011**, *50*, 4056-4066.
40. Storm, G.; Belliot, S.O.; Daemen, T.; Lasic, D.D. Surface modification of nanoparticles to oppose uptake by the mononuclear phagocyte system. *Adv. Drug Deliv. Rev.* **1995**, *17*, 31-48
41. Huo, Q.; Liu, J.; Wang, L.Q.; Jiang, Y.; Lambert, T.N.; Fang E. A new class of silica cross-linked micellar core-shell nanoparticles. *J. Am. Chem. Soc.* **2006**, *128*, 6447-6453.
42. Jeong, W.-J.; Bu, J.; Kubiawicz, L.J.; Chen, S.S.; Kim, Y.; Hong, S. Peptide-nanoparticle conjugates: A next generation of diagnostic and therapeutic platforms? *Nano Converg.* **2018**, *5*, 38.
43. Pudlarz, A.; Szymraj, J. Nanoparticles as carriers of proteins, peptides and other therapeutic molecules. *Open Life Sci.* **2018**, *13*, 285-298.
44. Rampazzo, E.; Boschi, F.; Bonacchi, S.; Juris, R.; Montalti, M.; Zaccheroni, N.; Prodi, L.; Calderan, L.; Rossi B.; Becchi, S.; et al. Multicolor core/shell silica nanoparticles for in vivo and ex vivo imaging. *Nanoscale* **2012**, *4*, 824-830.
45. Helle, M.; Rampazzo, E.; Monchanin, M.; Marchal, F.; Guillemin, F.; Bonacchi, S.; Salis, F.; Prodi, L.; Bezdetsnaya, L. Surface chemistry architecture of silica nanoparticles determine the efficiency of in vivo fluorescence lymph node mapping. *ACS Nano* **2013**, *7*, 8645-8657.
46. Rampazzo, E.; Bonacchi, S.; Juris, R.; Genovese, D.; Prodi, L.; Zaccheroni, N.; Montalti, M. Dual-mode, anisotropy-encoded, ratiometric fluorescent nanosensors: Towards multiplexed detection. *Chem. Eur. J.* **2018**, *24*, 16743-16746.
47. Adamou, R.; Coly, A.; Douabalé, S.E.; Saleck, M.L.; Gaye-Seye, M.D.; Tine, A. Fluorimetric determination of histamine in fish using micellar media and fluorescamine as labelling reagent. *J. Fluoresc.* **2005**, *15*, 679-688.

Chapter 7. MiniAP4 as Vehicle to Facilitate the Delivery of PEG-Cholic Acid Micellar Nanoparticle Encapsulated Anti-Cancer Drugs Across the Blood Brain Barrier.

The improvement of drug delivery efficiency into the brain across the blood-brain barrier (BBB) will significantly improve the therapeutic effects of loaded drugs on brain disease, such as brain tumor, Alzheimer's disease, and Parkinson's disease. In this work, a drug delivery platform was prepared specifically for brain tumors by combining the brain shuttle peptide MiniAP4 and the telodendrimer of PEG-Lys₇-Cholic Acid (PEG_{5k}-K₇-CA₈), which has the ability to penetrate tumor cell membranes. After encapsulation of cargos and formation of nanoparticles (NPs), MiniAP₄-PEG-K₇-CA₈ NPs was injected into mice via tail vein, it was found that MiniAP₄-PEG-K₇-CA₈ can indeed increase the ability of cargo delivery into the mice brain. More interestingly, compared with N₃-PEG-K₇-CA₈ NPs, MiniAP₄-PEG-K₇-CA₈ NPs also have more potential to improve the ability to delivery cargos into tumors.

1. Introduction

The BBB is extremely important in protecting people from harm by eliminating pathogens, macromolecules or hydrophilic molecules from entering the central nervous system (CNS). However, it also makes it very difficult to deliver therapeutic drugs into the CNS to treat brain diseases, especially macromolecular drugs and hydrophilic drugs. Therefore, it is very important to develop drug delivery platforms for the CNS, especially in the treatment of brain tumors which are not suitable for surgery. Over the last few years, a lot of proteins and peptides that can cross the BBB have been discovered and reported. [1] Among them, BBB shuttle peptides is the most popular topic nowadays, and the concept of BBB shuttle was first described by William M. Pardridge. [2] An extensive number of proteins and peptides used as BBB shuttles have been discovered, such as ApoB, ApoE, THR, THR retro-enantio, CRT, Leptin 30, ^DCDX, Apamin, MiniAP4, G23, g7, TGN, HIV TAT protein, RVG29, Angiopep-2, glutathione (GSH), SynB1, and so on. [1,3,4,5] Proteins are large molecules, they are complex, expensive to synthesize, and more immunogenic. Therefore, BBB shuttle peptides attracted more attention. For discovery more BBB shuttle peptides, a lot of study focused on highly expressed receptor on BBB, such as transferrin, low-density lipoproteins, insulin and leptin. Among all these BBB shuttles, Angiopep-2 and GSH have great clinical application prospects. [1,3,4,5] Apamin, a neurotoxin from bee venom, is capable of passing the BBB and blocks calcium-mediated potassium channels. As a cyclic nonapeptide simplified from peptide apamin, MiniAP4 has less toxicity and immunogenicity, and it is also safer, and inexpensive to synthesize. Further more, it has better BBB penetration ability than parent peptide and can be used to lead proteins and nanoparticles across the BBB. [6] MiniAP4 was first reported by Prof. Giralt and Prof. Teixidý. [6] MiniAP4 was used to delivery cargoes across the *in vitro* BBB model and *in vivo*.

Various of micellar nanoparticles based on polyethylene glycol (PEG) and dendritic cholic acids has been reported by Prof. Lam, [7] and such nanoplatfoms have been successfully used for tumor-targeting, sustained and controllable drug delivery, etc. The particle size of micelles is between 5-100nm and it is tunable. Micelles can improve the solubility and bioavailability of poorly soluble drugs, and they are excellent in delivering drugs, especially for macromolecular and hydrophobic drugs, such as anticancer drugs, proteins, genes, etc. Moreover, the therapeutic agents combined with the nanocarriers (such as micelles and liposomes) have better pharmacokinetic properties, thereby improving the therapeutic activity. Also, low toxicity and higher drug-loading ability make them an excellent drug delivery platform. The molecules contain polyethylene glycol (PEG) reduced immunogenicity, prolonged circulation time and reduced phagocytosis. [8] This makes PEG presented nanoparticles popular in drug delivery systems.

According to the phenomenon of enhanced permeability and retention (EPR) effects in solid tumor, the size and shape of the nanocarriers is closely related to the effect of drug delivery. The size of nanoparticles ranging from 10 to 500nm prefer to penetrate vascular bed and reaching the interstitial environment. ^[9] Prof. Lam described a series of tumor-targeting nanocarriers, ^[10,11,12,13,14,15,16,17] for the treatment of B-cell lymphoma ^[10], ovarian cancer ^[11], and so on. Also, there are several controlled release nanocarriers has been reported based on PEG and cholic acid micelles. ^[14, 16-18]

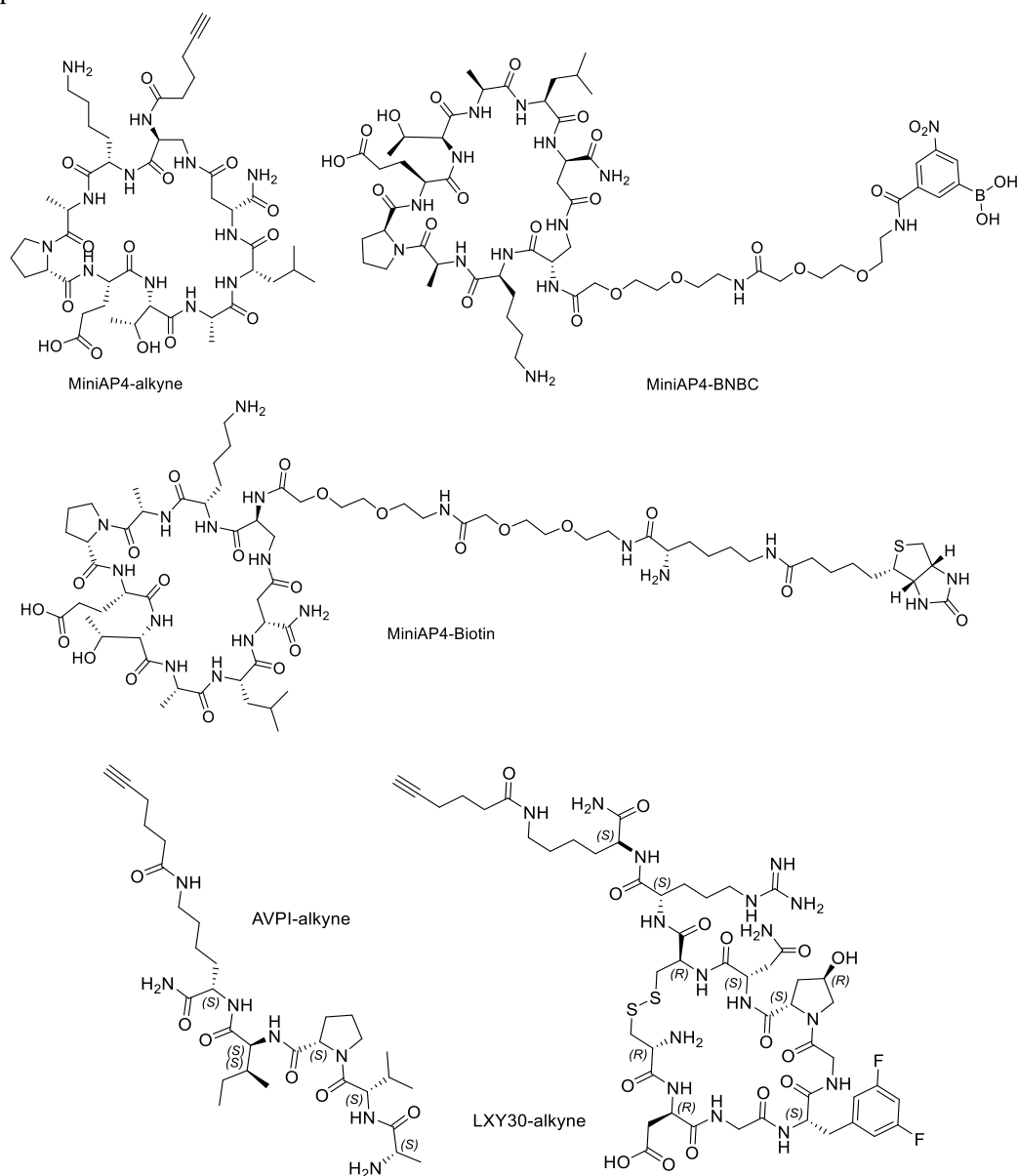
In a word, MiniAP4 and micellar nanoparticles are excellent in penetrating the BBB or delivery anticancer drugs into NCS. Consequently, combination of MiniAP4 and micellar nanoparticles provide an excellent drug delivery system to transport drugs into NCS. For achieving this purpose, we conjugate MiniAP4 at the distal end of PEG chain on micellar nanoparticles to prepare a novel brain-targeting drug delivery system. MiniAP4 will lead the nanoparticles across the BBB and facilitate the delivery of drugs into NCS to treat brain cancer or other NCS disorders. Due to population aging, various types of brain diseases have become more prominent topic, such as Alzheimer's disease, Parkinson's disease, brain tumors and so on. Therefore, it is necessary to develop a drug delivery system capable of successfully delivering drugs into the brain. About preparation, we firstly synthesized MiniAP4 and derivatized it with alkyne. At the same time, PEG-dendritic cholic acid (PEG-K₇-CA₈) was functionalized with azide group at the distal terminus of PEG. Afterward, MiniAP4 was linked to PEG-K₇-CA₈ via click chemistry. Then, the resulting MiniAP4-PEG-K₇-CA₈ was used for drug encapsulation via self-assembly. By intravenous injection, leading by MiniAP4, the nanoparticles crossed the BBB and were transported through the capillaries into the brain parenchyma.

2. Discussion and results

2.1 Synthesis procedure

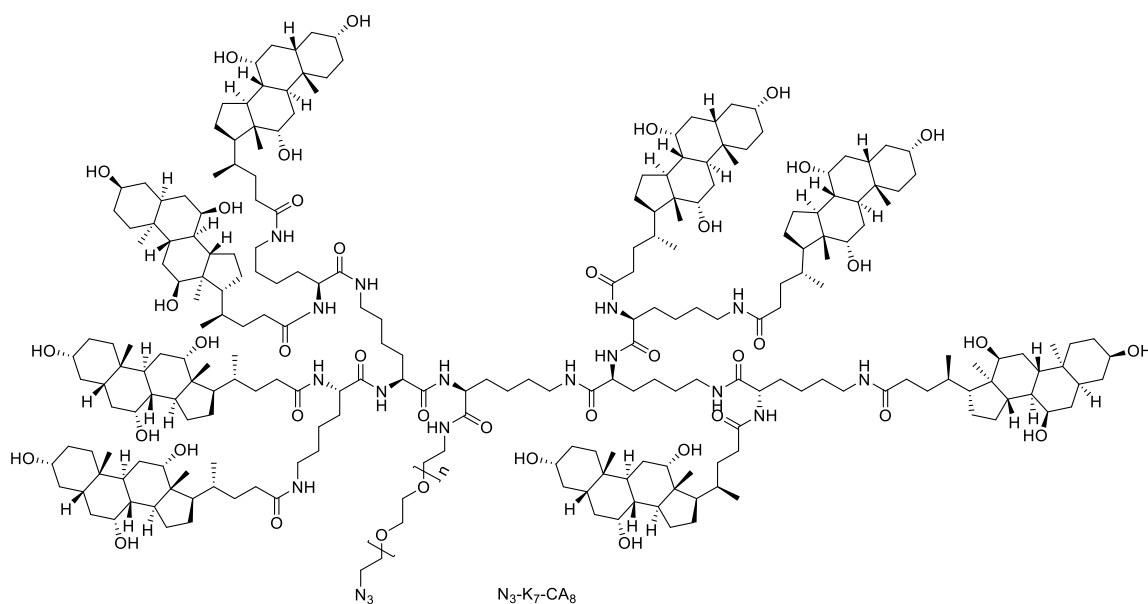
All the peptides were prepared according to solid phase peptides synthesis (SPPS) approach. Obtained peptides were purified by preparative HPLC and the purity was analyzed by analytical HPLC and final products were verified by mass spectrometry. MiniAP4 is a cyclic nonapeptide, and MiniAP4-alkyne (c[DAP(alkyne)-K-A-P-E-T-A-L-D]) was prepared according to previous work ^[3]. During the preparation of linear peptides, amino group on the side chain of Fmoc-DAP-OH was protected with Alloc, and carboxylic group of Fmoc-Asp-OH was protected with OAll. After obtaining linear peptides and removing Alloc and OAll with Tetrakis(triphenylphosphine)-palladium(0) and Phenylsilane, cyclization was performed. Before conjugating alkyne to cyclic peptide c[DAP(Fmoc)-K-A-P-E-T-A-L-D] to obtain c[DAP(alkyne)-K-A-P-E-T-A-L-D] (MiniAP4-alkyne), the Fmoc group was removed to give free amino group to couple with 5-hexynoic acid. LXY30-alkyne was prepared according to previous work. ^[19] Linear peptide c(trt)-d(trt)-G-Phe(3,5-diF)-G-Hyp-N(trt)-c(trt)-R(pbf)-K(dde) was prepared on Rink amide resin. After removing protect group Dde from Lysine on the end of linear peptide, 5-hexynoic acid was coupled on free amino group, then peptide cleavage was performed. After removing solvents in cleavage cocktail, cyclization was accomplished on ClearOx™ resin to obtain LXY30-alkyne. AVPI-alkyne ^[20] was prepared on solid phase, A-V-P-I-K(Dde)-resin was prepared firstly, then Dde was deprotected and 5-hexynoic acid was coupled followed by cleavage to obtain AVPI-alkyne. The synthesis procedure of MiniAP4-biotin and MiniAP4-BNBC (BNBC = 3-carboxy-5-nitrophenylboronic acid) was similar to the preparation of MiniAP4-alkyne, the only difference is the use of biotin or BNBC instead of alkynes. To conjugate MiniAP4 and biotin, the linker Fmoc-AEEA-OH was utilized, and biotin was introduced as a form of

Fmoc-Lys(biotin)-OH, then Fmoc was removed before cleavage. The structures of functionalized peptides were shown in Scheme 1.



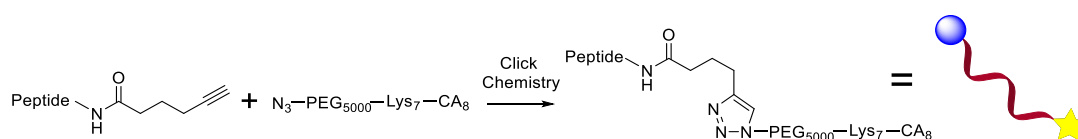
Scheme 1. Chemical structures of MiniAP4-Alkene, MiniAP4-Biotin, MiniAP4-BNBC, LXY30-Alkene, AVPI-Alkene.

To prepare N_3 -PEG_{5k}-K₇-CA₈, NH₂-PEG_{5k}-N₃ was coupled with Fmoc-K(Fmoc)-OH to get Fmoc-K(Fmoc)-PEG_{5k}-N₃. After removing Fmoc, 2 free amino groups on Lysine were coupled with 2 Fmoc-Lys(Fmoc)-OH to give (Fmoc-K(Fmoc))₂-K-PEG_{5k}-N₃. Then Fmoc was removed, followed by coupling 4 Fmoc-Lys(Fmoc)-OH with 4 amino groups on 2 Lysine to give (Fmoc-K(Fmoc))₄-K₃-PEG_{5k}-N₃, afterward, Fmoc was removed to obtain K₇-PEG_{5k}-N₃, which have 8 free amino groups. Freshly prepared CA-OSu was coupled with free amino groups on K₇-PEG_{5k}-N₃ to give CA₈-K₇-PEG_{5k}-N₃ (Scheme 2).



Scheme 2. Chemical structures of N₃-PEG_{5k}-K₇-CA₈

In order to obtain CA₈-K₇-PEG_{5k}-MiniAP4, BBB shuttle peptide derivative MiniAP4-alkyne and dendrimer CA₈-K₇-PEG_{5k}-N₃ were conjugated together via click chemistry (Scheme 3). And the preparation of CA₈-K₇-PEG_{5k}-LXY30 and CA₈-K₇-PEG_{5k}-AVPI followed the same procedure. Before *in vivo* studies, 1,1'-dioctadecyl-3,3,3',3'-tetramethylindo-dicyanine (DID) dye and CA₈-K₇-PEG_{5k}-MiniAP4 were dispersed in PBS to form DID-encapsulated nanoparticles, then the freshly prepared nanoparticles were filtered through a 0.22 μm filter to remove bacteria.



Scheme 3. The preparation of Peptide-PEG-Lys₇-CA₈ monomer by click chemistry, peptides are MiniAP4, LXY30, AVPI.

2.2 *in vivo* Assay of the Conjugates of MiniAP4-Biotin and Streptavidin-Cy5.5

In the presence (group A) or absence (group B) of MiniAP4-biotin, mice were injected with a streptavidin-Cy5.5 from the tail vein. After 24h, compared with group B, it was found that the fluorescence intensity of Cy5.5 in mice brain was much higher in Group A, which means that the presence of MiniAP4-biotin promoted streptavidin-Cy5.5 to cross the BBB and delivery cargos into mice brain (Show in figure 1). In order to verify the reliability of the result, this experiment was repeated again, and we observed the same result.

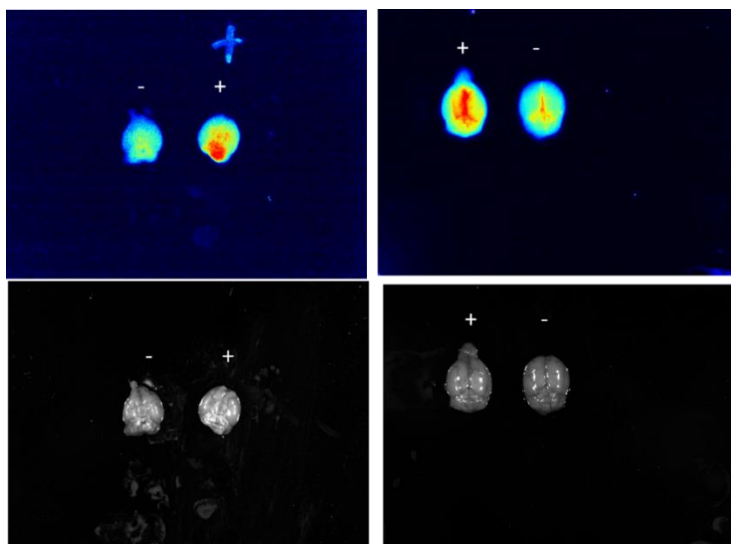


Figure 1. Positive: Group A, MiniAP4-Biotin + Streptavidin-Cy5.5; Negative: Group B, Streptavidin-Cy5.5, 24 h after injection.

2.3 *in vivo* Assay of Dye Loaded N_3 -NPs(DID) and MiniAP4-NPs(DID) in Healthy Mice

Dye (DID) loaded MiniAP4-NPs(DID) (group A) and N_3 -NPs(DID) (group B) were injected into healthy mice via tail vein, and the fluorescence intensity was recorded at 0.5h, 2h, 4h, 6h, 12h, 24h after injection. Figure 2 shows that the fluorescence intensity in the mice brain of group A is always stronger than that in mice brain of group B.

The relationship between the time and the concentration of dye-loaded NPs has also been investigated. Two hours after injection of dye-loaded NPs, fluorescence intensity was the strongest and then it was gradually decreased. And the fluorescence intensity decreased rapidly after 6 hours, and it became very weak after 12 hours. Compared with N_3 -NPs (DID), MiniAP4-NPs (DID) can transport more dyes (DID) into the mice brain (Figure 2). From figure 2, we are convinced that MiniAP4-NPs can promote the loaded cargos to cross the BBB and transport them into the brain.

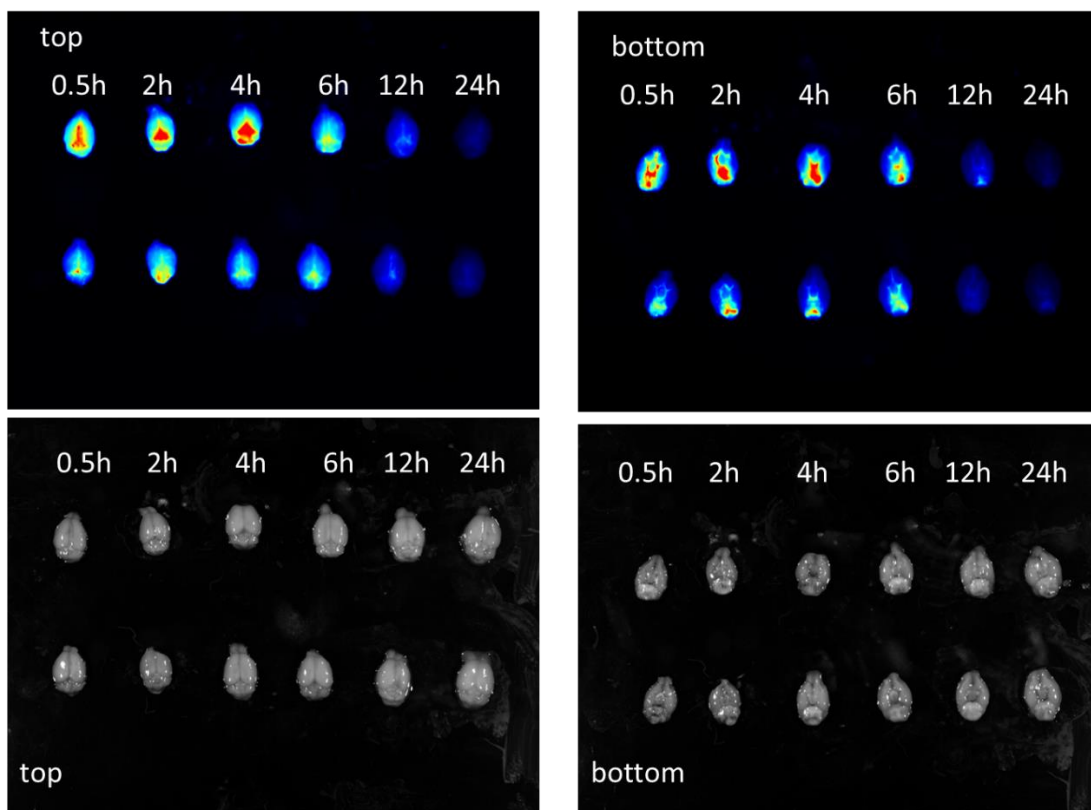


Figure 2. Healthy mice, Positive: Group A, MiniAP4-PEG_{5k}-K7-CA₈ (NPs), Negative: Group B, N₃-PEG_{5k}-K7-CA₈ (NPs), From left to right: 0.5h, 2h, 4h, 6h, 12h, 24h.

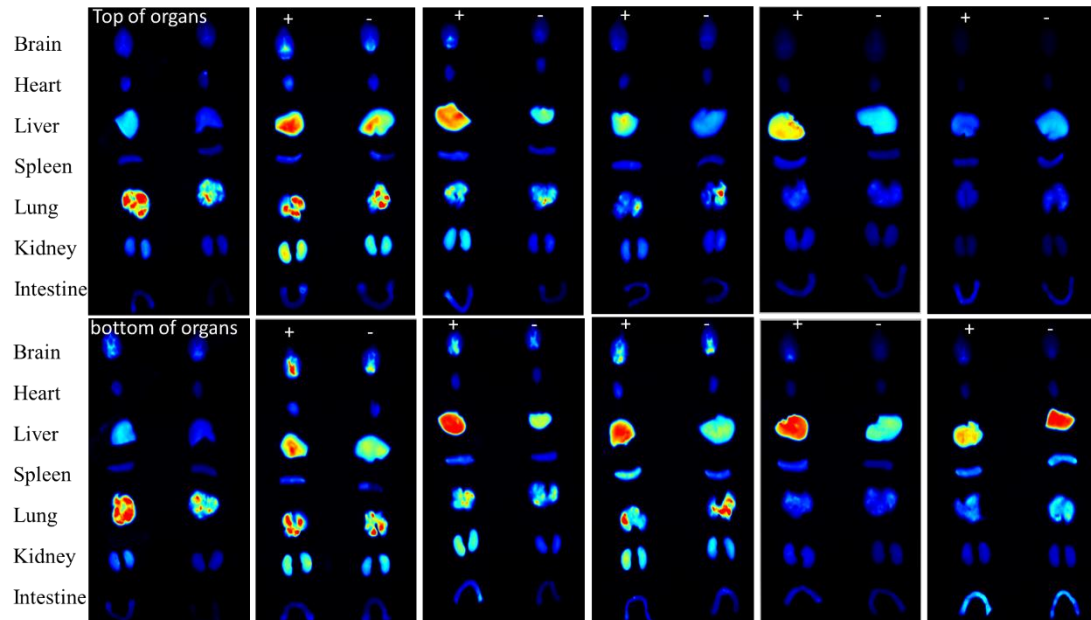


Figure 3. Healthy mice, Positive: MiniAP4-PEG_{5k}-K7-CA₈ (NPs), Negative: N₃-PEG_{5k}-K7-CA₈ (NPs), Left to right: 0.5 h, 2h, 4h, 6h, 12h, 24h after NPs injection.

We also investigated the distribution of NPs (MiniAP4-NPs (DID) and N₃-NPs(DID)) in mice organs. It was found that 0.5 hours after injection of NPs, most of the NPs were distributed in the lungs; by 2 hours, the accumulation of NPs in the liver, kidney and brain began to increase, while at the same time, the concentration of NPs in the lung was gradually decreased; by 4 hours, the concentration of NPs in the liver was the highest, but the concentration of NPs in the lungs,

kidneys and brain was reduced; by 12 hours, most of the nanoparticles were distributed in the liver for metabolism, and the concentration of NPs in the lungs, kidneys and brain keep declining; by 24 hours, the concentration of NPs distributed in the liver began to decrease significantly, and the concentration of NPs in the kidney and brain was already very low (Figure 3).

2.4 *in vivo* Assay of Dye Loaded N_3 -Nps(DID) and Miniap4-Nps(DID) in Tumor Bearing Mice

Dye loaded N_3 -NPs(DID) and MiniAP4-NPs(DID) were injected in mice with oral cancer via tail vein. Then the fluorescence intensity in the mice brain was detected 0.5h, 1h, 2h, 3h, 4h, 6h after injection. From imaging (Figure 4) and tissue homogenate (Figure 5), we found that the fluorescence intensity in the brain of mice injected with MiniAP4-NPs(DID) was significantly stronger than that in the brain of mice injected with N_3 -NPs(DID). 0.5 hours after the injection of MiniAP4-NPs(DID), the fluorescence intensity in the mice brain was highest, and then gradually decreased. After 2 hours, the fluorescence intensity increased again and began to decrease after 4 hours. On the other hand, 1 hour after N_3 -NPs(DID) was injected in mice, the fluorescence intensity in mice brain was strongest, and then it began to decrease. 3 hours after injection, the fluorescence intensity increased again, and by 4 hours after injection, it began to decrease. In the left panel of Figure 5, there are two peaks in the fluorescence intensity-time curve, which may be due to the secondary distribution of NPs. After tail vein injection, NPs quickly distributed to tissues or other organs. After the DID molecules in the blood were metabolized to a certain extent, a secondary release occurs. Compared with N_3 -NPs(DID), MiniAP4-NPs(DID) can transport more dyes into the brain. 0.5 hours after injection, the fluorescence intensity of MiniAP4-NPs(DID) transported into the mice brain are 3.37 times that of N_3 -NPs(DID). More interestingly, we found that MiniAP4-NPs (DID) have a higher tumor penetration ability than N_3 -NPs (DID). (Figure 6). Due to its brain penetration and tumor infiltration capabilities, MiniAP4-NPs(DID) becomes a potential drug delivery vehicle targeting brain tumors.

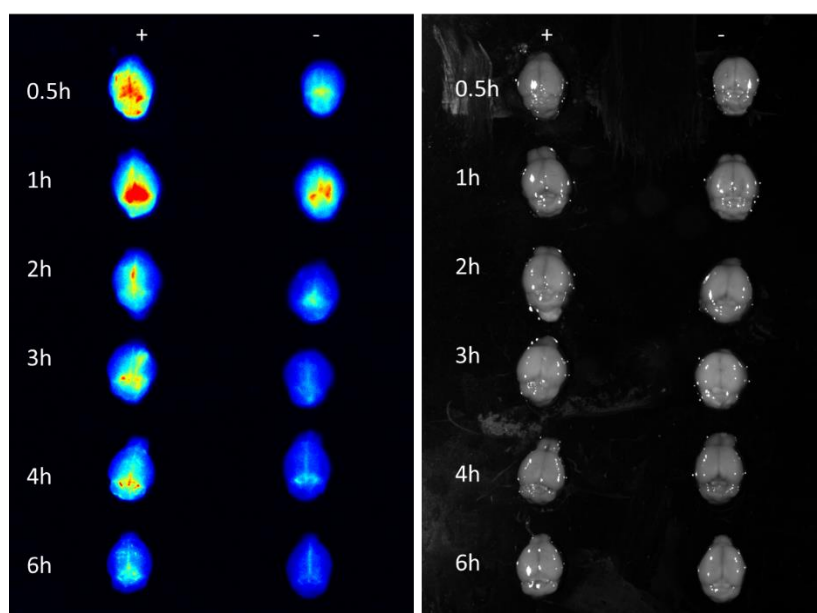


Figure 4. Mice bearing oral tumor, Positive: MiniAP₄-PEG_{5k}-K₇-CA₈ (NPs), Negative: N₃-PEG_{5k}-K₇-CA₈ (NPs)

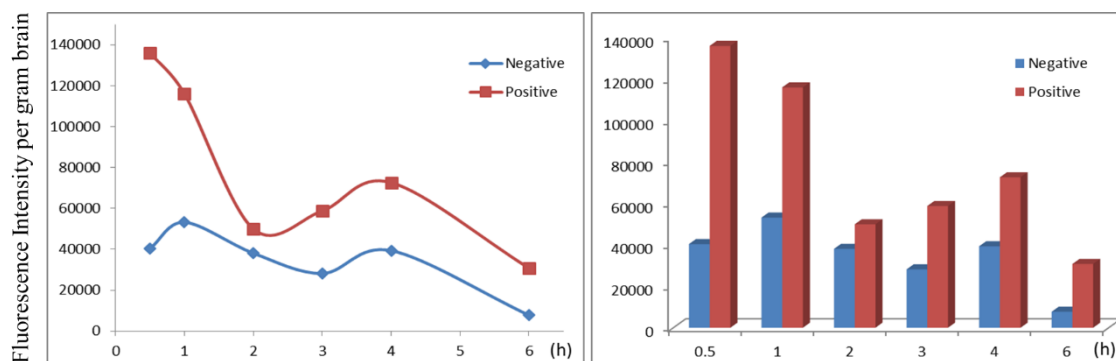


Figure 5. Mice bearing oral tumor, Positive: MiniAP₄-PEG_{5k}-K₇-CA₈ (NPs), Negative: N₃-PEG_{5k}-K₇-CA₈ (NPs)

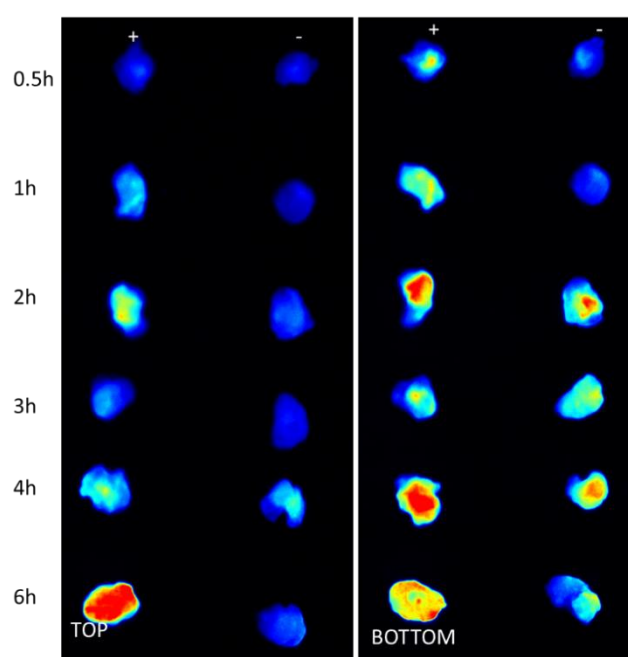


Figure 6. Mice bearing oral tumor, Positive: MiniAP₄-PEG_{5k}-K₇-CA₈ (NPs), Negative: N₃-PEG_{5k}-K₇-CA₈ (NPs)

3. Experimental Section

3.1 General Experimental Methods.

All purchased reagents were used without further purification. Matrix-assisted laser desorption/ionization time of flight mass spectrometry (MALDI-TOF MS) analysis was performed on a Bruker BIFLEX III mass spectrometer (Billerica, MA). Analytical HPLC was performed on a Waters 2996 HPLC system equipped with a 4.6 × 150 mm Waters XTerra MS C18 5.0 μm column and employed a 20-min gradient from 100 % H₂O/0.1 % TFA to 100 % acetonitrile (ACN)/0.1 % TFA at a flow rate of 1.0 mL/min. Preparative HPLC was performed on a System Gold 126NMP solvent module (Beckman) with a C18 column (Vydac, 10 μm, 2.2 cm i.d. × 25 cm). A gradient elution of 0–60 % ACN/0.1 % TFA in H₂O/0.1 % TFA over 30 min, then increased to 100 % in 1 min and keep for 5 min at a flow rate of 1.0 mL/min. DLS measurements

were performed with Zetasizer on Dynamic light scattering instrument (DLS, Nano ZS, Malvern); UV spectrum was performed on UV Probe2.52 on UV-Vis photospectrometer (UV-1800, Shimadzu); Fluorescence spectrum was performed on Lab Solutions RF on Fluorescence photospectrometer (RF6000, Shimadzu). Images were captured with a Kodak IS2000MM image station (Rochester, NY) with a 625/20 band-pass excitation filter, 700WA/35 band-pass emission filter, and 150 W quartz. Halogen lamp light source was set to maximum. Images were captured with a CCD camera set at F stop = 0, FOV = 150, and FP = 0.

3.2 Synthesis Procedure

3.2.1 Synthesis of MiniAP4-Alkyne

MiniAP4-alkynes were synthesized according to the typical SPPS procedure, depending on previous work [3]. To be brief, firstly, Fmoc-Asp(OAll)-OH (2 eq.) was loaded on Rink amide resin (1 eq.) by using coupling reagents DIC (2 eq.) and Oxima Pure (4 eq.) in DMF and shaken for 3 h, then the solvent was removed and the resin was washed with DMF, MeOH, and DCM 3 times each. Afterward, Fmoc was removed by using 20% piperidine in DMF, shaken for 20 min, and the resin was washed with DMF, MeOH, and DCM, and repeat the deprotection procedure again. Kaiser test was used to verify the success of deprotection. Subsequently, Fmoc protected amino acids were coupled in sequence, which was Fmoc-Leu-OH (2 eq.), Fmoc-Ala-OH (2 eq.), Fmoc-Thr(tBu)-OH (2 eq.), Fmoc-Pro-OH (2 eq.), Fmoc-Ala-OH (2 eq.), Fmoc-Glu(OtBu)-OH (2 eq.), Fmoc-Lys(Boc)-OH (2 eq.), Fmoc-DAP(Alloc)-OH (2 eq.). For removing allyl and alloc, Phenylsilane (20 eq.) and Tetrakis(triphenylphosphine) palladium(0) (0.2 eq.) were dissolved in DCM and then added in reactor and shaken for 30min under inert atmosphere. After removing solvents and washing with DCM, repeat the deprotection procedure. Followed by washing with DCM, 2% DIPEA in DMF, 0.5% diethyldithiocarbamate trihydrate in DMF, DCM 3 times each in sequence. Thereafter, cyclization was performed in DMF solution with DIC (4 eq.) and Oxima Pure (4 eq.) for 3 h, then solvent was removed and resin was washed with DMF, MeOH, and DCM 3 times each. After removing Fmoc group to obtain c[DAP-K-A-P-E-T-A-L-D]-resin, 5-hexynoic (2 eq.), DIC (2 eq.), Oxima Pure (4 eq.) was utilized to introduce alkyne in the side chain of DAP in the cyclic peptide sequence. After washing, peptide cleavage was carried out in the mixture of TFA, H₂O, Triisopropylsilane (TIPS), Thioanisole (93: 2.5: 2.5: 2, v/v) for 2 h. Then the cleavage cocktail was collected and the cleavage procedure was repeated again. Afterward, the collected cocktails were combined and solvents were removed under compressed air, and the residue was washed with cold ether to give a white powder. The peptide was purified by preparative HPLC, and then analytical HPLC was used to confirm that the purity was over 95% and the remaining time was 8.36 min (Figure 11a). The exact mass was analyzed by MALDI-TOF mass spectrometry, calcd. for C₄₅H₇₃N₁₂O₁₄ [M+H]⁺ 1005.5369, found 1005.803 (Figure 7).

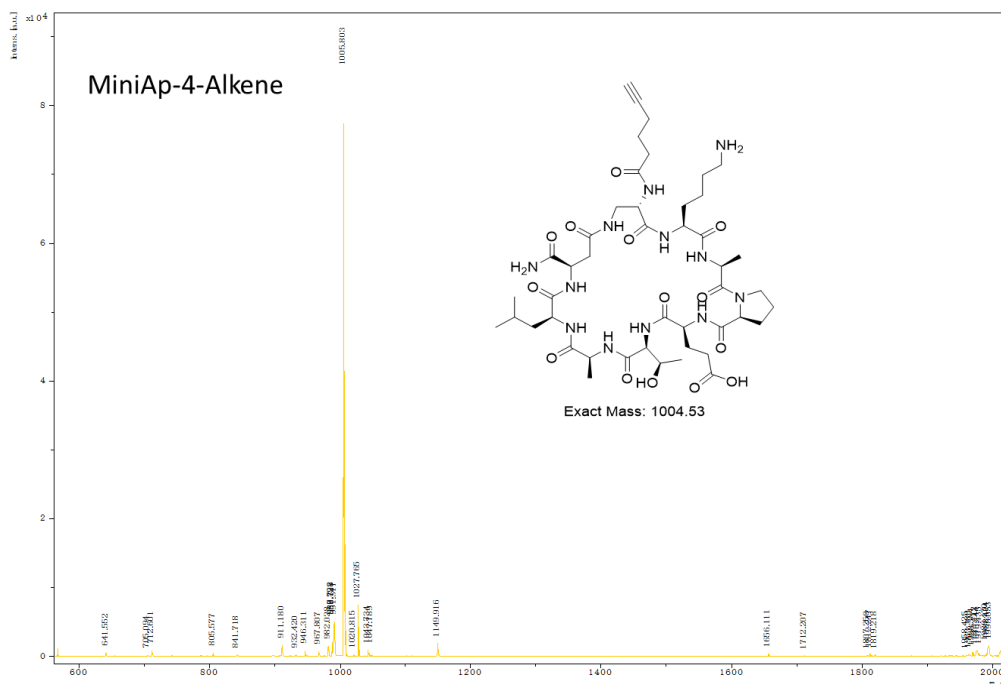


Figure 7. Mass spectrum of MiniAP4-Alkene.

3.2.2 Synthesis of MiniAP4-Biotin

The procedure was similar to the preparation of *MiniAP4-alkyne*. c[DAP-K-A-P-E-T-A-L-D]-resin was obtained as described above, then it was coupled with Fmoc-AEEA-OH (2 eq.) in DMF solution of DIC (2 eq.) and Oxima (4 eq.). After washing and Fmoc removing, another coupling of Fmoc-AEEA-OH was performed on peptides on the resin to obtain c[DAP(AEEA)₂-K-A-P-E-T-A-L-D]-resin. Afterward, Fmoc-Lys(Biotin)-OH (2 eq.) was coupled on the tail of AEEA of obtained peptides on the resin and then Fmoc was removed. After washing, peptide cleavage was performed in the mixture of TFA, H₂O, Triisopropylsilane (TIPS), Thioanisole (93: 2.5: 2.5: 2, v/v) for 2 h. The cleavage cocktail was collected and the cleavage procedure was repeated. Solvents were removed under compressed air, and the residue was washed with cold ether to give a white powder. The peptide was purified by Pre-HPLC, and then analytical HPLC was used to confirm that the purity was over 98% and the remaining time was 9.05 min (Figure 11b). The exact mass was analyzed by MALDI-TOF mass spectrometry, calcd. for C₆₇H₁₁₅N₁₈O₂₂S [M+H]⁺ 1555.8154, found 1556.404; [M+Na]⁺ 1577.7973, found 1578.391; [M+K]⁺ 1593.7713, found 1594.374 (Figure 8).

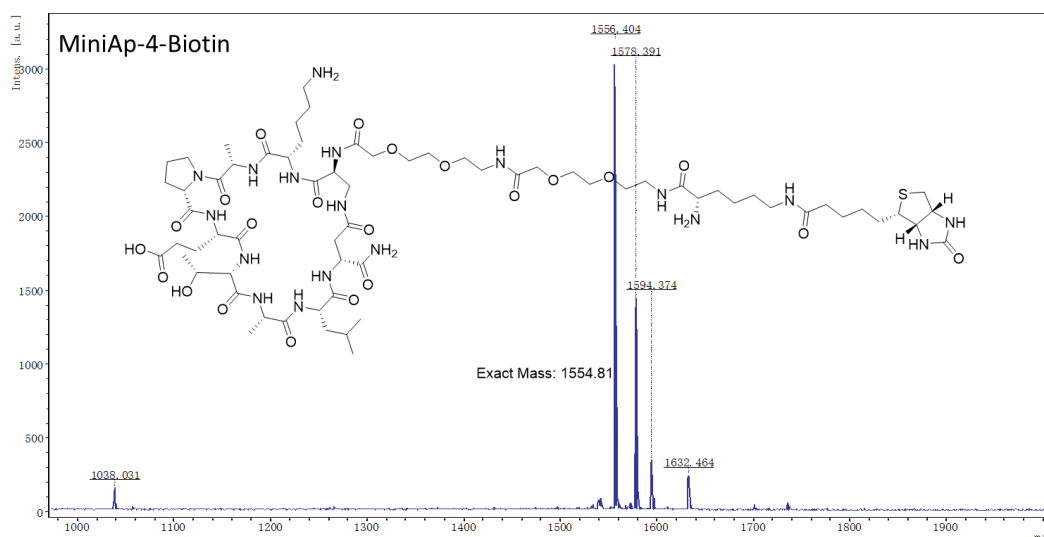


Figure 8. Mass spectrum of MiniAP4-boitin.

3.2.3 Synthesis of MiniAP4-BNBC

The procedure was similar to the preparation of *MiniAP4-alkyne*, c[DAP-K-A-P-E-T-A-L-D]-resin was coupled with Fmoc-AEEA-OH (2 eq.) in DMF solution of DIC (2 eq.) and Oxima (4 eq.). After washing and Fmoc removing, another coupling of Fmoc-AEEA-OH (2 eq.) was performed on peptides on the resin to obtain c[DAP(AEEA)₂-K-A-P-E-T-A-L-D]-resin. Afterward, 3-carboxy-5-nitrophenylboronic acid (CNBC, 2 eq.) was coupled on peptides on the resin. After washing, peptide cleavage was performed in the mixture of TFA, H₂O, Triisopropylsilane (TIPS), Thioanisole (93: 2.5: 2.5: 2, v/v) for 2 h. The cleavage cocktail was collected and the cleavage procedure repeated. The solvents were removed under compressed air, and the residue was washed with cold ether to give a white powder. The peptide was purified by Pre-HPLC, then analytical HPLC was used to confirm that the purity was over 94% and the remaining time was 11.33 min (Figure 11c).

3.2.4 Synthesis of LXY30-Alkyne

LXY30-Alkyne were synthesized according to the typical SPPS procedure, depending on previous work.^[19] To be brief, firstly, Fmoc-Lys(Dde)-OH (2 eq.) was loaded on Rink amide resin (1 eq.) by using coupling reagents DIC (2 eq.) and Oxima Pure(4 eq.) in DMF and shaken for 3 h, then the solvent was removed and the resin was washed with DMF, MeOH, and DCM 3 times each. Afterward, Fmoc was removed by using 20% Piperidine in DMF. Then, Fmoc amino acids were coupled in sequence, which was Fmoc-Arg(pbf)-OH (2 eq.), Fmoc-cys(Trt)-OH (2 eq.), Fmoc-Asn(trt)-OH (2 eq.), Fmoc-Hyp-OH (2 eq.), Fmoc-Gly-OH (2 eq.), Fmoc-Phe(3,5-diF)-OH (2 eq.), Fmoc-Gly-OH (2 eq.), Fmoc-asp(OtBu)-OH (2 eq.), Boc-cys(Trt)-OH (2 eq.). Thereafter, Dde was removed in a 2% hydrazine DMF solution for 10 min, and then the resin washed with DMF, the deprotection procedure was repeated again to obtain a free amino group on the side chain of Lysine on the peptides c(trt)-d(trt)-G-Phe(3,5-diF)-G-Hyp-N(trt)-c(trt)-R(pbf)-K-resin. After washing, 5-hexynoic (2 eq.), DIC (2 eq.), Oxima Pure (4 eq.) were utilized to introduce alkyne on side chain of Lysine in peptide sequence on the resin. Followed by wishing with DMF, Methanol, and DCM, and then peptide cleavage was performed in a mixture of TFA, H₂O, Triisopropylsilane (TIPS), Phenol, Thioanisole (87.5%: 2.5%: 2.5%: 2.5%: 5%, v/v, 20mL) for 5

h. The cleavage cocktail was collected and the cleavage procedure was repeated again. Solvents were removed, and the residue was washed with cold ether to obtain a white powder. In order to perform disulfide bond formation, ClearOx™ resin was utilized. Before using, ClearOx™ resin was shaken in DCM for 30 min, then washed with DMF, Methanol, DCM, H₂O, the mixture of 100 mM ammonium bicarbonate and acetonitrile (1:1) 3 times each. Peptide obtained above was dissolved in a mixture of 100 mM ammonium bicarbonate and acetonitrile (1:1), then it was added to the ClearOx™ resin and shaken for 2 h. Afterward, the solution with cyclized peptides was collected and the resin was washed with a mixture of 100 mM ammonium bicarbonate and acetonitrile (1:1), 100 mM ammonium bicarbonate, distilled water in sequence. Then all the washes were combined and lyophilized. The obtained peptide was purified by Pre-HPLC, then analytical HPLC was used to confirm that the purity was over 93% and the remaining time was 10.09 min (Figure 11d). The exact mass was analyzed by MALDI-TOF mass spectrometry, calcd. for C₅₀H₇₃F₂N₁₆O₁₅S [M+H]⁺ 1239.4851, found 1239.898 (Figure 9).

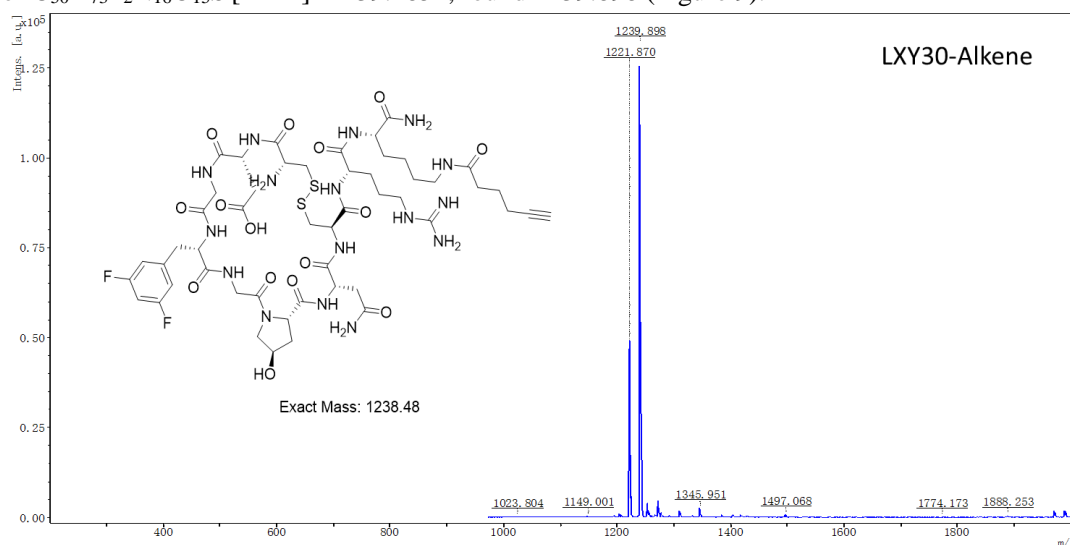


Figure 9. Mass spectrum of LXy30-Alkene.

3.2.5 Synthesis of AVPI-Alkyne

AVPI-Alkyne was synthesized according to typical SPPS procedure. To be brief, firstly, Fmoc-Lys(Dde)-OH (2 eq.) was loaded on Rink amide resin (1 eq.) by using coupling reagents DIC (2 eq.) and Oxima Pure (4 eq.) in DMF and shaken for 3 h, then the solvent was removed and the resin was washed with DMF, MeOH and DCM 3 times each. Afterward, Fmoc was removed by using 20% Piperidine in DMF. Then, Fmoc amino acids Fmoc-Ile-OH (2 eq.), Fmoc-Pro-OH (2 eq.), Fmoc-Val-OH (2 eq.), Boc-Ala-OH (2 eq.) were coupled in sequence. Thereafter, Dde was removed in 2% hydrazine in DMF solution for 10 min, and then the resin was washed with DMF. The deprotection procedure was repeated again to obtain Boc-A-V-P-I-K-resin. After washing, 5-hexynoic (2 eq.), DIC (2 eq.), Oxima Pure (4 eq.) were utilized to introduce alkyne in Lysine side chain in the peptide sequence. The resin was washed with DMF, Methanol, and DCM 3 times each, and peptide cleavage was performed in a mixture of TFA, H₂O, Triisopropylsilane (TIPS), Phenol, Thioanisole (87.5%: 2.5%: 2.5%: 2.5%: 5%, v/v, 20 mL) for 3h. The cleavage cocktail was collected and the cleavage procedure was repeated again. The solvents were removed under compressed air, and the residue was washed with cold ether to give a white powder. The obtained peptide was purified by Pre-HPLC, then analytical HPLC was used to confirm that the purity was

over 90% and remain time was 10.42 min (Figure 11e). The exact mass was analyzed by MALDI-TOF mass spectrometry, calcd. for $C_{45}H_{73}N_{12}O_{14}$ $[M+H]^+$ 620.4136, found 620.691; $[M+Na]^+$ 642.3955, found 642.634; $[M+K]^+$ 658.3694, found 658.621 (Figure 10).

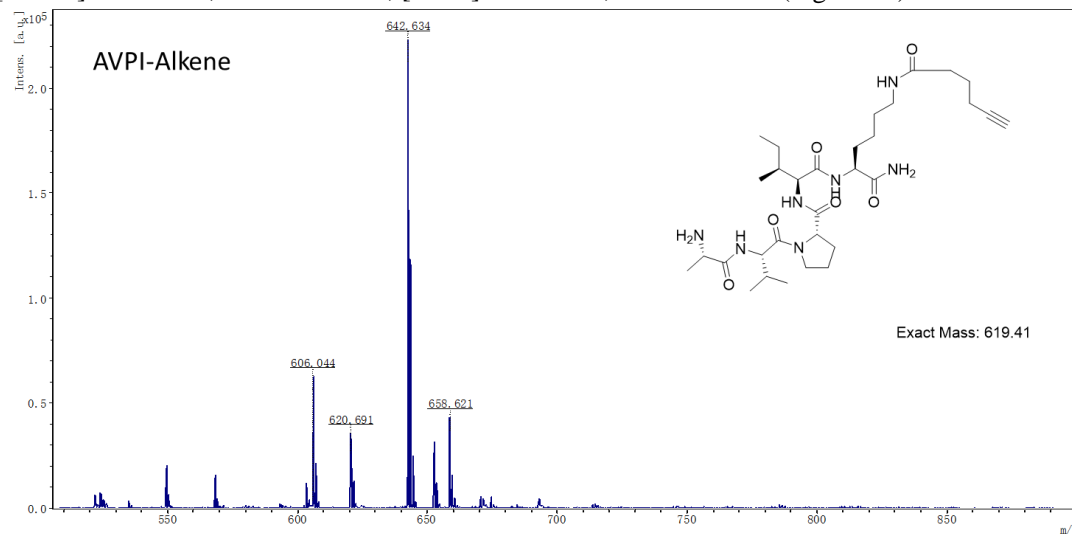


Figure 10. Mass spectrum of AVPI-Alkene

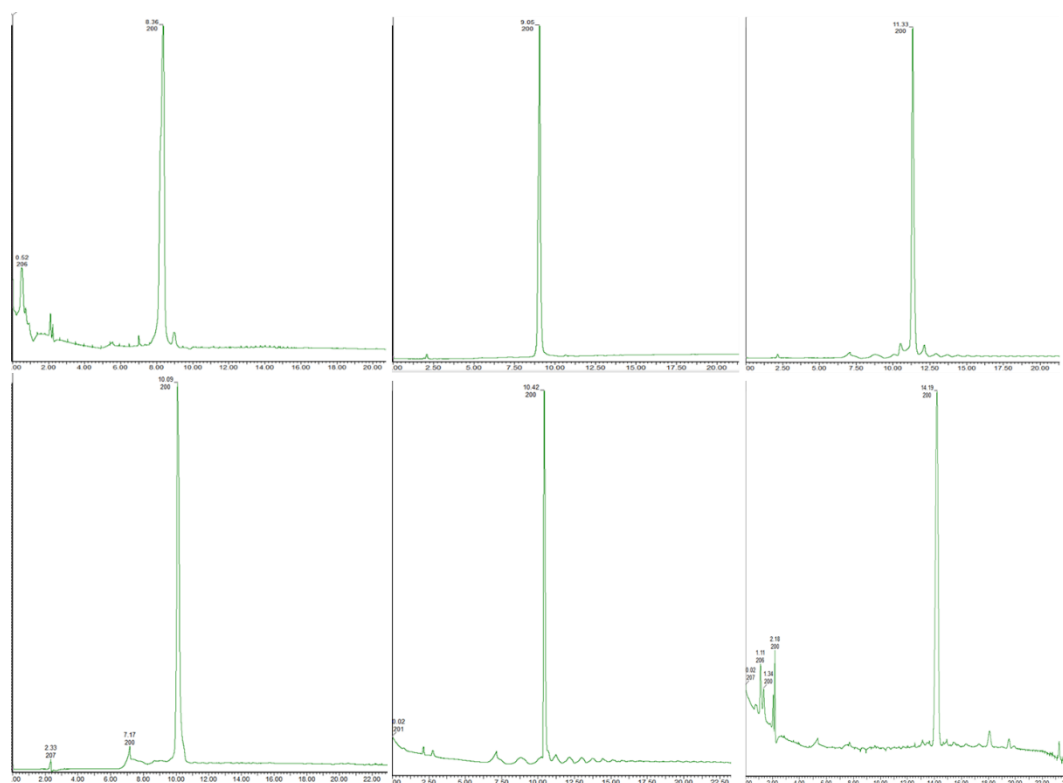


Figure 11. HPLC spectrum of (a) MiniAP4-Alkene, (b) MiniAP4-Biotin, (c) MiniAP4-BNBC, (d) LXY30-Alkene, (e) AVPI-Alkene, (f) CA-OSu.

3.2.6 Preparation of Peptide-PEG_{5k}-K₇-CA₈

3.2.6.1 Synthesis of N₃-PEG_{5k}-K₇

N₃-PEG_{5k}-K

Fmoc-Lys(Fmoc)-OH (709 mg, 3 eq.), DIC (188 μ L, 3 eq.), and Cl-HOBt (162.14 mg, 3 eq.) were dissolved in 15 mL DMF, and N₃-PEG_{5k}-NH₂ (2 g, 0.4 mmol) was dissolved in 10 mL DMF,

respectively. Then mix them up under 0°C and the mixture was shaken overnight at rt. The Kaiser test was performed to confirm the completion of the reaction. After that, cold ether was added to the mixture to generate precipitation, then it was centrifuged, and the supernatant was removed. In the obtained precipitate, another 15 mL of DMF was added to redissolve it. Then cold ether 60 mL was added to achieve precipitation, and the centrifugation and supernatant removal was performed. Repeat the above procedure again. The obtained white solid was washed with cold ether twice and dried under vacuum. Fmoc was removed in 20 mL 20% Piperidine in DMF for 3h. The Kaiser test was performed to confirm the completion of the deprotection. The subsequent washing step was then performed as described above, and the obtained white solid was dried under vacuum to obtain N₃-PEG_{5k}-K (N₃-PEG_{5k}-Lys-OH).

N₃-PEG_{5k}-K₃

The obtained N₃-PEG_{5k}-K was dissolved in 10 mL DMF. At the same time, Fmoc-Lys(Fmoc)-OH (1.418 g, 6 eq.), DIC (376 μL, 6 eq.) and Cl-HOBt (324.28 mg, 6 eq.) were dissolved in 15 mL DMF. Then mix them up under 0°C and the mixture was shaken overnight at rt. The Kaiser test was performed to confirm that the reaction was complete. And then the washing procedure was performed as described above. In obtained white solid, 20 mL of 20% Piperidine in DMF was added and it was shaken for 3h to remove Fmoc. After the Kaiser test, the washing procedure was accomplished as described above and the obtained white solid was dried under vacuum to obtain N₃-PEG_{5k}-K₃ (N₃-PEG_{5k}-Lys(Lys-OH)₂-OH).

N₃-PEG_{5k}-K₇

The obtained N₃-PEG_{5k}-K₃ was dissolved in 10 mL DMF, and Fmoc-Lys(Fmoc)-OH (2.836 g, 12 eq.), DIC (752 μL, 12eq.) and Cl-HOBt (648.56 mg, 12 eq.) were dissolved in 15 mL DMF. They were then mixed at 0°C and the reaction was shaken at room temperature overnight. The Kaiser test was performed to confirm the completion of the reaction, and the followed washing procedure as described above. In the obtained white solid, 20 mL of 20% piperidine in DMF was added and it was shaken for 3h to remove Fmoc. The Kaiser test was performed to conform the completion of the reaction. The washing procedure as described above and the obtained white solid was dried under vacuum to obtain N₃-PEG_{5k}-K₇ (N₃-PEG_{5k}-Lys(Lys((Lys-OH)₂)-OH)₂-OH). N₃-PEG_{5k}-K₇ was analyzed by MALDI-TOF mass spectrometry, calcd. for average 9018.8914, found average is 9000-9200 (Figure 13d).

3.2.6.2 Synthesis of CA-OSu (Cholic Acid NHS Ester)

Cholic acid (4 g, 1 eq.) was dissolved in 20 mL anhydrous DCM (solution A), NHS was dissolved (1.44 g, 1.2 eq.) in 20 mL anhydrous DCM (solution B), EDCI (2.88 g, 1.5 eq.) was dissolved in 20 mL anhydrous DCM (solution C), respectively. Solution B and solution A were combined and stirred for 10 min, then solution C was added to the mixture dropwise. Afterward, 4-methylmorpholine (5 mL, 4.5 eq.) was added and the mixture was stirred overnight. The solvents were removed under vacuum, and the residue was dissolved in 60 mL EA, then washed with water (15 mL × 3), NaHCO₃ aqueous solution (0.1 M, 15 mL × 3), HCl aqueous solution (1 M, 15 mL × 3) and brine (15 mL × 3), respectively. The organic layer was dried over Na₂SO₄ and the solvent was removed under vacuum. Analytical HPLC was utilized to analyze the purity of obtained CA-OSu, and the remaining time was 14.19 min (Figure 11f), the exact mass was analyzed by MALDI-TOF mass spectrometry, calcd. for C₂₈H₄₃NNaO₇ [M+Na]⁺ 528.2937, found 528.482 (Figure 12).

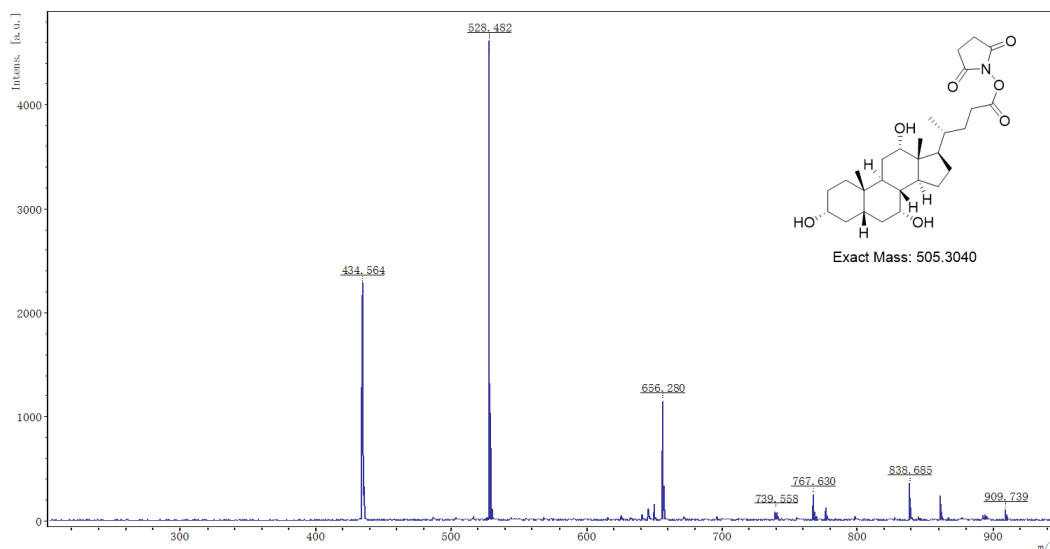


Figure 12. Mass spectrum of CA-OSu

3.2.6.3 Preparation of Peptide-PEG_{5k}-Lys₇-CA₈ Monomer by Click Chemistry

N₃-PEG_{5k}-K₇ (500 mg, 1.0 eq.) and MiniAP4-alkyne (84 mg, 1.5 eq.) were placed in a 50 mL round-bottom flask, and the oxygen in flask was removed under vacuum for 30 min, and 20 mL DMF was added under nitrogen. After dissolving N₃-PEG_{5k}-K₇ and MiniAP4-alkyne, PMDETA (300 μ L, 11.5 eq.) and CuBr (50 mg, 2.8 eq.) were added in the mixture, and the reaction was heated to 40°C under nitrogen and stirred for 48h. Subsequently, EDTA(500 mg) was added in reaction mixture and the mixture was stirred for 20 min, then it was transferred into a dialysis membrane (6-8 KDa). The mixture was dialyzed alternately with distilled water and 2.5% EDTA aqueous solution until the color of the mixture disappeared. After that, the mixture was dialyzed with distilled water for another 2 days, and lyophilized to obtain MiniAP4-PEG-Lys₇-CA₈ monomer. MiniAP4-PEG_{5k}-K₇ was analyzed by MALDI-TOF mass spectrometry, calcd. for average 10,024.4283, found average is 9900-10100 (Figure 13a).

The procedures of preparation of LXY30-PEG-Lys₇-CA₈ monomer and AVPI-PEG-Lys₇-CA₈ monomer via click chemistry was similar to the MiniAP4-PEG-Lys₇-CA₈ monomer. In MALDI-TOF mass spectrometry, LXY30-PEG-Lys₇-CA₈ monomer calcd. for average 10,258.3765, found average was 10100-10300 (Figure 13b); AVPI-PEG-Lys₇-CA₈ monomer calcd. for average 9639.3050, found average was 9600-9900 (Figure 13c).

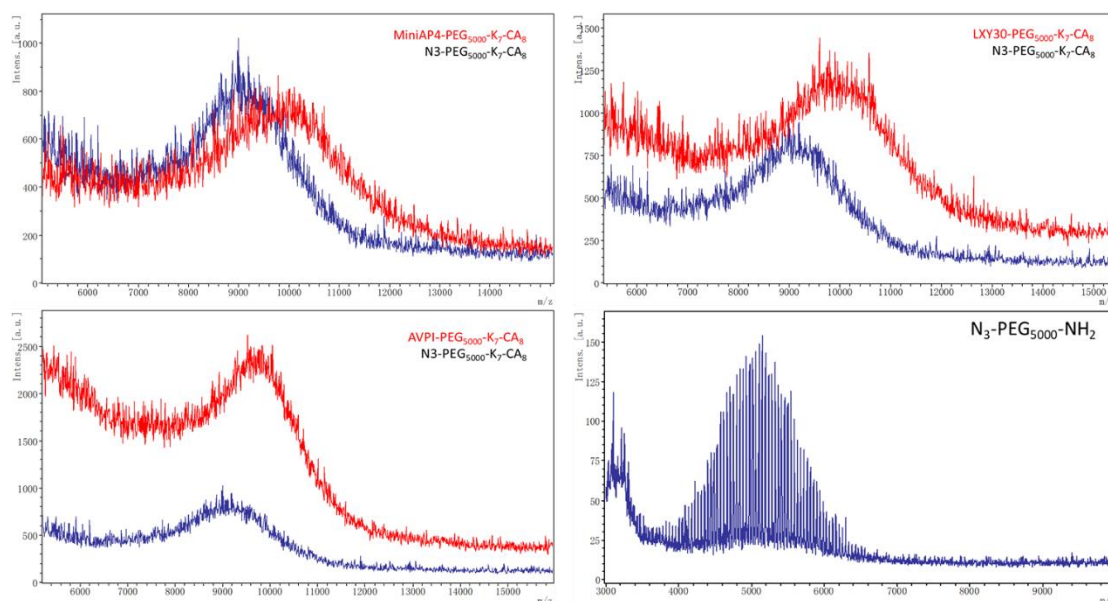


Figure 13. Mass spectrum of monomer of (a) MiniAP4-PEG_{5k}-K₇-CA₈, (b) LXY30-PEG_{5k}-K₇-CA₈, (c) AVPI-PEG_{5k}-K₇-CA₈, (d) N₃-PEG_{5k}-OH.

3.2.7 Preparation of Peptide-Conjugated Nanoparticles

The formation method of NPs was implemented as previous work. [21] To be brief, MiniAP4-PEG-Lys₇-CA₈ monomer (10 mg) was dissolved in chloroform (2 mL), and then combined with DID dye methanol solution (100 μL, 5 mg/mL). Subsequently, the solvents were slowly evaporated under vacuum to form a thin layer. Afterward, PBS (10×, 1 mL) was introduced into the flask and it was shaken for 3 h, then the solution of formed NPs was filtered through a 0.22 μm filter before using for *in vivo* assays. The particle size distribution and zeta potential of NPs were measured by DLS using Zetasizer (Malvern) (Figure 14). The preparation of NPs of N₃-PEG-Lys₇-CA₈, LXY30-PEG-Lys₇-CA₈, and AVPI-PEG-Lys₇-CA₈ followed the same procedure.

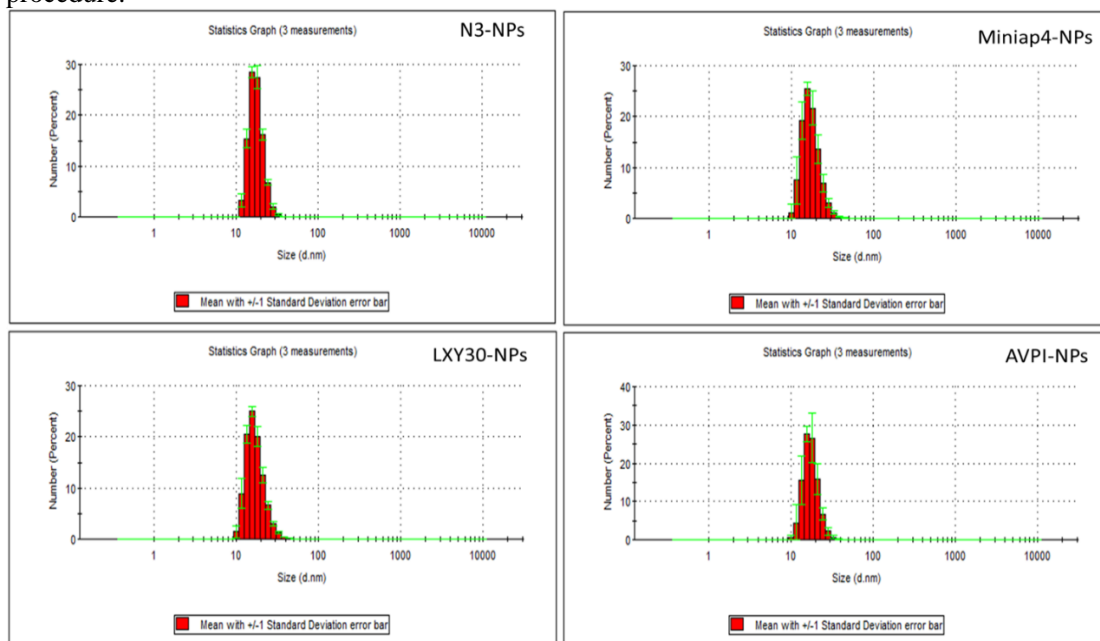


Figure 14. DLS of N₃-NPs, MiniAP4-NPs, LXY30-NPs, AVPI-NPs.

3.3 Biological and In Vivo Assays

3.3.1 The Conjugates of MiniAP4-Biotin and Streptavidin-Cy5.5

7.2 nmol of MiniAP4-biotin and 1.8 nmol of Streptavidin-Cy5.5 were co-incubated at 4°C overnight, another 1.8 nmol of Streptavidin-Cy5.5 was incubated at 4°C overnight. Then MiniAP4-biotin bonded (or not) Streptavidin-Cy5.5 was injected in mice (100 μL/10g body weight) via the tail vein. After 24h, the mice were euthanized and their organs were excised for imaging. Organs were placed on a transparent sheet and the images were captured on Kodak IS2000MM image station (Rochester, NY).

3.3.2 Dye (DID) Loaded N₃-NPs(DID) and MiniAP4-NPs(DID) in Healthy Mice

The mice were divided into two groups, group A and group B. In group A, MiniAP4-NPs(DID) (10 mg/mL NPs, 0.5 mg/mL DID) was injected into mice via the tail vein (100 μL/10g body weight). And in group B, N₃-NPs(DID) (10 mg/mL NPs, 0.5 mg/mL DID) was injected into mice. The injection time was scheduled 24h, 12h, 6h, 4h, 2h, 0.5h before euthanasia. Afterward, the mice were euthanized and their organs were excised for imaging. Organs were washed and settled

in PBS separately, then they were placed on transparent sheets, and images were captured on Kodak IS2000MM image station (Rochester, NY).

3.3.3 Dye (DID) Loaded N₃-NPs(DID) and MiniAP4-NPs(DID) in Tumor Bearing Mice

Mice bearing oral cancer were divided as group A and group B. In group A, MiniAP4-NPs(DID) (10 mg/mL NPs, 0.5 mg/mL DID) was injected via the tail vein (100 μ L/10 g body weight), and in group B, N₃-NPs(DID) (10 mg/mL NPs, 0.5 mg/mL DID) was injected into mice. The injection time was scheduled as 6h, 4h, 3h, 2h, 1h, 0.5h before euthanasia. Afterward, the mice were euthanized and their organs were excised for imaging. Brains and tumors were washed and settled in PBS separately, then they were placed on transparent sheets, and images were captured on Kodak IS2000MM image station (Rochester, NY). Tissue homogenization was performed to analyze the concentration of dye DID in the brain. First, the brain tissue was washed with PBS to remove the blood, dried with filter paper, and weighed. Then the tissue was cut into small pieces with scissors and placed in RIPA lysis buffer (the dosage is 6 times the tissue weight). Then the shredded tissue was poured into a homogenization tube, another portion of RIPA lysis buffer (the dosage is 3 times the tissue weight) was added, followed by homogenization for 10 minutes and sonication for 1 minute. Finally, DCM was added to the homogenized tissue and shaken for 24 hours, the organic phase was collected, then DCM was added to repeat the extraction. The organic phases were combined and diluted to 5 mL, and their fluorescence intensities were measured to calculate the concentration of DID in the mice brains.

4. Conclusion

Herein, the BBB shuttle peptide MiniAP4 and PEG_{5k}-Lys₇-CA₈ dendrimer were conjugated to prepare a novel drug delivery platform, which can penetrate BBB and BTB for the treatment of brain tumors, thereby enhancing the cellular uptake of nanoparticles payloads. *In vivo* assays have shown that MiniAP4-NPs can improve the delivery of cargo-loaded nanoparticles through the BBB. Compared with streptavidin-cy5.5 alone, it was found that the combination of MiniAP4-biotin and streptavidin-cy5.5 injected into mice showed greater potential to improve BBB penetration. Further *in vivo* study has shown that MiniAP4-NPs can transport more cargos to the brains of both healthy and tumor-bearing mice than N₃-NPs. By studying the metabolism and tissue distribution of NPs(DID), we also found that after 6 hours of injection, the concentration of N₃-NPs(DID) and MiniAP4-NPs(DID) in the mice brain dropped to a relatively low level. After injection, MiniAP4-NPs was first distributed in the lungs, and then the NPs(DID) concentration in the liver, kidneys, and brain began to increase. Thereafter, the NPs(DID) concentration in the liver continued to increase, while the cargo concentration in other organs began to decrease, which means that most NPs(DID) start metabolism and excretion. Interestingly, compared with N₃-NPs(DID), we also found that MiniAP4@NPs have more potential in penetrating tumors, there is a possibility that MiniAP4 peptide may also be a BTB shuttle peptide. Meanwhile, we introduced tumour targeting peptide LXY30 and cytotoxic peptide AVPI into this drug delivery system to obtain brain tumour targeting agent AVPI@MiniAP4@LXY30-NPs.

References

-
1. B. Oller-Salvia, M. Sánchez-Navarro, E. Giraltab and M. Teixidó. Blood-brain barrier shuttle peptides: an emerging paradigm for brain delivery. *Chem. Soc. Rev.*, **2016**, *45*, 4690-470.
 2. W. M. Pardridge. Receptor-mediated peptide transport through the blood-brain barrier. *Endocr. Rev.*, **1986**, *7*, 314-330.
 3. M. Malakoutikhah, M. Teixid, and Ernest Giralt. Shuttle-mediated drug delivery to the brain. *Angew. Chem. Int. Ed.* **2011**, *50*, 7998-8014.

-
4. M. Sánchez-Navarro, et al. Blood–brain barrier peptide shuttles. *Curr. Opin. Chem. Biol.* **2017**, *38*, 134-140.
 5. S. Silva, A. J. Almeida and N. Vale. Combination of cell-penetrating peptides with nanoparticles for therapeutic application: a review. *Biomolecules* **2019**, *9*, 22-45.
 6. B. Oller-Salvia, M. Sanchez-Navarro, S. Ciudad, M. Guiu, et al. MiniAp-4: A venom-inspired peptidomimetic for brain delivery. *Angew. Chem.* **2016**, *128*, 582-585.
 7. Y. Li, K. Xiao, W. Zhu, W. Deng, K.S. Lam. Stimuli-responsive cross-linked micelles for on-demand drug delivery against cancers. *Adv. Drug Deliv. Rev.* **2014**, *66*, 58-73.
 8. F. F. Davis. The origin of pegnology. *Adv. Drug Deliv. Rev.* **2002**, *54*, 457-458.
 9. V. Torchilin. Tumor delivery of macromolecular drugs based on the EPR effect. *Adv. Drug Deliv. Rev.* **2011**, *63*, 131-135.
 10. K. Xiao, J. Luo, Y. Li, J.S. Lee, G. Fung, K.S. Lam. PEG-oligocholeic acid telodendrimer micelles for the targeted delivery of doxorubicin to B-cell lymphoma. *J. Control. Release* **2011**, *155*, 272-281.
 11. K. Xiao, Y. Li, J.S. Lee, A.M. Gonik, T. Dong, et al. “OA02” peptide facilitates the precise targeting of paclitaxel-loaded micellar nanoparticles to ovarian cancer in vivo. *Cancer Res.* **2012**, *72*, 2100-2110.
 12. Y. Li, K. Xiao, J. Luo, J. Lee, S. Pan, K.S. Lam. A novel size-tunable nanocarrier system for targeted anticancer drug. *J. Control. Release* **2010**, *144*, 314-323.
 13. Y. Li, K. Xiao, W. Zhu, W. Deng, K.S. Lam. Stimuli-responsive cross-linked micelles for on-demand drug delivery against cancers. *Adv. Drug Deliv. Rev.* **2014**, *66*, 58-73.
 14. W. Xiao, N. Suby, K. Xiao, T. Lin, et al. Extremely long tumor retention, multi-responsive boronate crosslinked micelles with superior therapeutic efficacy for ovarian cancer. *J. Control. Release* **2017**, *264*, 169-179.
 15. X. Yang, X. Xue, Y. Luo, T. Lin, et al. Sub-100 nm, long tumor retention SN-38-loaded photonic micelles for tri-modal cancer therapy. *J. Control. Release* **2017**, *261*, 297-306.
 16. L. Zhang, D. Jing, L. Wang, Y. Sun, et al. Unique photochemo-immuno-nanoplatfrom against orthotopic xenograft oral cancer and metastatic syngeneic breast cancer. *Nano Lett.* **2018**, *18*, 7092-7103.
 17. L. Zhang, T. Yin, B. Li, R. Zheng, C. Qiu, K.S. Lam, Q. Zhang, and X. Shuai. Size-modulable nanoprobe for high-performance ultrasound imaging and drug delivery against cancer. *ACS Nano.* **2018**, *12*, 3449-3460.
 18. K. Xiao, T. Lin, K.S. Lam, Y. Li. A facile strategy for fine-tuning the stability and drug release of stimuli-responsive cross-linked micellar nanoparticles towards precision drug delivery. *Nanoscale* **2017**, *9*, 7765-7777.
 19. W. Xiao, T. Li, F.C. Bononi, D. Lac, I.A. Kekessie, Y. Liu, E. Sanchez, A. Mazloom, A. Ma, J. Lin, J. Tran, K. Yang, K.S. Lam and R. Liu, *EJNMMI Research*, **2016**, *6*, 18.
 20. J. Huang, Z. Zhang, B. Wu, J. F. Cellitti, X. Zhang, R. Dahl, C. Shiau, K. Welsh, A. Emdadi, J. L. Stebbins, J. C. Reed, M. Pellicchia. *J. Med. Chem.* **2008**, *51*, 7111-7118
 21. K. Xiao et al. The effect of surface charge on in vivo biodistribution of PEG-oligocholeic acid based micellar nanoparticles. *Biomaterials* **2011**, *32*, 3435-3436.

Acknowledgement

At the end of my doctoral research and study, when I look back on the entire study period, I am always grateful. First of all, I would like to sincerely thank my advisor Prof. Luca Gentilucci for his meticulous guidance and continuous support. Under his guidance, I have been researching and writing this thesis. His profound, rigorous academic knowledge, and unique scientific research insights have benefited me a lot. At the same time, I would also like to thank Prof. Kit Lam for his patient explanation and careful guidance of the research topics I engaged in during my study at UCdavis. In addition, I would like to thank Prof. Rosella De Marco for her help, guidance and support in my research work.

I would also like to thank the following people who helped, guided and supported my research:

Arianna Greco, Simone Ioannone for their contribution in chapter 2;

Prof. Andrea Bedini, Prof. Santi Spampinato, Lorenzo Comellini, Dr. Roberto Artali for their contribution in chapter 3;

Prof. Andrea Bedini, Francesco Fontaniva, Riccardo Quaia for their contribution in chapter 4;

Federica Santino, Prof. Daria Giacomini for their contribution in chapter 5;

Prof. Enrico Rampazzo, Prof. Luca Prodi, Prof. Mayra Paolillo, Pierre Picchetti, Francesca Gallo, Prof. Natalia Calonghi for their contribution in chapter 6;

Dr. Yi Wu, Dr. Lu Zhang, Dr. Ruiwu Liu, Dr. Wenwu Xiao, Dr. Luke Solano, Chris Baehr, Shivani Bansal, Xingjian Yu for their contribution in chapter 7.

Dr. Andrea Garelli, and Dr. Stefano Grilli, Dr. Lucia Ferrazzano for their help, and technical support;

My fellow labmates, Dr. Michele Anselmi, Periklis Karamanis, Rossella Petruzzelli, Francesco Fontaniva, Riccardo Quaia, Francesco giunchino, Michele Guerzoni, Davide di Giammatteo, Jessica Benetti, Eliana Muscoso, Pasquale Stavole;

China Scholarship Council (CSC) for financial support.

Last but not least, I want to thank my family, my parents, sister and brother for always being there for me.

With all your help and support, my three years of study and research have become substantial, exciting and meaningful.